Investigations into the Dynamic Molecular Mechanisms that Govern the Final Stages of Neurotransmitter Release

by

Alice D. Lam

A dissertation submitted in partial fulfillment
of the requirements for the degree of
Doctor of Philosophy
(Neuroscience)
in the University of Michigan
2008

Doctoral Committee:

Professor Edward L. Stuenkel, Chair
Professor Stephen K. Fisher
Professor Benjamin L. Margolis
Professor Michael D. Uhler
Assistant Professor Jose A. Esteban
Research Assistant Professor Mary A. Bittner

**for mom and dad,
with much love and gratitude**

Acknowledgements

Super thanks to my husband, Ziba Rifulus Scott, for all of his love, patience, support, diplomacy, and stealthy ninja moves. I couldn't have done this without you! Thank you for being ridiculously understanding all those times I said I had an hour's worth of experiments to do in the lab, and it ended up taking 5 hours instead. Thanks for bringing dinner and for keeping me company on those very-late-nights-turned-early-mornings in the lab, and for never complaining, even when you had to get up early to go to work the next day. Thanks for whole-heartedly supporting my scientific endeavours and escapades, even if it meant being apart for the summer, or for several days or weeks at a time. Thanks for your sound advice for all of those sticky situations I somehow always managed to get myself into. Thanks for being my technical guru and in-house 3-D graphics artist. Thanks for driving me to work in the winter because you know how much I hate the cold. Thanks for allowing me to vent all of the frustrations of science upon you, and for never once giving me the impression that you were sick of hearing about it. Thank you for being my flashlight when I was in a dark place.

Many many many many many many many many many many many many many many many many many many many many many many thanks to my mentor and friend Ed Stuenkel, for always pushing me to go one step beyond what I thought was possible, and for giving me the growing space to develop into an independently thinking scientist. Thank you for treating me as your colleague rather than as your student, and for giving me the confidence to pursue my own scientific ideas and interests. Thanks for putting up with my scientific growing pains, and for your words of encouragement during rough times. Thanks for helping me write my NRSA, and for suffering through the atrocities of someone who had never even heard of a specific aim before. Thanks for sending me to Woods Hole for a whole summer, even when money was tight and the situation was grim. Thanks for sending me to the Middle East, so that I could be caught under sniper fire as I disembarked my private jet. Thanks for reminding me to always keep a sense of humor about life in general. Thanks for the fun, the frustration, the good times and the bad, the fish tank, the skateboard rack, First Fridays, setting off illegal fireworks at my wedding, useless bickering that just boiled down to semantics in the end, ten shekels, teaching me how to drive stick shift, exciting travels all over the world, prank calls from the NIH, not getting mad all of those times I schooled you really really badly on the basketball court, and for your general irreverence.

Thanks to the many former and current members of the Stuenkel Lab for putting up with me, and for their help, camaraderie, encouragement, discouragement, DNA constructs, stale cookies, middle eastern pastries, thoughtfulness, amusements, dollar burger Tuesdays, and in general, for providing a highly memorable experience: Bill Ho, Quanwen Li, Svetlana Gladycheva, Dequan Tian, Jiang Liu, Flora Lee, Matt Merrins, Rishi Chaudhuri, Ray Wu, Ashhar Ali, Helen Lee, Randy Hlubek, Sahar Ismail, Woody Hoerauf, Ashley Fletcher, and Chris Jaeger. Special thanks to Matt Merrins, for teaching me most of the molecular biology techniques I now know. Thanks to Steve Ernst, for being willing to help out with wacky new ideas for imaging experiments, and for his refreshing presence.

Thanks to our neighboring labs, the Lopatin Lab and the Rui Lab, for coming to my rescue when I needed to borrow reagents or supplies, and for allowing me to use their lab equipment. Thanks to the Holz lab for helpful advice and reagents for secretion assays and chromaffin cells, and for advice on TIRF imaging. Thanks to the Ashery Laboratory in Tel Aviv for a fun and fruitful scientific collaboration. Thanks to

Adam Hoppe, for useful discussions on FRET imaging, and to Dan Axelrod, for useful discussions on TIRF imaging.

Thank you to the members of my Dissertation Committee (Mary Bittner, Jose Esteban, Steve Fisher, Ben Margolis, Ed Stuenkel, and Mike Uhler) for all of their time, encouragement, intellectual input and ideas, and for perhaps being the only people in the world who will ever read this dissertation in its entirety.

Thanks to the University of Michigan Medical Scientist Training Program (Ron Koenig, Penny Morris, Ellen Elkin, Hillka Ketola, Laurie Koivupalo) for all of their help, support, and funding through the years. Thanks also to the Neuroscience Program and to the Department of Molecular and Integrative Physiology for funding and administrative support. Thanks to the National Institutes of Health, for funding most of my graduate work (NRSA NS053263).

Thanks to my family for their unconditional love (even in times where I probably didn't warrant it). Thanks Mom and Dad, for doing everything in your power to make sure I would have all of the opportunities I needed to come as far as I have (and to maybe even go a bit further!). Thanks Mom for constantly worrying about everything (like a mother should), and for baking me cookies even though they aren't good for my health. Thanks Dad, for always going through your checklist over the phone to make sure everything was going fine, and for teaching me how to load the dishwasher correctly. Thanks to my sister Tina, for always understanding where I'm coming from (twin thing), and for encouraging me to "Be like Mike, but shorter, and don't play basketball." Thanks to my brother Albert, for not generally understanding from where it is I come, but for being a pretty decent piano player despite of it.

Chapter 2 of this dissertation was previously published in Molecular Biology of the Cell (http://www.molbiolcell.org/cgi/content/full/19/2/485) and copyrighted by the American Society for Cell Biology. Many thanks to the co-authors of this publication:

Petra Tryoen-Toth, Nicolas Vitale, and Bill Tsai. Thanks also to: Ron Holz and Mary Bittner for secretion assay advice, PC-12 cells, bovine adrenal glands, and other reagents; Matt Merrins for molecular biology advice; Rishi Chaudhuri and Ray Wu for technical assistance; and Joshua Zimmerberg and Stuart McLaughlin for helpful comments. This work was supported by grants from the National Institutes of Health (R01 NS039914 and NS053978, ELS; F31 NS053263-01, ADL), as well as from the Agence Nationale de la Recherche (ANR-05-BLAN-0326-01, NV) and by the Association pour la Recherche sur le Cancer (Grant 4051, NV). ADL was also supported in part by a Medical Scientist Training Grant from the National Institutes of Health (GM007863).

Chapter 3 of this dissertation was previously published in the Journal of Biological Chemistry (http://www.jbc.org/cgi/content/full/282/31/22887) and copyrighted by the American Society for Biochemistry and Molecular Biology. Many thanks to the co-authors of this publication: Svetlana Gladycheva, Jiang Liu, Matt Merrins, Ofer Yizhar, Stephen Lentz, Uri Ashery, and Stephen Ernst. This work was supported by National Institutes of Health (NIH) Grants NS39914 and NS053978 (to ELS), NIDDK, NIH, Grants P30DK 34933 and P60DK20572 (to SAE), and National Research Service Award RSA NS053263 (to ADL). ADL was also supported in part by National Institutes of Health Medical Scientist Training Grant GM007863. This work utilized the Morphology and Image Analysis Core of the Michigan Diabetes Research and Training Center funded by NIDDK, National Institutes of Health Grant NIH5P60 DK20572.

Table of Contents

Chapter

List of Figures

Figure

Chapter 1

Introduction

Membrane fusion is an important phenomenon that occurs ubiquitously throughout cell biology. Indeed, this process underlies the compartmentalized nature of eukaryotic cells, by allowing for communication between most intracellular compartments via vesicles that bud from one compartment and subsequently fuse and merge their contents with another. Membrane fusion plays many diverse and critical roles in the physiological integration of higher level, multi-cellular organisms. This process is an essential step in the regulation of homeostatic mechanisms involving hormone secretion, mast cell degranulation during an immune response, the acrosomal reaction that occurs during fertilization of an oocyte by a sperm cell, and release of pancreatic enzymes that allow for digestion of a meal. Membrane fusion is also paramount to the process of chemical neurotransmission, which ultimately underlies the ability of higher-level organisms to move, sense their environment, feel emotions, remember, forget, and ponder important issues such as, “What shall I have for dinner tonight?”.

Biological membrane fusion reactions involved in the secretion of proteins and other chemicals from the cell can be broadly classified into two types: constitutive and regulated (for review, see [1]). For secretion of proteins, both constitutive and regulated pathways involve translocation of the proteins first through the rough endoplasmic reticulum, and then through the Golgi stacks, where the proteins are ultimately sorted for secretion through either the constitutive or regulated pathways. Constitutive secretion is usually considered the default pathway for secretion, which (for proteins) occurs in the absence of the correct sorting signals on the protein to be secreted, and in general, occurs without the need for a specific physiological trigger. Granules destined for constitutive release do not contain proteins in high concentrations, and moreover, as these granules are constantly being secreted, large intracellular storage pools of these granules are not retained. In contrast, regulated secretion requires the sorting of specific proteins or chemicals into specialized secretory granules, in which these substances become highly concentrated. For secretory granules containing proteins, the concentrations of the proteins within the secretory granules can be as high as 10-200 times the concentration of these proteins in early Golgi compartments; as such, these granules appear electron-dense in EM micrographs, leading to their being termed dense-core granules. Notably, secretion of these granules requires a specific physiological stimulus, which generates a transient rise in intracellular calcium concentration that directly triggers the fusion of these granules with the plasma membrane. As these granules are only secreted in response to a stimulus, large intracellular storage pools of these granules are often present within the cell.

Of all the different types of regulated secretion, perhaps the most elegantly controlled process is that occurring when a synaptic vesicle filled with neurotransmitter fuses with the plasma membrane of a neuron to release its contents into the synaptic cleft. Neurotransmitter release is triggered by the influx of calcium that occurs in response to the arrival of an action potential at the nerve terminal, which depolarizes the plasma membrane and activates voltage-gated calcium channels. Unlike most other secretory processes, neurotransmission occurs on an extremely rapid timescale (on the order of microseconds to milliseconds) and requires precise spatial localization. Moreover, unlike the protein-filled dense-core granules described above, synaptic vesicles are filled with chemical neurotransmitters. As such, these vesicles can be synthesized and recycled directly from the plasma membrane or early endosome compartments, and can be filled by uptake of neurotransmitter directly from the cytoplasm, across transporters in the vesicle membrane. However, synaptic vesicles also require some protein constituents. These synaptic vesicle proteins are transported down the axon in membrane compartments, so that full assembly of synaptic vesicles can occur at the synapse (for review, see [2]). Notably, in contrast to dense-core vesicles, which can often be up to several hundred nanometers in diameter, synaptic vesicles are one of the smallest intracellular compartments known, with a diameter of roughly 50nm.

Neurotransmitter release and neurosecretion can both be described as multi-step, sequential processes (for review, see [3]). In neurosecretion, newly synthesized secretory granules are actively translocated from the Golgi network along microtubule tracks to the plasma membrane, where they then become tethered, or “docked.” Translocation of synaptic vesicles to the plasma membrane is a bit different, as synaptic vesicles are synthesized and recycled directly at the nerve terminal. Most vesicles in the nerve terminal are found in a diffusionally restricted vesicle cluster located adjacent to the presynaptic active zone, and are held together by actin filaments and other proteins. Mobilization of vesicles from this cluster, to allow vesicles to approach the active zone and become docked there, is thought to be under the control of the synapsin proteins (for review, see [4, 5]). Following docking, a series of biochemical reactions, termed “priming”, then takes place on or near the vesicle, to render the vesicle fusion-competent. At some point, influx of calcium into the nerve terminal triggers the fusion of docked and primed vesicles with the pre-synaptic plasma membrane, allowing for the release of neurotransmitter into the synaptic cleft. Following fusion, vesicles are recycled for reuse by the process of endocytosis, which has been shown to occur in units that exactly match the size of the exocytosed vesicles [6]. Notably, endocytosis is the rate-limiting step for nervous system throughput, as it occurs on a much slower time scale (on the order of tens of seconds) compared to exocytosis (for review, see [5, 7]).

A contemporary model on how the process of membrane fusion might be molecularly mediated is termed the “SNARE hypothesis” [8]. In the original model of the SNARE hypothesis (which has since been largely revised), specificity of the docking reaction was determined by proteins on the vesicle membrane and target membrane, termed v-SNAREs and t-SNAREs, respectively (SNARE = soluble NSF attachment protein (SNAP) receptor). As v-SNAREs and t-SNAREs were thought to be localized to specific and distinct intracellular compartments, and as each v-SNARE was believed to interact specifically with only one cognate t-SNARE, the idea of SNARE-pairing ensured that vesicles would only dock at membranes where they were destined to fuse. Moreover, the v-SNARE / t-SNARE complex was proposed to provide a binding site for the ATPase NSF (N-ethylmaleimide sensitive factor) and its SNAP (soluble NSF attachment protein) co-factors. Hydrolysis of ATP by NSF would then provide the energy required to drive membrane fusion, through the disassembly of the SNARE complex.

Since the original SNARE hypothesis was put forth in 1993, much progress has been made, and new experimental paradigms and methods developed, ultimately leading to modifications of this hypothesis, and generation of many new questions to address. A recent review of the molecular mechanisms of membrane fusion is presented below, with a primary focus on membrane fusion as it occurs during neurotransmission and neurosecretion (for an overview, see Figure 1.1). While these processes occur on very different time scales, and while experimental findings on regulated exocytosis from neurosecretory cells cannot always be assumed to extrapolate to synaptic vesicle release in neurons, these processes do in fact share remarkable similarities in their underlying molecular machinery. Moreover, as neurosecretory cells are much larger in size, they are, therefore, more amenable to study than central synapses. As a result, in many cases, experiments in neurosecretory cells have provided the first insights into regulatory mechanisms of membrane fusion.

Docking

The concept that vesicles must first become docked and tethered at the target membrane prior to membrane fusion arose primarily as a result of electron micrographs of neurons and neuroendocrine cells that demonstrated a distinct and non-random accumulation of vesicles in close proximity (<30nm) to the target membrane under resting conditions [9, 10]. As the number of docked vesicles far exceeded the number of vesicles released upon stimulation (ie, the readily releasable pool), it was assumed that further biochemical reactions were required following docking, to render each vesicle fully competent for fusion (see section on Priming).

More recently, docking of fluorescently-labeled vesicles in live cells has been studied using TIRF (total internal reflection fluorescence) microscopy, allowing for a more dynamic view of the vesicle motions that occur near the membrane prior to fusion. TIRF microscopy utilizes the exponentially decaying evanescent wave that is created when light is totally internally reflected at a glass-water interface, to selectively illuminate a thin (~100-300nm thick) “footprint” of a cell that includes only those regions of the cell closely apposed to the coverslip. As such, TIRF microscopy allows for extremely high axial resolution of events occurring at or near the plasma membrane; in the case of secretory vesicles, the Z-motions of individual vesicles can be closely tracked over time with millisecond and nanometer resolution (for review, see [11, 12]). TIRF studies have demonstrated that a population of secretory vesicles closely apposed to the plasma membrane in neuroendocrine cells undergoes highly restricted, non-Brownian motions, supporting the notion that these vesicles are somehow tethered at the membrane, or are trapped in some sort of a molecular cage [13-15]. However, these studies also bring into question whether docking is required for fusion, as during sustained stimulation, vesicles are sometimes (~20%) observed to approach the plasma membrane from deep within the cell and to fuse within 300msec, seemingly without the need to undergo a stable pre-docking stage [16].

One of the inherent problems with the concept of vesicle docking is that this process has almost always been defined morphologically, and as such, its exact functional significance is still not entirely clear. For instance, it is possible that some docked vesicles are actually in a dead-end, non-releasable state; moreover, the necessity of vesicles to be docked prior to fusion has not been clearly demonstrated (for review, see [17]). Surprisingly, at the frog neuromuscular junction, vesicles of the readily releasable pool were not preferentially localized adjacent to the plasma membrane, but rather, were dispersed throughout the nerve terminal [18]. On the other hand, in individual hippocampal synapses, the average number of docked vesicles at the active zone correlates to the size of the readily releasable pool, suggesting that the docked pool represents the readily releasable pool. Furthermore, studies in bovine adrenal chromaffin cells demonstrated that newly synthesized vesicles are preferentially localized to the plasma membrane, whereas older vesicles (~16 hours old) were found deeper with the cell; moreover, nicotine-stimulated exocytosis occurred primarily from the pool of newly synthesized vesicles [19]. Data regarding vesicle docking may also be difficult to interpret in a functionally meaningful way, due to the combination of the strict (yet somewhat arbitrary) morphological criteria set to define what constitutes a docked vesicle (eg, less than 30nm from the plasma membrane), in addition to fixation artifacts that may often arise during preparation of samples for electron microscopy [20]. However, future TIRF studies in which the mobility of vesicles can be tracked over time, concomitantly with genetic manipulations and functional readouts of fusion competence, will likely pave the way to establishment of a more meaningful, biochemical definition of docking. In other words, if docking does have a functional significance, this should be borne out by determination of molecular pathways that specifically mediate it.

The original SNARE hypothesis suggested that specificity of docking would be mediated through the specificity of SNARE pairing. However, SNARE proteins often demonstrate promiscuity in their interactions in vitro [21, 22], and moreover, can be found not only on the compartments on which they mediate fusion, but also on compartments involved in their biosynthesis and recycling. A primary role for SNARE proteins in docking was further ruled out by experiments demonstrating that vesicle docking remained intact even after genetic deletion or cleavage of the SNARE proteins using proteolytic toxins [23-25]. It is now widely believed that the initial specificity of docking and tethering is under control of the Rab family of proteins and their effectors. This is largely the result of extensive work carried out on Rab protein homologs in yeast secretory pathways (for review, see [26]).

Rab proteins are ubiquitously expressed members of the Ras family of small GTPases that play key roles in vesicular transport processes. Rabs act as molecular switches, cycling between GTP-bound (“active”) and GDP-bound (“inactive”) states. In their GTP-bound state, Rabs often associate with membrane compartments via an exposed C-terminal geranylgeranyl moiety. GTP-bound Rab proteins can also bind to and recruit specific effector molecules to these compartments. Upon GTP hydrolysis, GDP-bound Rabs associate with GDI (guanine dissociation inhibitor) proteins, which mask the geranylgeranyl moiety on the Rabs, thereby dissociating the Rab proteins from the membrane compartment. While Rab proteins thus exhibit clear active and inactive states, what is quickly becoming apparent is that it is not so much the particular state, but rather the cycling between states, that is critical for Rab protein function [27].

In neurons and neuroendocrine cells, Rab3 is highly abundant on synaptic vesicles and secretory granules [28]. Rab27 also localizes to secretory granules, but may or may not be present on synaptic vesicles, as Rab27 was not detected in mouse brain lysates, yet was detected in neurons in C. elegans [29, 30]. Overexpression and knockdown studies indicate that both Rab3 and Rab27 have effects on docking in neurosecretory cells [31-33]; however, the docking phenotype at neuronal synapses was unaffected in a complete Rab3 knockout mouse (ie, quadruple deletion of all four Rab3 isoforms) [34]. Among the known Rab3/27 effectors are Slps (synaptotagmin-like proteins, which contain two C2 domains) of which rabphilin and granuphilin-a are members; Slacs (synaptotagmin-like proteins lacking C2 domains), of which melanophilin, MyRIP, and Noc2 are members; RIMs (rab3 interacting molecules), and Munc13-4 proteins. Granuphilin-a (Slp4a) interacts with Rab27a (and may also interact with Rab3); moreover, it has been shown to bind to the Q-SNARE Syntaxin1 as well as Munc18-1, two key members of the secretory machinery [35, 36]. Importantly, the granuphilin-a knockout mouse exhibited reduced numbers of docked vesicles in pancreatic β cells (although surprisingly, secretion was found to be enhanced) [37]. Rabphilin is a soluble protein recruited to vesicles on interaction with Rab3 or Rab27, and has been shown to interact with the plasma membrane SNARE, SNAP-25 [38]. In PC12 cells, overexpression of rabphilin resulted in an increase in docked vesicles as visualized under TIRF; overexpression of a mutant rabphilin that was unable to bind to SNAP-25 resulted in a decrease in the number of docked vesicles [38]. However, as the rabphilin knockout mouse exhibited no synaptic phenotype, it is unclear what the exact function of these molecules are in neurons [39]. RIM proteins are large, plasma-membrane proteins that comprise part of the active zone complex in neurons. While the RIM1α knockout mouse demonstrated defects in hippocampal and cerebellar LTP (long term potentiation), there were no apparent defects in vesicle docking [40].

More recently, a compelling role for Munc18-1 in vesicle docking has also been described. Munc18-1 is a member of the highly conserved SM (Sec/Munc18) family of proteins (see section below on SNARE regulators) that exhibits a high affinity interaction with the plasma membrane SNARE, Syntaxin1. Vesicle docking in neurons was strongly reduced in mice heterozygous for Munc18-1, and expression levels of Munc18-1 were found to correlate to the number of docked vesicles detected at active zones [41]. In Munc18-1 null embryonic adrenal chromaffin cells, vesicle docking was reduced 10-fold, with no change in the total vesicle number [42]. The ability of the exogenously expressed Munc18-1 to rescue this phenotype required its ability to bind syntaxin1, as overexpression of Munc18-1 mutants that lacked the ability to bind syntaxin1 still resulted in reduced numbers of docked vesicles [15, 43]. A potential caveat to the studies using the Munc18-1 null mice is that knockout of Munc18-1 results in a 50% reduction in the expression levels of the plasma membrane SNARE syntaxin1; thus, the decrease in syntaxin1 levels may partially account for the Munc18-1 null phenotype [42]. However, in Munc18-1 null adrenal chromaffin cells, overexpression of a Munc18-1 mutant that was sufficient to rescue the expression level of syntaxin1 to that of control cells, was still not sufficient to rescue vesicle docking to control levels [43]. Furthermore, in C. elegans, mutant unc-18 worms also demonstrate severe defects in evoked neurotransmission, and the number of docked vesicles at the neuromuscular junctions of these worms is reduced to 36% of wild-type. While the expression level of syntaxin in these worms was also reduced by 50%, this effect cannot account for the unc-18 phenotype, as worms that are heterozygous for syntaxin do not phenocopy the unc-18 worm, and moreover, overexpression of syntaxin in unc-18 worms is not sufficient to rescue the unc-18 phenotype [44]. These experiments suggest that the effect of Munc18-1 knockout on docking is independent of the effects on syntaxin1 expression levels. Another compelling piece of evidence to suggest that Munc18-1 is important in vesicle docking is that the effect of Rab3A on docking has been shown to be dependent on Munc18-1. Overexpression of Rab3A in control chromaffin cells, but not in Munc18-1 null chromaffin cells, resulted in a substantial increase in docking [27]. Interestingly, Rab3A was also recently shown to directly bind to Munc18-1 [45]. Other additional mechanisms by which Munc18-1 mediates docking have also been proposed, and may involve interactions of Munc18-1 with proteins such as Mint (Munc18-interacting protein), DOC2, or granuphilin-a [46].

In sum, the molecular mediators and pathways involved in docking are continuing to be elucidated, but have also generated some puzzles. While small molecular weight GTPases (eg, Rabs/Ypt (yeast protein transport family)) and Munc18/Sec proteins especially appear to play key roles in docking, in many cases, these pathways converge onto SNARE proteins, for which a clear role for docking has not been demonstrated. Moreover, in the case of Rab3 and its effectors, the lack of a docking phenotype in neurons for these genetic knockouts is somewhat striking. An important consideration is that these results could potentially reflect the functional redundancy of proteins that operate in the docking pathway, particularly in the case of the Rab protein family, of which there are over 60 members in mammals [26]. Along these lines, despite the many genetic manipulations carried out to date, and despite the vast number of synaptic phenotypes that have been observed, surprisingly few of these genetic manipulations have resulted in notable docking phenotypes in neurons [17].

Priming

Unlike docking, which rests primarily on a morphological analysis, priming reactions required for regulated exocytosis have largely been defined functionally. The idea that vesicles must undergo a series of priming reactions following docking and prior to fusion was originally proposed as an explanation for why the number of vesicles docked at the plasma membrane or at active zones far exceeded the number of vesicles that was released upon stimulation (the readily releasable pool). However, many subsequent studies have supported the concept that specific biochemical priming reactions downstream of docking are required to attain fusion competence of vesicles. Indeed, the most convincing of these studies are the various genetic manipulations which alter the size of the primed (readily releasable) pool of vesicles, without altering the total number of docked vesicles [47-49].

Among the first studies of priming were secretion assays carried out on permeabilized neuroendocrine cells [50, 51]. Upon permeabilization, the secretory response of these cells to calcium was found to decrease with increasing time between permeabilization and the calcium stimulus, largely as a result of the diffusion of essential secretory factors out of the cell. As such, the term “priming” referred the biochemical reactions that were required to maintain sustained secretory competence following permeabilization. Notably, addition of concentrated fractions of cytosolic proteins to the semi-intact cells was sufficient to reconstitute secretion following permeabilization, and moreover, demonstrated that these reactions were readily reversible [52]. While secretion assays were critical for the initial discoveries of the key biochemical (ATP, pH, temperature) and protein requirements (phosphatidylinositol transfer protein, PITP; phosphatidylinositol phosphate kinase type I, PIP5KI; NSF; calcium-dependent activator protein for secretion, CAPS; etc) for vesicle priming (see below), they are inherently limited in terms of their low temporal resolution (on the order of seconds to minutes).

More recently, high temporal resolution membrane capacitance measurements made under patch-clamp recording in neuroendocrine cells or neurons have become a powerful tool to study the priming process with much higher temporal resolution (milliseconds). Capacitance measurements monitor changes in the total capacitance of the cell membrane, which based on the specific capacitance of cell membranes

($\sim 1\mu F/cm^2$), can be used to define the surface area of a cell's plasma membrane. These measurements thus report on the fusion of vesicles, where vesicle membrane is added to the cell membrane, resulting in an increase in total cell surface area. In conjunction with UV flash photolysis of caged calcium (which provides a globally uniform and instantaneous trigger to maximally drive secretion in a manner that is independent of localized calcium gradients), membrane capacitance measurements have clearly demonstrated that there exist multiple distinct kinetic steps by which vesicle fusion occurs [53, 54]. These studies have been carried out for a wide variety of cell types and preparations, including (and not limited to): adrenal chromaffin cells, the calyx of Held, retinal bipolar neurons, pancreatic β-cells, melanotrophs, and cardiac myocytes. Notably, the exocytotic responses of adrenal chromaffin cells in response to calcium uncaging have been the most thoroughly studied. Indeed, the response of adrenal chromaffin cells to calcium uncaging is characterized by an initial exocytic burst (occurring on the order of tens of milliseconds), followed by a slow and sustained phase of release (occurring on the order of seconds) (for review, see [55]). The exocytic burst is believed to represent fusion of two distinct readily releasable pools of vesicles that are docked and primed, whereas the sustained phase of release represents fusion of docked vesicles that must first undergo priming prior to release. Notably, these measurements allow for determination of both the size and release kinetics of each of these pools. In these experiments, the term "priming" refers to the processes that (re)fill/recruit vesicles to the readily releasable vesicle pools, and can be assessed by monitoring the refilling kinetics of these pools following their depletion. Importantly, the kinetic scheme established by these high time-resolution capacitance measurements has provided a quantitative and functional framework by which the effects of various genetic and biochemical manipulations on priming can be organized.

Data from both secretion assays and electrophysiological measurements have unequivocally established that priming reactions are dependent on Mg-ATP [52, 54, 56, 57] as well as calcium [56, 58-60]. The downstream effectors for these priming requirements have also begun to be defined, among which include the lipid messenger PI(4,5)P2 and NSF/SNAP.

Generation of PI(4,5)P2 is one of the major events occurring during the ATP-dependent priming process; indeed, PI(4,5)P2 production was estimated to account for 70% of the ATP-dependent component of secretion in permeabilized chromaffin cells [61]. Subsequently, two cytosolic enzymes involved in PI(4,5)P2 synthesis, PI(4)P 5-kinase [62] and PITP [63], were shown to be essential factors for the ATP-dependent priming of vesicles. More recently, genetic deletion of PI(4)P 5-kinase in mice resulted in multiple severe synaptic defects, including a reduction in the size of the readily releasable pool [64]. In adrenal chromaffin cells of these mice, both the size and refilling rates of the readily releasable pool were reduced, with a concomitant increase in the number of docked vesicles [65].

Despite clear evidence that PI(4,5)P2 is important in priming, the exact mechanisms by which it operates are still unclear. Notably, the requirement of PI(4,5)P2 in priming does not appear to be in its use as a substrate for PLC to produce diacylglycerol (DAG) and inosityol 1,4,5-triphosphate (IP3) [61]. One possibility is that PI(4,5)P2 may act to recruit key regulatory proteins to sites of fusion. A number of proteins critical for regulated exocytosis have been shown to bind to PI(4,5)P2, including synaptotagmin [66], rabphilin [67], CAPS [68], Munc18-interacting protein (MINT) [69], and syntaxin1 [70]. On a related note, PI(4,5)P2 may also be involved in clustering one or more of these proteins into membrane microdomains, which might then serve as hotspots for vesicle fusion. Clusters of PI(4,5)P2 have been observed in the plasma membrane of chromaffin cells and PC-12 cells, and in the latter case, a subset of

PI(4,5)P2 clusters was found to co-localize with syntaxin1 clusters [71, 72]. Another possibility is that effects of PI(4,5)P2 on priming may occur through interactions of PI(4,5)P2 with the cytoskeleton [73, 74].

A second use for Mg-ATP in priming occurs via its hydrolysis by NSF (N-ethylmaleimide sensitive fusion protein), an AAA-ATPase (AAA=ATPases associated with various cellular activities) that has been shown in yeast to be required for almost all intracellular trafficking steps [75]. NSF requires SNAP (soluble NSF attachment proteins) cofactors to allow it to bind to ternary SNARE complexes [76]. Upon binding, hydrolysis of ATP by NSF then provides the energy to disassemble these SNARE complexes [77]. As stated earlier, the original SNARE hypothesis posited that NSF was the fusion promoting protein, and that its disassembly of SNARE complexes would provide the energy required for membrane fusion. However, in vitro studies demonstrated that NSF activity is only required for a predocking stage that precedes fusion [78, 79], and moreover, that ATP, while required for priming, is not essential for the final triggering of exocytosis [80], necessitated a revision of this hypothesis [81].

It is now widely accepted that NSF and SNAP are involved in ATP-dependent priming, where they function to disassemble dead-end cis-ternary SNARE complexes (complexes that occur on the same membrane) to allow for the formation of functionally relevant, trans-ternary SNARE complexes (complexes that bridge the vesicle and target membranes). The evidence for this comes from studies in the yeast secretory pathway [82], secretion assays in neuroendocrine cells [83], synaptic physiology in the squid giant synapse [84], as well as membrane capacitance measurements in chromaffin cells [85]. In the latter study, dialysis of chromaffin cells with purified α-SNAP protein via patch pipette resulted in an increase in the size of the exocytic burst (with no effects on the release kinetics of the burst), in addition to an increase in the sustained phase of release, compared to control cells. Treatment with N-ethylmaleimide (NEM) had no effect on the initial size or release kinetics of the exocytic burst, but resulted in a decrease in the sustained phase of release. On repeated stimulation, however, NEM treatment resulted in a reduction in the sizes of both the exocytic burst as well as the sustained phase of release (with still no effect on the kinetics of the exocytic burst) [85]. This study clearly demonstrates effects of NSF/SNAP on vesicle priming, rather than on the final fusion step, and exemplifies the benefits of organizing the function of various proteins in terms of the kinetic framework established by high time-resolution capacitance measurements.

In addition to a dependence on Mg-ATP, priming has also been demonstrated to have a calcium dependence as well [58, 60]. The downstream effectors of calcium for vesicle priming are quite numerous and include a variety of proteins that have been shown to exert important roles in the priming process. These include (and are not limited to): Munc13 [47, 49], CAPS [86], PKC [87, 88] and PKA [89]. Of note, the calcium dependence for regulation of some of these proteins occurs indirectly, i.e., through molecules such as calmodulin. For the sake of brevity, an extensive discussion on these various proteins has been omitted here; the reader is instead referred to a number of recent reviews on the subject [46, 90].

Membrane Fusion

Upon entry of calcium into nerve terminals, synaptic vesicles that are fully primed are triggered to fuse with the presynaptic plasma membrane. While this is a seemingly simple task, fusing two lipid bilayers requires the surmounting of an extremely high energy barrier, in which membranes must be brought within very close proximity despite high electrostatic repulsions, and in which strong hydrophobic forces must be overcome to allow for the deformation and rupture of these membranes. Notably, several types of fusion have been demonstrated, ranging to full fusion, in which the vesicle membrane completely collapses into the target membrane upon fusion and is subsequently recycled via clathrin-dependent pathways, to kiss-and-run fusion, where the vesicle fuses only transiently with the target membrane and subsequently pinches off, having never fully collapsed into the plasma membrane [91].

Regardless of the mode of fusion, it is now widely agreed upon that SNARE (soluble N-ethylmaleimide-sensitive fusion factor attachment protein (SNAP) receptor) proteins constitute the minimal protein machinery required to catalyze membrane fusion events [92]. Evidence for this role comes from in vitro experiments demonstrating that SNARE proteins are sufficient to drive fusion (albeit, rather slowly) in reconstituted liposome assays [93], as well as in vivo experiments demonstrating that the loss of SNARE protein function as a result of proteolytic cleavage by clostridial and tetanus toxins [94-96], or by genetic deletion [25, 97, 98] or mutation [99-101], results in a strong inhibition, and in many cases, complete abolishment of evoked neurotransmitter release. Another compelling piece of evidence (or lack thereof) supporting the concept that SNAREs catalyze the final step in membrane fusion is that despite the many years in which genetic screens have been carried out in yeast, no gene products have been found to date that act downstream of the SNAREs in fusion [102].

SNARE proteins were originally discovered as the membrane-associated receptors for the NSF/SNAP complex, hence their name (SNAP receptors) [8]. The fundamental characteristic shared by all SNARE proteins is the presence of a SNARE domain: a 60-70 residue, cytoplasmic, amphipathic helix containing conserved heptad repeats. Many SNARE proteins are anchored to the membrane via a C-terminal transmembrane domain located adjacent to the SNARE domain, while other SNAREs associate with the plasma membrane via palmitoylated cysteine residues. Some SNARE proteins contain additional regulatory domains located N-terminally to the SNARE motif.

Central to the function of SNAREs is their ability to form into a core complex, consisting of 4 SNARE domains, contributed by either 3 or 4 SNARE proteins [103]. The SNARE core complex is remarkably stable, and has been demonstrated to be resistant to denaturing by SDS, resistant to cleavage by a number of proteases, and thermally stable in temperatures of up to 90^oC [21, 104]. The crystal structure of the neuronal SNARE core complex demonstrated a coiled coil of 4 alpha helices aligned in parallel, with all N-termini on one end of the coil, and all C-termini on the other end [105]. Fifteen layers of hydrophobic contacts are formed along the entire length of the coiled coil, with all helices contributing an interacting hydrophobic residue at each layer. A central, ionic layer of contacts is also present, and consists of three glutamine (Q) residues and an arginine (R) residue. As this central layer is highly conserved, it has been used to classify the SNARE proteins into the Q- and R-SNAREs, depending on whether the residue they contribute to the central layer of the SNARE core complex is a glutamine or an arginine, respectively [106].

SNARE proteins are believed to play a predominantly mechanical role in catalyzing membrane fusion. This requires the formation of a trans-SNARE core complex that spans two membranes, with each membrane contributing at least one transmembrane-anchored SNARE protein to the core complex. Nucleation and zippering of this stable trans-SNARE core complex from the N-terminal end to the C-terminal end of the coiled coil (where the transmembrane domains of the SNAREs are located) is believed to generate the free energy required to bring the two membranes within close enough proximity to initiate the fusion event [107]. While the exact number of SNARE core complexes required to catalyze the fusion of a single vesicle with the plasma membrane is unknown (and likely depends on the type of vesicle undergoing fusion), current estimates in neuroendocrine cells range from anywhere between three and fifteen [108].

The SNARE proteins that mediate regulated exocytosis in neurosecretory cells and neurons are syntaxin1 [109], SNAP-25 (synaptosomal-associated protein of 25 kDa) [110], and synaptobrevin / VAMP2 (vesicle-associated membrane protein 2) [111, 112]. Syntaxin1 is a 37kDa plasma membrane Q-SNARE that is found only in neuronal/neuroendocrine cells, and constitutes 1% of total brain protein [113]. Interestingly, syntaxin1 is evenly distributed throughout the neuronal plasma membrane (ie, it does not localize uniquely to active zones), suggesting that other proteins are required to spatially restrict syntaxin1's fusogenic activity to the active zone. The structure of syntaxin1 consists of an N-terminal regulatory domain termed Habc (comprised of 3 alpha helices arranged in anti-parallel), connected to a SNARE domain via a flexible linker, and followed closely by a C-terminal transmembrane domain. Syntaxin1 can assume two different conformations: a closed conformation, in which the Habc domain folds over to interact with the SNARE domain, thus precluding it from participating in SNARE core complex formation; and an open conformation, in which the SNARE domain is free to participate in SNARE complex formation, with the Habc domain extended away from this complex [114]. Deletion of syntaxin1A in Drosophila abolished both evoked and spontaneous neurotransmitter release [25, 115]. Cleavage of syntaxin1 by the botulinum neurotoxin type C occurs between the SNARE domain and the transmembrane domain, and can completely abolish neurotransmitter release [54, 95]. In addition to its interaction with other SNARE proteins, syntaxin1 has been demonstrated to interact with a number of other proteins critical for regulated exocytosis, including Munc18-1, Munc13, synaptotagmin, and even calcium channels (for review, see [102]). Interestingly, the transmembrane domain of syntaxin1 was recently proposed to form part of the fusion pore [116, 117].

SNAP-25 is also a plasma-membrane Q-SNARE, and contains two SNARE domains, separated by a linker region, which contains palmitoylated cysteine residues allowing for its association with the plasma membrane. SNAP-25 contains multiple phosphorylation sites, including Thr138 (PKA) and Ser187 (PKC), which may be involved in regulation of the size of the readily releasable pool [118-120]. In SNAP-25 knockout mice, evoked neurotransmission was abolished, although spontaneous neurotransmitter release was still observed [121]. SNAP-25 is also the target for the botulinum neurotoxins A, C, and E, which cleave SNAP-25 at its C-terminal end [94, 122, 123]. Proteolysis by botulinum C and E completely abolishes evoked secretion, whereas proteolysis by botulinum A results in only partial inhibition of secretion [54], which can be overcome in vivo by elevation of calcium levels [124]. This suggests that cleavage of SNAP-25 by botulinum A somehow shifts the calcium sensitivity of exocytosis.

Synaptobrevin is a small vesicle-anchored R-SNARE, consisting of a cytosolic, N-terminal proline-rich stretch and SNARE domain, and a C-terminal transmembrane domain. Genetic deletion of synaptobrevin in Drosophila resulted in the complete abolishment of evoked neurotransmitter release; however, spontaneous release events were still observed [25]. In synaptobrevin knockout mice, evoked neurotransmitter release was decreased 100-fold, whereas spontaneous release was decreased only 10-fold [125]. Synaptobrevin is the target for tetanus toxin and the botulinum toxins B, D, F, and G. These toxins cleave synaptobrevin largely within its SNARE domain, and result in a profound inhibition of secretion [54, 126].

While it is clear from the genetic deletion studies that the neuronal SNARE proteins are essential for evoked neurotransmitter release, what is interesting is that only in the case of syntaxin1 deletion was spontaneous neurotransmitter release completely abolished. While this could suggest functional redundancy in the roles for SNAP-25 and synaptobrevin for spontaneous fusion events, another possibility is that there may be a fundamental molecular difference between spontaneous fusion events and evoked fusion events.

Regulators of the Neuronal SNARE Complex

As SNARE complexes play a pivotal role in the process of membrane fusion, there exist many proteins whose function is to regulate SNARE complex formation. One of the most critical proteins involved in this task is Munc18-1 (for review, see [127]). Munc18-1 is a member of the Sec/Munc18 (SM) family, and is the mammalian homolog of unc (uncoordinated)-18, a gene that was first discovered in C. elegans during genetic screens for mutants displaying defects in membrane trafficking and secretion [128]. Homologs in yeast (termed Sec proteins) were identified in parallel, in genetic screens for secretory defects [129, 130]. Munc18-1 is a soluble, 65kDa protein consisting of 3 domains that fold into an arch-shaped structure with a central cleft [114]. A role for Munc18-1 in neurotransmitter release was first identified when Munc18-1 was shown to bind syntaxin1 with nanomolar affinity [131, 132]. Genetic deletion of Munc18-1 in mice completely abolished both evoked and spontaneous neurotransmitter release, demonstrating that Munc18-1 is essential for synaptic vesicle exocytosis [133]. (Remarkably, despite the complete silencing of synapses in these mice, the nervous systems of these mice still developed normally up until embryonic day 12!). Interestingly, and somewhat unexpectedly, however, the crystal structure of the Munc18-1 / syntaxin1 complex demonstrated that Munc18-1 bound to the N-terminus of syntaxin1, stabilizing syntaxin1 in its closed, non-SNARE pairing conformation [114]. These apparently contradictory results left the field in a state of confusion for several years: how could Munc18-1 be so clearly essential for neurotransmitter release, and yet negatively regulate SNARE core complex formation? Recent evidence has now begun to shed light on a new role for Munc18-1 in promoting SNARE core complex activity.

First, a novel and high affinity binding mode of Munc18-1 to the neuronal SNARE complex was observed [134, 135]. Next, in vitro liposome fusion assays demonstrated that addition of Munc18-1 to liposomes containing pre-formed SNARE complexes resulted in a 20-fold increase in the initial rate of fusion, compared to liposomes in which Munc18-1 was not added. Notably, this effect of Munc18-1 occurred selectively for SNARE complexes involved in exocytosis; moreover, mutations in VAMP that decreased the ability of Munc18-1 to facilitate liposome fusion in vitro were found to correlate to previously published effects of these mutations in inhibiting exocytosis in vivo [135]. Thus, it now appears that Munc18-1 exhibits different binding modes to SNARE proteins, and that Munc18-1 may both negatively and positively regulate the activity of SNARE complexes. Future challenges in understanding Munc18-1 action will involve sequencing its transitions between these states (if such a transition occurs) and determining how the positive and negative roles of Munc18-1 are regulated. Moreover, while it is now clear that Munc18-1 can positively regulate SNARE-catalyzed fusion events, it is still unclear mechanistically how deletion of this gene would result in the complete silencing of synapses. Notably, the genetic deletion of Munc18-1 in mice resulted in a phenotype stronger than that seen on deletion of either SNAP-25 or synaptobrevin—which suggests at least two possibilities: 1) Munc18-1 and syntaxin1 may mediate a separate fusion pathway for “spontaneous” release events, independent of SNAP-25 and synaptobrevin; or 2) Munc18-1 may be at least, if not more important, in membrane fusion than some of the SNARE proteins themselves.

Another protein that has recently been implicated in regulation of the SNARE core complex assembly is tomosyn, a 130kDa soluble R-SNARE protein that was originally identified as a high affinity binding partner of syntaxin1 [136]. Tomosyn belongs to a family of proteins that includes the yeast proteins Sro7p and Sro77p, as well as the lethal giant larvae family of proteins in Drosophila [137]. Tomosyn consists of a large N-terminal domain comprised of repeating WD-40 motifs, followed by a linker region known as the hypervariable domain, where most of the variability between tomosyn isoforms occurs. At its C-terminus, tomosyn contains an R-SNARE domain similar to that in synaptobrevin. The crystal structure of the yeast tomosyn homolog Sro7 was recently determined, and demonstrated that the N-terminal WD-40 motifs folded into two 7-bladed β-propellers, followed by a long tail that bound to the bottom of the N-terminal propeller. (The C-terminal SNARE/helical region was not included in this crystal structure) [138].

Much evidence exists to support an inhibitory role for tomosyn in regulated exocytosis. First, overexpression of tomosyn in a number of different neuroendocrine cells resulted in an inhibition of regulated secretion [48, 136, 139-141]. In chromaffin cells, a specific role for tomosyn in inhibiting vesicle priming was identified, as overexpression of tomosyn resulted in a decrease in both the size and refilling kinetics of the readily releasable pool, with no effect on vesicle docking [48]. Moreover, loss-of-function tomosyn mutants in C.elegans resulted in an increase in the size of the readily releasable pool at neuromuscular junctions, consistent with a role for tomosyn in inhibiting vesicle priming [142, 143].

Tomosyn exhibits multiple modes of binding to SNARE proteins. In one mode, it can form binary interactions with syntaxin1. This binding mode is of high enough affinity that tomosyn can compete with Munc18-1 for binding to syntaxin1 and dissociate syntaxin1-Munc18-1 complexes [136, 144]. Tomosyn can also form into ternary SNARE complexes with syntaxin1 and SNAP-25; the crystal structure for this complex was nearly identical to that formed by syntaxin1-SNAP-25-synaptobrevin [139, 145]. The basis of tomosyn’s inhibitory action on secretion is widely believed to result from the formation of non-fusogenic tomosyn-SNARE core complexes, as tomosyn replaces synaptobrevin in this SNARE complex but is not actually anchored to a vesicle membrane to be able to catalyze fusion. Formation of tomosyn-SNARE ternary complexes would thus reduce the availability of syntaxin1 and SNAP-25 to form into functional SNARE complexes, thereby resulting in an inhibition of secretion.

The experiments presented in Chapter 3 of this dissertation examine the spatiotemporal properties of the tomosyn-syntaxin1A interaction in response to a secretory stimulus, to test the hypothesis that tomosyn's inhibitory function on secretion is regulated by secretory demand.

Calcium Sensing for Neurotransmitter Release

How does the influx of calcium into the nerve terminal trigger synaptic vesicles to fuse with the plasma membrane? Most evidence points to a role for Synaptotagmin-1 as the calcium sensor for fast neurotransmitter release. Synaptotagmin-1 is a 65kDa integral vesicle protein, comprised of a short intravesicular domain and a transmembrane domain at its N-terminus, and two cytosolic C2 domains (C2A and C2B) connected by a linker at the C-terminus [146-148]. C2A and C2B are the calcium sensing portions of synaptotagmin-1, and bind 3 or 2 calcium ions, respectively. Importantly, the affinity of these domains for calcium greatly increases in the presence of anionic phospholipids. Notably, it was determined in vitro that in response to calcium, both C2A and C2B become partially inserted into lipid bilayers [149-151]. Synaptotagmin-1 has also been reported to bind to syntaxin1 individually, as well as to the ternary SNARE complex [77]. The ability of synaptotagmin-1 to interact simultaneously with both SNAREs as well as with lipid bilayers in response to calcium is thought to be crucial to its role as a calcium sensor ((for review, see [152]).

The role of synaptotagmin-1 as a calcium sensor for neurotransmitter release is suggested by studies demonstrating that point mutations of this protein within the C2 domains alter the fourth-order calcium dependence of release [153, 154]. Some of the first studies on synaptogamin-1 carried out in neuronal cultures suggested that this protein was required for normal levels of neurotransmitter release, as genetic deletion of this protein abolished the synchronous component of release, with no detected changes in the asynchronous component of release [155]. However, more recent studies at the Drosophila neuromuscular junction and in hippocampal neurons demonstrated that deletion of synaptotagmin-1 actually resulted in the same total amount of neurotransmitter being released in response to a stimulus compared to control neurons. However the rate of release was found to be decreased dramatically, and release occurred mostly asynchronously and was not tightly coupled to the stimulus [156, 157]. Thus, it appears that synaptotagmin-1's function is not absolutely required for neurotransmission. Rather, this protein seems to be involved in synchronization and acceleration of release events in response to the calcium trigger.

Of note, 16 mammalian isoforms for synaptotagmin have been identified to date, most of which are synthesized in neurons or neuroendocrine cells [158, 159]. Synaptotagmins 1, 2, and 9 have been shown to localize to synaptic and secretory vesicles, whereas Synaptotagmins 3, 6 and 7 localize to the plasma membrane. Notably, not all synaptotagmins bind calcium and phospholipids. Synaptotagmins 4 and 11 contain conserved mutations within the C2A domain and therefore likely bind fewer than 5 calcium ions; synaptotagmins 8, 12, and 13 lack almost all of the aspartate and glutamate residues in C2A and C2B that coordinate calcium binding, and thus likely do not even bind calcium. Why there exist so many synaptotagmin isoforms is unknown, but perhaps these proteins play complementary roles in calcium sensing at multiple sites of the cell, or allow for extremely fine control over the calcium sensitivity of neurotransmitter release [159]. The role for synaptotagmins that do not bind calcium is even less clear.

Lipids in Membrane Fusion

While the discussion thus far has focused largely on the role of proteins in mediating biological membrane fusion, it would hardly do justice to the topic of membrane fusion to exclude the importance of lipids in this process-- after all, this process by definition must involve lipids! The tools for studying lipids in biological systems are still rather under-developed compared to those for studying proteins, but it is becoming increasingly apparent that lipids play important structural, electrostatic, and signaling roles in biological membrane fusion.

Membrane fusion is an intrinsically energy-demanding process. In the aqueous context of a biological cell, the hydrophobic effect is paramount to the assembly of lipids into bilayers, whereby the phosphate headgroups of the lipids associate with the water, thus shielding the hydrophobic acyl chains of the lipids. It is this powerful hydrophobic effect that must ultimately be overcome to rupture two bilayers to allow for their fusion. Any forces that are less powerful than the hydrophobic effect can result in bending and deformation of membranes, but will not result in fusion (for review, see [160, 161]). The energy barriers that are encountered when two lipid bilayers undergo fusion, and the membrane intermediates that minimize these energetic requirements, have been modeled extensively [162, 163], and are illustrated in Figure 1.2. Membranes must first be brought within close enough proximity (several nanometers) to establish a region of dehydrated contact; this requires surmounting the electrostatic forces repelling the two bilayers. An initial connection between the two bilayers, termed a fusion stalk, is then formed. Radial expansion of this stalk generates a hemifusion diaphragm, in which the contacting leaflets of the bilayers have merged, while the distal leaflets of the bilayers remain separate. Importantly, in vitro fusion assays in bulk solution as well as on a single liposome level, demonstrated that SNARE-mediated fusion events indeed occur through a hemifusion intermediate [164, 165]. Following hemifusion, lateral tension must be generated within the hemifusion diaphragm to allow for membrane rupture and formation of a fusion pore, the initial aqueous connection between the two compartments. Expansion of this fusion pore results in membrane collapse and full fusion. Notably, formation and expansion of the fusion pore are thought to be the most energetically demanding steps of this process [163].

The amount of work that must be performed on membranes to deform them into the intermediates described above depends largely on the spontaneous curvature of the membranes involved. The spontaneous curvature of a membrane bilayer is the curvature that it naturally exhibits in the absence of any external forces acting upon it. The spontaneous curvature of a bilayer depends on the spontaneous curvatures of its individual monolayers, which in turn, depend on the individual lipid constituents of each monolayer. Lipids can be classified based on spontaneous curvatures that they promote [166, 167]; in most cases, this is closely related to their overall structure and the electrostatic properties of their polar head groups. Most lipids with two acyl chains, such as DOPC (dioleoylphosphatidylcholine), are termed cylindrical lipids, and favor the formation of flat bilayers with relatively little curvature. Lysolipids, such as LPC (lysophosphatidylcholine), that contain only one acyl chain and relatively large polar headgroups, are termed inverted cone-shaped lipids. These lipids favor strong positive spontaneous curvatures (membranes that bend toward the hydrocarbon tails of the lipid). On the other hand, lipids such as DOPE (dioleoylphosphatidylethanolamine), that contain two acyl chains and relatively small polar headgroups, are termed cone-shaped lipids and favor strong negative spontaneous curvatures (membranes that bend away from the hydrocarbon tails). In the model for membrane fusion described above, the energetic requirements for stalk and hemifusion formation can be greatly increased or decreased by the presence of positive or negative curvature-favoring lipids, respectively, in the proximal contacting leaflets of the two membranes [168]. On the other hand, formation of a fusion pore is largely favored by the presence of positive curvature-favoring lipids in the distal leaflets of the fusing bilayers.

The importance of lipid shape in determining the energetics of membrane fusion can be highlighted by a family of snake neurotoxins termed SPANs (snake presynaptic phospholipase A2 neurotoxins), which are known to generate paralysis by the induction of neurotransmitter release and subsequent depletion of vesicle pools. It was recently observed that the mechanism underlying this effect was the hydrolysis of phospholipids in the outer leaflet of the plasma membrane, into positive curvature-promoting lysophospholipids that favored the formation of fusion pores and the subsequent release of neurotransmitter [169]. Conversely, injection of these toxins into the cytosol of PC-12 cells strongly inhibited secretion, likely because these toxins generated positive curvatures on the inner leaflet of the plasma membrane that were unfavorable for fusion [170]. The strong dependency on lipid shape for determining the energetic requirements of membrane fusion is also evident in in vitro liposome assays of SNARE-catalyzed fusion, and in many other biological fusion reactions including cell-cell fusion, organelle-organelle fusion, and organelle-plasma membrane fusion [171, 172].

Given that work must be done on the lipid bilayers in order to induce fusion, and given that SNARE proteins are the machinery that carries out this task, how mechanistically might this occur? The energy released upon SNARE core complex formation must somehow be transmitted to the lipid bilayers, and the anchoring of SNARE proteins to the lipid bilayers via transmembrane domains (TMDs) is crucial to this function. However, it is becoming increasingly apparent that the SNARE TMDs may play a more active role in fusion than just acting as mechanical anchors that allow for close apposition of the fusing bilayers. Indeed, targeted disruptions within the TMD of various SNARE proteins, including shortening of the TMD [173], replacement of the TMD with lipid anchors [174, 175], and mutation of the TMD to alter its helical structure

[176], have all been shown to adversely affect the fusion reaction. As stated above, the most energetically demanding step in the process of membrane fusion is the formation and expansion of the fusion pore. Interestingly, the TMD of syntaxin1 was recently suggested to form part of the fusion pore, based on amperometric studies that showed that mutation of key resides in syntaxin1's TMD could alter the flux of catecholamines through the fusion pore in a size and charge-dependent fashion [116, 117]. Another role for SNARE proteins in membrane fusion could be to generate the lateral tension required for expansion of the fusion pore; this could achieved through electrostatic interactions that might occur between the SNARE proteins and acidic phospholipids [160]. Notably, the juxtamembrane regions of both syntaxin1 and synaptobrevin contain clusters of basic residues which could mediate these effects. Electron paramagnetic resonance studies demonstrated that the juxtamembrane regions of syntaxin1 and synaptobrevin were buried within the lipid bilayer. However, synaptobrevin was unable to form into SNARE complexes while its juxtamembrane region was lipid-associated, implying that synaptobrevin-lipid interactions are a negative regulator of exocytosis [177-180]. Interestingly, molecular dynamics studies of the juxtamembrane region and TMD of syntaxin1 suggested just the opposite case for syntaxin1, and demonstrated that interaction between the juxtamembrane region and acidic phospholipids in the membrane might result in an increase in the helicity and tilt angle of syntaxin1's TMD, allowing for accelerated rates of fusion [181]. Further evidence suggesting that syntaxin1-lipid interactions might facilitate membrane fusion is that syntaxin1 was found to localize to cholesterol dependent clusters in the plasma membrane [182, 183], as well as to clusters which co-localized with PI(4,5)P2 clusters [71]; importantly, exocytosis seemed to occur preferentially at these syntaxin1-lipid microdomains.

The experiments presented in Chapter 2 of this dissertation identify the specific lipids that directly interact with syntaxin1, and test the hypothesis that these protein-lipid interactions play important functional roles with respect to the energetics of membrane fusion.

Emerging Tools for the Study of Regulated Exocytosis: FRET

For the most part, many of the key protein and lipid players for regulated exocytosis have now been identified. Biochemical, genetic, and functional studies have further allowed for the elucidation of specific protein-protein interactions that are critical to each specific step of neurotransmitter release. However, these experimental results, in many cases, provide just a single snapshot of how these proteins might interact over the course of the highly dynamic process of membrane fusion. Clearly, an understanding of neurotransmitter release will require unraveling the spatial and temporal dynamics of the associations and dissociations of the many proteins and lipids that orchestrate this process. One tool that has rapidly emerged to carry out such a task is FRET (fluorescence resonance energy transfer) imaging. This approach is used in completion of the first two data chapters of this dissertation, and is further expanded and developed in the third data chapter, such as to open new avenues for discovery of specific protein interaction events occurring just proximal to the plasma membrane. What is presented below is an introduction to FRET methodology, starting from basic principles of fluorescence imaging and working up to the derivation of a sensitized emission FRET method termed FRET stoichiometry [184].

Fundamental to the understanding of fluorescence imaging is a working knowledge of the processes that occur when fluorescent molecules in the ground state are excited to and decay from higher level energy states. These processes can be visualized in a Jablonski diagram, as shown in Figure 1.3. Upon the absorption of energy (usually in the form of a photon of wavelength λ_{ex}), fluorescent molecules transition from an electronic ground state, s_0, to a higher energy excited state, s_1.

These excited fluorophores then rapidly (on the order of nanoseconds) decay back to the ground state via one of several pathways. In the first pathway, termed nonradiative decay, the excited state energy is dissipated thermally or through collisional quenching. In the second pathway, termed radiative decay, the fluorophore decays to the ground state via emission of a photon of light (λ_{em}), which is always of a longer wavelength (ie, lower energy) than the photon of light used to excite the molecule. The difference in wavelengths (and thus, energies) of the excitation and emission photons is termed the Stokes shift. Notably, it is the radiative pathway of decay that is essential to the utility of fluorescence microscopy.

Several key terms should be defined at this point. The *extinction coefficient*, ε(λ), is a measure of how easily a fluorophore can absorb (ie, be excited by) photons of a particular wavelength, λ. The *quantum yield*, Q, of a fluorophore is a measure of the "brightness" of the fluorescence emission of a fluorophore. More precisely, the quantum yield represents the fraction of excited state fluorophores that decay through the process of radiative emission. As such, the quantum yield can be defined using rate constants: $Q = \frac{k_r}{k_r + k_{nr}}$, where k_r and k_{nr} are the rate constants for radiative and nonradiative decay, respectively, for a fluorophore. Notably, both the extinction coefficient and the quantum yield are properties unique to each and every fluorophore.

In the presence of an "acceptor" fluorophore, an excited state "donor" fluorophore can decay back to the ground state via a third pathway, termed fluorescence resonance energy transfer (FRET) (see Figure 1.4). This process requires the presence of a suitable acceptor fluorophore, whose excitation spectrum overlaps with the emission spectrum of the donor fluorophore. When an excited state donor fluorophore comes within close enough proximity (<10nm) to an acceptor fluorophore, the donor can transfer its excited state energy to the acceptor, via a dipole-dipole interaction. When this occurs, the donor decays back to its ground state without emitting a photon, and the acceptor transitions from its ground state to its excited state. The excited state acceptor can then decay back to its ground state either radiatively or nonradiatively.

The frequency with which FRET occurs between a donor-acceptor fluorophore pair can be described by the *characteristic FRET efficiency*, E, which represents the fraction of excited state donor molecules in complex with the acceptor, that decays back to the ground state via FRET. The characteristic FRET efficiency is a physical property of each bimolecular interaction that exhibits FRET; in other words, its value is a constant that should be independent of the instruments used to measure it. It is important to distinguish between the "true" or characteristic FRET efficiency and the "apparent" FRET efficiency, which, as described below, results from measurements in which neither the characteristic FRET efficiency nor the fraction of molecules in complex are known.

Like quantum yield, the FRET efficiency can be defined in terms of rate constants: $E = \frac{k_t}{k_r + k_{nr} + k_t}$, where as before, k_r and k_{nr} are the rate constants for radiative and nonradiative decay, and k_t is the rate of energy transfer. It should be noted that k_t is remarkably sensitive to the distance between the donor and acceptor fluorophores ($k_t \propto distance^{-6}$) as well as to the relative orientation of the donor and acceptor dipoles. Importantly, for most genetically encoded fluorophores, the distances over which FRET is highly sensitive are on the order of tens of angstroms—precisely the distance scale over which bimolecular interactions within living cells might occur.

The use of FRET to study molecular interactions within biological systems requires that the molecules of interest first be tagged with donor and acceptor fluorophores. Interaction of these molecules is required to bring the donor and acceptor fluorophores within close enough proximity such that they can undergo FRET. As such, FRET should only be observed when the labeled molecules directly interact; moreover, changes in FRET can report on changes in the extent of this bimolecular interaction (ie, a change in the total number of molecules that are interacting), or in the orientation of molecules involved in the bimolecular interaction. It is important to re-emphasize here that not all donor-acceptor complexes will undergo FRET; only a fraction (equal to the FRET efficiency, E) of the total number of donor-acceptor complexes undergoes FRET.

An understanding of how FRET is measured requires first understanding how fluorescence signals are measured. The simplest case of a fluorescence measurement that will be considered here is shown in the left panel of Figure 1.5. Here, light of wavelength λ_D, is used to directly excite either donor or acceptor molecules. In either case, the total fluorescence intensity (FI) of the donor and acceptor molecules can be described by the equations below:

$$Donor\ FI = I(\lambda_D) \cdot \varepsilon_D(\lambda_D) \cdot N_D \cdot Q_D \tag{1}$$

$$Acceptor\ FI = I(\lambda_D) \cdot \varepsilon_A(\lambda_D) \cdot N_A \cdot Q_A \tag{2}$$

In both cases, the fluorescence intensity takes into account the intensity of the excitation light, $I(\lambda_D)$; how easily the donor or acceptor molecules absorb light of this wavelength, given by the extinction coefficients of the donor and acceptor at λ_D, $\varepsilon_D(\lambda_D)$ and $\varepsilon_A(\lambda_D)$, respectively; the total number of donor or acceptor molecules present (N_D and N_A, respectively); as well as the brightness of the donor and acceptor fluorescence emission, given by their quantum yields, Q_D and Q_A, respectively. In practical terms, the intensity of the excitation light takes into consideration the intensity of the light source, as well as the extent to which this light is attenuated by filters and other optical elements in the path between the light source and the sample. Similarly, the brightness of the donor or acceptor fluorescence emission takes into account not only the quantum yields of the donor and acceptor, but also the filters and other optical elements downstream of the sample that may attenuate the fluorescence emission, as well as the wavelength-dependent quantum efficiency of the camera that is used to detect the fluorescence emission. To keep the equations simple, however, it is assumed that these factors are all accounted for in the variables above.

How does fluorescence intensity of the donor and acceptor molecules change when a fraction of these molecules (f_D or f_A, respectively) undergoes FRET with characteristic efficiency E? This example is illustrated in the right panel of Figure 1.5. When a donor molecule undergoes FRET, its fluorescence becomes quenched (as FRET precludes the excited state donor from decaying radiatively). The donor molecules whose fluorescence is quenched are those that are both 1) in complex with acceptor, and 2) undergoing FRET. (Recall that the former does not necessarily imply the latter). As such, the total number of quenched donors is equal to $N_D \cdot f_D \cdot E$, and the fluorescence intensity that is quenched as a result of FRET is:

$$Donor\ FI\ quenched\ by\ FRET = I(\lambda_D)\ \cdot\ \varepsilon_D(\lambda_D)\ \cdot N_D\, f_D E\ \cdot Q_D \qquad (3)$$

Subtracting equation (3) from equation (1), the total amount of donor fluorescence that would be observed in the presence of FRET is:

$$Donor\ FI\ with\ FRET = I(\lambda_D) \cdot \varepsilon_D(\lambda_D) \cdot N_D(1 - f_D E)\ \cdot Q_D \qquad (4)$$

In contrast to the donor fluorescence decreasing in the presence of FRET, the acceptor fluorescence is enhanced in the presence of FRET. This is because the acceptor can now be excited either directly by λ_D, or indirectly, through FRET. The number of acceptor molecules that is excited indirectly through FRET is the same as the number of donor molecules whose fluorescence was quenched by FRET, and is equal to: $N_D \cdot f_D \cdot E$. As such, the enhanced fluorescence emission of the acceptor as a result of FRET (also termed sensitized emission) can be represented as:

$$Sensitized\ emission\ of\ acceptor =\ I(\lambda_D)\ \cdot\ \varepsilon_D(\lambda_D)\ \cdot N_D\, f_D E\ \cdot Q_A \qquad (5)$$

Note that in comparison to equation (2) above, the donor's extinction coefficient is used here rather than the acceptor's extinction coefficient. This is because the acceptor that is undergoing FRET is excited indirectly, via the excited-state donor, and thus it is the donor's absorption of the excitation light that is relevant. Equations (2) and (5) can be summed to determine the total fluorescence intensity of the acceptor in the presence of FRET:

$$Acceptor\ FI\ with\ FRET\ = [I(\lambda_D) \cdot \varepsilon_A(\lambda_D) \cdot N_A \cdot Q_A] + \ [I(\lambda_D) \cdot \ \varepsilon_D(\lambda_D) \cdot N_D\, f_D E\ \cdot Q_A] \qquad (6)$$

Armed with this basic understanding of the theory underlying FRET, we are now in a position to understand how FRET is measured experimentally. The two most common methods to measure FRET in biological systems are termed donor dequenching, and sensitized emission. Often in these experiments, two different molecules are labeled with donor and acceptor, respectively, and the fraction of donor or acceptor molecules in complex is unknown. Moreover, it is also usually the case that the characteristic FRET efficiency of the specific bimolecular interaction is not known (as experimental determination of this value requires highly specialized equipment, eg, a fluorescence lifetime microscope). As such, the FRET methods described here can be used to calculate only an "apparent" FRET efficiency, which represents the product of the "true" or characteristic FRET efficiency, with the fraction of donor or acceptor molecules in complex.

In the method of FRET by donor dequenching, the population of acceptor fluorophores is irreversibly destroyed via photobleaching, thus precluding FRET from occurring. As such, FRET that was present before photobleaching is detected as an increase (dequenching) in donor fluorescence following photobleaching. This situation is illustrated in the left panel of Figure 1.6. Donor dequenching is usually performed on a confocal microscope (although it is possible to perform this technique on a conventional epifluorescence microscope as well). While it is easy to perform (as no calibrations are required), time lapse FRET imaging of the same subcellular location cannot be measured using this technique, due to the direct and permanent loss of the acceptor fluorescence. In donor dequenching, the apparent FRET efficiency is usually calculated by measurement of the donor fluorescence intensity before and after photobleaching:

$$Apparent\ FRET\ efficiency = Donor\ FI \left\{\frac{Postbleach - Prebleach}{Postbleach}\right\} = \frac{(De)quenched\ donor}{Total\ donor} \tag{7}$$

Note in equation (7) that the amount of dequenched donor is normalized to the total amount of donor, so that the apparent FRET efficiency is independent of differences in donor expression levels between cells. Substituting equations (1) and (3) into equation (7) demonstrates that the apparent FRET efficiency as measured using donor dequenching is equal to the product of the characteristic FRET efficiency and the fraction of donor molecules in complex:

$$Apparent\ FRET\ efficiency = \frac{I(\lambda_D) \cdot \varepsilon_D(\lambda_D) \cdot N_D f_D E \cdot Q_D}{I(\lambda_D) \cdot \varepsilon_D(\lambda_D) \cdot N_D \cdot Q_D} = E \cdot f_D \tag{8}$$

While the apparent FRET efficiency obtained in donor dequenching is independent of donor expression levels, it is important to note that the degree of molecular interaction between the acceptor and donor, and hence, the apparent FRET efficiency, is still dependent upon acceptor expression levels. Notably, donor dequencing provides little information as to what fraction of acceptor molecules are in complex with the donor.

In contrast to donor dequenching, the method of sensitized emission FRET is non-destructive, and determines an apparent FRET efficiency by measuring the enhancement in acceptor emission (ie, sensitized emission) due to FRET. This is shown in the right panel of Figure 1.6. Sensitized emission can be performed on epifluorescence or confocal microscopes, and as it is non-destructive, can be used for time lapse FRET imaging. However, sensitized emission FRET is more complicated to perform than donor dequenching FRET, because due to the nature of the optical filters and fluorophores used, the sensitized emission signal is often buried among other spectral contaminants. As such, this method requires the user to perform various calibrations for the imaging system and the fluorophores used, in order to specifically isolate the sensitized emission signal. Apparent FRET efficiency under sensitized emission is usually measured as:

$$Apparent\ FRET\ efficiency = \frac{Sensitized\ emission}{Total\ acceptor} \tag{9}$$

Note that in equation (9), the amount of sensitized emission fluorescence is normalized to the amount of total acceptor fluorescence, so that the apparent FRET efficiency is independent of differences in acceptor expression levels between cells. Substitution of equations (2) and (5) into equation (9) demonstrates that the apparent FRET efficiency measured by sensitized emission FRET is the product of the “true” FRET efficiency with the fraction of acceptor molecules in complex, and the ratio of extinction coefficients of the donor to acceptor at the donor excitation wavelength, as shown in Equations (10) and (11) below:

$$Apparent\ FRET\ efficiency = \frac{I(\lambda_D)\cdot \varepsilon_D(\lambda_D)\cdot N_D\, f_D E \cdot Q_A}{I(\lambda_D)\cdot \varepsilon_A(\lambda_D)\cdot N_A\cdot Q_A} \tag{10}$$

$$Apparent\ FRET\ efficiency = \frac{\varepsilon_D(\lambda_D)}{\varepsilon_A(\lambda_D)}\cdot E\ \cdot \frac{N_D\cdot f_D}{N_A} = \frac{\varepsilon_D(\lambda_D)}{\varepsilon_A(\lambda_D)}\cdot E\cdot f_A \tag{11}$$

While the apparent FRET efficiency obtained from sensitized emission measurements is independent of the expression levels of the acceptor, it is important to realize that the extent of the acceptor-donor interaction and hence, the apparent FRET efficiency, will still depend on donor expression levels. However, the fraction of donor molecules in complex with the acceptor remains undetermined with this mode of analysis.

Note from equations (8) and (11) that while donor dequenching provides an apparent FRET efficiency that is dependent upon the fraction of donor molecules in complex, the apparent FRET efficiency determined using sensitized emission is dependent upon the fraction of acceptor molecules in complex. Thus, use of either of these methods alone yields information limited to either the donor alone, or the acceptor alone. However, a method of sensitized emission FRET termed FRET stoichiometry [184] operates as somewhat of a marriage between sensitized emission FRET and donor dequenching FRET. In other words, FRET stoichiometry allows for the determination of the apparent FRET efficiency of both the donor, as well as the acceptor, in complex; moreover, this method allows for determination of the molar ratio of acceptor to donor.

In FRET stoichiometry, three images are taken of each cell and are background subtracted and shade corrected to yield CIDD, CIDA, and CIAA images (where CI = corrected image, and DD = donor excitation / donor emission; DA = donor excitation / acceptor emission; and AA = acceptor excitation / acceptor emission) (see Figure 1.7). Both the CIDD and CIAA images are relatively free of spectral contaminants and represent “clean” images of the donor and acceptor, respectively. The CIDA image contains the sensitized emission FRET signal, but is contaminated by two other elements: 1) spectral bleeding (spillover of donor emission into the acceptor emission channel); and 2) cross-talk (direct excitation of the acceptor by the donor excitation wavelength). Note that the extent of these spectral contaminants is dependent upon the fluorophores used, the bandwidths of the excitation lines, and the optical filters used. However, the contribution of each of these contaminants can be determined and subtracted out of the CIDA image, using proportionality constants. For instance, the amount of spectral bleedthrough of the donor is equal to a certain fraction (β) of the total donor fluorescence:

$$Spectral\ bleedthrough\ in\ CIDA = \beta\ \cdot CIDD \qquad (12)$$

Importantly, the value of β for a specific optical setup can be determined experimentally by imaging cells that express donor only, and taking the ratio of $\frac{CIDA}{CIDD}$.

Similarly, the amount of acceptor directly excited at donor wavelengths is equal to a certain fraction (α) of the total acceptor fluorescence intensity arising from excitation at acceptor wavelengths:

$$Crosstalk\ of\ acceptor\ in\ CIDA = \alpha \cdot CIAA \tag{13}$$

The value of α for a particular optical setup can be determined experimentally by imaging cells that express acceptor only, and taking the ratio of $\frac{CIDA}{CIAA}$. Combining equations (12) and (13), the spectral contaminants can be subtracted from the CIDA image to isolate the sensitized emission signal:

$$Sensitized\ emission = CIDA - \alpha \cdot CIAA - \beta \cdot CIDD \tag{14}$$

Recall from equations (9) and (11), that

$$Apparent\ FRET\ efficiency = \frac{Sensitized\ emission}{Total\ acceptor} = \frac{\varepsilon_D(\lambda_D)}{\varepsilon_A(\lambda_D)} \cdot E \cdot f_A \tag{15}$$

Using equation (14), and setting the total acceptor fluorescence equal to $\alpha \cdot CIAA$, equation (15) can be rewritten to yield the equation for the apparent FRET efficiency of the acceptor in complex, EA:

$$EA = E \cdot f_A = \gamma \cdot \frac{\mathrm{CIDA} - \alpha \cdot \mathrm{CIAA} - \beta \cdot \mathrm{CIDD}}{\alpha \cdot \mathrm{CIAA}} \tag{16}$$

where $\gamma = \frac{\varepsilon_A(\lambda_D)}{\varepsilon_D(\lambda_D)}$. Note that both the numerator and denominator of the latter portion of equation 16 are expressed in terms of fluorescence images where the molecules are excited with donor excitation wavelengths, and fluorescence intensity is determined using acceptor emission wavelengths; moreover, the constant γ normalizes for differences in the extinction coefficients of the acceptor and donor at donor excitation wavelengths. (In other words, the “units” of the numerator and denominator match, and dividing them is physically meaningful). Also note that γ, like α and β, is a constant that can be determined experimentally for the fluorophores and optical setup used. This is done by imaging a linked donor-acceptor construct (where $f_A = 1$, and E has been pre-determined), and solving equation (16) for γ:

$$\gamma = \frac{\mathrm{E} \cdot \alpha \cdot \mathrm{CIAA}}{\mathrm{CIDA} - \alpha \cdot \mathrm{CIAA} - \beta \cdot \mathrm{CIDD}} \qquad (17)$$

Importantly, while the linked probe must incorporate the same donor and acceptor fluorophores used in the experiment, the FRET efficiency of the linked probe need not match the apparent FRET efficiencies determined in the experiment. In other words, the linked probe is simply used to calibrate the system, and knowing the FRET efficiency of the linked probe is required only so that the fluorescent properties of the acceptor and donor fluorophores, as measured under the user's imaging system, can be determined.

As mentioned earlier, FRET stoichiometry combines the benefits of sensitized emission with donor dequenching. Recall from equation (7) that the apparent FRET efficiency in donor deqeunching is equal to the ratio of $\frac{(De)quenched\ donor}{Total\ donor}$. The complicated factor here is in obtaining the fluorescence intensity associated with the quenched donor; after all, how does one measure a signal that does not exist? Measuring the total amount of donor is equally complicated, as the total amount of donor is comprised of donor molecules that are fluorescing, as well as those whose fluorescence is quenched. The key to solving this problem is in understanding that the "would-be fluorescence" of the quenched donor is closely related to the sensitized emission fluorescence; indeed, both result from the excitation of donor molecules that undergo FRET. In the case of the quenched donor, it is the donor molecules that (would have) emitted photons; in the case of sensitized emission, the acceptor molecules emit photons. (A comparison of equations (3) and (5) illustrates this principle nicely). Thus, the sensitized emission signal from the acceptor can be converted to its equivalent in quenched donor fluorescence, by multiplying the sensitized emission signal with the ratio of brightness of the donor and acceptor fluorescence emission:

$$Quenched\ donor\ FI = Sens. emission\ FI \cdot \frac{Q_D}{Q_A} = (\mathrm{CIDA} - \alpha \cdot \mathrm{CIAA} - \beta \cdot \mathrm{CIDD}) \cdot \xi \qquad (18)$$

Equation (18) can be substituted into equation (7) to yield the equation for the apparent FRET efficiency of the donor in complex:

$$ED = E \cdot f_D = \frac{(De)quenched\ donor}{Total\ donor} = \frac{\xi\,(\mathrm{CIDA} - \alpha{\cdot}\mathrm{CIAA} - \beta{\cdot}\mathrm{CIDD})}{\mathrm{CIDD} + \xi\,(\mathrm{CIDA} - \alpha{\cdot}\mathrm{CIAA} - \beta{\cdot}\mathrm{CIDD})} \qquad (19)$$

Again, as with γ, the value for ξ can be determined using the linked donor-acceptor FRET probe (where $f_D = 1$, and E has been pre-determined), and solving equation (19) for ξ:

$$\xi = \frac{\mathrm{E} \cdot \mathrm{CIDD}}{(1-\mathrm{E})(\mathrm{CIDA} - \alpha{\cdot}\mathrm{CIAA} - \beta{\cdot}\mathrm{CIDD})} \qquad (20)$$

Lastly, FRET stoichiometry allows for the determination of the molar ratio of acceptor to donor in each cell. This is possible, because the calibration constants allow for determination of the total amount of acceptor, as well as the total amount of donor, in each cell. Dividing these two values, we obtain:

$$Ratio = \frac{Total\ Acceptor}{Total\ Donor} = \frac{\alpha{\cdot}\mathrm{CIAA}}{\mathrm{CIDD} + \xi\,(\mathrm{CIDA} - \alpha{\cdot}\mathrm{CIAA} - \beta{\cdot}\mathrm{CIDD})} \qquad (21)$$

Equation (21) is not quite correct, however, as the “units” of the numerator and denominator are not comparable. The numerator is written in terms of excitation of the acceptor at donor excitation wavelengths, while measuring emission of the acceptor, whereas the denominator is written in terms of excitation of the donor at donor excitation wavelengths, while measuring emission of the donor. Thus, Equation (21) must be corrected for 1) differences in extinction coefficients between the acceptor and donor at donor excitation wavelengths, and 2) differences in the brightness of the acceptor compared to the donor. The first correction can be performed by dividing equation (21) by γ, and the second correction can be performed by multiplying equation (21) by ξ. As such, the equation for the molar ratio is:

$$Ratio = \frac{\alpha\cdot\mathrm{CIAA}}{\mathrm{CIDD} + \xi\,(\mathrm{CIDA} - \alpha\cdot\mathrm{CIAA} - \beta\cdot\mathrm{CIDD})} \cdot \frac{\xi}{\gamma} \qquad (22)$$

In summary, the method of sensitized emission FRET via FRET stoichiometry can be performed using a widefield microscope, and involves taking 3 pictures (CIDD, CIDA, and CIAA). Calculation of FRET parameters requires prior determination of 4 calibration constants (α, β, γ, and ξ) that are specific to the fluorophores and the optical components of the imaging system used. Importantly, the 3 images and 4 calibration constants can be used for determination of the apparent FRET efficiencies of the acceptor and donor in complex, as well as for determination of the molar ratio of total acceptor : total donor. Determination of the molar ratio is especially important, as a low apparent FRET efficiency could either result from a low characteristic FRET efficiency, or a low fraction of molecules in complex. The molar ratio can provide an idea as to which of these possibilities is occurring, as molar ratio values close to unity would tend to suggest the former, whereas very low or high ratio values would tend to suggest the latter.

Preview to the Investigations of this Dissertation

An understanding of SNARE protein function and the dynamic processes that regulate the activity of SNARE core complexes is clearly critical to understanding the molecular mechanisms that underlie neurotransmitter release. These topics are the primary focus of investigations of this dissertation, which is comprised of three major studies.

The first study of this dissertation tests the general hypothesis that there exist direct interactions between SNARE proteins and lipids, and that these interactions are functionally relevant to the ability of SNARE proteins to catalyze membrane fusion events. As SNARE proteins form the minimal machinery required for membrane fusion, they also therefore define the sites at which fusion can occur. Moreover, the presence of specific fusogenic lipids in the membranes undergoing fusion has been shown to have profound effects on lowering the energy barrier for fusion. We hypothesize that direct interactions between SNARE proteins and fusogenic lipids might provide a mechanism by which the energy barrier for membrane fusion could be reduced at sites of fusion.

The second study of this dissertation tests the general hypothesis that the regulation of SNARE core complex assembly/disassembly is a dynamic process that is itself regulated by secretory demand. Specifically, this study focuses on the soluble R-SNARE protein, tomosyn, and tests the hypotheses that tomosyn's interaction with the plasma membrane SNARE syntaxin1A occurs dynamically, is regulated by specific signaling pathways that occur downstream of secretory stimuli, and is functionally relevant to the regulation of neurotransmitter release.

The final study of this dissertation focuses on the development of an imaging technique that provides the unique capability to dynamically visualize, at the single vesicle level, molecular interactions that occur at or near the plasma membrane during the process of neurotransmitter release. This approach combines the high sensitivity and high temporal resolution of sensitized emission FRET measurements with the unprecedented axial resolution afforded by TIRF microscopy. Importantly, development and testing of this novel technical approach will allow for quantitative changes in molecular interactions to be directly correlated to a functional outcome, such as vesicle docking, priming, or fusion. We believe that the ability to spatially and temporally match the dynamics of protein interactions in live cells with specific subcellular functions of the cell will herald in a new frontier in the study of cell biology.

Taken together, these studies further our understanding of both lipid-mediated and protein-mediated processes that regulate the final stages of neurotransmitter release. Moreover, they set the groundwork for the application of an imaging approach likely to revolutionize the way in which we gain information on the temporal and spatial dynamics of molecular assemblies associated with specific cellular functions, and in particular, will yield many novel insights into the dynamic processes that regulate neurotransmitter release.

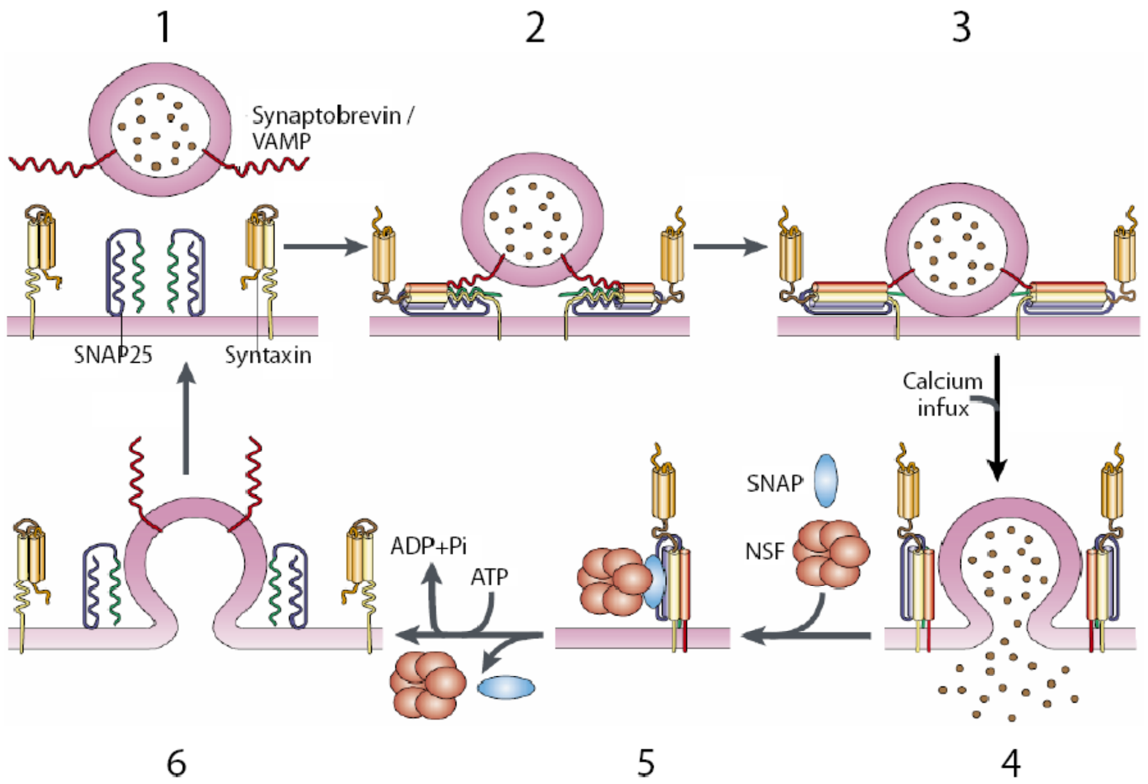

Figure 1.1. The synaptic vesicle cycle (figure adapted from [185]). (1) The synaptic vesicle, containing the R-SNARE synaptobrevin/VAMP2, must first approach the plasma membrane, where the Q-SNAREs syntaxin and SNAP25 reside, to become docked. (2) Nucleation of a “loose” trans-SNARE core complex occurs, followed by (3) formation of SNAREs into a “tight” SNARE core complex. (4) Upon calcium entry into the nerve terminal, complete zippering of the SNARE core complex catalyzes the membrane fusion event, resulting in formation of cis-SNARE complexes at the plasma membrane. (5) Hydrolysis of ATP by NSF/SNAP results in disassembly of cis-SNARE complexes into the individual SNARE constituents. (6) The vesicle membrane is recycled by endocytosis to begin the cycle anew.

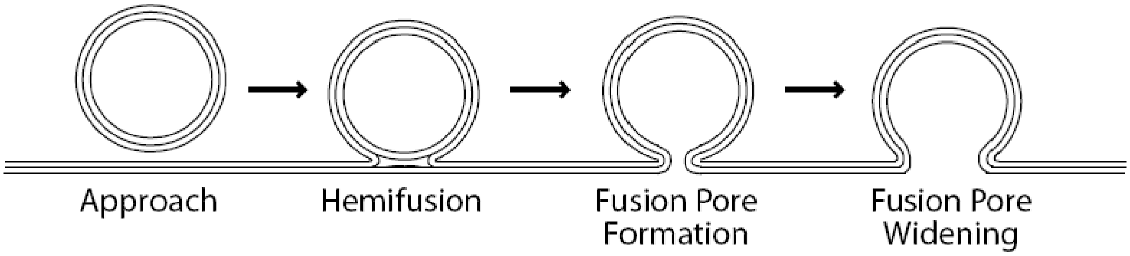

Figure 1.2. Lipid intermediates in membrane fusion. Fusion of two lipid bilayers first requires close apposition of the two membranes. Fusion of the proximal contacting leaflets occurs first, resulting in hemifusion. Expansion of the hemifusion diaphragm then results in the fusion of the distal leaflets of the bilayers, generating a fusion pore. Lateral tension results in widening of the fusion pore, and in full fusion of the membranes.

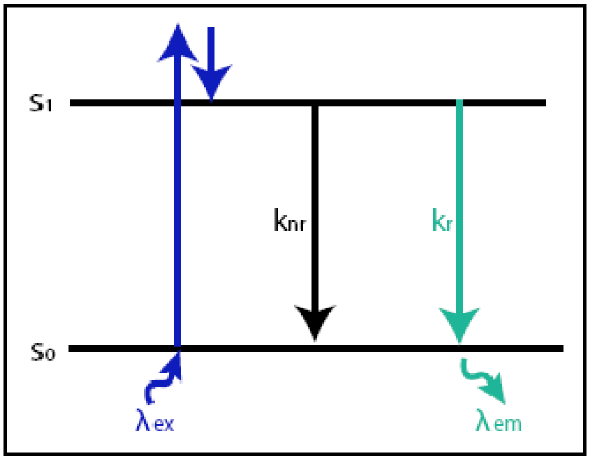

Figure 1.3. Jablonski diagram illustrating the transitioning of a fluorophore between the electronic ground (s_o) and excited (s_1) states. The fluorophore is excited by absorption of a photon of wavelength λ_{ex}, and can decay back to the ground state via nonradiative or radiative pathways, with rate constants k_{nr} and k_r respectively. In the radiative pathway, the fluorophore emits a photon of wavelength λ_{em}.

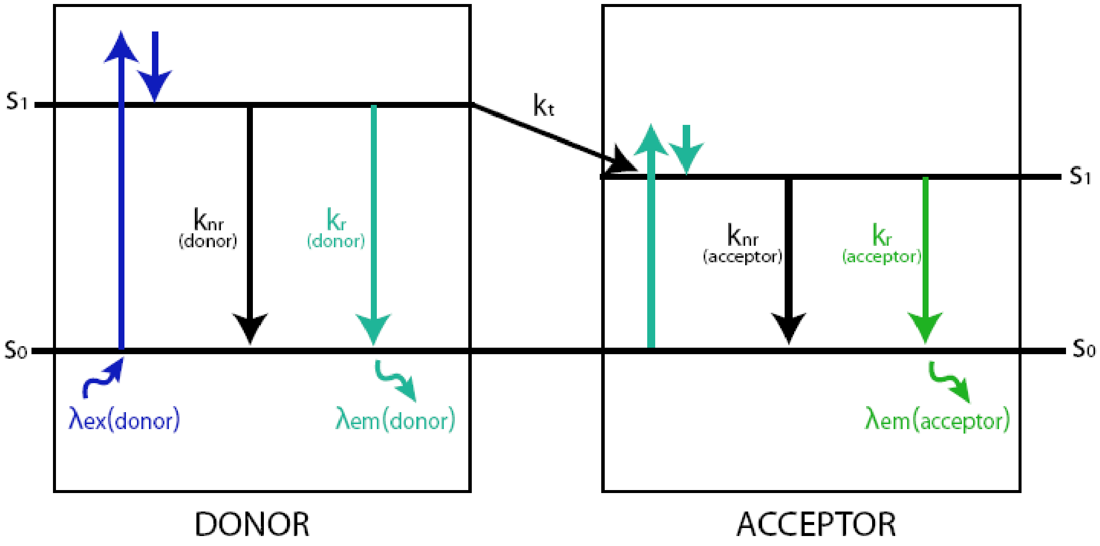

Figure 1.4. Jablonski diagram illustrating the process of fluorescence resonance energy transfer (FRET). The left panel demonstrates the transitioning of a donor fluorophore between its electronic ground and excited states, and is identical to Figure 1.3. In the right panel, the excited state donor fluorophore decays back to its ground state by transferring its energy to an acceptor fluorophore via FRET (with rate constant k_t). This causes the acceptor fluorophore to transition from its ground state to its excited state. Subsequently, the acceptor decays back to the ground state via the nonradiative or radiative pathways.

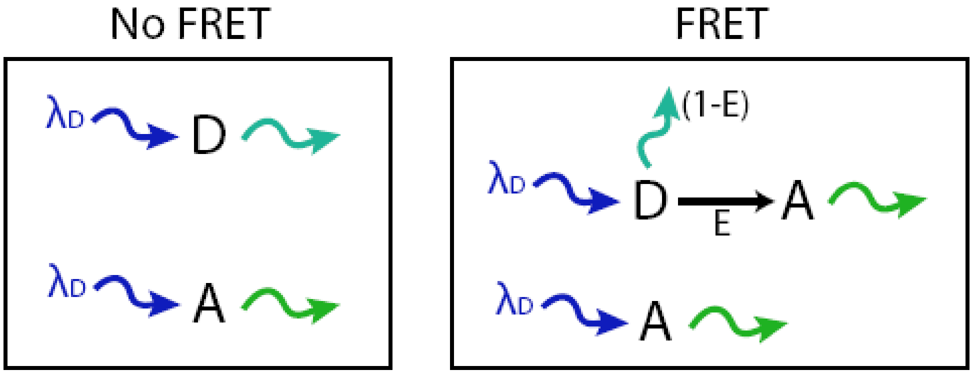

Figure 1.5. Schematic of the excitation and emission of donor and acceptor fluorophores in the absence or presence of FRET. Left panel, absence of FRET. Right panel, FRET occurs. In the right panel, E represents the characteristic FRET efficiency, or the fraction of excited-state donor molecules in complex with the acceptor that undergo FRET with the acceptor. (1-E) represents the fraction of excited state donors in complex with the acceptor that do not decay through FRET (ie, they decay either radiatively or non-radiatively).

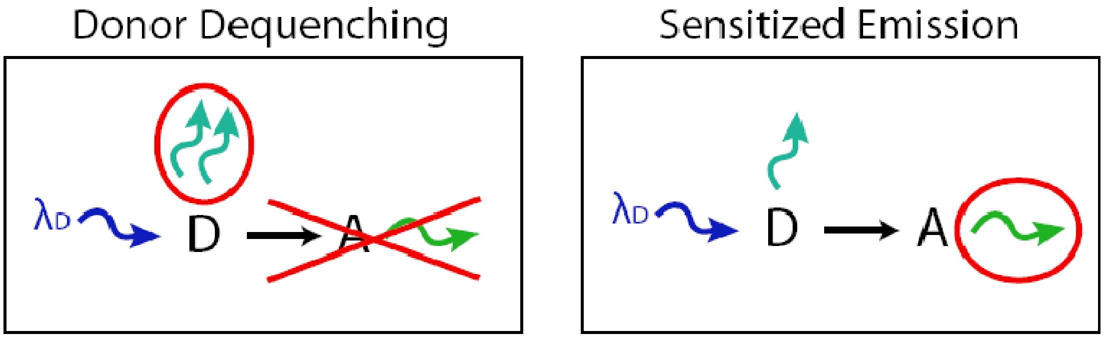

Figure 1.6. Schematic of FRET as measured using donor dequenching or sensitized emission. Left panel, schematic of donor dequenching. Photodestruction of the acceptor fluorophore precludes the donor fluorophore from undergoing FRET. This can be detected as an increase (ie, dequenching) in the donor fluorescence following photodestruction of the acceptor. Right panel, schematic of sensitized emission. FRET is visualized as an increase in acceptor fluorescence intensity upon excitation with the donor excitation wavelength, λ_D.

Figure 1.7. Schematic of the three images required for determination of apparent FRET efficiency, using the method of FRET stoichiometry. CIDD, corrected image with donor excitation and donor emission; CIDA, corrected image with donor excitation and acceptor emission; CIAA, corrected image with acceptor excitation and acceptor emission. Note that CIDA contains the sensitized emission signal, but is spectrally contaminated with cross-talk and bleedthrough components.

References

1. Burgess, T.L. and R.B. Kelly, *Constitutive and regulated secretion of proteins.* Annu Rev Cell Biol, 1987. **3**: p. 243-93.
2. Hannah, M.J., A.A. Schmidt, and W.B. Huttner, *SYNAPTIC VESICLE BIOGENESIS.* Annual Review of Cell and Developmental Biology, 1999. **15**(1): p. 733.
3. Sudhof, T.C., *Neurotransmitter release.* Handb Exp Pharmacol, 2008(184): p. 1-21.
4. E. Evergren, F.B.O.S., *The synapsin cycle: A view from the synaptic endocytic zone.* Journal of Neuroscience Research, 2007. **85**(12): p. 2648-2656.
5. Schweizer, F.E. and T.A. Ryan, *The synaptic vesicle: cycle of exocytosis and endocytosis.* Current Opinion in Neurobiology, 2006. **16**(3): p. 298-304.
6. Murthy, V.N. and C.F. Stevens, *Synaptic vesicles retain their identity through the endocytic cycle.* Nature, 1998. **392**(6675): p. 497-501.
7. Kavalali, E.T., *Multiple vesicle recycling pathways in central synapses and their impact on neurotransmission.* J Physiol, 2007. **585**(3): p. 669-679.
8. Sollner, T., et al., *SNAP receptors implicated in vesicle targeting and fusion.* Nature, 1993. **362**(6418): p. 318-324.
9. Plattner, H., A.R. Artalejo, and E. Neher, *Ultrastructural Organization of Bovine Chromaffin Cell Cortex---Analysis by Cryofixation and Morphometry of Aspects Pertinent to Exocytosis.* J. Cell Biol., 1997. **139**(7): p. 1709-1717.
10. Steyer, J.A., H. Horstmann, and W. Almers, *Transport, docking and exocytosis of single secretory granules in live chromaffin cells.* Nature, 1997. **388**(6641): p. 474-478.
11. Axelrod, D.D., *Total internal reflection fluorescence microscopy in cell biology.* Traffic, 2001. **2**(11): p. 764-74.
12. Oheim, M., *Imaging Transmitter Release. II. A Practical Guide to Evanescent-wave Imaging.* Lasers in Medical Science, 2001. **16**(3): p. 159-170.
13. Degtyar, V.E., et al., *Increased motion and travel, rather than stable docking, characterize the last moments before secretory granule fusion.* Proceedings of the National Academy of Sciences, 2007. **104**(40): p. 15929-15934.
14. Oheim, M., et al., *The last few milliseconds in the life of a secretory granule.* European Biophysics Journal, 1998. **27**(2): p. 83-98.
15. Toonen, R.F., et al., *Dissecting docking and tethering of secretory vesicles at the target membrane.* EMBO J, 2006. **25**(16): p. 3725-37.
16. Allersma, M.W., et al., *Visualization of Regulated Exocytosis with a Granule-Membrane Probe Using Total Internal Reflection Microscopy.* Mol. Biol. Cell, 2004. **15**(10): p. 4658-4668.
17. Verhage, M. and J.B. Sorensen, *Vesicle Docking in Regulated Exocytosis.* Traffic, 2008.
18. Rizzoli, S.O. and W.J. Betz, *The Structural Organization of the Readily Releasable Pool of Synaptic Vesicles.* Science, 2004. **303**(5666): p. 2037-2039.
19. Duncan, R.R., et al., *Functional and spatial segregation of secretory vesicle pools according to vesicle age.* Nature, 2003. **422**(6928): p. 176-180.
20. Rostaing, P., et al., *Preservation of Immunoreactivity and Fine Structure of Adult C. elegans Tissues Using High-pressure Freezing.* J. Histochem. Cytochem., 2004. **52**(1): p. 1-12.

21. Yang, B., et al., *SNARE Interactions Are Not Selective. IMPLICATIONS FOR MEMBRANE FUSION SPECIFICITY.* J. Biol. Chem., 1999. **274**(9): p. 5649-5653.
22. Fasshauer, D., et al., *Mixed and non-cognate SNARE complexes. Characterization of assembly and biophysical properties.* J Biol Chem, 1999. **274**(22): p. 15440-6.
23. El Far, O., et al., *Protein interactions implicated in neurotransmitter release.* Journal of Physiology-Paris, 1998. **92**(2): p. 129-133.
24. Hunt, J.M., et al., *A post-docking role for synaptobrevin in synaptic vesicle fusion.* Neuron, 1994. **12**(6): p. 1269-1279.
25. Broadie, K., et al., *Syntaxin and synaptobrevin function downstream of vesicle docking in drosophila.* Neuron, 1995. **15**(3): p. 663-673.
26. Zerial, M. and H. McBride, *Rab proteins as membrane organizers.* Nat Rev Mol Cell Biol, 2001. **2**(2): p. 107-17.
27. van Weering, J.R.T., R.F. Toonen, and M. Verhage, *The Role of Rab3a in Secretory Vesicle Docking Requires Association/Dissociation of Guanidine Phosphates and Munc18-1.* PLoS ONE, 2007. **2**(7): p. e616.
28. Schlüter, O.M.O.M., et al., *Localization versus function of Rab3 proteins. Evidence for a common regulatory role in controlling fusion.* The Journal of biological chemistry, 2002. **277**(43): p. 40919-29.
29. Mahoney, T.R.T.R., et al., *Regulation of synaptic transmission by RAB-3 and RAB-27 in Caenorhabditis elegans.* Molecular biology of the cell, 2006. **17**(6): p. 2617-25.
30. Yi, Z.Z., et al., *The Rab27a/granuphilin complex regulates the exocytosis of insulin-containing dense-core granules.* Molecular and cellular biology, 2002. **22**(6): p. 1858-67.
31. Martelli, A.M., et al., *Rab3A and Rab3D Control the Total Granule Number and the Fraction of Granules Docked at the Plasma Membrane in PC12 Cells.* Traffic, 2000. **1**(12): p. 976-986.
32. Tsuboi, T. and M. Fukuda, *Rab3A and Rab27A cooperatively regulate the docking step of dense-core vesicle exocytosis in PC12 cells.* J Cell Sci, 2006. **119**(11): p. 2196-2203.
33. Kasai, K., et al., *Rab27a mediates the tight docking of insulin granules onto the plasma membrane during glucose stimulation.* J Clin Invest, 2005. **115**(2): p. 388-96.
34. Schluter, O.M., et al., *A Complete Genetic Analysis of Neuronal Rab3 Function.* J. Neurosci., 2004. **24**(29): p. 6629-6637.
35. Coppola, T., et al., *Pancreatic beta -Cell Protein Granuphilin Binds Rab3 and Munc-18 and Controls Exocytosis.* Mol. Biol. Cell, 2002. **13**(6): p. 1906-1915.
36. Torii, S., et al., *Granuphilin Modulates the Exocytosis of Secretory Granules through Interaction with Syntaxin 1a.* Mol. Cell. Biol., 2002. **22**(15): p. 5518-5526.
37. Gomi, H., et al., *Granuphilin molecularly docks insulin granules to the fusion machinery.* J. Cell Biol., 2005. **171**(1): p. 99-109.
38. Tsuboi, T. and M. Fukuda, *The C2B Domain of Rabphilin Directly Interacts with SNAP-25 and Regulates the Docking Step of Dense Core Vesicle Exocytosis in PC12 Cells.* J. Biol. Chem., 2005. **280**(47): p. 39253-39259.
39. Schluter, O.M., et al., *Rabphilin Knock-Out Mice Reveal That Rabphilin Is Not Required for Rab3 Function in Regulating Neurotransmitter Release.* J. Neurosci., 1999. **19**(14): p. 5834-5846.

40. Schoch, S., et al., *RIM1[alpha] forms a protein scaffold for regulating neurotransmitter release at the active zone.* Nature, 2002. **415**(6869): p. 321-326.
41. Toonen, R.F., et al., *Munc18-1 expression levels control synapse recovery by regulating readily releasable pool size.* Proc Natl Acad Sci U S A, 2006. **103**(48): p. 18332-7.
42. Voets, T., et al., *Munc18-1 Promotes Large Dense-Core Vesicle Docking.* Neuron, 2001. **31**(4): p. 581-591.
43. Gulyas-Kovacs, A., et al., *Munc18-1: Sequential Interactions with the Fusion Machinery Stimulate Vesicle Docking and Priming.* J. Neurosci., 2007. **27**(32): p. 8676-8686.
44. Weimer, R.M., et al., *Defects in synaptic vesicle docking in unc-18 mutants.* Nat Neurosci, 2003. **6**(10): p. 1023-30.
45. Graham, M.E., et al., *A gain-of-function mutant of Munc18-1 stimulates secretory granule recruitment and exocytosis and reveals a direct interaction of Munc18-1 with Rab3.* Biochem J, 2008. **409**(2): p. 407-16.
46. Becherer, U. and J. Rettig, *Vesicle pools, docking, priming, and release.* Cell Tissue Res, 2006. **326**(2): p. 393-407.
47. Ashery, U.U., et al., *Munc13-1 acts as a priming factor for large dense-core vesicles in bovine chromaffin cells.* The EMBO journal, 2000. **19**(14): p. 3586-96.
48. Yizhar, O.O., et al., *Tomosyn inhibits priming of large dense-core vesicles in a calcium-dependent manner.* Proceedings of the National Academy of Sciences of the United States of America, 2004. **101**(8): p. 2578-83.
49. Augustin, I.I., et al., *Munc13-1 is essential for fusion competence of glutamatergic synaptic vesicles.* Nature, 1999. **400**(6743): p. 457-61.
50. Dunn, L.L.A. and R.R.W. Holz, *Catecholamine secretion from digitonin-treated adrenal medullary chromaffin cells.* The Journal of biological chemistry, 1983. **258**(8): p. 4989-93.
51. Knight, D.D.E. and P.P.F. Baker, *Calcium-dependence of catecholamine release from bovine adrenal medullary cells after exposure to intense electric fields.* The Journal of membrane biology, 1982. **68**(2): p. 107-40.
52. Hay, J.C. and T.F. Martin, *Resolution of regulated secretion into sequential MgATP-dependent and calcium-dependent stages mediated by distinct cytosolic proteins.* J Cell Biol, 1992. **119**(1): p. 139-51.
53. Heinemann, C., et al., *Kinetics of the secretory response in bovine chromaffin cells following flash photolysis of caged Ca2+.* Biophys. J., 1994. **67**(6): p. 2546-2557.
54. Xu, T., et al., *Multiple kinetic components of exocytosis distinguished by neurotoxin sensitivity.* Nat Neurosci, 1998. **1**(3): p. 192-200.
55. Sørensen, J.B., *Formation, stabilisation and fusion of the readily releasable pool of secretory vesicles.* Pflügers Archiv European Journal of Physiology, 2004. **448**(4): p. 347-362.
56. Bittner, M.A. and R.W. Holz, *Kinetic analysis of secretion from permeabilized adrenal chromaffin cells reveals distinct components.* J Biol Chem, 1992. **267**(23): p. 16219-25.
57. Holz, R.W., et al., *MgATP-independent and MgATP-dependent exocytosis. Evidence that MgATP primes adrenal chromaffin cells to undergo exocytosis.* J Biol Chem, 1989. **264**(10): p. 5412-9.
58. Smith, C.C., et al., *Cytosolic Ca2+ acts by two separate pathways to modulate the supply of release-competent vesicles in chromaffin cells.* Neuron, 1998. **20**(6): p. 1243-53.

59. Voets, T.T., *Dissection of three Ca2+dependent steps leading to secretion in chromaffin cells from mouse adrenal slices.* Neuron, 2000. **28**(2): p. 537-45.
60. von Rüden, L.L. and E.E. Neher, *A Ca-dependent early step in the release of catecholamines from adrenal chromaffin cells.* Science, 1993. **262**(5136): p. 1061-5.
61. Eberhard, D.A., et al., *Evidence that the inositol phospholipids are necessary for exocytosis. Loss of inositol phospholipids and inhibition of secretion in permeabilized cells caused by a bacterial phospholipase C and removal of ATP.* Biochem J, 1990. **268**(1): p. 15-25.
62. Hay, J.J.C., et al., *ATP-dependent inositide phosphorylation required for Ca(2+)-activated secretion.* Nature, 1995. **374**(6518): p. 173-7.
63. Hay, J.J.C. and T.T.F. Martin, *Phosphatidylinositol transfer protein required for ATP-dependent priming of Ca(2+)-activated secretion.* Nature, 1993. **366**(6455): p. 572-5.
64. Paolo, G.D., et al., *Impaired PtdIns(4,5)P2 synthesis in nerve terminals produces defects in synaptic vesicle trafficking.* Nature, 2004. **431**(7007): p. 415-422.
65. Gong, L.-W., et al., *Phosphatidylinositol phosphate kinase type I{gamma} regulates dynamics of large dense-core vesicle fusion.* Proceedings of the National Academy of Sciences, 2005. **102**(14): p. 5204-5209.
66. Schiavo, G., et al., *Calcium-dependent switching of the specificity of phosphoinositide binding to synaptotagmin.* Proceedings of the National Academy of Sciences, 1996. **93**(23): p. 13327-13332.
67. Chung, S.-H., et al., *The C2 Domains of Rabphilin3A Specifically Bind Phosphatidylinositol 4,5-Bisphosphate Containing Vesicles in a Ca2+-dependent Manner. IN VITRO CHARACTERISTICS AND POSSIBLE SIGNIFICANCE.* J. Biol. Chem., 1998. **273**(17): p. 10240-10248.
68. Loyet, K.M., et al., *Specific Binding of Phosphatidylinositol 4,5-Bisphosphate to Calcium-dependent Activator Protein for Secretion (CAPS), a Potential Phosphoinositide Effector Protein for Regulated Exocytosis.* J. Biol. Chem., 1998. **273**(14): p. 8337-8343.
69. Okamoto, M. and T.C. Sudhof, *Mints, Munc18-interacting Proteins in Synaptic Vesicle Exocytosis.* J. Biol. Chem., 1997. **272**(50): p. 31459-31464.
70. Lam, A.D., et al., *SNARE-catalyzed Fusion Events Are Regulated by Syntaxin1A-Lipid Interactions.* Mol Biol Cell, 2008. **19**(2): p. 485-97.
71. Aoyagi, K., et al., *The Activation of Exocytotic Sites by the Formation of Phosphatidylinositol 4,5-Bisphosphate Microdomains at Syntaxin Clusters.* J. Biol. Chem., 2005. **280**(17): p. 17346-17352.
72. Milosevic, I., et al., *Plasmalemmal Phosphatidylinositol-4,5-Bisphosphate Level Regulates the Releasable Vesicle Pool Size in Chromaffin Cells.* J. Neurosci., 2005. **25**(10): p. 2557-2565.
73. Bittner, M.A. and R.W. Holz, *Phosphatidylinositol-4,5-bisphosphate: Actin Dynamics and the Regulation of ATP-Dependent and -Independent Secretion.* Mol Pharmacol, 2005. **67**(4): p. 1089-1098.
74. Yin, H.L. and P.A. Janmey, *PHOSPHOINOSITIDE REGULATION OF THE ACTIN CYTOSKELETON.* Annual Review of Physiology, 2003. **65**(1): p. 761-789.
75. Block, M.R., et al., *Purification of an N-ethylmaleimide-Sensitive Protein Catalyzing Vesicular Transport.* Proceedings of the National Academy of Sciences, 1988. **85**(21): p. 7852-7856.
76. Wilson, D.W., et al., *A multisubunit particle implicated in membrane fusion.* J. Cell Biol., 1992. **117**(3): p. 531-538.

77. Söllner, T., et al., *A protein assembly-disassembly pathway in vitro that may correspond to sequential steps of synaptic vesicle docking, activation, and fusion.* Cell, 1993. **75**(3): p. 409-418.
78. Colombo, M.M.I., et al., *A possible predocking attachment site for N-ethylmaleimide-sensitive fusion protein. Insights from in vitro endosome fusion.* The Journal of biological chemistry, 1996. **271**(31): p. 18810-6.
79. Mayer, A., W. Wickner, and A. Haas, *Sec18p (NSF)-Driven Release of Sec17p ([alpha]-SNAP) Can Precede Docking and Fusion of Yeast Vacuoles.* Cell, 1996. **85**(1): p. 83-94.
80. Parsons, T.T.D., et al., *Docked granules, the exocytic burst, and the need for ATP hydrolysis in endocrine cells.* Neuron, 1995. **15**(5): p. 1085-96.
81. Morgan, A.A. and R.R.D. Burgoyne, *Is NSF a fusion protein?* Trends in cell biology, 1995. **5**(9): p. 335-9.
82. Ungermann, C., et al., *A Vacuolar v-t-SNARE Complex, the Predominant Form In Vivo and on Isolated Vacuoles, Is Disassembled and Activated for Docking and Fusion.* J. Cell Biol., 1998. **140**(1): p. 61-69.
83. Banerjee, A., et al., *N-Ethylmaleimide-sensitive Factor Acts at a Prefusion ATP-dependent Step in Ca2+-activated Exocytosis.* J. Biol. Chem., 1996. **271**(34): p. 20223-20226.
84. Schweizer, F.E., et al., *Regulation of Neurotransmitter Release Kinetics by NSF.* Science, 1998. **279**(5354): p. 1203-1206.
85. Xu, T., et al., *Early requirement for alpha-SNAP and NSF in the secretory cascade in chromaffin cells.* EMBO J, 1999. **18**(12): p. 3293-304.
86. Jockusch, W.J.W.J., et al., *CAPS-1 and CAPS-2 are essential synaptic vesicle priming proteins.* Cell, 2007. **131**(4): p. 796-808.
87. Gillis, K.K.D., R.R. Mossner, and E.E. Neher, *Protein kinase C enhances exocytosis from chromaffin cells by increasing the size of the readily releasable pool of secretory granules.* Neuron, 1996. **16**(6): p. 1209-20.
88. Stevens, C.C.F. and J.J.M. Sullivan, *Regulation of the readily releasable vesicle pool by protein kinase C.* Neuron, 1998. **21**(4): p. 885-93.
89. Evans, G.G.J.O. and A.A. Morgan, *Regulation of the exocytotic machinery by cAMP-dependent protein kinase: implications for presynaptic plasticity.* Biochemical society transactions, 2003. **31**(Pt 4): p. 824-7.
90. Klenchin, V.A. and T.F. Martin, *Priming in exocytosis: attaining fusion-competence after vesicle docking.* Biochimie, 2000. **82**(5): p. 399-407.
91. Harata, N.C., A.M. Aravanis, and R.W. Tsien, *Kiss-and-run and full-collapse fusion as modes of exo-endocytosis in neurosecretion.* Journal of Neurochemistry, 2006. **97**(6): p. 1546-1570.
92. Jahn, R. and R.H. Scheller, *SNAREs--engines for membrane fusion.* Nat Rev Mol Cell Biol, 2006. **7**(9): p. 631-43.
93. Weber, T., et al., *SNAREpins: Minimal Machinery for Membrane Fusion.* Cell, 1998. **92**(6): p. 759-772.
94. Blasi, J., et al., *Botulinum neurotoxin A selectively cleaves the synaptic protein SNAP-25.* Nature, 1993. **365**(6442): p. 160-163.
95. Blasi, J., et al., *Botulinum neurotoxin C1 blocks neurotransmitter release by means of cleaving HPC-1/syntaxin.* EMBO J, 1993. **12**(12): p. 4821-8.
96. Schiavo, G.G., et al., *Tetanus and botulinum-B neurotoxins block neurotransmitter release by proteolytic cleavage of synaptobrevin.* Nature, 1992. **359**(6398): p. 832-835.

97. Littleton, J.T., et al., *Temperature-Sensitive Paralytic Mutations Demonstrate that Synaptic Exocytosis Requires SNARE Complex Assembly and Disassembly.* Neuron, 1998. **21**(2): p. 401-413.
98. Saifee, O., L. Wei, and M.L. Nonet, *The Caenorhabditis elegans unc-64 Locus Encodes a Syntaxin That Interacts Genetically with Synaptobrevin.* Mol. Biol. Cell, 1998. **9**(6): p. 1235-1252.
99. Sorensen, J.B., et al., *Sequential N- to C-terminal SNARE complex assembly drives priming and fusion of secretory vesicles.* EMBO J, 2006. **25**(5): p. 955-66.
100. Sorensen, J.B., et al., *The SNARE protein SNAP-25 is linked to fast calcium triggering of exocytosis.* Proceedings of the National Academy of Sciences, 2002. **99**(3): p. 1627-1632.
101. Borisovska, M., et al., *v-SNAREs control exocytosis of vesicles from priming to fusion.* EMBO J, 2005. **24**(12): p. 2114-26.
102. Gerst, J.E., *SNARE regulators: matchmakers and matchbreakers.* Biochim Biophys Acta, 2003. **1641**(2-3): p. 99-110.
103. Fasshauer, D., et al., *Identification of a minimal core of the synaptic SNARE complex sufficient for reversible assembly and disassembly.* Biochemistry, 1998. **37**(29): p. 10354-62.
104. Hayashi, T.T., et al., *Synaptic vesicle membrane fusion complex: action of clostridial neurotoxins on assembly.* The EMBO journal, 1994. **13**(21): p. 5051-61.
105. Sutton, R.B., et al., *Crystal structure of a SNARE complex involved in synaptic exocytosis at 2.4[thinsp]A resolution.* Nature, 1998. **395**(6700): p. 347-353.
106. Fasshauer, D., et al., *Conserved structural features of the synaptic fusion complex: SNARE proteins reclassified as Q- and R-SNAREs.* Proc Natl Acad Sci U S A, 1998. **95**(26): p. 15781-6.
107. Sørensen, J.B.J.B., et al., *Sequential N- to C-terminal SNARE complex assembly drives priming and fusion of secretory vesicles.* The EMBO journal, 2006. **25**(5): p. 955-66.
108. Montecucco, C., G. Schiavo, and S. Pantano, *SNARE complexes and neuroexocytosis: how many, how close?* Trends Biochem Sci, 2005. **30**(7): p. 367-72.
109. Bennett, M.M.K., N.N. Calakos, and R.R.H. Scheller, *Syntaxin: a synaptic protein implicated in docking of synaptic vesicles at presynaptic active zones.* Science, 1992. **257**(5067): p. 255-9.
110. Oyler, G.G.A., et al., *The identification of a novel synaptosomal-associated protein, SNAP-25, differentially expressed by neuronal subpopulations.* The Journal of cell biology, 1989. **109**(6 Pt 1): p. 3039-52.
111. Baumert, M.M., et al., *Synaptobrevin: an integral membrane protein of 18,000 daltons present in small synaptic vesicles of rat brain.* The EMBO journal, 1989. **8**(2): p. 379-84.
112. Trimble, W.W.S., D.D.M. Cowan, and R.R.H. Scheller, *VAMP-1: a synaptic vesicle-associated integral membrane protein.* Proceedings of the National Academy of Sciences of the United States of America, 1988. **85**(12): p. 4538-42.
113. Lang, T. and R. Jahn, *Core proteins of the secretory machinery.* Handb Exp Pharmacol, 2008(184): p. 107-27.
114. Misura, K.K.M., R.R.H. Scheller, and W.W.I. Weis, *Three-dimensional structure of the neuronal-Sec1-syntaxin 1a complex.* Nature, 2000. **404**(6776): p. 355-62.
115. Schulze, K.L., et al., *Genetic and electrophysiological studies of drosophila syntaxin-1A demonstrate its role in nonneuronal secretion and neurotransmission.* Cell, 1995. **80**(2): p. 311-320.

116. Han, X. and M.B. Jackson, *Electrostatic interactions between the syntaxin membrane anchor and neurotransmitter passing through the fusion pore.* Biophys J, 2005. **88**(3): p. L20-2.
117. Han, X., et al., *Transmembrane segments of syntaxin line the fusion pore of Ca2+-triggered exocytosis.* Science, 2004. **304**(5668): p. 289-92.
118. Risinger, C. and M.K. Bennett, *Differential Phosphorylation of Syntaxin and Synaptosome-Associated Protein of 25 kDa (SNAP-25) Isoforms.* Journal of Neurochemistry, 1999. **72**(2): p. 614-624.
119. Shimazaki, Y.Y., et al., *Phosphorylation of 25-kDa synaptosome-associated protein. Possible involvement in protein kinase C-mediated regulation of neurotransmitter release.* The Journal of biological chemistry, 1996. **271**(24): p. 14548-53.
120. Nagy, G.G., et al., *Regulation of releasable vesicle pool sizes by protein kinase A-dependent phosphorylation of SNAP-25.* Neuron, 2004. **41**(3): p. 417-29.
121. Washbourne, P.P., et al., *Genetic ablation of the t-SNARE SNAP-25 distinguishes mechanisms of neuroexocytosis.* Nature neuroscience, 2002. **5**(1): p. 19-26.
122. Schiavo, G.G., et al., *Botulinum neurotoxins serotypes A and E cleave SNAP-25 at distinct COOH-terminal peptide bonds.* FEBS letters, 1993. **335**(1): p. 99-103.
123. Williamson, L.C., et al., *Clostridial Neurotoxins and Substrate Proteolysis in Intact Neurons.* J. Biol. Chem., 1996. **271**(13): p. 7694-7699.
124. Huang, X., et al., *Ca2+ influx and cAMP elevation overcame botulinum toxin A but not tetanus toxin inhibition of insulin exocytosis.* Am J Physiol Cell Physiol, 2001. **281**(3): p. C740-750.
125. Schoch, S., et al., *SNARE Function Analyzed in Synaptobrevin/VAMP Knockout Mice.* Science, 2001. **294**(5544): p. 1117-1122.
126. Rossetto, O., et al., *The metallo-proteinase activity of tetanus and botulism neurotoxins.* Journal of Physiology-Paris, 1995. **89**(1): p. 43-50.
127. Toonen, R.F.G. and M. Verhage, *Vesicle trafficking: pleasure and pain from SM genes.* Trends in cell biology, 2003. **13**(4): p. 177-186.
128. Hosono, R., T. Sassa, and S. Kuno, *Mutations affecting acetylcholine levels in the nematode Caenorhabditis elegans.* J Neurochem, 1987. **49**(6): p. 1820-3.
129. Aalto, M.K., S. Keranen, and H. Ronne, *A family of proteins involved in intracellular transport.* Cell, 1992. **68**(2): p. 181-2.
130. Novick, P., C. Field, and R. Schekman, *Identification of 23 complementation groups required for post-translational events in the yeast secretory pathway.* Cell, 1980. **21**(1): p. 205-15.
131. Hata, Y., C.A. Slaughter, and T.C. Sudhof, *Synaptic vesicle fusion complex contains unc-18 homologue bound to syntaxin.* Nature, 1993. **366**(6453): p. 347-351.
132. Pevsner, J., S. Hsu, and R.H. Scheller, *n-Sec1: A Neural-Specific Syntaxin-Binding Protein.* Proceedings of the National Academy of Sciences, 1994. **91**(4): p. 1445-1449.
133. Verhage, M., et al., *Synaptic Assembly of the Brain in the Absence of Neurotransmitter Secretion.* Science, 2000. **287**(5454): p. 864-869.
134. Dulubova, I., et al., *Munc18-1 binds directly to the neuronal SNARE complex.* Proceedings of the National Academy of Sciences, 2007. **104**(8): p. 2697-2702.
135. Shen, J., et al., *Selective Activation of Cognate SNAREpins by Sec1/Munc18 Proteins.* Cell, 2007. **128**(1): p. 183-195.

136. Fujita, Y., et al., *Tomosyn: a Syntaxin-1-Binding Protein that Forms a Novel Complex in the Neurotransmitter Release Process.* Neuron, 1998. **20**(5): p. 905-915.
137. Lehman, K., et al., *Yeast Homologues of Tomosyn and lethal giant larvae Function in Exocytosis and Are Associated with the Plasma Membrane SNARE, Sec9.* J. Cell Biol., 1999. **146**(1): p. 125-140.
138. Hattendorf, D.A., et al., *Structure of the yeast polarity protein Sro7 reveals a SNARE regulatory mechanism.* Nature, 2007. **446**(7135): p. 567-571.
139. Hatsuzawa, K., et al., *The R-SNARE Motif of Tomosyn Forms SNARE Core Complexes with Syntaxin 1 and SNAP-25 and Down-regulates Exocytosis.* J. Biol. Chem., 2003. **278**(33): p. 31159-31166.
140. Widberg, C.H., et al., *Tomosyn Interacts with the t-SNAREs Syntaxin4 and SNAP23 and Plays a Role in Insulin-stimulated GLUT4 Translocation.* J. Biol. Chem., 2003. **278**(37): p. 35093-35101.
141. Zhang, W., et al., *Tomosyn Is Expressed in {beta}-Cells and Negatively Regulates Insulin Exocytosis.* Diabetes, 2006. **55**(3): p. 574-581.
142. Gracheva, E.O., et al., *Tomosyn Inhibits Synaptic Vesicle Priming in Caenorhabditis elegans.* PLoS Biology, 2006. **4**(8): p. e261.
143. Gracheva, E.O., et al., *Tomosyn negatively regulates both synaptic transmitter and neuropeptide release at the C. elegans neuromuscular junction.* J Physiol, 2007. **585**(3): p. 705-709.
144. Gladycheva, S.E., et al., *Receptor-mediated regulation of tomosyn-syntaxin 1A interactions in bovine adrenal chromaffin cells.* J Biol Chem, 2007. **282**(31): p. 22887-99.
145. Pobbati, A.V., et al., *Structural Basis for the Inhibitory Role of Tomosyn in Exocytosis.* J. Biol. Chem., 2004. **279**(45): p. 47192-47200.
146. Matthew, W.D., L. Tsavaler, and L.F. Reichardt, *Identification of a synaptic vesicle-specific membrane protein with a wide distribution in neuronal and neurosecretory tissue.* J. Cell Biol., 1981. **91**(1): p. 257-269.
147. Perin, M.M.S., et al., *Domain structure of synaptotagmin (p65).* The Journal of biological chemistry, 1991. **266**(1): p. 623-9.
148. Perin, M.M.S., et al., *Structural and functional conservation of synaptotagmin (p65) in Drosophila and humans.* The Journal of biological chemistry, 1991. **266**(1): p. 615-22.
149. Bai, J., et al., *Membrane-embedded synaptotagmin penetrates cis or trans target membranes and clusters via a novel mechanism.* J Biol Chem, 2000. **275**(33): p. 25427-35.
150. Bai, J., W.C. Tucker, and E.R. Chapman, *PIP2 increases the speed of response of synaptotagmin and steers its membrane-penetration activity toward the plasma membrane.* Nat Struct Mol Biol, 2004. **11**(1): p. 36-44.
151. Davis, A.F., et al., *Kinetics of synaptotagmin responses to Ca2+ and assembly with the core SNARE complex onto membranes.* Neuron, 1999. **24**(2): p. 363-76.
152. Chapman, E.R., *How Does Synaptotagmin Trigger Neurotransmitter Release?* Annual Review of Biochemistry, 2008. **77**(1).
153. Fernandez-Chacon, R., et al., *Synaptotagmin I functions as a calcium regulator of release probability.* Nature, 2001. **410**(6824): p. 41-49.
154. Littleton, J.T., et al., *Calcium Dependence of Neurotransmitter Release and Rate of Spontaneous Vesicle Fusions are Altered in Drosophila Synaptotagmin Mutants.* Proceedings of the National Academy of Sciences, 1994. **91**(23): p. 10888-10892.

155. Geppert, M., et al., *Synaptotagmin I: A major Ca2+ sensor for transmitter release at a central synapse.* Cell, 1994. **79**(4): p. 717-727.
156. Nishiki, T.-i. and G.J. Augustine, *Synaptotagmin I Synchronizes Transmitter Release in Mouse Hippocampal Neurons.* J. Neurosci., 2004. **24**(27): p. 6127-6132.
157. Yoshihara, M. and J.T. Littleton, *Synaptotagmin I functions as a calcium sensor to synchronize neurotransmitter release.* Neuron, 2002. **36**(5): p. 897-908.
158. Craxton, M., *Synaptotagmin gene content of the sequenced genomes.* BMC Genomics, 2004. **5**(1): p. 43.
159. Sudhof, T.C., *Synaptotagmins: Why So Many?* J. Biol. Chem., 2002. **277**(10): p. 7629-7632.
160. Zimmerberg, J. and K. Gawrisch, *The physical chemistry of biological membranes.* Nat Chem Biol, 2006. **2**(11): p. 564-7.
161. Zimmerberg, J. and M.M. Kozlov, *How proteins produce cellular membrane curvature.* Nat Rev Mol Cell Biol, 2006. **7**(1): p. 9-19.
162. Chernomordik, L.V. and M.M. Kozlov, *Protein-lipid interplay in fusion and fission of biological membranes.* Annu Rev Biochem, 2003. **72**: p. 175-207.
163. Cohen, F.S. and G.B. Melikyan, *The energetics of membrane fusion from binding, through hemifusion, pore formation, and pore enlargement.* J Membr Biol, 2004. **199**(1): p. 1-14.
164. Yoon, T.-Y., et al., *Multiple intermediates in SNARE-induced membrane fusion.* Proceedings of the National Academy of Sciences, 2006. **103**(52): p. 19731-19736.
165. Lu, X., et al., *Membrane Fusion Induced by Neuronal SNAREs Transits through Hemifusion.* J. Biol. Chem., 2005. **280**(34): p. 30538-30541.
166. Fuller, N. and R.P. Rand, *The influence of lysolipids on the spontaneous curvature and bending elasticity of phospholipid membranes.* Biophys J, 2001. **81**(1): p. 243-54.
167. Szule, J.A., N.L. Fuller, and R.P. Rand, *The effects of acyl chain length and saturation of diacylglycerols and phosphatidylcholines on membrane monolayer curvature.* Biophys J, 2002. **83**(2): p. 977-84.
168. Kozlovsky, Y. and M.M. Kozlov, *Stalk model of membrane fusion: solution of energy crisis.* Biophys J, 2002. **82**(2): p. 882-95.
169. Rigoni, M., et al., *Equivalent effects of snake PLA2 neurotoxins and lysophospholipid-fatty acid mixtures.* Science, 2005. **310**(5754): p. 1678-80.
170. Wei, S., et al., *Group IIA secretory phospholipase A2 stimulates exocytosis and neurotransmitter release in pheochromocytoma-12 cells and cultured rat hippocampal neurons.* Neuroscience, 2003. **121**(4): p. 891-898.
171. Melia, T.J., et al., *Lipidic Antagonists to SNARE-mediated Fusion.* J. Biol. Chem., 2006. **281**(40): p. 29597-29605.
172. Chernomordik, L.L.V., et al., *Lysolipids reversibly inhibit Ca(2+)-, GTP- and pH-dependent fusion of biological membranes.* FEBS letters, 1993. **318**(1): p. 71-6.
173. Xu, Y., et al., *Hemifusion in SNARE-mediated membrane fusion.* Nat Struct Mol Biol, 2005. **12**(5): p. 417-22.
174. Grote, E., et al., *Geranylgeranylated SNAREs are dominant inhibitors of membrane fusion.* J Cell Biol, 2000. **151**(2): p. 453-66.
175. McNew, J.A., et al., *Close Is Not Enough: SNARE-dependent Membrane Fusion Requires an Active Mechanism that Transduces Force to Membrane Anchors.* J. Cell Biol., 2000. **150**(1): p. 105-118.

176. Langosch, D., et al., *Peptide mimics of SNARE transmembrane segments drive membrane fusion depending on their conformational plasticity.* J Mol Biol, 2001. **311**(4): p. 709-21.
177. Kim, C.S.C.S., D.H.D.-H. Kweon, and Y.K.Y.-K. Shin, *Membrane topologies of neuronal SNARE folding intermediates.* Biochemistry, 2002. **41**(36): p. 10928-33.
178. Kweon, D.H.D.-H., C.S.C.S. Kim, and Y.K.Y.-K. Shin, *Regulation of neuronal SNARE assembly by the membrane.* Nature structural biology, 2003. **10**(6): p. 440-7.
179. Hu, K.K., et al., *Vesicular restriction of synaptobrevin suggests a role for calcium in membrane fusion.* Nature, 2002. **415**(6872): p. 646-50.
180. Hu, K.K., et al., *A common mechanism for the regulation of vesicular SNAREs on phospholipid membranes.* The Biochemical journal, 2004. **377**(Pt 3): p. 781-5.
181. Knecht, V. and H. Grubmuller, *Mechanical coupling via the membrane fusion SNARE protein syntaxin 1A: a molecular dynamics study.* Biophys J, 2003. **84**(3): p. 1527-47.
182. Lang, T.T., et al., *SNAREs are concentrated in cholesterol-dependent clusters that define docking and fusion sites for exocytosis.* The EMBO journal, 2001. **20**(9): p. 2202-13.
183. Ohara-Imaizumi, M., et al., *Site of Docking and Fusion of Insulin Secretory Granules in Live MIN6 {beta} Cells Analyzed by TAT-conjugated Anti-syntaxin 1 Antibody and Total Internal Reflection Fluorescence Microscopy.* J. Biol. Chem., 2004. **279**(9): p. 8403-8408.
184. Hoppe, A., K. Christensen, and J.A. Swanson, *Fluorescence Resonance Energy Transfer-Based Stoichiometry in Living Cells.* Biophys. J., 2002. **83**(6): p. 3652-3664.
185. Rizo, J.J. and T.C.T.C. Südhof, *Snares and Munc18 in synaptic vesicle fusion.* Nature reviews. Neuroscience, 2002. **3**(8): p. 641-53.

Chapter 2

SNARE-Catalyzed Fusion Events are Regulated by Syntaxin1A-Lipid Interactions

Abstract

Membrane fusion is a process that intimately involves both proteins and lipids. While the SNARE proteins, which ultimately overcome the energy barrier for fusion, have been extensively studied, regulation of the energy barrier itself, determined by specific membrane lipids, has been largely overlooked. Our findings reveal a novel function for SNARE proteins in reducing the energy barrier for fusion, by directly binding and sequestering fusogenic lipids to sites of fusion. We demonstrate a high affinity interaction between the Q-SNARE Syntaxin1A and the fusogenic lipid, phosphatidic acid, and define a polybasic juxtamembrane region within Syntaxin1A as its lipid binding domain. In PC-12 cells, Syntaxin1A mutations that progressively reduced lipid binding resulted in a progressive reduction in evoked secretion. Moreover, amperometric analysis of fusion events driven by a lipid binding-deficient Syntaxin1A mutant (5RK/A) demonstrated alterations in fusion pore dynamics suggestive of an energetic defect in secretion. Overexpression of the phosphatidic acid-generating enzyme, phospholipase D1, completely rescued the secretory defect seen with the 5RK/A mutant. Moreover, knockdown of phospholipase D1 activity drastically reduced control secretion, while leaving 5RK/A-mediated secretion relatively unaffected. Altogether, these data suggest that Syntaxin1A-phosphatidic acid interactions are a critical determinant of the energetics of SNARE-catalyzed fusion events.

Introduction

Membrane fusion is a process that underlies compartmentalization within all eukaryotic cells, and allows for the many critical and diverse physiological functions in higher organisms. Despite the essential and ubiquitous nature of this process, a considerable energetic expenditure is required to overcome the electrostatic repulsion between opposing lipid bilayers, and to deform and ultimately rupture these bilayers [1, 2]. As a result, substantial effort has been placed on defining the molecular machinery that overcomes this energetic barrier to accomplish regulated and rapid membrane fusion.

SNARE (soluble N-ethylmaleimide-sensitive fusion factor attachment protein receptor) proteins have now been identified as the minimal protein machinery required for membrane fusion [3]. Their critical role is supported by multiple lines of evidence, including that SNARE proteins are sufficient to drive membrane fusion when reconstituted into liposomes in vitro [4], and that cleavage of SNARE proteins by clostridial toxins [5-7] as well as genetic mutations resulting in loss of SNARE protein function [8-10], strongly inhibit neurotransmitter release. Currently, the role of SNARE proteins in membrane fusion is believed to be predominantly mechanical. During neurotransmitter release, nucleation and zippering of a highly stable SNARE core complex formed from two plasma membrane SNARE proteins, Syntaxin1A (Syn1A) and SNAP25, and a vesicle membrane SNARE protein, VAMP2, is believed to generate the energy required to bring opposing membranes to a state of proximity that initiates the fusion event [3]. As such, the majority of studies in this field have focused on characterizing SNARE protein-protein interactions, although the fusion process, by definition, must also involve lipids.

That the specific lipid composition of the membrane can have profound consequences on the energetic barrier for membrane fusion has been demonstrated both theoretically as well as in several *in vitro* membrane fusion systems [11-14], although this topic has been difficult to study in the context of secretion from live cells. Shapes of individual lipids can have dramatic effects on membrane curvature [1, 15]. For example, cone-shaped lipids (e.g., phosphatidylethanolamine, diacylglycerol, or phosphatidic acid) spontaneously form negative membrane curvatures [16-18], and the presence of these lipids in the contacting leaflets of merging membranes has been shown to favor the formation of the stalk and hemifusion intermediates that underlie membrane fusion [19]. Effects of spontaneous curvature are a highly local phenomenon [1], however, and in order for fusogenic lipids to exert such effects on exocytosis, they must be directly localized to the sites at which membrane fusion occurs. As the minimal machinery for membrane fusion, SNARE proteins physically define the sites at which exocytosis occurs, and therefore, would be ideal molecular partners to bind and sequester fusogenic lipids, thus reducing the energy barrier at exocytotic sites.

The purpose of this study was to determine whether Syntaxin1A (Syn1A), a plasma membrane Q-SNARE, forms functional interactions with structural lipids which might then exert a controlling influence over the fusion event. Syn1A [20] is a 35kDa SNARE protein that is fully-anchored to the plasma membrane via a C-terminal transmembrane domain. Several recent reports suggest that Syn1A may form key interactions with lipids. First, biochemical isolation of lipid rafts demonstrated that Syn1A localizes to cholesterol-dependent membrane microdomains; disruption of these rafts resulted in an inhibition of stimulated exocytosis in PC-12 cells [21, 22]. Second, optical studies in unroofed PC-12 cells [22], and TIRF studies in intact MIN6 cells [23], demonstrated that Syn1A forms cholesterol-dependent clusters within the plasma membrane, which were preferential sites at which vesicle docking and fusion occurs. Moreover, Syn1A clusters partially colocalized with PI(4,5)P2 clusters within the plasma membrane, and vesicle fusion could be correlated with the extent of cluster colocalization [24]. Third, analysis of single fusion events by carbon fiber amperometry demonstrated that Syn1A's transmembrane domain forms part of the fusion pore [25]. Fourth, FRAP analysis of Syn1A in reconstituted polymer-supported lipid bilayers demonstrated an increase in the immobile fraction of Syn1A in the presence of acidic phospholipids [26]. Lastly, Syn1A contains a polybasic juxtamembrane region which, while unstructured, was recently found to be inserted into the lipid bilayer [27]. While these data indicate that Syn1A forms key interactions with acidic phospholipids, the specificity of these interactions and the physiological significance has not, to date, been directly evaluated.

Here, we identify a novel, high affinity interaction between Syn1A and the fusogenic lipid phosphatidic acid, in addition to demonstrating interactions of Syn1A with multiple phosphoinositol lipids, including PI(4,5)P2. Progressive neutralizing mutations within the conserved, polybasic juxtamembrane region in Syn1A reduce Syn1A's affinity for acidic phospholipids in a graded fashion that correlates with the graded reduction in the secretory function of these mutants. Using carbon fiber amperometry, we demonstrate that this reduction in secretory function results from a decrease in fusion event frequency; moreover, successful fusion events that occurred demonstrated significantly longer fusion pore durations and smaller fusion pore diameters compared to control. Importantly, the secretory defect seen with a lipid-binding-deficient Syn1A (5RK/A) could be completely rescued by overexpression of the phosphatidic acid-generating enzyme, phospholipase D1 (PLD1), whereas knockdown of PLD1 activity strongly reduced control secretion without affecting secretion from Syn1A 5RK/A expressing cells. We therefore propose that Syn1A's interaction with phosphatidic acid is critical in determining the energetics of SNARE-mediated fusion events. Sequence alignment across multiple SNARE protein families demonstrates a high level of conservation of the polybasic juxtamembrane region [28], suggesting that this lipid binding role may be a common and important one for many SNARE proteins in membrane fusion.

Materials and Methods

Antibodies

The following antibodies were used: α-Syntaxin1A clone HPC-1 (Sigma); α-Syntaxin1A clone 78.3 (Synaptic Systems), α-GST (Pharmacia Biotech); α-GFP (Clontech), donkey α-mouse HRP and donkey α-rabbit HRP (Jackson Immunoresearch Laboratories).

Clones

Rat Syntaxin1A was used for all syntaxin constructs. Site-directed mutagenesis was carried out using the Quickchange Site-Directed Mutagenesis kit (Stratagene). The GST-Syn1A(252-265) peptide construct was made by ligating an annealed oligo (F= TCGAAAGAAGGCCGTCAAGTACCAGAGCAAGGCACGCAGGAAGAAGTAG; R= AGCTCTACTTCTTCCTGCGTGCCTTGCTCTGGTACTTGACGGCCTTCTT) with 5' and 3' overhangs into the pGex-KG vector cut at the XhoI and HindIII sites of the MCS downstream of GST. Fluorophore-tagged proteins were constructed using the Cre-recombinase based Creator system (Clontech), in which syntaxin1A, SNAP25, and Munc18-1 were subcloned into recipient fluorophore vectors (pEGFP-C1, or monomeric mutants of pECFP-C1, pEcYFP-C1 (citrine), and RFP vectors) containing LoxP sequences at the C-terminal end of the fluorophore sequence. For the mRFP-Syntaxin1A-pHluorin construct, the pHluorin (with an associated N-terminal 17 amino acid linker) was PCR subcloned from synaptopHluorin, and ligated into the C-terminal end of syntaxin1A (with a mutated stop codon). The PLD1 mammalian expression vector (pCGN-PLD1) encoding human wildtype PLD1 was as previously described [29]. The siRNA-PLD1 construct used was a single bicistronic plasmid that expresses both hGH and an siRNA targeted to PLD1, as previously described [30]. The sequence fidelity of all new constructs was confirmed by DNA sequencing (University of Michigan DNA Sequencing Core).

Cell Culture

PC-12 cells were cultured in 10% CO_2, in DMEM supplemented with 10% horse serum, 5% fetal bovine serum, penicillin (100 units/ml), streptomycin (100 µg/ml), and 1% gentamicin (10 µg/ml). HEK293-S3 cells were cultured in 5% CO_2, in RPMI 1640 with L-glutamine, supplemented with 10% fetal bovine serum, penicillin (100 units/ml), streptomycin (100 µg/ml), 0.4 mg/ml of hygromycin and 0.6 mg/ml of geneticin. PC-12 cells and HEK293-S3 cells were transfected using Lipofectamine 2000 (Invitrogen) according to manufacturer's protocol. Bovine adrenal chromaffin cells were isolated and cultured as described previously [31].

Purification of GST-Fusion Proteins

BL21 DE3 cells were transformed with pGex KG vectors coding for the soluble forms of Syn1A (aa 1-267, or aa 252-267) or specific soluble mutants of Syn1A. Cells were grown to an OD600 of 0.4-0.6, induced with 0.1mM IPTG, and grown for 5-8 hours with shaking at 23C. Cells were harvested by centrifugation for 15 minutes at 5000xg (Beckman JA-14 rotor), and resuspended in PBST buffer (in mM: 16 Na_2HPO4, 4 NaH_2PO4, 150 NaCl, 2 EDTA, 1% TX-100, pH 7.3) supplemented with protease inhibitors and 1% β-mercaptoethanol. Cells were then mechanically lysed using a French Press at 15000psi. GST-fusion proteins were purified from the cell lysate using Glutathione-Sepharose 4B beads (Amersham), according to the manufacturer's protocol. For select experiments, the fusion protein was cleaved from the GST moiety with 1.4 NIH units of thrombin (Amersham) for 30 minutes at 25C, and the cleaved GST was removed by incubation with Glutathione-Sepharose beads for 1 hour at room temperature. Purity of each protein was determined by fractionation by SDS-PAGE followed by Coomassie staining and estimated to be ~90%.

Protein Lipid Overlay

“PIP Strips” (nitrocellulose membranes pre-spotted with 100pmoles each of 15 defined lipids) were purchased from Echelon Biosciences and binding overlay experiments were carried out according to the manufacturer's protocol. For phosphatidic acid (PA) binding overlay experiments, stock solutions of Dipalmitoyl-PA (Avanti Polar Lipids) solubilized in 2:1:0.8 MeOH:chloroform:H2O were spotted onto Hybond C nitrocellulose and allowed to dry. The nitrocellulose was then blocked for 1 hour in TBS-T + 0.1% ovalbumin prior to initial protein-lipid binding, and then incubated with a molar excess of specific Syn1A mutants or control protein in TBS-T + 0.1% ovalbumin overnight at 4C. The nitrocellulose was then washed extensively with TBS-T + 0.1% ovalbumin, and the bound protein was detected using antibodies followed by an ECL reaction. Digital images were taken using a BioRad Fluor-S-Max Imager. Integrated densities at each PA spot (4 replicates for each PA spot, for each mutant or control protein tested) were measured and normalized to the maximum integrated density for each protein treatment.

Liposome Flotation Binding Analysis

All lipids were purchased from Avanti. Liposomes (small unilamellar vesicles) were made by mixing stock solutions of porcine brain phosphatidylcholine (PC), porcine brain phosphatidylethanolamine (PE), and dipalmitoyl-phosphatidic acid or oleoyl-lysophosphatidic acid (PA/LPA) in chloroform at a 3:2:1 (w/w) ratio (in mole % composition, equivalent to 49% PC, 33% PE, and 18% PA for PA-containing liposomes; for LPA-containing liposomes, mole % composition is 45% PC, 30% PE, and 25% LPA).

Lipid mixtures were spun dry at 25C in a tabletop centrifuge and resuspended in liposome buffer (in mM: 50 HEPES, 250 Sucrose, 150 potassium acetate). The suspended liposome solution was placed in a bath sonicator for 30 minutes at 4C followed by incubation on a thermomixer to equilibrate overnight at 4C. For assaying binding of protein to the liposomes, 100ng of purified soluble Syn1A or specific Syn1A mutants (aa 1-267) was mixed with liposomes and liposome buffer in a total reaction volume of 20µL, and the reaction mixture was placed on a thermomixer at 37C for 1 hour at 800rpm. Reaction mixtures were loaded under a 40/30/20/10% sucrose density flotation gradient and centrifuged at 390,000 x g for 1 hour at 4C (Beckman rotor TLA-100) to separate liposomes from unbound protein. Equal volume fractions were collected from the top of each flotation gradient, loaded onto an SDS-PAGE gel, and Syn1A immunoreactivity in each fraction was detected via western blot analysis.

Co-Immunoprecipitations

HEK 293-S3 cells were plated into 6-well plates and transiently transfected with WT or mutant Syntaxin1A, Munc18-1, and EGFP-SNAP25. Control transfections used Munc18-1 and EGFP-SNAP25, but excluded the Syntaxin1A. Following 48 hours of expression, cells were rinsed in ice-cold physiological saline solution (PSS1, in mM: 140 NaCl, 5 KCl, 10 HEPES, 10 glucose, 5 $NaHCO_3$, 1 $MgCl_2$, 2.2 $CaCl_2$, pH 7.3), scraped into ice-cold lysis buffer (in mM: 20 Tris pH 7.4, 1 EDTA, and 2% sucrose, supplemented with a Mammalian Protease Arrest protease inhbitor cocktail (G-Biosciences)), dounce homogenized by 35 strokes, and centrifuged at 800xg to remove the nuclei. Subsequently, 1.5 volumes IP buffer (in mM: 150 Tris pH 7.4, 1 $MgCl_2$, 0.1 EGTA, 2% Triton X-100, with protease inhibitors) were added to each tube and tubes were incubated on ice for 30 minutes to allow solubilization of membranes. Protein concentrations and volumes of the lysates were then equalized across conditions, and immunoprecipitation was carried out with a 2 hour incubation with α-Syntaxin1A (clone 78.3) at 4C with rotation. Immunopure protein G beads (Pierce) were then added to each sample and the incubation continued for 1 hour. The beads were pelleted by centrifugation (1500xg for 2 minutes at 4C), washed twice in IP buffer, and washed a final time in PBS. Syntaxin1A and EGFP-SNAP25 immunoreactivity was determined in each sample using SDS-PAGE fractionation and Western blot analysis, probing with α-Syntaxin1A (clone HPC-1) and α-GFP, followed by an ECL reaction. Digital images were taken using a BioRad Fluor-S-Max Imager, and integrated densities of the EGFP-SNAP25 and Syn1A signals were determined. For each transfection condition, the ratio of the integrated densities of EGFP-SNAP25 to Syn1A in the immunoprecipitated fraction was determined. All ratios were then normalized to the ratio from the condition containing WT Syn1A, to allow comparison and quantification across experiments.

Human Growth Hormone Secretion Assay

PC-12 cells were plated onto 24-well plates and co-transfected with specific constructs, including human growth hormone (hGH), the light chain of the Botulinum C neurotoxin (BoNT-C), Munc18-1, and full-length Syntaxin1A (wild-type or mutant forms). The total DNA concentration was held constant across treatments, by addition of a neomycin control plasmid. At 48-72 hours post-transfection, cells were rinsed for 6 minutes in a physiological saline solution (PSS2, in mM: 145 NaCl, 5.6 KCl, 15 NaHEPES, 0.5 $MgCl_2$, 2.2 $CaCl_2$, 5.6 Glucose, 0.5 NaAscorbate, 2mg/mL BSA, pH 7.3), followed by a 6 minute stimulation with 70mM K^+ (same as PSS2, with equimolar substitution of K^+ for Na^+). PSS2 containing the secreted hGH was collected, and cells were lysed (lysis buffer, in mM: 0.2 EDTA, 10 HEPES, 1% Triton X-100, pH 7.4) to determine percent of total hGH content secreted. hGH content was measured using an hGH ELISA kit (Roche Diagnostics). Each experiment was performed with quadruplicate replicates for each treatment, and each experiment was repeated a minimum of 3 independent times. hGH secretion experiments using LPC, PLD1 overexpression, and siRNA-PLD1 were completed in France and thus were carried out on a different strain of PC-12 cells than in all other experiments. For experiments utilizing external application of LPC, 1μM palmitoyl-lysophosphatidylcholine (Avanti Polar Lipids) was added during both the rinse and the stimulation period.

Imaging

Conventional Fluorescence Microscopy: Cells were transferred from media to PSS1 for imaging. Cellular fluorescence was imaged at 25C using an Olympus 60x 1.2NA PlanApo water objective on an Olympus IX71 microscope coupled to a TILL polychrome monochromator for illumination. Appropriate dichroic mirrors and emission filters were used for each fluorophore imaged. Image capture was performed using a TILL-Imago QE camera under the control of TILL software.

Confocal Imaging: Confocal images were taken on an Olympus FluoView 500 Laser Scanning Confocal Microscope, using an LD405 laser, 60x 1.2NA objective, and a pinhole aperture of 260μm.

FRET Imaging: A detailed description of the FRET 3-cube sensitized emission imaging methodology can be found in our previous publication [32]. In addition to 3 different excitation/emission images (excitation/emission in nm): 436/465 (donor excitation, donor emission); 436/535 (donor excitation, acceptor emission), and 500/535 (acceptor excitation, acceptor emission), background and shade correction images were also taken. Image correction and analysis were performed offline using the method of FRET stoichiometry [32, 33], and implemented with a custom written IGOR macro (Wavemetrics).

FURA Imaging: PC-12 cells transfected with full-length Syn1A (K253I or K253I-5RK/A), Munc18-1, BoNT-C, and RFP (to allow identification of transfected cells) were loaded for 20 minutes at 37C with 3µM Fura2-AM (Molecular Probes) in PSS1 for calcium imaging. Cells were then rinsed with PSS1, and following 15 minutes, time-lapse fluorescence images were acquired with excitation fluorescence alternating between 340nm and 380nm, and emission acquired at 510nm. Fura ratios were calculated as F340/F380.

Amperometry

At 48 hours before recording, bovine chromaffin cells were transfected with Syn1A (K253I or K253I-5RK/A), BoNT-C light chain, and GFP, using biolistic bombardment (Gene Gun, Biorad). Conditions for biolistic transfection, and preparation of gold beads were as suggested by the manufacturer, with 2µg DNA/mg gold beads. Cells were replated onto poly-L-lysine coated glass coverslips 24 hours prior to recording. 5µm carbon fiber electrodes (ALA Scientific) held at +650mV were used for amperometric recordings. Cells were bath perfused with PSS1. Secretion was stimulated by local application of 100mM K^+ (same composition as PSS1, with K^+ substituted equimolar for Na^+) for 60 seconds, and currents were recorded during these 60 seconds, in addition to a 5 second pre-stimulus baseline recording. Currents were collected using an Axopatch 200A amplifier modified for extended voltage output (Axon Instruments), filtered at 2kHz, and sampled at 4kHz. No digital filtering was applied. Currents were analyzed using an Igor XOP written by Eugene Mosharov (Columbia University) and available online (http://cumc.columbia.edu/dept/neurology/sulzer/download.html) [34]. For spike frequency analysis, only spikes with amplitudes > 10pA above the RMS noise level were used. Pre-spike foot (PSF) analysis was limited only to those PSF whose amplitudes were <30pA and whose durations were >1ms (>4x sampling frequency).

Data Analysis and Statistics

Statistical analyses were carried out using GraphPad Prism software. For most comparisons, unpaired t-tests were used; statistical significance was designated at a p-value < 0.05.

Results

Syn1A binds with high affinity to the fusogenic lipid phosphatidic acid

We initially set out to determine whether Syn1A specifically interacts with lipids that might decrease the energetic requirements for membrane fusion. In these experiments, bacterially expressed soluble Syn1A (aa1-267) was overlaid in decreasing concentrations onto nitrocellulose spotted with equimolar amounts of given lipids. Figure 2.1A demonstrates that Syn1A bound to multiple acidic phospholipids in a dose-dependent manner. Importantly, Syn1A bound with highest apparent affinity to the fusogenic lipid, phosphatidic acid (PA), although lower apparent affinity interactions with several phosphatidylinositol phosphates (PIPs), including PI(3)P, PI(4)P, PI(5)P, PI(3,4)P2, PI(4,5)P2, and PI(3,4,5)P3, were also observed (Figure 2.1B). Notably, all of the lipids to which Syn1A bound were acidic, although Syn1A did not interact with every acidic phospholipid tested (e.g., phosphatidylserine (PS) or lysophosphatidic acid (LPA)). Furthermore, Syn1A exhibited a greater apparent affinity for the monophosphate lipid PA than the polyphosphate inositol lipids, which contain a greater negative valence compared to PA. These data suggest that while electrostatic interactions have an important role in mediating Syn1A's lipid interactions, other structural features ultimately underlie the specificity.

A correlative series of liposome flotation binding experiments was also performed, in which Syn1A was mixed with liposomes of defined composition and loaded under a sucrose density gradient. Following ultracentrifugation, Syn1A bound to liposomes floats to the top of the gradient with the liposome fraction. Figure 2.1C shows Syn1A immunoreactivity in the collected gradient fractions of a representative experiment, and demonstrates that Syn1A specifically bound to liposomes containing PA but not to those containing LPA. Furthermore, Syn1A did not bind to control liposomes (containing only PC and PE). Together, the data demonstrate that Syn1A specifically binds the fusogenic lipid, PA.

The polybasic juxtamembrane region in Syn1A comprises a lipid interaction domain

Sequence analysis of Syn1A revealed a polybasic juxtamembrane region within Syn1A that is highly conserved across multiple species (Figure 2.2A, top). To determine if this region is responsible for Syn1A's interactions with acidic phospholipids, a series of progressive neutralizing mutations was generated within this region, in which one (R262A), two (R262A/R263A), or all five (5RK/A) basic residues were neutralized to alanines (Figure 2.2A, bottom). Mutant proteins were purified and tested for lipid binding capacity using nitrocellulose blots on which PA had been spotted in increasing amounts. Binding curves were fit using the Hill equation, which allowed determination of the apparent binding affinity (EC_{50}) of each protein for PA (Figure 2.2B). Progressive neutralizing mutations resulted in a progressive reduction in apparent binding affinity to PA, with the 5RK/A mutant demonstrating the greatest reduction in apparent binding affinity ($EC_{50} \sim 3.2 \times 10^5$ fmoles), followed by the R262A/R263A mutant ($EC_{50} \sim 6.1 \times 10^4$ fmoles), and lastly, the R262A mutant ($EC_{50} \sim 2.9 \times 10^3$ fmoles), which demonstrated binding similar to the wild-type (WT) protein ($EC_{50} \sim 2.0 \times 10^3$ fmoles). Thus, complete neutralization of the polybasic juxtamembrane region in Syn1A resulted in a greater than 2 log shift in EC_{50}.

Qualitatively similar results were obtained using liposome flotation assays, in which the relative affinities of the WT and 5RK/A Syn1A proteins for PA-containing liposomes was tested. Figure 2.2C shows that 24.3 ± 3.4% (n=5) of the total WT protein, versus 6.1 ± 2.0 % (n=3) of the total 5RK/A mutant protein, bound to the liposomes ($p<0.01$). Moreover, the 5RK/A mutation eliminated binding to all acidic lipids as demonstrated by the protein-lipid overlays shown in Figure 2.2D. Thus, Syn1A's juxtamembrane basic residues are critical in mediating Syn1A's interactions with acidic phospholipids.

Additional structural determinants underlie Syn1A's lipid binding properties

To determine whether structure within the juxtamembrane basic region was important for lipid binding, we constructed a Syn1A RKRK mutant, in which the order of the juxtamembrane basic residues was rearranged, while the overall charge was maintained. The apparent PA binding affinity of the RKRK mutant ($EC_{50} \sim 2.6 \times 10^3$ fmoles) was indistinguishable from WT, indicating that Syn1A-lipid interactions can tolerate small structural changes within the juxtamembrane region (Figure 2.2B).

To establish whether domains outside the polybasic juxtamembrane region affect Syn1A's lipid binding specificity, we synthesized a peptide corresponding to this region (aa 252-265), as well as the corresponding 5RK/A peptide. Protein-lipid overlays demonstrated that the WT peptide closely recapitulated Syn1A's lipid binding profile, while the 5RK/A mutation abrogated the peptide's ability to bind acidic phospholipids (Figure 2.2E). One notable difference between the WT peptide and Syn1A (1-267) was that the WT peptide demonstrated a high apparent affinity for PS, a lipid for which Syn1A (1-267) exhibited almost no binding (compare Figures 2.2D&E). Importantly, lipid binding to Syn1A (1-259), in which the polybasic juxtamembrane region had been truncated, was largely eliminated (data not shown). Thus, while other regions in Syn1A may modify its lipid binding profile, the basic juxtamembrane residues are clearly required for these interactions.

Full-length Syn1A juxtamembrane mutants traffic normally to the plasma membrane in live cells

To assess the relevance of Syn1A-lipid interactions in an in vivo situation, full-length, juxtamembrane mutant Syn1A proteins were next studied in living cells. Initial experiments examined whether these mutant Syn1A proteins were expressed and targeted properly. ECFP-tagged, full-length Syn1A mutants were generated and transiently transfected into PC-12 cells. All Syn1A constructs were co-transfected with Munc18-1, which facilitated high levels of targeting of Syn1A to the plasma membrane regions. Figure 2.3A demonstrates that the fluorescence signal associated with both the WT and 5RK/A ECFP-Syn1A proteins trafficked normally to the plasma membrane region, as determined by confocal microscopy.

To quantify the extent of surface labeling between mutants, we next used dual-fluorophore-labeled Syn1A constructs, which were tagged with mRFP at the N-terminus and pHluorin at the C-terminus. pHluorin is a pH-sensitive variant of GFP, whose signal is quenched within acidic intracellular compartments, but becomes highly fluorescent upon exposure to the neutral, extracellular solution (which in this case, occurs upon insertion of Syn1A's C-terminal transmembrane domain into the plasma membrane). We thus reasoned that the pHluorin signal would report only on the pool of exogenous Syn1A that had been correctly inserted into the plasma membrane, whereas the mRFP signal would report on the entire pool of exogenous Syn1A expressed within a cell. Figure 2.3B shows representative epifluorescence images of PC-12 cells transiently co-transfected with the mRFP-Syn1A-pHluorin constructs and Munc18-1. The notable fluorescence of the pHluorin label at the plasma membrane region demonstrates that both the WT and 5RK/A Syn1A constructs were correctly trafficked and inserted into the plasma membrane. Importantly, measurements of the average pHluorin and mRFP fluorescence intensities across a large number of cells were comparable between the

WT and 5RK/A conditions, demonstrating that both the surface levels and total expression levels of WT and 5RK/A Syn1A proteins were similar (Figure 2.3C). Figure 2.3D shows a scatterplot in which the mean pHluorin intensity was plotted against the mean mRFP intensity for each individual cell. Notably, there occurred a large overlap in the distribution of points between the WT and 5RK/A cells, and linear fits of these data for cells expressing moderate levels of the Syn1A (RFP mean intensities between 20 and 170) were not significantly different. Thus, the WT and 5RK/A Syn1A constructs demonstrate not only comparable expression levels, but also similar abilities to traffic and insert within the plasma membrane.

Full-length Syn1A juxtamembrane mutants demonstrate intact protein-protein interactions within live cells

Having determined that the full-length juxtamembrane neutralization mutants of Syn1A were capable of trafficking correctly, we next asked whether these mutants were capable of forming appropriate protein-protein interactions in vivo. The above data suggested that both WT and 5RK/A Syn1A constructs interacted similarly with Munc18-1, as co-expression of these constructs with Munc18-1 greatly facilitated trafficking of both constructs to the plasma membrane. To confirm the normal Munc18-1 interaction properties between these Syn1A constructs, we used a sensitized emission FRET approach to compare binding of the CFP-tagged WT Syn1A or 5RK/A mutant to citrine-Munc18-1 in live cells. That this FRET stoichiometry approach is an accurate reporter of the Syn1A-Munc18-1 interaction was established in our earlier publication [32]. Figure 2.4A demonstrates that both WT and 5RK/A proteins associated with Munc18-1 similarly, across a wide range of molar ratios. This result is quantified in Figure 2.4B, where at equimolar ratios (molar ratio between 0.9 – 1.1), the 5RK/A mutant exhibited a FRET efficiency (ED) with Munc18-1 that was similar to that of the wild-type protein

(WT= 24.2±0.01, 5RK/A= 24.8±0.01). In contrast, a Syn1A mutant (I233A) that was previously shown to have reduced binding to Munc18-1 [35], demonstrated a reduced FRET efficiency (I233A = 5.6±0.01) compared to WT. Thus, neutralizing mutations within the juxtamembrane region of Syn1A do not appear to affect Syn1A's interaction with Munc18-1.

We next asked whether Syn1A 5RK/A possessed the ability to interact normally with SNARE proteins, in particular, the Q-SNARE SNAP25. For these experiments, HEK293-S3 cells were transiently transfected with Syn1A (WT or mutant), Munc18-1, and EGFP-SNAP25. Co-immunoprecipitation experiments were performed to determine whether the 5RK/A mutant was capable of pulling down equal amounts of EGFP-SNAP25 compared to the WT Syn1A. Figure 2.4C shows a blot from a representative experiment, which demonstrates that both the WT and 5RK/A Syn1A proteins bound a similar amount of EGFP-SNAP25. In contrast, a mutant of Syn1A (L205A/E206A) which was previously shown to have reduced binding to SNARE proteins [36], demonstrated a marked reduction in binding to EGFP-SNAP25. To quantify these results, we measured the integrated densities of the Syn1A and EGFP-SNAP25 bands, and determined the ratio of EGFP-SNAP25 to Syn1A in the immunoprecipitated fractions for each condition. For each experiment, the ratio for each treatment was normalized to the ratio from the WT treatment, to allow comparison of treatments across experiments. Figure 2.4D shows the average results for 3 independent experiments, and again demonstrates that the 5RK/A Syn1A displays similar interactions with SNAP25 as compared with the WT Syn1A.

Taken together, these data demonstrate that, despite profound differences in lipid binding capabilities, the 5RK/A mutant Syn1A behaves nearly identically to the WT Syn1A in live cells, with respect to expression levels, membrane trafficking, and forming appropriate protein-protein interactions.

Use of BoNT-C knockdown of Syn1A to specifically isolate the functional phenotypes of exogenous Syn1A constructs

To test whether disruption of Syn1A-lipid interactions would have a functional effect on regulated exocytosis, we transfected Syn1A juxtamembrane neutralization mutant constructs into live secretory cells (PC-12 cells or bovine adrenal chromaffin cells). To reduce potentially confounding effects from endogenous Syn1A in these cells, we transfected the cells with the light chain of the Botulinum C neurotoxin (BoNT-C), which cleaves Syn1A and precludes it from mediating membrane fusion [37]. Syntaxin 4 was previously reported to be resistant to cleavage by BoNT-C and to contain an Ile in place of Lys at residue 253 of the BoNT-C cleavage site [37]. We therefore tested whether a similar mutation (K253I) in Syn1A, would generate a BoNT-C-resistant Syn1A. For this analysis, PC-12 cells were co-transfected with an N-terminally tagged CFP-Syn1A and Munc18-1, with or without BoNT-C. Cells were then imaged using conventional fluorescence microscopy. In the absence of BoNT-C, both the WT Syn1A and Syn1A$_{K253I}$ constructs targeted to plasma membrane regions (Figure 2.5A). In the presence of BoNT-C, however, the WT Syn1A signal was redistributed as a diffuse cytosolic signal within the cells, indicating cleavage by BoNT-C, whereas the Syn1A$_{K253I}$ signal distributed to the plasma membrane, indicating resistance to cleavage by BoNT-C (Figure 2.5A). These experiments were quantified by scoring at least 100 random cells from each condition (while blinded to the conditions) as demonstrating either a cytosolic or membrane fluorescence distribution. Importantly, in the presence of BoNT-C, the percent of cells demonstrating a cytosolic fluorescence distribution was 63% for WT Syn1A, compared to only 5% for Syn1A$_{K253I}$.

We next tested whether a BoNT-C resistant Syn1A$_{K253I}$ construct could rescue secretion in BoNT-C treated cells. Human growth hormone (hGH) secretion assays [38] were performed on PC-12 cells transfected with various combinations of the BoNT-C light chain, Munc18-1, and either WT Syn1A or Syn1A$_{K253I}$. Figure 2.5B shows that transfection of the BoNT-C light chain into PC-12 cells effectively reduced secretion to 30% of control secretion. Importantly, Syn1A$_{K253I}$ rescued secretion in BoNT-C-transfected cells, to roughly 78% of control secretion, but only when co-transfected with Munc18-1. This requirement for Munc18-1 was likely the result of enhanced membrane targeting of Syn1A, as Munc18-1 itself was insufficient to rescue the BoNT-C knockdown of secretion (35% of control secretion). Importantly, WT Syn1A was also unable to rescue secretion in BoNT C-transfected cells, even when co-transfected with Munc18-1 (29% of control secretion). This clearly indicates that rescue of the BoNT-C knockdown is specific to the expression and proper targeting of a functional BoNT-C-resistant Syn1A to the plasma membrane region in these cells. Of note, while higher expression levels of BoNT-C were sufficient to achieve a more complete knockdown of secretion (reduction to <10% of control secretion), we were often unable to rescue this phenotype by coexpression of Syn1A$_{K253I}$ and Munc18 (data not shown). We attribute this to the fact that at higher concentrations, BoNT-C may also cleave SNAP25 in addition to Syn1A [39].

Neutralizing mutations within Syn1A's polybasic juxtamembrane region result in a progressive inhibition of Syn1A's secretory function

To compare the ability of full-length Syn1A juxtamembrane neutralization mutants to rescue secretion, we used the BoNT-C knockdown assay in cotransfected PC-12 cells. Figure 2.6A demonstrates that neutralizing mutations within Syn1A's polybasic juxtamembrane domain resulted in a progressive decrease in secretory function. When normalized to the extent of rescue seen with Syn1A$_{K253I}$, the Syn1A$_{K253I}$(5RK/A) mutant was only capable of rescuing secretion to 67 ± 3% of the Syn1A$_{K253I}$ control level (n=20). The Syn1A$_{K253I}$(R262A/R263A) mutant rescued secretion to 77 ± 4% of the Syn1A$_{K253I}$ control level (n=16), whereas the Syn1A$_{K253I}$(R262A) mutant exhibited a phenotype similar to Syn1A$_{K253I}$, rescuing secretion to 97 ± 4% (n=16) of the Syn1A$_{K253I}$ control level. Considering that the residual baseline secretion following BoNT-C knockdown accounts for roughly 45% of the rescued control secretion (Figures 2.5B and 2.6A left, dotted line), the actual deficit in secretion resulting from neutralization of Syn1A's juxtamembrane region was quite substantial, with the Syn1A$_{K253I}$(5RK/A) mutant rescuing secretion to only 43% of the Syn1A$_{K253I}$ control (Figure 2.6A, right). Importantly, this decline in secretory function of the juxtamembrane Syn1A mutants correlates well with the decrease in apparent affinity of these mutants for binding phosphatidic acid (Figure 2.2B) and presumably, with their affinity for other acidic phospholipids as well.

Neutralizing mutations within Syn1A's polybasic juxtamembrane region result in a reduction in fusion event frequency

We next sought to determine the mechanism by which neutralization of Syn1A's juxtamembrane region resulted in secretory inhibition. Importantly, both Syn1A$_{K253I}$ and Syn1A$_{K253I}$(5RK/A) cells demonstrated comparable calcium fluxes upon depolarization, as measured using the calcium indicator Fura-2 (Figure 2.6B). PC-12 cells were transfected with BoNT-C, Syn1A$_{K253I}$ or Syn1A$_{K253I}$(5RK/A), Munc18-1, and RFP (to identify transfected cells), pre-loaded with the Fura-2 AM ester, and depolarized using a brief, 5 second local perfusion with 100mM K^+. Changes in intracellular [Ca^{2+}], reported by a change in F340/F380, were comparable between Syn1A$_{K253I}$ (control) and Syn1A$_{K253I}$(5RK/A) cells in all parameters analyzed, including the baseline calcium levels (control: 0.91±0.01, n=51; 5RK/A: 0.91±0.01, n=59), the peak change in calcium (control: 0.20±0.02, n=51; 5RK/A: 0.19±0.01; n=59), as well as the kinetics of the calcium fluxes. This suggests that the decrease in evoked secretion seen in the 5RK/A cells occurs downstream of calcium influx.

To probe the temporal resolution and analyze the dynamics of individual fusion events, we next used carbon fiber amperometry. For these single-cell experiments, bovine adrenal chromaffin cells were used rather than PC-12 cells, as we found the exocytotic responses produced by these cells to be far more robust than those of PC-12 cells. Chromaffin cells were biolistically transfected with BoNT-C, either Syn1A$_{K253I}$ (control) or Syn1A$_{K253I}$(5RK/A), and GFP. Co-expression of Munc18-1 was not necessary in these experiments, as we have previously shown that Syn1A can traffic to the plasma membrane in chromaffin cells without the need for Munc18-1 overexpression [40]. Transfected cells were stimulated to secrete by local perfusion of 100mM K^+ for 60 seconds, during which time amperometric spikes were recorded. Representative amperometric traces are displayed in Figure 2.6C. In agreement with the hGH data above, the average number of spikes (fusion events) per cell was substantially reduced in the 5RK/A cells compared to control (control: 33.6 ± 4.0 spikes/cell, n=86; 5RK/A: 24.3 ± 2.6, n=82) (Figure 2.6D). However, the frequency distribution of the spikes, when normalized to the total number of spikes for each condition, was identical between control and 5RK/A cells (Figure 2.6E). This suggests that, rather than affecting a specific subpopulation of vesicles, the decrease in fusion events observed in the 5RK/A condition results from a generalized decrease in fusogenicity.

Syn1A's polybasic juxtamembrane region regulates fusion pore dynamics

We hypothesized that the generalized decrease in fusogenicity seen in 5RK/A cells might also be manifest in individual fusion events, particularly with regards to fusion pore dynamics. Many amperometric spikes contain a pre-spike foot (PSF), which is believed to represent the initial flux of catecholamine through the fusion pore, prior to dilation of the fusion pore and full fusion of the vesicle with the plasma membrane [41, 42]. Analysis of pre-spike feet can thus elucidate details surrounding the late stages of vesicle fusion, especially those regarding the formation and expansion of the fusion pore. Changes in PSF amplitudes are believed to represent changes in fusion pore diameter, whereas changes in PSF duration are thought to represent changes in stability of the fusion pore and kinetics of fusion pore expansion.

Representative pre-spike feet are shown in Figure 2.7A. Interestingly, the Syn1A$_{K253I}$(5RK/A) cells demonstrated decreased PSF amplitudes, in addition to increased PSF durations, compared to control Syn1A$_{K253I}$ (control) PSF (Figure 2.7B and C). In other words, the fusion pores in the 5RK/A cells were not only smaller in diameter, but also took longer to expand to full fusion. The mean PSF amplitude for control cells was 7.66 ± 0.27pA, which was slightly reduced to 6.18 ± 0.24pA for 5RK/A cells (n=584 control PSF, n=576 5RK/A PSF) (Figure 2.7B, left). The mean PSF duration for control cells was 7.28 ± 0.74ms, which was lengthened to 12.33 ± 1.05ms in 5RK/A cells (n=584 control PSF, n=576 5RK/A PSF) (Figure 2.7C, left). Qualitatively, these results also held true under a more stringent analysis scheme, in which the median PSF parameters for each cell were first determined, and the medians then averaged across cells. Median PSF amplitudes were 6.16 ± 0.43pA and 4.42 ± 0.22pA for control and 5RK/A cells, respectively (n=66 control cells, n=78 5RK/A cells) (Figure 2.7B, right). Median PSF durations were 5.44 ± 0.54ms for control, compared to 8.23 ± 0.95ms for 5RK/A cells (n=66 control cells, n=78 5RK/A cells) (Figure 2.7C, right). In all analysis schemes, the differences between control and 5RK/A PSF parameters were statistically significant ($p<0.05$). Thus, neutralization of Syn1A's polybasic juxtamembrane region results in a decrease in fusion pore diameter, as well as a delay in fusion pore expansion. As formation and expansion of the fusion pore have been modeled to be among the most energetically expensive steps in the membrane fusion process[1, 2], these data suggest that energetic inefficiencies in the fusion process may, in part, account for the secretory defects observed with the 5RK/A mutant.

Manipulation of intracellular phosphatidic acid levels differentially regulates secretion from control and 5RK/A cells

Thus far, we have demonstrated that Syn1A binds multiple acidic phospholipids, including the fusogenic lipid, phosphatidic acid, and that these interactions are mediated through Syn1A's polybasic juxtamembrane domain. Moreover, we have shown that neutralization of Syn1A's polybasic juxtamembrane domain (5RK/A mutant) results in a significant decrease in stimulated secretion, in addition to effects on fusion pore amplitude and duration that are suggestive of an energetic defect in the fusion process. To determine whether the functional effects seen with the 5RK/A mutant are a direct result of the inability of this mutant to bind lipids, we performed hGH secretion assays to test how various alterations in membrane lipid composition affected the abilities of the Syn1A$_{K253I}$(control) or Syn1A$_{K253I}$(5RK/A) mutant to rescue BoNT-C mediated knockdown of secretion in PC-12 cells. As in prior experiments, all results have been normalized to the level of rescued secretion observed in the Syn1A$_{K253I}$ control cells in the absence of any lipid manipulations, and are reported as a % rescued secretion.

To determine whether the secretory defect in the 5RK/A cells might be related to the energetics of fusion, we first tested the effects of externally applied lysophosphatidylcholine (LPC, 1 μM), an inverted-cone-shaped lipid that facilitates fusion pore formation and expansion by inducing positive curvature to the outer leaflet of the membrane bilayer. In these experiments, using an LPC concentration that was low enough so as not to affect stimulated secretion from the Syn1A$_{K253I}$ control cells, we observed a statistically significant and substantial (>50%) increase in secretion from the Syn1A$_{K253I}$(5RK/A) cells (38.6% vs 59.8% rescued secretion in the absence or presence of LPC, respectively) (Figure 2.8). This result suggests that the exocytotic defect in the 5RK/A mutant occurs at a late step in fusion and is likely energetic in nature.

The partial rescue of the 5RK/A secretory phenotype by externally applied LPC (which induces positive curvature on the outer bilayer leaflet) nicely complemented our previous result demonstrating that Syn1A binds with high apparent affinity to phosphatidic acid, a cone-shaped, fusogenic lipid (which induces negative curvature on the inner bilayer leaflet). We then investigated whether specific Syn1A-phosphatidic acid interactions are important for regulated exocytosis. For these experiments, the BoNT-C knockdown and rescue assay was repeated, while overexpressing either phospholipase D1 (PLD1), or an siRNA construct previously demonstrated to target PLD1 [30]. PLD1 is a stimulus-activated enzyme which cleaves phosphatidylcholine to generate free choline and phosphatidic acid. Overexpression of PLD1 has been shown to enhance regulated exocytosis, whereas knockdown of PLD1 activity results in a decrease in secretion [30, 43-46]. While the extent to which PLD1 overexpression and knockdown affected control secretion in our BoNT-C knockdown experiments (Figure 2.8) was slightly less than has been previously reported, this likely resulted from the BoNT-C knockdown assay's requirement for simultaneous overexpression of multiple constructs. As such, changes in PLD1 levels achieved in this system were likely more limited than when PLD1 or siRNA-PLD1 are the only constructs being overexpressed (as in prior studies).

Importantly, we found that overexpression of PLD1 resulted in a near complete phenotypic rescue of the 5RK/A mutant (117% vs 103% rescued secretion, for PLD1-treated Syn1A$_{K253I}$ control cells or PLD1-treated Syn1A$_{K253I}$(5RK/A) cells, respectively) (Figure 2.8). Also of substantial interest was the finding that siRNA-mediated knockdown of PLD1 drastically reduced secretion from Syn1A$_{K253I}$ control cells, while having little effect on secretion from Syn1A$_{K253I}$(5RK/A) cells (74% reduction in secretion for Syn1A$_{K253I}$ control cells, compared to a 24% reduction for Syn1A$_{K253I}$(5RK/A) cells, in the presence of siRNA-PLD1) (Figure 2.8). These data provide strong evidence that the loss of interaction between Syn1A and phosphatidic acid primarily accounts for the secretory defects seen with the Syn1A 5RK/A mutation and largely rule out the possibility that this secretory defect resulted from disruption of untested Syn1A-protein interactions or from alterations in Syn1A structure. More importantly, these results demonstrate that the Syn1A - phosphatidic acid interaction is critically important in regulating the overall levels of evoked secretion in live neuroendocrine cells.

Discussion

SNARE complexes comprise the minimal protein machinery required for membrane fusion, hence most studies have focused on defining the regulation of their assembly and disassembly. However, the fusion process also involves lipids, and the specific lipid composition of membranes undergoing fusion has profound consequences on the energetic barrier for fusion [11]. A central and unresolved issue is whether specific mechanisms exist to recruit and sequester fusogenic lipids at preferential sites of membrane fusion.

In this study, we establish that the Q-SNARE Syntaxin1A (Syn1A) forms functional interactions with acidic phospholipids and that these interactions facilitate membrane fusion. Syn1A formed a high apparent affinity interaction with the fusogenic lipid, phosphatidic acid, in addition to lower apparent affinity interactions with polyphosphoinositides, including PI(4,5)P2. Neutralizing mutations within a highly conserved, polybasic juxtamembrane region of Syn1A (aa252-265) progressively reduced Syn1A's ability to bind lipids, while leaving intact these mutants' abilities to traffic correctly to the plasma membrane and to form appropriate protein-protein interactions. Development of a novel BoNT-C knockdown and rescue assay allowed the secretory function of exogenous mutant Syn1A constructs to be studied in isolation from endogenous WT Syn1A, and demonstrated that progressive neutralization of Syn1A's juxtamembrane region resulted in a progressive decrease in secretory function. Moreover, amperometric analysis uncovered a lengthening in fusion pore duration and a decrease in fusion pore diameter in fusion events catalyzed by a lipid-binding-deficient Syn1A (5RK/A), suggesting an energetic defect in fusion. Importantly, we found that the inhibition of secretion observed with the Syn1A 5RK/A mutant could be completely rescued by overexpression of PLD1, and that knockdown of PLD1 activity strongly inhibited control secretion, while having little effect on 5RK/A secretion. Altogether, these data suggest that Syn1A-lipid interactions play a key role in regulating the energetics of membrane fusion.

We propose that Syn1A-lipid interactions function both structurally as well as electrostatically to reduce the energetic barrier for fusion specifically at sites of exocytosis. This energy barrier can be modeled as a series of membrane intermediates formed during the merging of two lipid bilayers [1, 2]. First, the membranes are brought within proximity to establish a region of dehydrated contact. A fusion stalk forms as the initial connection between the membranes, and radial expansion of this stalk yields a hemifusion diaphragm, where contacting leaflets of the bilayers have merged, while the distal leaflets remain separate. Importantly, the presence of negative curvature-favoring lipids in the contacting leaflets greatly reduces the energetic requirements for stalk and hemifusion formation [19]. PA, under physiological conditions, exhibits negative spontaneous curvature approaching that of PE [17, 47]. Thus, a first *structural* function of the Syn1A-lipid interaction may be to localize PA to sites of fusion, thereby generating negative curvature to facilitate stalk formation and stabilize the hemifusion intermediate.

Beyond hemifusion, generation of lateral tension within the hemifusion diaphragm leads to membrane rupture and formation of a fusion pore, whereby the distal leaflets of the two bilayers merge. Expansion of this fusion pore results in full membrane collapse and fusion. These steps are believed to be the most energetically expensive in membrane fusion [1, 2]. It has been proposed that the lateral tension required for formation and expansion of the fusion pore may be generated by electrostatic interactions between fusogenic proteins and acidic lipids [14]. Indeed, generation of the lateral tension to drive fusion pore expansion may be a second *electrostatic* function of the Syn1A-lipid interaction. This is supported by our amperometry results, which demonstrated that neutralization of Syn1A's polybasic juxtamembrane region resulted in a delay in fusion pore expansion and a decrease in fusion pore diameter.

Among the lipids tested in this study, Syn1A bound with highest apparent affinity to PA, a lipid known to exert substantial effects on regulated exocytosis. Phospholipase D1 (PLD1), an enzyme which generates PA from PC, potently enhances regulated exocytosis at a late stage in vesicle fusion, in a variety of cell types including PC12 cells, adrenal chromaffin cells, adipocytes, and neurons [30, 43-46]. While specific effectors for the PLD1-generated PA have remained elusive, our results strongly suggest that the facilitatory effects of PLD on secretion may be mediated in part by Syn1A-PA interactions. Namely, we found that the Syn1A 5RK/A mutant, which lacks the ability to bind PA, demonstrated reduced levels of secretion. Overexpression of PLD1 rescued this defect, presumably because the increased local concentrations of PA generated by PLD1 compensated for the 5RK/A's inability to sequester PA. Similarly, knockdown of PLD1 activity resulted in the inhibition of control secretion, because in the absence of PA, Syn1A's function becomes similar to that of the 5RK/A mutant. Accordingly, knockdown of PLD1 activity had little effect on Syn1A 5RK/A, since this mutant cannot normally bind PA.

We have focused largely on Syn1A-PA interactions, but our finding that Syn1A directly binds PI(4,5)P2 is also of interest. PI(4,5)P2 is perhaps the most notable lipid signal for regulated exocytosis, given its requirement in the ATP-dependent priming of vesicles [48-50]. Endogenous PI(4,5)P2 clusters partially colocalize with Syn1A clusters in membrane sheets of PC12 cells, and exocytosis was promoted at sites of Syn1A-PI(4,5)P2 cluster co-localization [24]. Of substantial interest is that PA and PI(4,5)P2 participate in a positive feed-forward cycle that results in the local generation of both lipids: PA positively regulates PIP5KI, an enzyme which generates PI(4,5)P2 [51], and in turn, PI(4,5)P2 positively regulates PLD1, which generates PA [52]. That such specific membrane microdomains can have profound implications on the energetics of SNARE-mediated fusion events is a concept conserved down through yeast. Indeed, it was shown that a yeast SNARE complex (Spo20p- Sso1p-Snc1p) that normally mediates fusion at the prospore membrane was insufficient to drive fusion at the plasma membrane [53]. This insufficiency could be overcome by overexpression of MSS4p (a yeast PI5K). Interestingly, the effect of MSS4p was mediated via recruitment of Spo14p (a yeast PLD), to the plasma membrane. It was suggested that Spo14p-mediated generation of PA at the plasma membrane reduced the energetic requirements for fusion such that the energy released by the Spo20p-Sso1p-Snc1p complex became sufficient to drive fusion at the plasma membrane.

While the current report is the first to establish the identity of specific Syn1A-lipid interactions, map the interacting domain, and determine direct functional effects of these interactions, it is clear that SNARE-lipid interactions are emerging as significant functional interactions that underlie membrane fusion [13, 54-57]. Of substantial importance is that sequence alignment across multiple families of SNARE proteins demonstrates high conservation of the lipid-interacting polybasic juxtamembrane region [28]. Therefore, the concept of membrane fusion driven by SNARE proteins must be enlarged to encompass the possibility that SNAREs also function to spatially sequester bioactive lipids as a means to alter the energetic requirements for fusion.

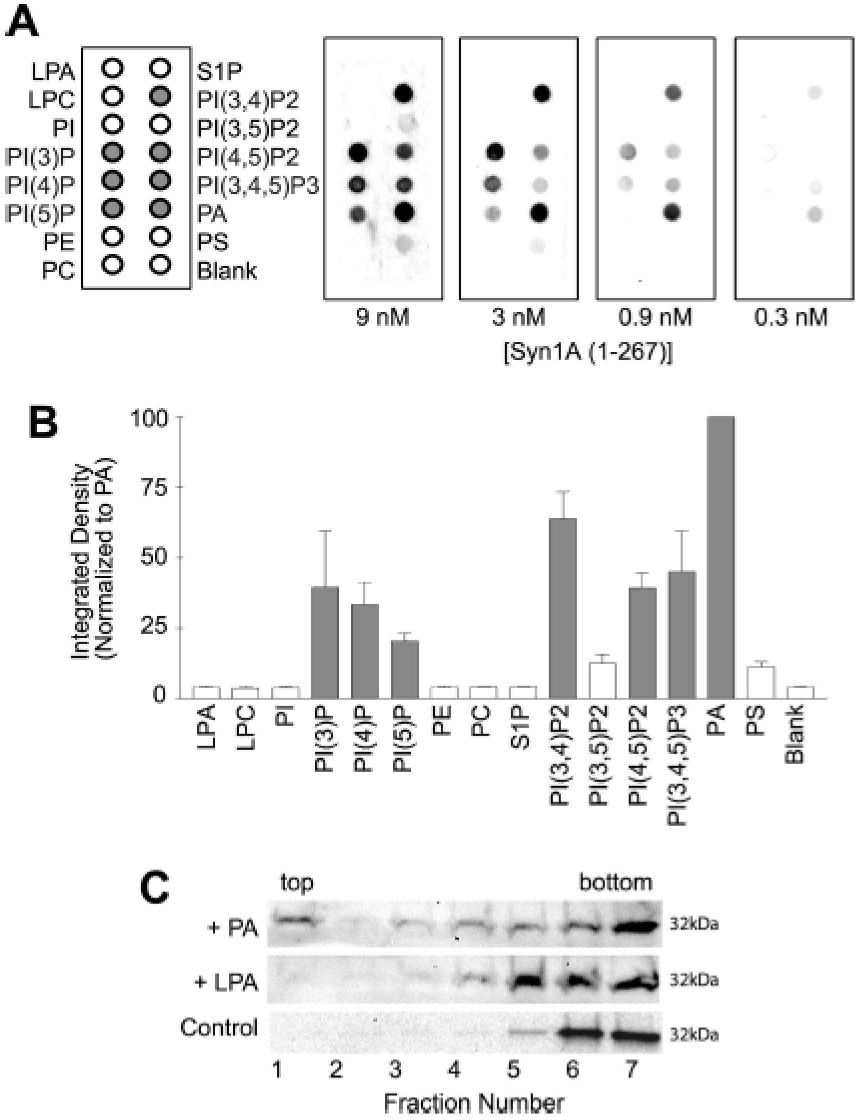

Figure 2.1. Syn1A directly binds a subset of acidic phospholipids that includes the fusogenic lipid phosphatidic acid. (A) Protein-lipid overlay demonstrating concentration-dependent binding between soluble Syn1A(1-267) and multiple acidic phospholipids. Left: Schematic representing the arrangement of lipids spotted on the nitrocellulose. Filled circles indicate those lipids for which an interaction was demonstrated. Right: α-Syn1A immunoreactivity from four representative protein-lipid overlay experiments, in which decreasing concentrations of Syn1A were overlaid onto nitrocellulose membranes spotted with 100pmoles each of indicated phospholipids. (B) Averaged level of interaction of Syn1A for each phospholipid relative to that of PA. Integrated immunoreactive density associated with each lipid on the overlays was averaged from 3 independent experiments where [Syn1A] = 3nM, and normalized to the integrated density for PA. Bars show means ± SEM. (C) Representative Western blots of Syn1A immunoreactivity in fractions collected from liposome flotation assays. Bound Syn1A floats with liposomes to the top of the gradient.

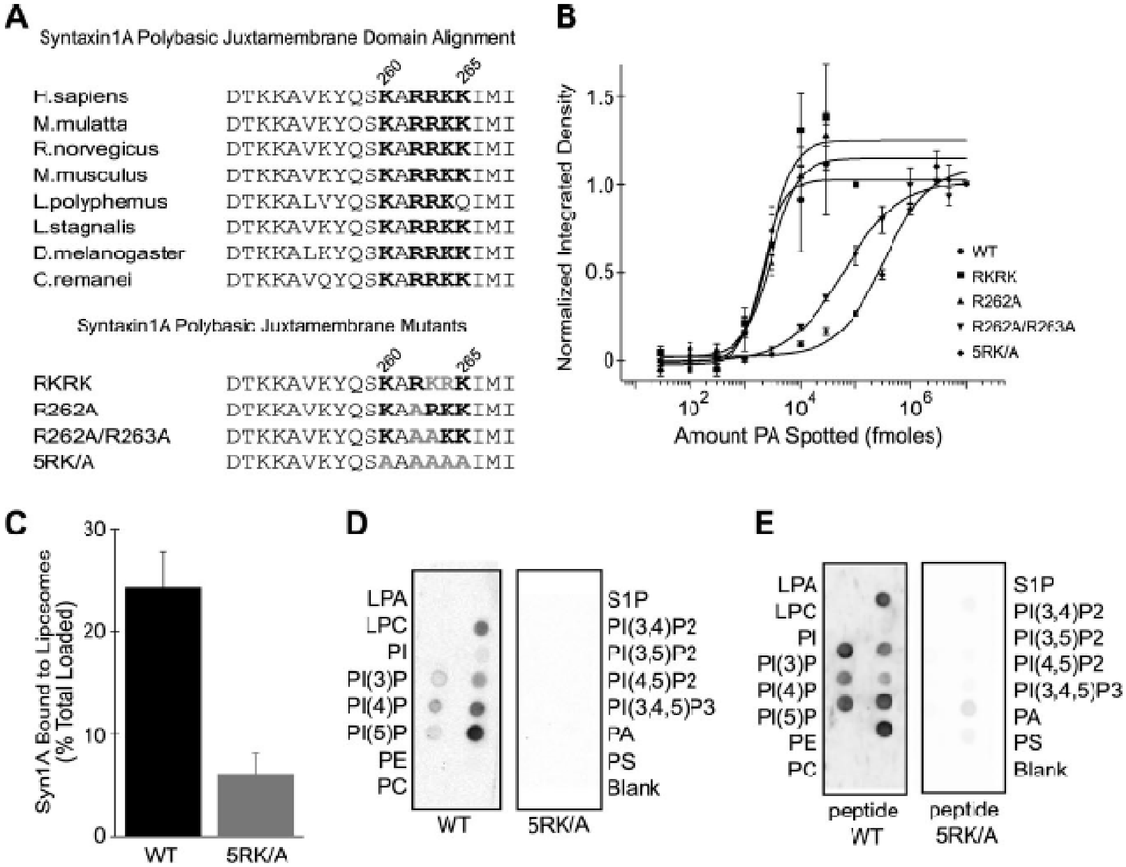

Figure 2.2. A polybasic juxtamembrane sequence in Syn1A comprises the lipid binding domain. (A) Top: Sequence alignment of juxtamembrane regions of Syn1A across species. Note the five highly conserved basic residues between positions 260-265. (NCBI accession numbers: HS: AAA53519; MMul: NP_001028037; RN: AAF23017; MMus: NP_058081; LP: AAK70494; LS: AAO83845; DM: A55673; CR: AAY54265). Bottom: Sequence alignments of Syn1A juxtamembrane mutants used in this study. (B) Progressive neutralization of Syn1A juxtamembrane basic residues correlates to a progressive reduction in apparent binding affinity for PA. Binding between Syn1A mutants and PA was determined using protein-lipid overlays (n=4), in which increasing amounts of PA were spotted on nitrocellulose. Soluble Syn1A(1-267) was at a 5-fold molar excess to PA. Integrated Syn1A immunoreactivity was measured at each PA spot, normalized for each mutant, and the data fitted with a Hill equation. (C) The 5RK/A Syn1A mutant exhibits significantly reduced binding to PA-containing liposomes compared to WT Syn1A. % of Syn1A bound to liposomes was defined as the % of Syn1A immunoreactivity in the top 3 gradient fractions relative to the total Syn1A immunoreactivity. (D) Representative protein-lipid overlay demonstrating that Syn1A 5RK/A has reduced binding to all acidic phospholipids tested. (E) Representative protein-lipid overlay demonstrating that a peptide of Syn1A's juxtamembrane region (aa252-265) closely recapitulates the lipid binding of the full-length soluble Syn1A.

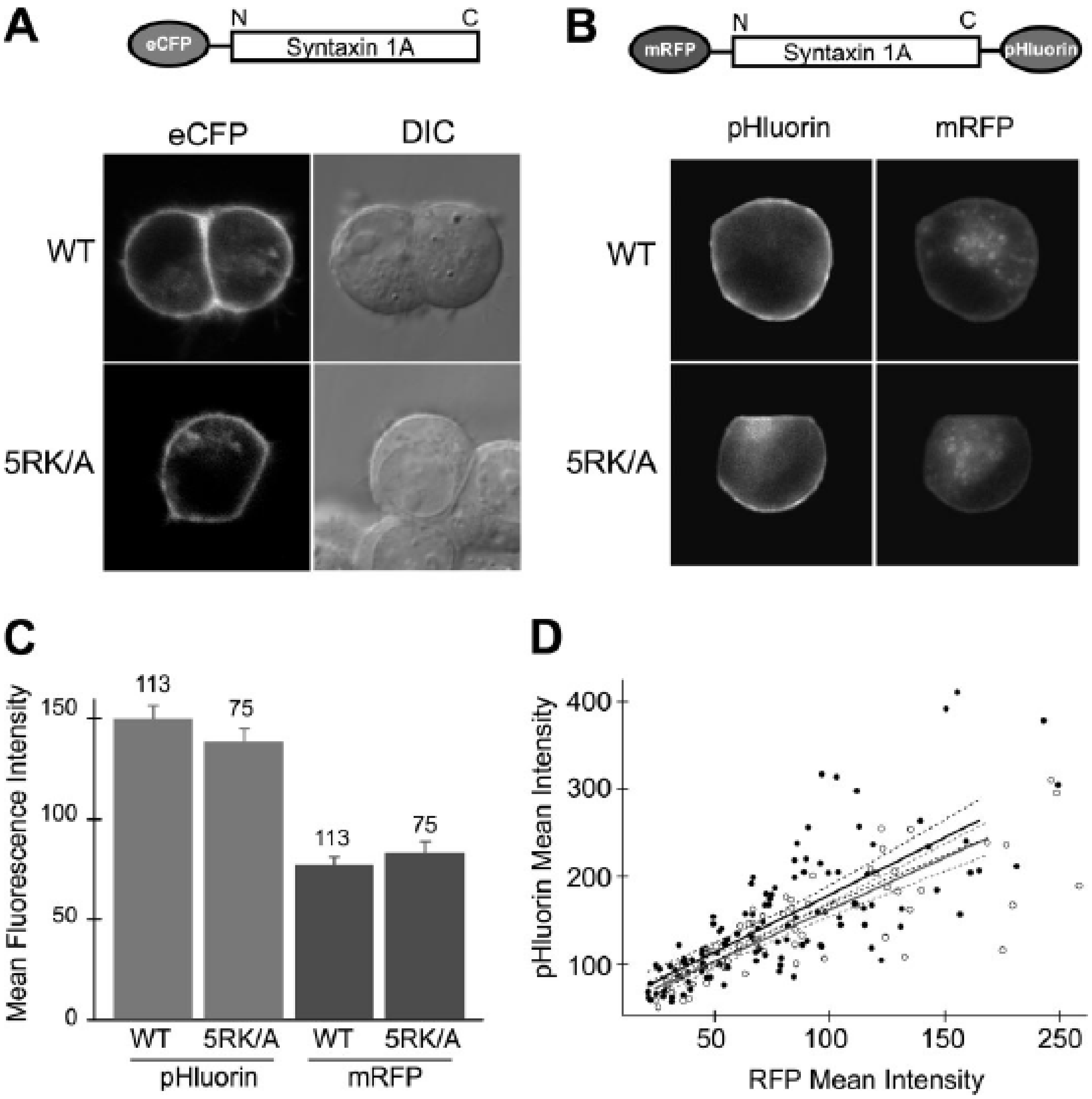

Figure 2.3. Syn1A 5RK/A targets to plasma membrane regions in PC-12 cells. (A) Representative confocal fluorescence and corresponding DIC images of PC-12 cells transiently transfected with eCFP-tagged Syn1A(WT) and Syn1A (5RK/A) together with Munc18-1. (B) Representative epifluorescence images of PC-12 cells transiently transfected with mRFP-Syn1A-pHluorin (WT or 5RK/A) and Munc18. The pHluorin signal (left) reports only on the pool of Syn1A present at the cell surface, whereas the mRFP signal (right) reports on the entire pool of exogenous Syn1A within the cell. (C) Average pHluorin and mRFP fluorescence intensity for PC-12 cells transfected as in (B). Bars represent means ± SEM. Numbers above each bar represent the number of cells used to calculate the average for each condition. (D) Scatterplot of mean pHluorin intensity vs mean mRFP intensity for each individual cell. Cells demonstrating moderate Syn1A expression levels (defined as a mean RFP signal between 20 and 170, a range within which >85% of the cells analyzed fell) were used to generate linear fits for each data set, as indicated by the solid lines. Dotted lines represent the 95% confidence intervals of the linear fits, which overlap for the WT and 5RK/A data sets.

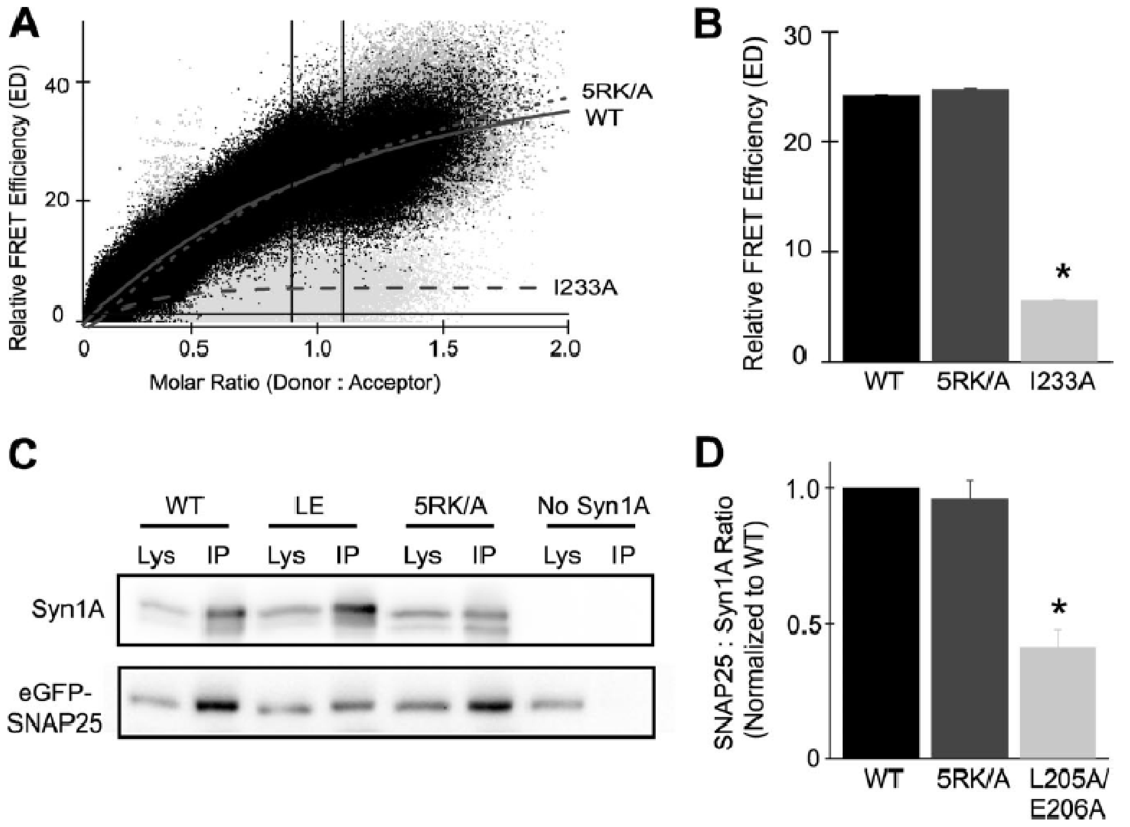

Figure 2.4. Syn1A 5RK/A interacts normally with Munc18-1 and SNAP25. (A) Analysis of direct CFP-Syn1A-citrine-Munc18-1 interactions by sensitized emission FRET imaging. Graph shows a pixel-by-pixel plot of FRET efficiency vs molar ratio (Syn1A:Munc18-1). Both Syn1A (WT) and Syn1A (5RK/A) bind Munc18-1 with similar FRET efficiency. By comparison, Syn1A I233A demonstrates strongly reduced FRET efficiencies with Munc18-1 compared to WT. Solid horizontal line demonstrates background FRET values determined from coexpression of CFP and citrine fluoroproteins. (B) Average FRET efficiency for each Syn1A construct, at equimolar ratios of Syn1A and Munc18-1 (0.9 < ratio < 1.1; see vertical lines in (B)). Bars represent the mean ± SEM. (C) Representative immunoblot demonstrating co-immunoprecipitation of EGFP-SNAP25 with Syn1A from HEK293-S3 cells transiently transfected with Syn1A (WT, L205A/E206A, or 5RK/A), Munc18-1, and EGFP-SNAP25. Note that Syn1A 5RK/A pulls down similar amounts of EGFP-SNAP25 compared to WT Syn1A. In contrast, a mutant of Syn1A (L205A/E206A) previously shown to have reduced binding to SNARE proteins, demonstrates a reduced amount of EGFP-SNAP25 pulldown. (D) Integrated densities of Syn1A and EGFP-SNAP25 bands were measured to determine a ratio of EGFP-SNAP25 to Syn1A for each condition. Ratios within a single experiment were then normalized to that of WT Syn1A to allow for comparison across experiments. Bars represent means ± SEM, from 3 independent experiments.

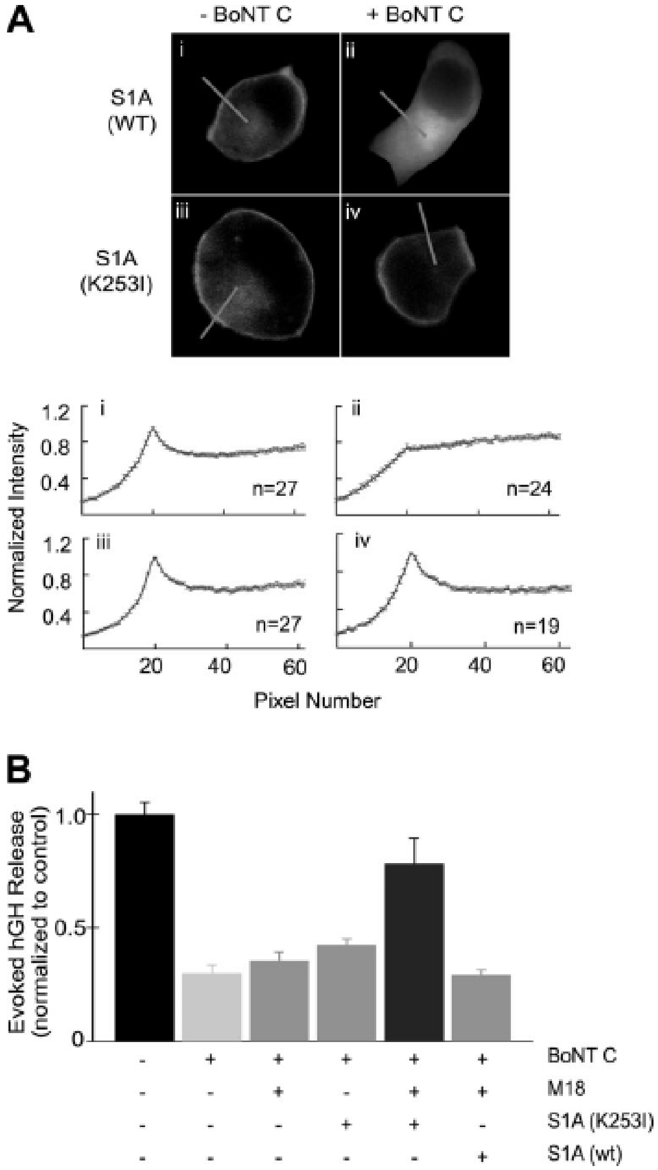

Figure 2.5. BoNT-C knockdown allows isolation of functional effects of exogenous Syn1A constructs in live secretory cells. (A) Top: Representative epifluorescence images demonstrating that Syn1A (K253I) is resistant to cleavage by BoNT-C. Images compare the subcellular distribution of fluorescent signal in PC-12 cells transfected with CFP-Syn1A (WT) and CFP-Syn1A (K253I) with/without the light chain of BoNT-C. Munc18-1 was coexpressed in each condition. Bottom: Normalized fluorescence intensity profiles, as determined by averaging line scans taken from the outside to the middle of each cell, corresponding to the expression conditions shown above. Line scans were normalized, the peaks were aligned, and scans were averaged for each condition. (B) Functional rescue of BoNT-C knockdown in elevated K^+ evoked (70mM, 6min) hGH secretion, by co-transfection with Syn1A (K253I) and Munc18-1. Note that S1A (K253I) or Munc18-1 alone did not rescue secretion, nor did Syn1A (WT) co-transfected with Munc18-1. Bars represent the means ± SEM.

Figure 2.6. Neutralization of Syn1A's polybasic juxtamembrane region results in a decrease in evoked secretion. (A) Progressive neutralizing mutations of Syn1A's polybasic juxtamembrane domain result in a graded reduction in evoked hGH secretion. Transfected PC-12 cells were stimulated with 70mM K+ for 6 min. Data was normalized to control rescue ($\text{Syn1A}_{\text{K253I}}$) for each experiment and pooled across at least 3 independent experiments for each condition. Dotted line represents the baseline level of remaining secretion following BoNT-C treatment. Bars represent means ± SEM. Asterisks indicate statistical significance ($p<0.001$) from control Graph at right shows the same data as on the left, but with the average residual BoNT-C baseline secretion for each experiment subtracted from each condition prior to normalization to control rescue. Note that when the data is corrected for residual BoNT-C secretion, the actual effect of the Syn1A neutralization mutants becomes substantially larger. (B) Evoked [Ca^{2+}] dynamics reported by changes in Fura-2 fluorescence intensity ratio (F340nm/380nm) demonstrate that depolarization-induced (100mM K+ for 5 sec) calcium fluxes are similar between control and 5RK/A cells. Left: Averaged ratio traces for control and 5RK/A cells. Horizontal bar indicates period of stimulus application. Averaged baseline (Middle) and evoked change (Right) in F340nm/380nm ratio for control and 5RK/A cells. (C) Representative amperometric recordings from bovine adrenal chromaffin cells transfected with $\text{Syn1A}_{\text{K253I}}$ or $\text{Syn1A}_{\text{K253I}}$ (5RK/A) together with BoNT-C. Exocytotic secretion was evoked by a 60s application of locally perfused 100mM K+. Amperometric spikes were detected and quantified by an automated analysis software program written by Eugene Mosharov (Columbia University). (D) Comparison of averaged number of spikes per cell in control and 5RK/A cells. Bars show mean ± SEM. Only spikes >10pA in amplitude above rms baseline were considered for analysis. (E) Cumulative spike frequency distribution, normalized for the total number of spikes for control ($\text{Syn1A}_{\text{K253I}}$) and $\text{Syn1A}_{\text{K253I}}$ (5RK/A) cells. The distributions were not significantly different.

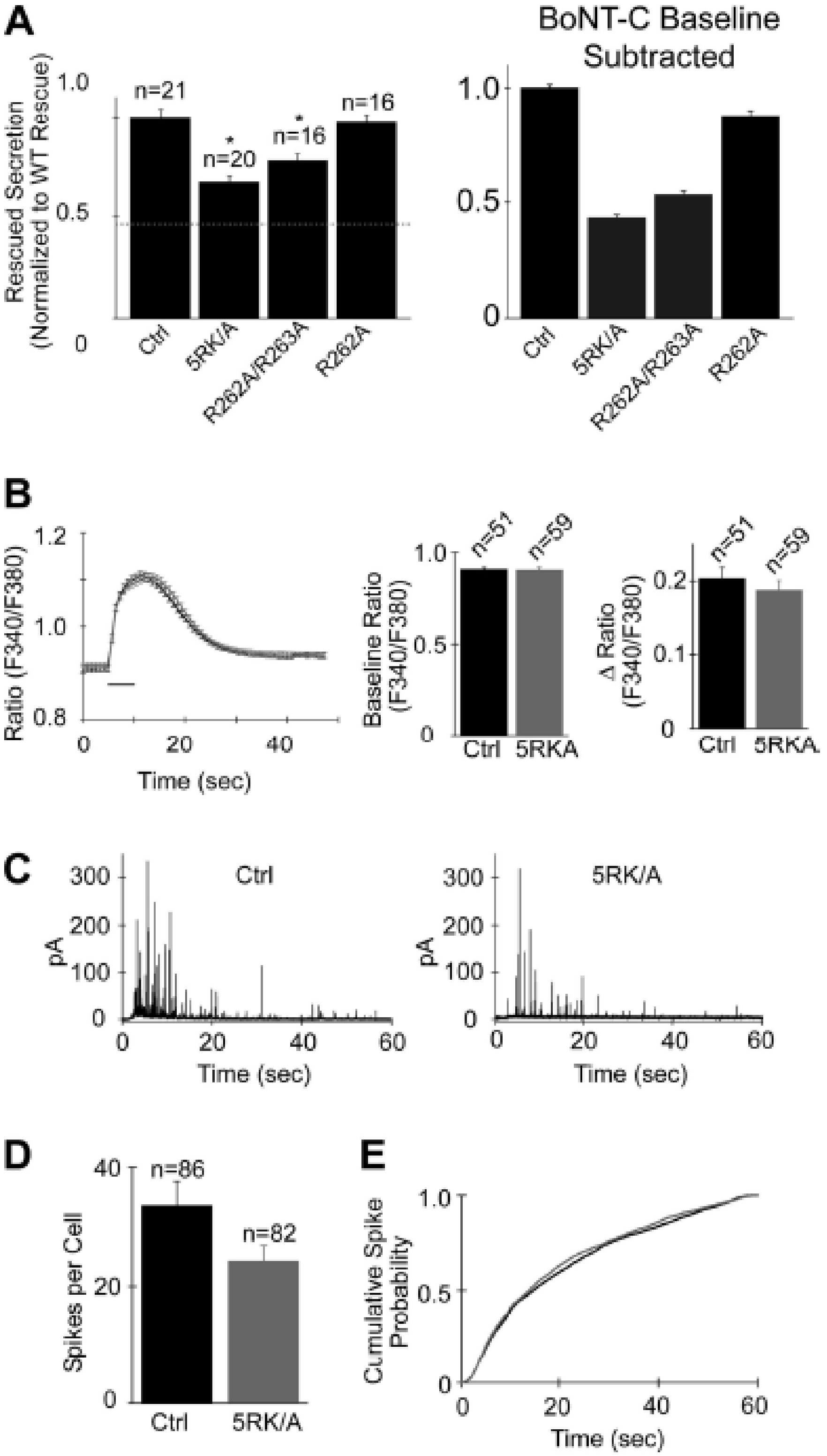
A
BoNT-C Baseline Subtracted
Rescued Secretion (Normalized to WT Rescue)
1.0
0.5
0
n=21
n=20
n=16
n=16
*
*
Ctrl
5RK/A
R262A/R263A
R262A
B
1.2
1.0
0.8
Ratio (F340/F380)
Time (sec)
0
20
40
Baseline Ratio (F340/F380)
n=51
n=59
Ctrl
5RKA
Δ Ratio (F340/F380)
0.2
0.1
C
Ctrl
5RK/A
pA
300
200
100
60
D
Spikes per Cell
n=86
n=82
E
Cumulative Spike Probability

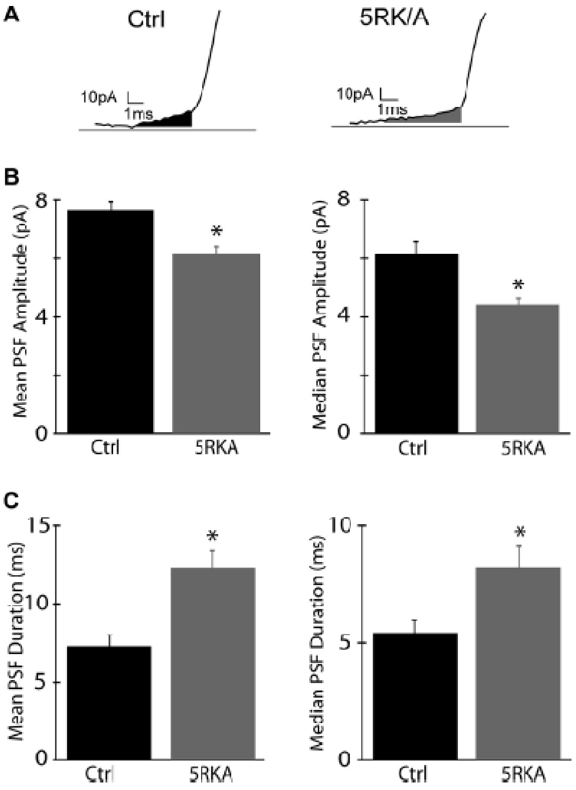

Figure 2.7. Neutralization of Syn1A's polybasic juxtamembrane region results in a decrease in fusion pore diameter and a lengthening of fusion pore duration. (A) Representative pre-spike feet for control ($\text{Syn1A}_{\text{K253I}}$) or $\text{Syn1A}_{\text{K253I}}$ (5RK/A) expression conditions (+ BoNT-C) during stimulation by 60s application of locally perfused 100mM K^+. (B) *Left*, Mean PSF amplitudes for control and 5RK/A cells, from all PSF >1ms in duration and <30pA in amplitude (n=584 control PSF analyzed, n=576 5RK/A PSF analyzed). *Right*, Averaged median PSF amplitudes (n=66 control cells analyzed, n=78 5RK/A cells analyzed). In both cases, the PSF from 5RK/A cells demonstrate statistically significant decreases in amplitude ($p<0.05$). Bars represent the mean ± SEM. (C) *Left*, Mean PSF durations for control and 5RK/A cells, from all PSF >1ms in duration and <30pA in amplitude (n=584 control PSF analyzed, n=576 5RK/A PSF analyzed). *Right*, Averaged median PSF durations (n=66 control cells analyzed, n=78 5RK/A cells analyzed). In both cases, the PSF from 5RK/A cells demonstrate statistically significant lengthening in duration ($p<0.05$). Bars represent the mean ± SEM.

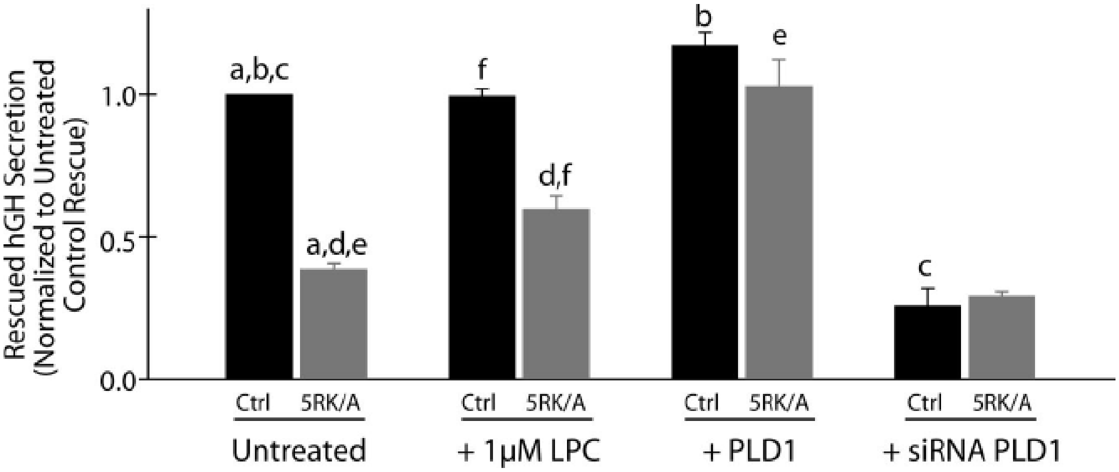

Figure 2.8. Functional phenotypes of Syn1A$_{K253I}$ control and 5RK/A mutant are differentially regulated by manipulation of phosphatidic acid levels in live PC-12 cells. Graph demonstrates averaged results from hGH secretion assays utilizing the BoNT-C knockdown and rescue. External application of 1μM LPC has no effect on control secretion, but results in a partial rescue of the 5RK/A phenotype. Overexpression of PLD1 results in near-complete rescue of the 5RK/A phenotype to control secretion levels. On the other hand, knockdown of PLD1 activity via a targeted siRNA construct results in a drastic decrease in control secretion, while having little to no effect on secretion from 5RK/A cells. Results are normalized to the untreated Syn1A$_{K253I}$ control rescue in each experiment to allow comparison across multiple experiments, and data was pooled from at least 3 independent experiments. Bars represent the mean ± SEM. Letters above bars indicate pairs of conditions in which the differences are statistically significant ($p<0.05$).

References

1. Chernomordik, L.V. and M.M. Kozlov, *Protein-lipid interplay in fusion and fission of biological membranes.* Annu Rev Biochem, 2003. **72**: p. 175-207.
2. Cohen, F.S. and G.B. Melikyan, *The energetics of membrane fusion from binding, through hemifusion, pore formation, and pore enlargement.* J Membr Biol, 2004. **199**(1): p. 1-14.
3. Jahn, R. and R.H. Scheller, *SNAREs--engines for membrane fusion.* Nat Rev Mol Cell Biol, 2006. **7**(9): p. 631-43.
4. Weber, T., et al., *SNAREpins: minimal machinery for membrane fusion.* Cell, 1998. **92**(6): p. 759-72.
5. Schiavo, G., et al., *Tetanus and botulinum-B neurotoxins block neurotransmitter release by proteolytic cleavage of synaptobrevin.* Nature, 1992. **359**(6398): p. 832-5.
6. Blasi, J., et al., *Botulinum neurotoxin A selectively cleaves the synaptic protein SNAP-25.* Nature, 1993. **365**(6442): p. 160-3.
7. Blasi, J., et al., *Botulinum neurotoxin C1 blocks neurotransmitter release by means of cleaving HPC-1/syntaxin.* Embo J, 1993. **12**(12): p. 4821-8.
8. Broadie, K., et al., *Syntaxin and synaptobrevin function downstream of vesicle docking in Drosophila.* Neuron, 1995. **15**(3): p. 663-73.
9. Littleton, J.T., et al., *Temperature-sensitive paralytic mutations demonstrate that synaptic exocytosis requires SNARE complex assembly and disassembly.* Neuron, 1998. **21**(2): p. 401-13.
10. Saifee, O., L. Wei, and M.L. Nonet, *The Caenorhabditis elegans unc-64 locus encodes a syntaxin that interacts genetically with synaptobrevin.* Mol Biol Cell, 1998. **9**(6): p. 1235-52.
11. Chernomordik, L., M.M. Kozlov, and J. Zimmerberg, *Lipids in biological membrane fusion.* J Membr Biol, 1995. **146**(1): p. 1-14.
12. Melia, T.J., et al., *Lipidic antagonists to SNARE-mediated fusion.* J Biol Chem, 2006. **281**(40): p. 29597-605.
13. Vicogne, J., et al., *Asymmetric phospholipid distribution drives in vitro reconstituted SNARE-dependent membrane fusion.* Proc Natl Acad Sci U S A, 2006. **103**(40): p. 14761-6.
14. Zimmerberg, J. and K. Gawrisch, *The physical chemistry of biological membranes.* Nat Chem Biol, 2006. **2**(11): p. 564-7.
15. Chernomordik, L.V., et al., *Lysolipids reversibly inhibit Ca(2+)-, GTP- and pH-dependent fusion of biological membranes.* FEBS Lett, 1993. **318**(1): p. 71-6.
16. Epand, R.M., N. Fuller, and R.P. Rand, *Role of the position of unsaturation on the phase behavior and intrinsic curvature of phosphatidylethanolamines.* Biophys J, 1996. **71**(4): p. 1806-10.
17. Kooijman, E.E., et al., *Spontaneous curvature of phosphatidic acid and lysophosphatidic acid.* Biochemistry, 2005. **44**(6): p. 2097-102.
18. Leikin, S., et al., *Measured effects of diacylglycerol on structural and elastic properties of phospholipid membranes.* Biophys J, 1996. **71**(5): p. 2623-32.
19. Kozlovsky, Y. and M.M. Kozlov, *Stalk Model of Membrane Fusion: Solution of Energy Crisis.* Biophys. J., 2002. **82**(2): p. 882-895.
20. Bennett, M.K., N. Calakos, and R.H. Scheller, *Syntaxin: a synaptic protein implicated in docking of synaptic vesicles at presynaptic active zones.* Science, 1992. **257**(5067): p. 255-9.

21. Chamberlain, L.H., R.D. Burgoyne, and G.W. Gould, *SNARE proteins are highly enriched in lipid rafts in PC12 cells: Implications for the spatial control of exocytosis.* PNAS, 2001. **98**(10): p. 5619-5624.
22. Lang T, B.D., Wenzel D, Riedel D, Holroyd P, Thiele C, Jahn R, *SNAREs are concentrated in cholesterol-dependent clusters that define docking and fusion sites for exocytosis.* The EMBO Journal, 2001. **20**: p. 2202–2213.
23. Ohara-Imaizumi, M., et al., *Site of docking and fusion of insulin secretory granules in live MIN6 beta cells analyzed by TAT-conjugated anti-syntaxin 1 antibody and total internal reflection fluorescence microscopy.* J Biol Chem, 2004. **279**(9): p. 8403-8.
24. Aoyagi, K., et al., *The activation of exocytotic sites by the formation of phosphatidylinositol 4,5-bisphosphate microdomains at syntaxin clusters.* J Biol Chem, 2005. **280**(17): p. 17346-52.
25. Han, X., et al., *Transmembrane segments of syntaxin line the fusion pore of Ca2+-triggered exocytosis.* Science, 2004. **304**(5668): p. 289-92.
26. Wagner, M.L. and L.K. Tamm, *Reconstituted syntaxin1a/SNAP25 interacts with negatively charged lipids as measured by lateral diffusion in planar supported bilayers.* Biophys J, 2001. **81**(1): p. 266-75.
27. Kim, C.S., D.H. Kweon, and Y.K. Shin, *Membrane topologies of neuronal SNARE folding intermediates.* Biochemistry, 2002. **41**(36): p. 10928-33.
28. Weimbs, T., et al., *A model for structural similarity between different SNARE complexes based on sequence relationships.* Trends Cell Biol, 1998. **8**(7): p. 260-2.
29. Hammond, S.M., et al., *Characterization of two alternately spliced forms of phospholipase D1. Activation of the purified enzymes by phosphatidylinositol 4,5-bisphosphate, ADP-ribosylation factor, and Rho family monomeric GTP-binding proteins and protein kinase C-alpha.* J Biol Chem, 1997. **272**(6): p. 3860-8.
30. Zeniou-Meyer, M., et al., *Phospholipase D1 production of phosphatidic acid at the plasma membrane promotes exocytosis of large dense-core granules at a late stage.* J Biol Chem, 2007. **282**(30): p. 21746-57.
31. Armstrong, S.M. and E.L. Stuenkel, *Progesterone regulation of catecholamine secretion from chromaffin cells.* Brain Res, 2005. **1043**(1-2): p. 76-86.
32. Liu, J., et al., *Fluorescence resonance energy transfer reports properties of syntaxin1a interaction with Munc18-1 in vivo.* J Biol Chem, 2004. **279**(53): p. 55924-36.
33. Hoppe, A., K. Christensen, and J.A. Swanson, *Fluorescence resonance energy transfer-based stoichiometry in living cells.* Biophys J, 2002. **83**(6): p. 3652-64.
34. Mosharov, E.V. and D. Sulzer, *Analysis of exocytotic events recorded by amperometry.* Nat Methods, 2005. **2**(9): p. 651-8.
35. Kee, Y., et al., *Distinct domains of syntaxin are required for synaptic vesicle fusion complex formation and dissociation.* Neuron, 1995. **14**(5): p. 991-8.
36. Dulubova, I., et al., *A conformational switch in syntaxin during exocytosis: role of munc18.* Embo J, 1999. **18**(16): p. 4372-82.
37. Schiavo, G., et al., *Botulinum neurotoxin type C cleaves a single Lys-Ala bond within the carboxyl-terminal region of syntaxins.* J Biol Chem, 1995. **270**(18): p. 10566-70.
38. Wick, P.F., et al., *Transient transfection studies of secretion in bovine chromaffin cells and PC12 cells. Generation of kainate-sensitive chromaffin cells.* J Biol Chem, 1993. **268**(15): p. 10983-9.

39. Williamson, L.C., et al., *Clostridial neurotoxins and substrate proteolysis in intact neurons: botulinum neurotoxin C acts on synaptosomal-associated protein of 25 kDa.* J Biol Chem, 1996. **271**(13): p. 7694-9.
40. Gladycheva, S.E., et al., *Receptor-mediated regulation of tomosyn-syntaxin 1A interactions in bovine adrenal chromaffin cells.* J Biol Chem, 2007. **282**(31): p. 22887-99.
41. Chow, R.H., L. von Ruden, and E. Neher, *Delay in vesicle fusion revealed by electrochemical monitoring of single secretory events in adrenal chromaffin cells.* Nature, 1992. **356**(6364): p. 60-3.
42. Zhou, Z., S. Misler, and R.H. Chow, *Rapid fluctuations in transmitter release from single vesicles in bovine adrenal chromaffin cells.* Biophys J, 1996. **70**(3): p. 1543-52.
43. Huang, P., et al., *Insulin-stimulated plasma membrane fusion of Glut4 glucose transporter-containing vesicles is regulated by phospholipase D1.* Mol Biol Cell, 2005. **16**(6): p. 2614-23.
44. Humeau, Y., et al., *A role for phospholipase D1 in neurotransmitter release.* Proc Natl Acad Sci U S A, 2001. **98**(26): p. 15300-5.
45. Hughes, W.E., et al., *Phospholipase D1 regulates secretagogue-stimulated insulin release in pancreatic beta-cells.* J Biol Chem, 2004. **279**(26): p. 27534-41.
46. Vitale, N., et al., *Phospholipase D1: a key factor for the exocytotic machinery in neuroendocrine cells.* Embo J, 2001. **20**(10): p. 2424-34.
47. Kooijman, E.E., et al., *What makes the bioactive lipids phosphatidic acid and lysophosphatidic acid so special?* Biochemistry, 2005. **44**(51): p. 17007-15.
48. Eberhard, D.A., et al., *Evidence that the inositol phospholipids are necessary for exocytosis. Loss of inositol phospholipids and inhibition of secretion in permeabilized cells caused by a bacterial phospholipase C and removal of ATP.* Biochem J, 1990. **268**(1): p. 15-25.
49. Hay, J.C., et al., *ATP-dependent inositide phosphorylation required for Ca(2+)-activated secretion.* Nature, 1995. **374**(6518): p. 173-7.
50. Wiedemann, C., T. Schafer, and M.M. Burger, *Chromaffin granule-associated phosphatidylinositol 4-kinase activity is required for stimulated secretion.* Embo J, 1996. **15**(9): p. 2094-101.
51. Jenkins, G.H., P.L. Fisette, and R.A. Anderson, *Type I phosphatidylinositol 4-phosphate 5-kinase isoforms are specifically stimulated by phosphatidic acid.* J Biol Chem, 1994. **269**(15): p. 11547-54.
52. Liscovitch, M., et al., *Novel function of phosphatidylinositol 4,5-bisphosphate as a cofactor for brain membrane phospholipase D.* J Biol Chem, 1994. **269**(34): p. 21403-6.
53. Coluccio, A., M. Malzone, and A.M. Neiman, *Genetic evidence of a role for membrane lipid composition in the regulation of soluble NEM-sensitive factor receptor function in Saccharomyces cerevisiae.* Genetics, 2004. **166**(1): p. 89-97.
54. Hu, K., et al., *Vesicular restriction of synaptobrevin suggests a role for calcium in membrane fusion.* Nature, 2002. **415**(6872): p. 646-50.
55. Kweon, D.H., C.S. Kim, and Y.K. Shin, *Insertion of the membrane-proximal region of the neuronal SNARE coiled coil into the membrane.* J Biol Chem, 2003. **278**(14): p. 12367-73.
56. Kweon, D.H., C.S. Kim, and Y.K. Shin, *Regulation of neuronal SNARE assembly by the membrane.* Nat Struct Biol, 2003. **10**(6): p. 440-7.
57. Quetglas, S., et al., *Ca2+-dependent regulation of synaptic SNARE complex assembly via a calmodulin- and phospholipid-binding domain of synaptobrevin.* Proc Natl Acad Sci U S A, 2000. **97**(17): p. 9695-700.

Chapter 3

Receptor-Mediated Regulation of Tomosyn-Syntaxin1A Interactions in Bovine Adrenal Chromaffin Cells

Abstract

Tomosyn, a soluble R-SNARE protein identified as a binding partner of the Q-SNARE syntaxin1A, is thought to be critical in setting the level of fusion-competent SNARE complexes for neurosecretion. To date, there has been no direct evaluation of the dynamics in which tomosyn transits through tomosyn-SNARE complexes or of the extent to which tomosyn-SNARE complexes are regulated by secretory demand. Here, we employed biochemical and optical approaches to characterize the dynamic properties of tomosyn-syntaxin1A complexes in live adrenal chromaffin cells. We demonstrate that secretagogue stimulation results in the rapid translocation of tomosyn from the cytosol to plasma membrane regions, and that this translocation is associated with an increase in the tomosyn-syntaxin1A interaction, including increased cycling of tomosyn into tomosyn-SNARE complexes. The secretagogue-induced interaction was strongly reduced by pharmacological inhibition of the Rho-associated coiled-coil forming kinase (ROCK), a result consistent with findings demonstrating secretagogue-induced activation of RhoA. Stimulation of chromaffin cells with LPA, a non-secretory stimulus that strongly activates RhoA, resulted in effects on tomosyn similar to that of application of the secretagogue. In PC-12 cells overexpressing tomosyn, secretagogue stimulation in the presence of LPA resulted in reduced evoked secretory responses, an effect that was eliminated upon inhibition of ROCK. Moreover, this effect required an intact

interaction between tomosyn and syntaxin1A. Thus, modulation of the tomosyn-syntaxin1A interaction in response to secretagogue activation is an important mechanism allowing for dynamic regulation of the secretory response.

Introduction

Regulated neurotransmitter release requires the well-orchestrated spatial and temporal actions of many presynaptic proteins [1]. Although the primary molecular entities in the release pathway have been identified, the exact mechanics of synaptic vesicle fusion and its precise regulation is still not established. Central to the fusion process is the transient formation of SNARE core complexes that include the target membrane SNARE proteins syntaxin1A and SNAP25 and the vesicle SNARE protein synaptobrevin/VAMP [2-4]. A SNARE core complex is a highly stable, four-α-helix parallel bundle consisting of one SNARE motif from each of syntaxin1A and synaptobrevin/VAMP, and two SNARE motifs from SNAP25 [5, 6]. Although these proteins alone are sufficient to induce a slow fusion when reconstituted into liposomes [7], additional proteins are necessary to establish the properties that describe fast, Ca^{2+}-dependent neurotransmitter release [8]. For example, assembly of SNARE core complexes is subject to temporal and spatial regulation by a variety of protein families, including Rab-GTPases [9-13], Sec/Munc18s [14-16], exocyst tethering complexes [17-20], and Munc13s [21-24]. In addition, recent evidence suggests that the temporal and spatial availability of SNAREs for membrane fusion may be subject to precise regulation by the presence of *soluble* R-SNARE motif containing proteins, such as amisyn [25, 26], and tomosyn [27-29].

Tomosyn was originally identified in neurons as a binding partner of the Q-SNARE, syntaxin1A [27], and belongs to a larger family of proteins that includes the yeast proteins Sro7p and Sro77p, the Drosophila tumor suppressor lethal giant larvae family, and the mammalian M*gl*l family [30-33]. Tomosyn homologues also appear in the Fungi and Plantae kingdoms [34]. Structurally, tomosyns are soluble proteins that contain two distinguishable domains. An R-SNARE homology motif near the C-terminus defines tomosyn's primary interaction with the Q-SNARE syntaxin1A, while the remaining N-terminal region contains 7 to 9 repeating β-transducin-like WD40 motifs that form additional protein-protein interaction sites [27, 35, 36]. In the mouse genome, two paralogous genes for tomosyn exist (tomosyn-1 and 2) and lead to the expression of 7 tomosyn isoforms [37]. Variability between these tomosyn isoforms is clustered within a hypervariable domain that separates the N-terminal WD-40 repeats from the C-terminal SNARE domain. Functional actions of tomosyn family members have been ascribed to their interaction with cognate Q-SNAREs; however, as the lethal giant larvae family and Sro7p and Sro77p proteins do not possess a well-defined C-terminal R-SNARE homology domain, interactions between these families and their cognate Q-SNAREs has been proposed to involve alternative interaction motifs [30, 31, 38].

Increasing evidence demonstrates that tomosyn and its homologues are critical regulators in vesicular trafficking and membrane fusion processes. Overexpression of tomosyn in PC-12 and adrenal chromaffin cells negatively regulates neurotransmitter secretion [27, 29], which, in chromaffin cells, results from inhibition in priming of large dense-core vesicles and decreased readily releasable pool (RRP) pool size [28]. Tomosyn has also been shown to exert an important role in polarized exocytosis in yeast and epithelial cells [30, 39], to negatively modulate insulin release from pancreatic β-cells[40], and to interact with syntaxin4 and SNAP23 and inhibit insulin-induced fusion of GLUT4-containing vesicles in 3T3-L1 adipocytes [41]. Recent genetic studies in C. elegans have also clearly established that tom-1, the ortholog of mammalian tomosyn, exerts an inhibitory role on neurotransmitter secretion by negatively regulating synaptic vesicle priming [42, 43]

The inhibitory effects of tomosyn have been proposed to result from the formation of specific tomosyn-protein complexes that reduce the availability of interacting proteins to perform functional roles in exocytosis. For example, tomosyn has been shown to compete with Munc18 for binding to syntaxin, and likely of greater significance, tomosyn competes with synaptobrevin for binding to syntaxin/SNAP25 dimers to form tomosyn-SNARE complexes [27]. The latter complexes, as shown by their resolved crystal structure, are almost identical to the synaptobrevin/VAMP-containing SNARE complexes [34], including a required action by the ATPase NSF for complex disassembly and reuse of the interacting proteins [29]. However, while tomosyns can participate in the formation of stable tomosyn-SNARE complexes, the absence of a membrane anchor in all tomosyn family members precludes them from acting as fusogenic synaptobrevin/VAMP analogues. Rather, formation of these non-fusogenic tomosyn-SNARE complexes diminishes the availability and formation of fusion competent SNARE complexes between membrane-anchored SNAREs, and it is this feature that has been proposed to underlie tomosyn's negative regulation of exocytotic activity.

The interaction of tomosyn with syntaxin1A has recently been reported to be differentially regulated by the Rho/ROCK [44] and protein kinase A signaling pathways [45]. Activation of RhoA and its signaling effector ROCK facilitated syntaxin1A phosphorylation and formation of tomosyn-SNARE complexes at the palms of growth cones in extending neurites in NG108 neuroblastoma cells and cultured neurons [44]. This resulted in the localized inhibition of functional SNARE complex formation in these areas, and spatially directed fusion of plasmalemmal precursor vesicles to the leading edge of growth cones. On the other hand, PKA-catalyzed phosphorylation of tomosyn decreased tomosyn's interaction with syntaxin1A and thereby upregulated SNARE complex formation and enhanced neurotransmitter release in cultured superior cervical ganglion neurons [45]. Thus, while tomosyn is not essential for neurotransmitter release, its complex regulation suggests that it may play a critical role in integrating multiple receptor-mediated signaling pathways to ultimately achieve a fine modulatory control over the site and extent of secretory responses.

To date, there has been no direct evaluation in living cells of the time course or extent to which the assembly/disassembly of tomosyn-SNARE complexes is regulated by secretory demand for neurotransmitter release. Furthermore, although a Rho signaling pathway has been demonstrated to alter tomosyn-SNARE interactions during neurite development, it remains unknown whether this signaling pathway operates to direct tomosyn-SNARE complex assembly during regulated neurotransmitter release. In this paper, we evaluated the spatiotemporal dynamics and regulation of the tomosyn-syntaxin1A interaction during stimulated secretion in neuroendocrine chromaffin cells. We show that activation of nicotinic acetylcholine receptors (nAChR), as occurs normally during neural-evoked secretory responses, as well as treatment with lysophosphatidic acid (LPA), activates Rho-GTPase and increases tomosyn-syntaxin1A complex formation at the plasma membrane in chromaffin cells. These effects of secretagogue stimulation and LPA treatment were inhibited by Y27632, a specific inhibitor of the Rho-GTP effector ROCK. We also show using dynamic FRET measurements between CFP-tomosyn and cYFP-syntaxin1A that the formation of these complexes is strongly augmented under conditions where NSF action is inhibited, suggesting that a rapid and dynamic cycling of tomosyn-syntaxin1A interactions occurs in vivo. Finally, we present functional data to demonstrate that LPA activation of the RhoA/ROCK pathway during evoked secretion enhances tomosyn-mediated inhibition of secretion.

Materials and Methods

Chemicals and expression constructs

pEGFP-C1, and monomeric mutants (A206K) of pECFP-C1 and pEcYFP-C1 (citrine) vectors containing the LoxP sequence were used as recipient vectors for subcloning using the Cre-recombinase-mediated Creator system (Clontech). Rat syntaxin1A, m-tomosyn, SNAP25 and Munc18-1 were merged to the C terminus of the EGFP, ECFP and EcYFP. Effector binding mutants of syntaxin1A (I209A and I233A), a soluble mutant of SNAP25 (SNAP25c/a, C-80, 88, 90, 92-A), as well as a carboxy terminal deletion of tomosyn$_{1\text{-}1067}$ (tomosyn ΔCT, glutamate at residue 1068 changed to stop codon) were constructed using the PCR-based Quickchange site-directed mutagenesis kit (Stratagene). The sequence fidelity of all constructs was confirmed by DNA sequencing (University of Michigan DNA Sequencing Core). RhoA activation was measured using an ELISA-based kit (Cytoskeleton). HEK293 cells stably expressing the rat α_{1B} and human β_{2B} and $\alpha_2\delta$ voltage gated calcium channel subunits (HEK293-S3 cells) were a gift from D. Rock (Warner-Lambert Parke Davis, Ann Arbor, MI). All other chemicals were obtained from Sigma, unless specifically indicated otherwise.

Cell culture and transfection

HEK293-S3 cells were plated and cultured in RPMI 1640 with L-glutamine supplemented with 10% fetal bovine serum, 1% penicillin/streptomycin (Life Technologies, Inc.), 0.4 mg/ml of hygromycin and 0.6 mg/ml of geneticin at 37^oC in 95% O_2/5% CO_2 for 2 days on coverslips (thickness 1) attached to the bottom of 35 mm culture dishes before transfection. Transfections were performed using Lipofectamine 2000 (Invitrogen) according to manufacturer instructions. One hour before transfection, cells were placed into DMEM lacking antibiotics and supplemented with 1% L-glutamine, 1% non-essential amino acids and 10% fetal bovine serum. 4-6 hours after the transfection, cells were returned to the RPMI 1640 medium. Cells were used for imaging 24-48 hours after transfection.

Chromaffin cells were isolated from bovine adrenal glands using divalent metal ion-free rinse, collagenase digestion and gradient centrifugation as described previously [46]. Cells were cultured in 6-well plates in DMEM/F12 supplemented with 10% fetal bovine serum, 100 units/ml penicillin/streptomycin, 10 µg/ml gentamicin, and 10 µM cytosine arabinofurosemide. Three days following isolation, cells were transfected using biolistic particle bombardment according to manufacturer instructions with plasmid DNA laden (2µg/mg beads) 1 µm diameter gold beads (Bio-Rad). Cells were replated 4 to 24 hours before imaging onto collagen coated glass coverslips.

PC-12 cells were cultured in 10% CO_2, in DMEM supplemented with 10% horse serum, 5% fetal bovine serum, penicillin (100 units/ml), streptomycin (100 µg/ml), and 1% gentamicin (10 µg/ml). PC-12 cells were transfected using Lipofectamine 2000 (Invitrogen) according to manufacturer's protocol. 30 minutes before transfection, cells were placed in Optimem media; cells were returned to the DMEM media 4-6 hours following transfection.

Tomosyn translocation assay

Cells were serum starved in DMEM/F-12 medium for 4 hours prior to treatment with selected receptor agonists or signaling antagonists. Following the serum starve period, medium was changed to physiological saline (PSS) containing (mM): NaCl, 140, KCl, 5, $CaCl_2$, 2.2, $MgCl_2$, 1, glucose, 10 and HEPES, 10 (pH 7.4 adjusted with NaOH). Treatments included incubation with lysophosphatidic acid (LPA, 10 µM, Biomol) or the nicotinic acetylcholine receptor agonist 1,1-dimethyl-4-phenylpiperazinium iodide (DMPP, 20 µM), alone or in combination with the Rho kinase inhibitor, (Y27632, 20 µM, Calbiochem). In Rho kinase inhibitor experiments, the Y27632 was applied during the serum deficient preincubation period and to the PSS during agonist treatment. Each treatment was followed by an additional incubation (10 min) with the NSF alkylating agent N-ethylmaleimide (NEM, 100 μM) prior to cell lysis. Cells were then scraped into the ice-cold lysis buffer containing 2% sucrose, 1 mM EDTA, 20 mM Tris-HCl (pH 7.4) and 100 μM NEM, with a mixture of protease inhibitors (1 μg/μL each of PMSF, leupeptin, pepstatin, aprotinin and benzamidine). The collected lysis buffer was then subjected to Dounce homogenization (20 strokes) followed by centrifugation (800g, 2 min, 4^{o}C) to remove nuclei. A membrane fraction was then extracted by ultra-centrifugation of the samples at 100,000g, for 30 min at 4^{o}C, with the pellets resuspended in immunoprecipitation (IP) buffer containing (mM): NaCl, 150, Tris (pH 7.4), 50, and EDTA, 2 supplemented with 1% Triton and the above-mentioned protease inhibitor mixture. Immunoprecipitation using a monoclonal α-tomosyn antibody (Transduction Laboratories) was then performed on all samples that had been initially adjusted to contain equal starting amounts of protein and volume. Immunoprecipitation was carried out by overnight incubation with the antibody at 4^{o}C with rotation, after which Immunopure protein G beads (Pierce) were added and the incubation continued another 90 min. The beads were then pelleted by centrifugation (1,000g for 2 min at 4^{o}C) and washed in TNM buffer containing (mM): NaCl, 50, $MgCl_2$, 50, Tris-HCl (pH 7.5), 50. Tomosyn immunoreactivity in the resulting samples was determined by SDS-PAGE fractionation and immunoblotting. Blots were probed with monoclonal α-tomosyn antibody and subsequently with HRP-conjugated goat α-mouse antibody (Developmental Studies Hybridoma Bank, Iowa City, IA). Immunoreactive signals were developed by ECL detection (Amersham), visualized using a FluoroMax Imager (Bio-Rad, Hercules, CA, USA) and quantified from digital images using Quantity One software (Bio-Rad).

Rho activation assay

Cells in 6-well plates (1.5 x 10^6 cells/well) were serum starved in DMEM/F-12 medium for 12 hours prior to use. Following the serum starve period, medium was changed to physiological saline (PSS) that contained lysophosphatidic acid (LPA, 10 µM, Biomol), nicotinic acetylcholine receptor agonist 1,1-dimethyl-4-phenylpiperazinium iodide (DMPP, 20 µM), or, for control, PSS alone. Following either a 2 or 10 min period of receptor activation the medium was rapidly removed and the cells were rinsed once in ice cold PBS. Lysis buffer was then rapidly added and the cells scraped and lysates collected and immediately frozen in liquid N_2. The relative level of RhoA activation with respect to control conditions was then measured using an ELISA based assay according to the manufacturer's instructions (Cytoskeleton). Each sample was assayed in duplicate and each condition was repeated on at least three individual cell preparations. The level of Rho activation was calculated with respect to that of the control condition following subtraction of the assay blank.

Human Growth Hormone Secretion Assay

PC-12 cells were plated onto 24 well plates and co-transfected with plasmids coding for human growth hormone (hGH), in addition to full-length tomosyn, tomosynΔCT, or a neomycin control. The total concentration of DNA was held equal across all treatments. hGH was used as a reporter for regulated secretion specifically from transfected cells[47]. Secretion assays were performed 48-72 hours following transfection. 16-20 hours before the start of the assay, cells were placed in serum-free media; where applicable, cells were pre-treated with Y27632 (20 µM) 4 hours prior to the start of the assay. To test secretion, cells were rinsed for 10 minutes in a physiological saline solution (in mM: NaCl, 145, KCl, 5.6, NaHEPES, 15, $MgCl_2$, 0.5, $CaCl_2$, 2.2, Glucose, 5.6, NaAscorbate, 0.5, 2mg/mL fatty acid-free BSA, pH 7.3) in the presence or absence of Y27632. Cells were then stimulated to secrete by a 6 minute treatment with 70mM K^+ (same saline solution but with equimolar substitution of K^+ for Na^+). Where applicable, 10μM LPA and/or (20 μM) Y27632 were added to the stimulus solution. The saline solution containing the secreted hGH was collected, and cells were lysed to determine the percent of total hGH content secreted. hGH content was measured using an hGH ELISA kit (Roche Diagnostics). Each experiment was performed with quadruplicate replicates for each treatment.

GST-Syntaxin1A-tomosyn binding in vitro and immunoblotting

Soluble syntaxin1A (residues 1-264) was expressed in E. coli as a glutathione-S-transferase (GST)-fusion protein. GST was expressed in a similar manner. Both proteins were purified by glutathione-Sepharose (Sigma) binding and extensive washing. The bound GST or GST-syntaxin1A were then incubated for 16 hours at 4°C with lysates prepared from PC-12 cells expressing EGFP-tomosyn or EGFP-tomosyn ΔCT. The lysis buffer contained (100 mM KCl, 20 mM HEPES-KOH, 2 mM EDTA, 1% Triton-X100, 1 mM DTT) with protease inhibitor cocktail (Roche, PI Complete). The beads were then collected by centrifugation and washed 4 times with PBS and bound proteins were analyzed by SDS-PAGE and immunoblotting with anti-GFP antibody (Stressgen).

Fluorescence photobleaching in subcellular localization of EGFP-tagged proteins

Chromaffin cells were plated onto collagen-coated glass-bottom 35 mm culture dishes and cultured for 24 hours prior to use and imaged in PSS. Localization of expressed EGFP-tagged soluble proteins to plasma membrane regions was determined following a spatially directed laser-induced (488 nm line of the argon laser) photobleach of EGFP fluorescence in a rectangular region of the cytosol of live cells using a Zeiss LSM 510 confocal microscope. A targeting factor (TF) for distribution of EGFP-tagged proteins to the plasma membrane region was determined from images of the cell taken pre- and post-application of the photobleach. Initially, averaged fluorescence intensities of the whole cell (I_{tot}) and its cytosolic (I_{Cyt}) and membrane (I_{Mem}) regions in pre- and post-bleach images where measured along with the corresponding total (A_{cyt}), membrane (A_{mem}) and cytosolic (A_{cyt}) areas. The value of membrane targeting of a protein was defined as fraction of membrane-bound EGFP-tagged protein in total fluorescence of the cell before the photobleach. For each photobleached cell, relative membrane fluorescence parameter $M=(I_{post}/I_{pre})^{tot}{}_{Mem}$ was determined. Assuming that total intensity in a membrane region consists of contributions from that of membrane-bound and near-membrane cytosol fluorescence ($I^{mem}{}_{tot} = I_{TrueMem} + I_{Cyt} \cdot A_{mem}$), and that $I_{TrueMem}$ does not change with photobleach, the targeting factor value was calculated as $TF = I_{TrueMem}/(I_{tot})_{pre,}$ where $I_{TrueMem} = [(I_{pre})_{cyt} \cdot M-(I_{post})_{cyt}] \cdot A_{mem}/(1-M)$.

Confocal and conventional fluorescence microscopy of ECFP and EcYFP tagged proteins and imaging of FRET

Chromaffin cells were cultured for 36 hours after transfection, then plated and cultured for 4 to 24 hours on collagen-coated glass coverslips prior to fluorescence imaging. For fluorescence imaging of fixed cells, the cells were fixed in 4% paraformaldehyde in physiological saline solution (PSS) for 20 min, rinsed with PSS, and quenched with 50 mM NH_4Cl-PSS for 12 min. After rinsing with PSS, cells were submerged in 75% glycerol-PSS and subjected to fluorescence imaging on a Zeiss LSM 510 META confocal microscope. Imaging and morphological analysis of subcellular localization of expressed fluorophore-tagged proteins was primarily performed on the Zeiss confocal microscope. Imaging of FRET was carried out using acceptor photobleach (i.e. donor dequenching) methodology on the Zeiss confocal microscope and by detection and analysis of sensitized EcYFP emission on a conventional Olympus fluorescence microscope. FRET imaging with the Zeiss LSM 510 META relied on pixel-by pixel linear unmixing calculations (Meta software) performed prior and following photobleach of the acceptor. This software utilizes control emission spectra of the fluoroproteins to completely decompose or digitally separate the contribution from the ECFP and EcYFP tagged signals in the mixed emission spectrum recorded from cotransfected cells. Relative FRET efficiency by acceptor photobleach was calculated as (1-[ECFP $I_{\text{pre-bleach}}$/ ECFP $I_{\text{post-bleach}}$]) X 100%. Sensitized emission FRET was detected using a Olympus microscope coupled to a Till-Photonics Polychrome IV xenon lamp based monochrometer (Till-Photonics, Grafelfing, Germany), a polychroic mirror that allowed detection of multiple fluorophores (436-500 nm, Chroma Technology Corp. Brattleboro, VT), a Planapo 60X water immersion objective (1.2 NA), a multispec microimager (Optical Insights, Sante Fe, NM) containing a dichroic splitter (505dcxr) and emission filters (D465/30 and HQ535/30) and a cooled digital CCD camera (TILL-IMAGO QE). Images corresponding to three excitation/emission wavelength settings (ex/em, 436/465, 436/535, and 500/535) were collected. Quantification of sensitized emission FRET efficiency from shade and background corrected images was determined according to a method termed FRET stoichiometry [48]. Analysis of the acquired cell images determined three parameters for each pixel of an image. The first parameter is the apparent FRET efficiency EA, which is the product of the FRET efficiency of the specific bimolecular interaction, termed characteristic FRET efficiency (E_C), and the fraction of acceptor in complex with the donor. The second parameter is ED, which is the apparent donor efficiency and is the product of Ec and the fraction of donor in complex. The third parameter is the acceptor-donor molar ratio (Ratio). Ratio indicates the mole fraction of acceptor to donor in each pixel of the cell image. Because EA and ED are proportional to the fraction of acceptor and donor in complex, respectively, they can be used to measure time- or agonist-dependent changes in the fraction of acceptor and donor in complex. Full details concerning controls performed for validation of FRET signals, acquisition parameters of background and shade images, methods used for determination of proportionality constants required for complete separation of ECFP and EcYFP and FRET signals and of the specific calculations performed to quantify FRET efficiency values are given in our recent report [49].

Data analysis and statistics – Data were analyzed and statistical analysis performed using IGOR PRO (Wavemetrics Inc) and GraphPad Instat (GraphPad Software Inc. San Diego, CA, USA) software. Population data were expressed as means ± S.E.M., and statistical significance was determined using Student's unpaired t tests, or for multiple comparisons using ANOVA with Dunnett's post hoc test on normally distributed data. In the case of non-parametric data, a Mann-Whitney U test was performed using the original calculated values. Significant differences were defined by $p \leq 0.05$ and indicated by an asterisk.

Results

Expression and targeting of fluorescently-tagged tomosyn, syntaxin1A and Munc18-1 in HEK-293 cells

HEK-293 cells were initially used to demonstrate expression and targeting of the recombinant fluoroprotein-tagged tomosyn, syntaxin1A and Munc18-1 proteins and to test for specific interactions between these proteins in an in vivo situation. The HEK-293 cell line does not demonstrate endogenous expression of these proteins [50] and, therefore, provides a clean background upon which to test interactions. Figure 3.1A shows confocal fluorescence images that compare the subcellular distribution of cYFP-tomosyn, cYFP-syntaxin1A, and CFP-Munc18-1 when individually expressed. While both the cYFP-tomosyn and CFP-Munc18-1 showed a diffuse distribution in the cytosol typical of soluble proteins, syntaxin1A was observed to accumulate primarily in perinuclear membrane regions, and in some cells in a number of highly localized sites in the cytosol characterized by intense fluorescence. By comparison, coexpression of cYFP-syntaxin1A with CFP-Munc18-1 resulted in efficient targeting of cYFP-syntaxin1A to the plasma membrane region (Figure 3.1B), and cells were remarkably devoid of perinuclear fluorescence. The coexpression of CFP-tomosyn with cYFP-syntaxin1A did not result in a similar dramatic targeting consequence, as strong perinuclear cYFP-syntaxin1A labeling was retained with little enrichment of fluorescence at the plasma membrane. Thus, tomosyn and Munc18-1 are functionally distinct with regard to their ability to facilitate syntaxin1A targeting to the plasma membrane in HEK-293 cells.

We next determined whether overexpressed CFP-tomosyn directly interacted with syntaxin1A in this cell line. For this purpose we used fluorescence resonance energy transfer (FRET) between the CFP/cYFP pair to visualize and quantify direct CFP-tomosyn/cYFP-syntaxin1A interactions. FRET measurements were performed by acceptor photobleach on fixed cells using a LSM Zeiss 510 META confocal microscope, which was optimal for acquiring images in a single optical plane coincident with FRET and analysis of its subcellular compartmentation. Figure 3.2A compares images acquired prior to and following a localized photobleach of the cYFP acceptor from a representative HEK-293 cell. A marked increase in CFP fluorescence occurred following photobleach that was restricted to the bleached perinuclear membrane region, a result indicative of FRET between CFP-tomosyn and cYFP-syntaxin1A. The increased CFP signal following photobleach was readily apparent on comparison of spectrally pseudocolored images of this cell region prior and following photobleach (shown below cell images). Averaged relative FRET efficiency values for photobleached and non-photobleached cell regions are presented in Figure 3.2C and clearly establish that a

CFP-tomosyn/cYFP-syntaxin1A interaction occurred in HEK-293 cells. Thus, the compartmentalization of CFP-tomosyn observed in the presence of syntaxin1A coexpression is reflective of a colocalization of these proteins that results from a direct protein-protein interaction. As we have previously reported, analysis of non-photobleached regions of CFP-expressing cells also demonstrates a slight increase in CFP signal of approximately 9% following the laser photobleach protocol, which we define as background [49]. The cause of this small and consistent change remains undetermined, and has not been subtracted from the relatively large FRET values determined for photobleached regions of the cells.

As Munc18-1 and tomosyn both interact with syntaxin1A, we next determined whether overexpression of Munc18-1 altered the interaction between syntaxin1A and tomosyn. As shown in Figure 3.2B, coexpression of tomosyn, syntaxin1A and Munc18-1 resulted in targeting of syntaxin1A to plasma membrane regions, indicative of Munc18-1 facilitation of syntaxin1A targeting. Of specific importance, with these coexpression conditions, CFP-tomosyn retained significant FRET with cYFP-syntaxin1A, although it was now present spatially at plasma membrane regions (Figure 3.2B), versus the perinuclear/ER and Golgi localization that was observed in the absence of Munc18-1 coexpression. In addition, the averaged relative FRET efficiency was reduced slightly but significantly from that measured in the absence of Munc18-1 coexpression (Figure 3.2C). These results are complementary to prior reports for the HEK-293 cell line in establishing that Munc18-1 is important for the distribution of overexpressed syntaxin1A to the plasma membrane region [50-52]. The present FRET results demonstrate that, while tomosyn is capable of interacting with syntaxin1A in multiple subcellular compartments, it is likely to preferentially associate with syntaxin1A at the plasma membrane in neurons where munc18-1, syntaxin1A and tomosyn are endogenously expressed.

In additional experiments we tested whether the tomosyn/syntaxin1A heterodimeric complex at the plasma membrane in HEK-293 cells was capable of progression to a SNARE core complex by the incorporation of a cognate t-SNARE, SNAP25. For these experiments we used a SNAP25 mutant that contained EGFP fused to the N-terminus of a SNAP25 mutant in which the four normally palmitoylated cysteine residues that direct SNAP25 membrane targeting were mutated to alanine (EGFP-S25 c/a). We have previously demonstrated that this SNAP25 mutant becomes membrane localized only if it is capable of pairing its SNARE motifs with that of syntaxin1A [50], or presumably, a syntaxin1A/tomosyn complex. The subcellular distribution of EGFP-S25 c/a was determined by calculating a targeting factor (TF) that compares EGFP fluorescence at the plasma membrane region relative to that in the cytosol from confocal images taken prior to and following a laser-induced photobleach (488 nm line of Argon laser) of the cytosolic fluorescence using the Zeiss LSM confocal microscope. Figure 3.2D shows that EGFP-S25 c/a expressed alone in HEK-293 cells show little labeling of the plasma membrane, but that its coexpression with syntaxin1A resulted in a substantial increase in targeting. Under these coexpression conditions, targeting of syntaxin1A to the plasma membrane occurred in the absence of Munc18-1. Notably, the syntaxin1A induced increase in EGFP-S25 c/a targeting was completely inhibited with the added expression of Munc18-1, likely as a result of stabilizing syntaxin1A in an inactive SNARE complex forming conformation. Coexpression of EGFP-S25 c/a with syntaxin1A and tomosyn also resulted in significant targeting of EGFP-S25 c/a to the plasma membrane and this targeting was unaffected by the additional expression of Munc18-1. These data, taken together with the prior FRET results (Figure 3.2C), indicate that tomosyn competes with Munc18-1 for binding to plasma membrane localized syntaxin1A in vivo and permits formation of SNARE complexes.

Location and properties of tomosyn interaction with syntaxin1A in adrenal chromaffin cells

To establish the components that normally regulate tomosyn/syntaxin1A interactions and to relate changes in their interaction to functional consequences within the exocytotic pathway, the properties of the interaction were further investigated in bovine adrenal chromaffin cells, where these proteins are endogenously present and demonstrated to be functionally important [26, 28]. In these cells, exogenously expressed CFP-tomosyn and cYFP-syntaxin1A localized to the plasma membrane region without exogenous coexpression of Munc18-1 (Figure 3.3A). To establish that the colocalized CFP-tomosyn and cYFP-syntaxin1A at the plasma membrane region was indicative of a direct bimolecular interaction, we examined the properties of colocalization using both acceptor photobleach and sensitized emission FRET approaches. Sensitized emission FRET was performed on live chromaffin cells using a conventional fluorescence microscope, and was beneficial for examining FRET under low protein overexpression conditions. Both FRET approaches demonstrated that CFP-tomosyn bound directly to cYFP-syntaxin1A at the cell periphery (Figure 3.3A and 3.3D). Relative FRET efficiency at the plasma membrane region by acceptor photobleach averaged 42.9 ± 3.6% (n= 5), which was > 5 fold over that of background, as calculated from the non-photobleached region of the same cells (Figure 3.3B). The averaged apparent FRET efficiency (EA, ED) values determined by sensitized emission (14 ± 2.9%) were lower than those calculated by acceptor photobleach FRET. The values differ as a result of the specific analysis schemes applied, particularly as the expression levels of the fusion protein constructs which define the degree of FRET interaction were not accounted for in the analysis of acceptor photobleach FRET. Indeed, a plot of molar ratio (cYFP/CFP) against corresponding apparent efficiency of donor in complex ED for each imaged pixel of a single cell as determined by sensitized emission illustrates the sensitivity of FRET efficiency to the relative expression of acceptor and donor proteins (Figure 3.3E). Therefore, all subsequent comparisons between FRET values by sensitized emission have included only those FRET values where the molar ratio fell within 0.9 to 1.1 Ratio range.

Requirement of SNARE/SNARE interaction for CFP-tomosyn/cYFP-syntaxin1A FRET

The R-SNARE homology domain near the C-terminus of tomosyn is believed to be primarily responsible for tomosyn's interaction with the Q-SNARE motif of syntaxin1A. Therefore, to define the extent to which the in vivo interaction of tomosyn with syntaxin1A is dependent upon formation of an R-SNARE/Q-SNARE complex, we measured, using FRET, the effect of specific Q-SNARE mutations of syntaxin1A on the interaction. Two site-directed mutants of cYFP-syntaxin1A were tested: cYFP-syntaxin1A (I209A) and cYFP-syntaxin1A (I233A). The I209A mutation occurs within the SNARE motif of syntaxin1A, and it has been shown to strongly reduce syntaxin1A's binding to its cognate t-SNARE, SNAP25 [53]. By comparison, the I233A mutation lies within the N-terminal domain of the SNARE motif that normally occupies the central cavity of Munc18 during syntaxin1A interaction with Munc18. Correspondingly, the syntaxin1A (I233A) mutant has been shown to reduce syntaxin1A/Munc18 binding *in vitro* without reduction in syntaxin1A/SNAP25 binding [54]. As shown in Figure 3.3B and Figure 3.3F, expression of cYFP-syntaxin1A (I209A) with CFP-tomosyn resulted in a significant reduction in FRET (by approximately 50%) with respect to control. These results are consistent with the R-SNARE/Q-SNARE interaction being critically important to the tomosyn/syntaxin1A interaction. The retention of measurable binding may be representative of the lowered affinity of interaction with the mutant syntaxin1A or may result from interacting sites beyond the SNARE motifs that may also be important for the tomosyn/syntaxin1A interaction in vivo. By comparison, FRET between CFP-tomosyn and cYFP-syntaxin1A (I233A) measured by sensitized emission was similar to that of control (Figure 3.3F). Evaluation of the syntaxin1A (I233A)/tomosyn interaction was limited to sensitized emission as a result of low levels of exogenous expression of the cYFP-syntaxin1A (I233A) protein. A central interaction of tomosyn with syntaxin1A is, therefore, similar to that of SNAP25 with syntaxin1A, which is mediated by SNARE/SNARE motif interactions.

Tomosyn and Munc18-1 have also been reported to interact with structurally distinct conformations of syntaxin1A. In addition, these differences in binding interactions are proposed to reflect the important functional differences these proteins exert on the exocytotic pathway. To determine if tomosyn and Munc18-1 compete for syntaxin1A within chromaffin cells, we analyzed the effect of Munc18-1 coexpression on CFP-tomosyn/cYFP-syntaxin1A FRET. The results showed that Munc18-1 overexpression reduced CFP-tomosyn binding to cYFP-syntaxin1A, as evidenced by an approximately 40% reduction in apparent FRET efficiency (Figure 3.3B and 3.3F). In complementary experiments, overexpression of tomosyn was found to reduce the apparent FRET efficiency between coexpressed CFP-Munc18-1 and cYFP-syntaxin1A (Figure 3.3C and 3.3G), as would be expected for a competitive binding reaction.

Tomosyn association with a membrane fraction is enhanced by a secretory stimulus and activation of Rho-GTPase

Interaction of syntaxin1A with Munc18-1 is essential for regulated exocytosis, while its interaction with tomosyn is believed to negatively impact exocytotic activity through the formation of fusion incompetent SNARE core complexes. Therefore, a key question is whether the level of tomosyn-SNARE complexes is subject to dynamic regulation as would be required to fine-tune secretory responses. As an initial test for dynamic regulation, we determined if stimulation of chromaffin cells for secretion by activation of ACh receptors with DMPP induced changes in the association of *endogenous* tomosyn with the plasma membrane. Figure 3.4 shows that the amount of membrane-localized tomosyn significantly increased upon treatment of the chromaffin cells with DMPP (30 min, 10 μM), a stimulus that normally evokes a strong secretory response. In these experiments, tomosyn was immunoprecipitated from a membrane fraction prepared from control or DMPP-treated chromaffin cells. In each case, cells were subjected to N-ethylmaleimede (NEM, 100 μM, 10 min) treatment prior to lysis to inhibit NSF-mediated disassembly of formed tomosyn-SNARE complexes (100 μM NEM was also included in the lysis buffer). Immunoprecipitation was required in these experiments as the level of tomosyn associated with the membrane fraction under control and secretagogue stimulation conditions represented a small fraction of total tomosyn within the chromaffin cell lysate.

We next sought to establish the signaling mechanism that mediates the increase in tomosyn association with the membrane in response to a secretory stimulus in chromaffin cells. Previous studies have established that activation of Rho-GTPase/ROCK signaling pathways can enhance formation of tomosyn-SNARE complexes in cultured embryonic neurons. Therefore, we investigated whether DMPP stimulation of chromaffin cells may act via the Rho-GTPase signaling pathway to alter tomosyn association with the plasma membrane. As an initial experiment, we determined whether lysophosphatidic acid (LPA), a well-known receptor-mediated activator of Rho-GTPase signaling pathways in many cell types, induced measurable Rho activation (Rho-GTP) in chromaffin cells. As shown in Figure 3.4B, LPA treatment (10 μM) resulted in a rapid increase (< 2min) in activated Rho, and remained elevated throughout a sustained stimulus (10 min). In corresponding experiments, LPA treatment also was found to elicit a translocation of tomosyn to the membrane fraction with respect to control chromaffin cells (Figure 3.4A). Additional experiments determined that DMPP-stimulation (20 µM) also activated Rho-GTPase, although the level of activation was substantially less than that observed to LPA stimulation (Figure 3.4B). Of particular importance, preincubation of the cells with Y27632 (4 hours, 20 µM), a specific Rho-kinase (ROCK) inhibitor, completely eliminated both the DMPP and LPA mediated increase in tomosyn within the membrane fraction (Figure 3.4A). These data suggest that enhancement of tomosyn association with the membrane in response to DMPP stimulation of chromaffin cells occurred via activation of the Rho-GTPase/ROCK signaling pathway.

Photobleaching of Freely Diffusible EGFP Fluorescence Reports DMPP- and LPA-Induced Targeting of EGFP-Tomosyn to Cell Periphery in Live Chromaffin Cells

The previous studies established that DMPP and LPA treatment of adrenal chromaffin cells promoted tomosyn association with a membrane particulate fraction prepared by ultracentrifugation of cell lysates. Our expectation was that in response to these stimulation conditions, tomosyn translocated and localized to the plasma membrane prior to cell lysis through direct interactions with syntaxin1A. However, cell lysis disrupts subcellular integrity, thereby precluding direct assignment of tomosyn in a particulate fraction to have been specifically associated with the plasma membrane. In addition, syntaxin1A may form protein complexes following cell lysis, which compromises interpretations on physiological relevance of immunoprecipitated tomosyn/syntaxin1A complexes. To overcome these problems, a fluorescence photobleach approach was used to visualize and quantify the subcellular distribution of overexpressed EGFP-tomosyn in confocal images of living chromaffin cells that were exposed to DMPP or LPA stimulation. As a soluble protein, the contribution of cytosolic EGFP-tomosyn to the fluorescent image of the cell was selectively removed by application of brief laser photobleaching within a discrete area in the cell's cytoplasm.

The remaining EGFP fluorescence reflected EGFP-tomosyn that was diffusionally restricted, presumably through its specific interaction with proteins or lipids associated with membrane delimited organelles or the plasma membrane. As shown in the images of Figure 3.5A, and the averaged TF data (Figure 3.5B), this approach was able to detect EGFP-tomosyn that was specifically localized to the plasma membrane region in response to a series of specific treatments. The results showed that expression of EGFP-tomosyn alone demonstrated little specific EGFP fluorescence at the membrane region while, by comparison, a strong EGFP-tomosyn signal was observed at the plasma membrane region when it was coexpressed with exogenous syntaxin1A. The difference in plasma membrane localized fluorescence to these conditions indicated that it is EGFP-tomosyn's interaction with syntaxin1A that brings EGFP-tomosyn to the plasma membrane. Most importantly, the results demonstrated that application of DMPP or LPA led to a significant increase in EGFP-tomosyn membrane targeting over control. Furthermore, the LPA-induced increase was inhibited by preincubation of the cells the Rho kinase inhibitor, Y27632 (Figure 3.5B).

Kinetics of receptor-mediated change in tomosyn-syntaxin1A interaction and involvement of Rho/ROCK signaling pathways

Our next goal was to use the developed sensitized emission FRET assay between CFP-tomosyn and cYFP-syntaxin1A together with time-lapse fluorescent imaging to define the kinetics of the receptor-mediated targeting of tomosyn to the plasma membrane and to establish that this targeting resulted in a direct interaction of tomosyn with syntaxin1A. For these FRET experiments we optimized our ability to detect changes in the fraction of cYFP-syntaxin1A in complex with CFP-tomosyn (proportional to ΔEA) by transfection with a DNA ratio of cYFP-syntaxin1A to CFP-tomosyn that resulted in a low cYFP/CFP molar ratio of protein expression (cYFP/CFP ratio ~ 0.3). As shown in Figure 3.6A, application of 20μM LPA to the CFP-tomosyn/cYFP-syntaxin1A expressing chromaffin cells resulted in a rapid *step*-increase from the baseline FRET EA value that was sustained throughout the application period. Subsequent addition of NEM, while continuing LPA treatment, resulted in a marked further time-dependent increase in EA from baseline. As shown in Figure 3.6B, preincubation of chromaffin cells for 4 hours with the Rho kinase inhibitor Y27632 (10 μM) eliminated the effect of LPA to increase an interaction between CFP-syntaxin1A-cYFP-tomosyn. This was evidenced by no significant change in the EA values from baseline over the time frame of the recordings. These data are consistent with LPA-mediated activation of Rho-ROCK pathway in chromaffin cells promoting a steady-state increase in tomosyn-syntaxin1A SNARE complexes. In additional experiments, FRET measurements were also used to examine the effect of DMPP stimulation on the kinetics of direct interaction of CFP-tomosyn/cYFP-syntaxin1A in transfected chromaffin cells. As shown in Figure 3.6C, DMPP stimulation resulted in an increased interaction between these proteins similar to that observed with LPA stimulation, and the interaction was further increased upon application of NEM. Preincubation with the Rho kinase inhibitor abolished the DMPP-induced increase in FRET (Figure 3.6D). The substantial increase in FRET from baseline by addition of NEM occurred only in LPA or DMPP stimulated cells (Figure 3.6E), thereby indicating that it likely resulted from an inhibition of NSF-mediated disassembly of tomosyn-SNARE complexes and that LPA and DMPP strongly enhance cycling of tomosyn-SNARE complexes.

Stimulus-induced secretion is modulated by Rho-mediated regulation of tomosyn.

In a final series of experiments we investigated whether there was a functional link between Rho/ROCK signaling pathways and tomosyn on regulation of evoked secretion. For these experiments we compared the effects of tomosyn with that of a tomosyn mutant that lacks the R-SNARE motif (tomosyn ΔCT) on secretion from PC-12 cells. Our rationale was that if Rho/ROCK pathways augment tomosyn's inhibitory action on secretion by promoting a direct tomosyn-syntaxin interaction, then these effects should be mitigated by a tomosyn mutant (tomosyn ΔCT) which lacks the syntaxin1A interacting SNARE motif. The lack of a direct high-affinity interaction between the tomosyn ΔCT construct and syntaxin1A was confirmed using GST-syntaxin1A pull-down experiments (Figure 3.7A). By comparison, considerable interaction was observed between GST-syntaxin1A and wild-type tomosyn. For the secretion experiments we used PC-12 cells cotransfected with the regulated secretory pathway reporter human growth hormone (hGH) to report on effects of the exogenously expressed tomosyn constructs on regulated secretion only from transfected cells. As shown in Figure 3.7B, transfection with tomosyn or tomosyn ΔCT inhibited elevated K^+-induced secretion by approximately 25% with respect to control transfected (neo plasmid) PC-12 cells. Moreover, LPA, applied at the onset of the elevated K^+ stimulus, increased the extent of secretory inhibition in tomosyn, but not tomosyn ΔCT expressing cells, with respect to control cells. Importantly, the effect of LPA to increase secretory inhibition in tomosyn transfected cells was reversed by preincubation of the cells with the Rho kinase inhibitor (Y27632). Preincubation with the Rho kinase inhibitor had no effect on the secretory inhibition mediated by tomosyn ΔCT. The differences to LPA treatment on secretion between tomosyn and tomosyn ΔCT were unlikely to have resulted from differences in relative levels of expression of these constructs, as no significant difference in levels of expression of CFP-tagged variants of the constructs was observed from measurements of CFP intensity (Figure 3.7C and D). Taken together, these data demonstrate that LPA exposure augments tomosyn inhibition of stimulus-induced secretion from PC-12 cells, and that this likely occurs as a result of tomosyn interaction with syntaxin1A. That is, the ability of LPA to augment inhibition of secretion was absent in the tomosyn ΔCT mutant expressing cells.

Discussion

Recent studies suggest that tomosyn exerts regulatory control over specific presynaptic pathways including neurite extension and neurotransmitter release [27, 29, 44]. Furthermore, the activity of tomosyn in these pathways has been reported to be fine-tuned by the phosphorylation state of tomosyn, as well as that of its immediate effectors (e.g., syntaxin1A) [44, 45]. We hypothesized that physiological regulation of these key tomosyn-protein interactions during neurosecretion might occur rapidly in response to receptor-mediated signals of secretory demand. In this study, we examined the spatiotemporal dynamics of tomosyn's interaction with the t-SNARE syntaxin1A, both in the non-secretory HEK293 cell line, as well as in neurosecretory bovine adrenal chromaffin cells. Our findings establish that the tomosyn-syntaxin interaction is upregulated in response to secretory demand, and that under these conditions, there is a substantial increase in the rate of tomosyn-SNARE complex cycling (i.e., formation and dissolution). Moreover, modulation of the tomosyn-syntaxin1A interaction by secretagogue stimulation provides for dynamic regulation of the secretory response.

Our characterization of the tomosyn-syntaxin1A interaction in HEK293 cells illustrates an important difference between Munc18-1-syntaxin1A and tomosyn-syntaxin1A heterodimer complexes. In HEK293 cells, targeting of syntaxin1A to plasma membrane regions is dramatically facilitated by co-expression and direct interaction with Munc18-1 [50-52]. Although facilitating, the Munc18-1-syntaxin1A interaction is not, however, essential for syntaxin1A targeting, as has been identified in several recent studies [55-57]. Indeed, SNAP25, as well as other syntaxin1A interacting proteins, may enhance syntaxin1A membrane localization [50]. Here, we have extended those findings to show that, unlike the Munc18-1-syntaxin1A interaction, syntaxin1A's interaction with tomosyn does not promote the targeting of either syntaxin1A or tomosyn to plasma membrane regions. Rather, coexpression of tomosyn and syntaxin1A results in localization of these proteins to perinuclear compartments, whereas coexpression of these proteins with Munc18-1 results in the targeting of syntaxin1A and tomosyn to the plasma membrane region. We propose a model whereby an initial interaction of Munc18-1 with syntaxin1A facilitates syntaxin1A targeting to the plasma membrane; once syntaxin1A localizes to the plasma membrane, tomosyn can effectively compete with Munc18-1 to interact with syntaxin1A. Indeed, our FRET data indicate that the tomosyn-syntaxin1A interaction is reduced on overexpression of Munc18-1, and likewise, that the Munc18-1-syntaxin1A interaction is reduced on overexpression of tomosyn. The competition between Munc18-1 and tomosyn for binding to syntaxin1A at the plasma membrane may comprise a critical site of regulation over the location and extent of regulated exocytosis.

While there is substantial evidence for the effects of tomosyn on regulating neurotransmitter release, to date, there has been no direct evaluation in live cells of the dynamics or extent to which tomosyn transits through tomosyn-SNARE complexes or of the extent to which tomosyn-SNARE complexes are regulated by secretory demand. Here, we demonstrate that treatment of adrenal chromaffin cells with DMPP (a secretory stimulus that activates nAChR's) resulted in the rapid translocation of EGFP-tomosyn from the cytosol to the plasma membrane, as shown in our photobleach experiments. Moreover, the translocation of tomosyn to the plasma membrane in response to DMPP was associated with an increase in the bimolecular interaction between tomosyn and syntaxin at the plasma membrane, as established by time-lapse imaging experiments of FRET between CFP-tomosyn and cYFP-syntaxin1A. The FRET signal was a relevant reporter of tomosyn-syntaxin1A interactions in vivo, as control experiments demonstrated predictable changes in FRET efficiency with site directed mutations within syntaxin1A's SNARE motif. Interestingly, the DMPP-induced interaction between tomosyn and syntaxin1A was markedly increased by addition of the NSF inhibitor, NEM. Tomosyn-syntaxin1A interactions were not, however, increased by treatment with NEM in non-receptor activated chromaffin cells. As tomosyn-SNARE (i.e., tomosyn-syntaxin1A-SNAP25) complexes, but not the heterodimeric tomosyn-syntaxin1A complexes, are sensitive to NSF inhibition by NEM [29], these data demonstrate that secretagogue receptor activation results in a rapid and substantial increase in the cycling of tomosyn-containing ternary SNARE complexes. In addition, using membrane localization of soluble EGFP-SNAP25 c/a as a reporter of a syntaxin1A-SNAP25 interaction we show that tomosyn can compete with Munc18-1 to promote the formation of EGFP-SNAP25 c/a containing SNARE complexes.

Importantly, we determined that secretagogue-induced interaction between tomosyn and syntaxin1A occurs downstream of the Rho-GTPase/ROCK signaling pathway. First, we demonstrated that DMPP stimulation results in activation of the Rho signaling pathway in chromaffin cells. Second, treatment of chromaffin cells with LPA, a non-secretory stimulus that also activates the Rho pathway, was sufficient to recapitulate the effects of DMPP both on translocation of tomosyn to the plasma membrane region, as well as on the increased interaction between tomosyn and syntaxin1A. Notably, while DMPP stimulation induced only a modest increase in RhoA activation relative to that induced by LPA, it resulted in a substantially larger change in CFP-tomosyn/cYFP-syntaxin1A FRET. Both the DMPP and LPA induced increases in FRET were mitigated by Y27632. The differences in tomosyn/syntaxin1A association likely result from the diversity in the extent and type of signaling pathways activated by these different stimuli, and suggest that additional signaling pathways may be activated by DMPP that facilitate the RhoA/ROCK pathway. Taken together the data are consistent with a model whereby the level of tomosyn-syntaxin1A interaction rapidly responds to activation of receptors mechanistically linked to RhoA and is likely mediated by signaling via RhoA/ROCK phosphorylation of syntaxin1A. While certain of the experiments necessitated the overexpression of a fluorophore-tagged tomosyn, the effects seen in these overexpression studies were corroborated in a non-overexpression system, by biochemical assays establishing that endogenous tomosyn also translocated to membrane fractions in response to both DMPP and LPA and that this translocation was similarly blocked by Y27632.

While a Rho signaling pathway was previously demonstrated to alter tomosyn-SNARE interactions during neurite development in NG108 cells and cultured hippocampal neurons [44], it was unknown whether the Rho signaling pathway also modulated tomosyn-SNARE complex assembly during regulated neurotransmitter release. Members of the Rho GTPase family are primary regulators of actin cytoskeleton organization, although they regulate a wide range of cellular processes including exocytosis [58-60]. A potential role for GTPases in regulated exocytosis in chromaffin cells was initially suggested from in vitro observations indicating their presence on purified chromaffin granule membranes [61-63]. Several distinct GTPases were found, including heterotrimeric Go protein, ARF6, Rab3 and, importantly, RhoA. Most of the RhoA in chromaffin cells is associated with secretory granules, and selective activation of the trimeric G-protein Go on chromaffin granules was found to inhibit priming steps of exocytosis [64, 65]. This inhibition was significantly reduced in cells treated with Clostridium botulinum C3 exoenzyme, which selectively inactivates the small G-protein Rho [66, 67]. Activation of Go thus induces RhoA activation, which acts through an effector pathway to decrease vesicle priming. While phosphatidylinositol 4-kinase has been proposed as a RhoA effector, no direct link of it to vesicle priming has been demonstrated, and other mediators such as ROCK have not been tested. Our data indicate that tomosyn must be considered as a target for agonist activation of the

Rho/ROCK signaling pathway in chromaffin cells, and that this pathway may contribute to the previously reported effect of RhoA-GTP to inhibit vesicle priming.

A central and important question that remains is whether the increased cycling of tomosyn-SNARE complexes exerts a positive or negative role on the maintenance of exocytotic secretion. Our present results indicate that the increase in tomosyn-SNARE cycling in response to receptor activation functions as a negative feedback system that ultimately limits the extent or sites of secretion. Moreover, comparison of the wild-type and ΔCT tomosyn suggests that the Rho-mediated augmentation of tomosyn's inhibitory effects on secretion is mediated primarily via the tomosyn-syntaxin1A interaction. It should be noted that overexpression of the tomosyn ΔCT mutant resulted in secretory inhibition only slightly less than that of full-length tomosyn. As tomosyn ΔCT does not bind syntaxin, these data suggest that the tomosyn SNARE motif, while not critical for tomosyn's inhibitory effect, might be involved in activity-dependent regulation of the inhibition imposed by tomosyn. Interactions of tomosyn's R-SNARE with syntaxin1A could designate spatial information, while the N-terminal WD40 domains, or the hypervariable linker region in tomosyn could carry out the actual inhibitory function on exocytotic activity. Interestingly, a prior report [26] demonstrated that overexpression of a tomosyn mutant with reduced syntaxin1A interaction, still resulted in secretory inhibition.

The participation of the N-terminal motifs and the hypervariable domain in tomosyn must be considered along with the R-SNARE motif as a regulator of tomosyn's protein interactions or as a scaffold for additional protein interactions important for tomosyn's inhibitory function. Tomosyn's N-terminus contains 7 to 9 repeating β-transducin-like WD-40 motifs that comprise approximately 90% of the protein sequence and represent the region of highest conservation among tomosyn homologues. Moreover, tomosyn also contains a hypervariable region that separates the N-terminal

WD-40 repeats and the C-terminal SNARE domain. Serine phosphorylation by protein kinase A within this region has recently been reported to exert negative regulatory action on tomosyn-syntaxin1A interaction [45]. In addition, tomosyn homologues such as the lethal giant larvae family and yeast Sro7p and Sro77p and the mammalian Lgl1 (Mlgl), which do not possess well defined SNARE motifs [34], still interact with SNARE proteins. Importantly, deletion of the yeast proteins Sro7p and Sro77p results in a strong cold-sensitive block in exocytosis [30].

In summary, these present studies are among the first to illustrate, in real-time and in live cells, a physiological and dynamic modulation of tomosyn's localization and interaction with syntaxin1A in response to secretagogue activation. Moreover, they demonstrate the functional relevance of this modulation in enhancing tomosyn's inhibitory effect on secretion. Thus, the functions of proteins that regulate the secretory exocytotic pathway may themselves be regulated by secretory demand. Further work remains to elucidate the structural roles of tomosyn's N-terminal and hypervariable linker domains in mediating tomosyn's inhibitory effects on neurosecretion.

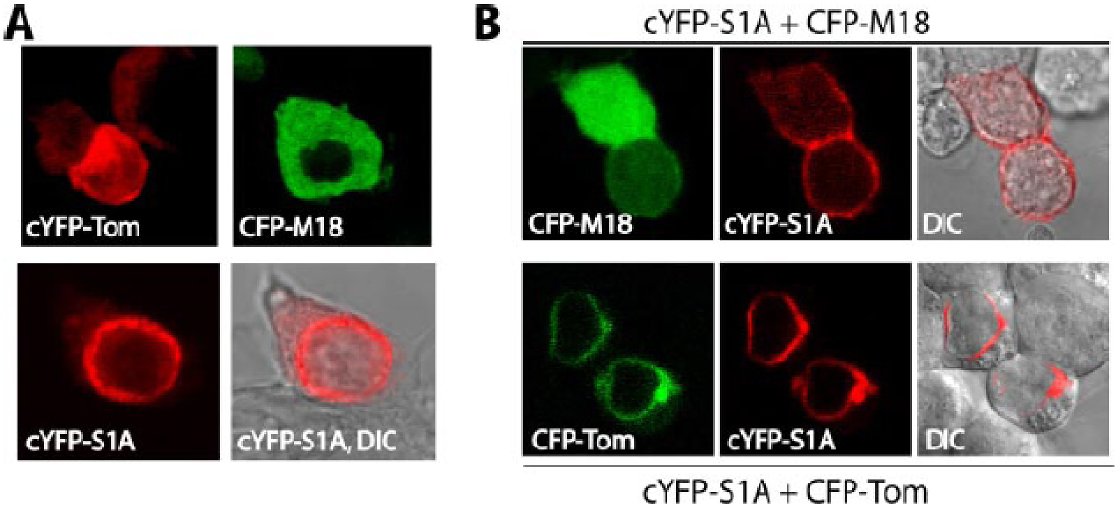

Figure 3.1. Expression of fluoroprotein-tagged syntaxin1A, Munc18-1 and m-tomosyn in HEK293 cells and selective action of Munc18-1 to facilitate syntaxin1A targeting the plasma membrane. A, representative confocal fluorescence images of cells transfected with cYFP-tomosyn,CFP-Munc18-1 or cYFP-syntaxin1A. Lower right panel shows cYFP-syntaxin1A fluorescent signal and differential interference contrast (DIC) image overlay, which demonstrates localization of the majority of the fluorescent signal to a perinuclear region. B, confocal fluorescence images of representative cells transfected with cYFP-syntaxin1A, along with CFP-Munc18 (upper image set) or CFP-tomosyn (lower image set). Right column of each image set shows overlay of cYFP-syntaxin1A and DIC.

Figure 3.2. Interaction and surface distribution of cYFP-syntaxin1A and CFP-tomosyn as defined by acceptor photobleach FRET in fixed HEK293 cells. Representative sets of unmixed CFP and cYFP confocal fluorescent images taken from cells cotransfected with CFP-tomosyn and cYFP-syntaxin1A (A) or CFP-tomosyn, cYFP-syntaxin1A and Munc18-1 (B). Left and right image columns show images taken before and following, respectively, photobleach (at 514 nm argon laser line) of the region above the line. Increased post-bleach CFP intensity in photobleached region indicates FRET between CFP-tomosyn and cYFP-syntaxin1A. A spectrally pseudocolored representation of CFP intensity (blue to red, low to high intensity) in the photobleached region is shown below the image sets for pre and post-bleach conditions. In absence of Munc18 coexpression the bulk of fluorescent signal is restricted to perinuclear region and localized intensities of fluorescence in cytosol. C, averaged FRET efficiency in bleached (black bars) and unbleached (grey bars) regions in cells cotransfected with CFP-tomosyn and cYFP-syntaxin1A or CFP-tomosyn, cYFP-syntaxin1A and Munc18-1. D, comparison of EGFP-SNAP25 C/A targeting factors in cells (co)transfected with the conditions indicated. Targeting factor (see methods) describes the relative proportion of EGFP-SNAP25 at plasma membrane region with respect to total EGFP-fluorescence of cell. Representative cell images for each condition pre- and post-photobleach are shown below graph. Arrow on left-most image set indicates cell subjected to photobleach. Number of observations for the averaged data in this and all subsequent plots is indicated above bars. Asterisks indicate significant difference ($p<0.05$) from the control condition in each plot of averaged data.

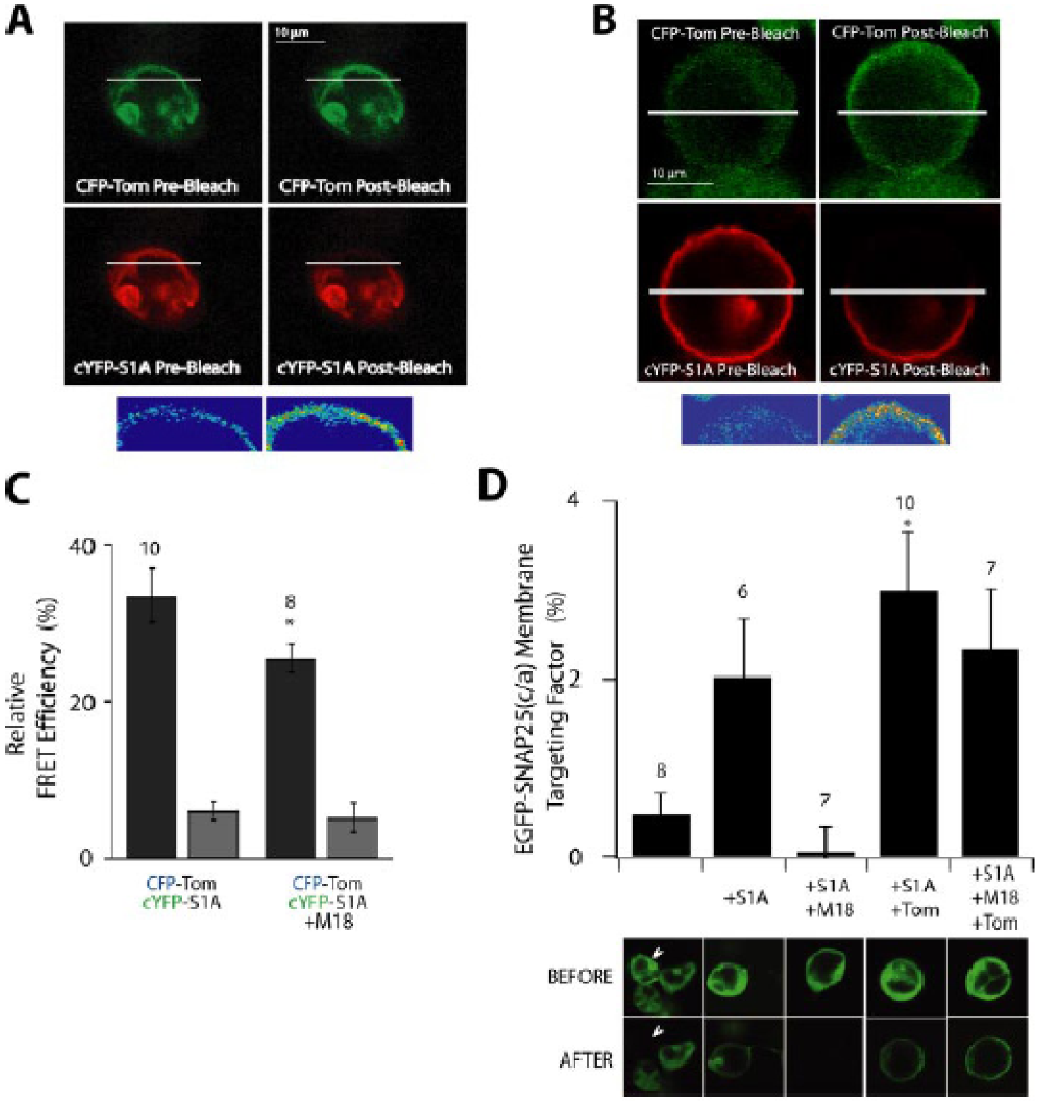
A
10 µm
CFP-Tom Pre-Bleach
CFP-Tom Post-Bleach
cYFP-S1A Pre-Bleach
cYFP-S1A Post-Bleach
B
CFP-Tom Pre-Bleach
CFP-Tom Post-Bleach
10 µm
cYFP-S1A Pre-Bleach
cYFP-S1A Post-Bleach
C
Relative FRET Efficiency (%)
40
20
0
10
8
*
CFP-Tom
cYFP-S1A
CFP-Tom
cYFP-S1A
+M18
D
EGFP-SNAP25(C/A) Membrane Targeting Factor (%)
4
2
0
8
6
7
10
*
7
+S1A
+S1A
+M18
+S1A
+Tom
+S1A
+M18
+Tom
BEFORE
AFTER

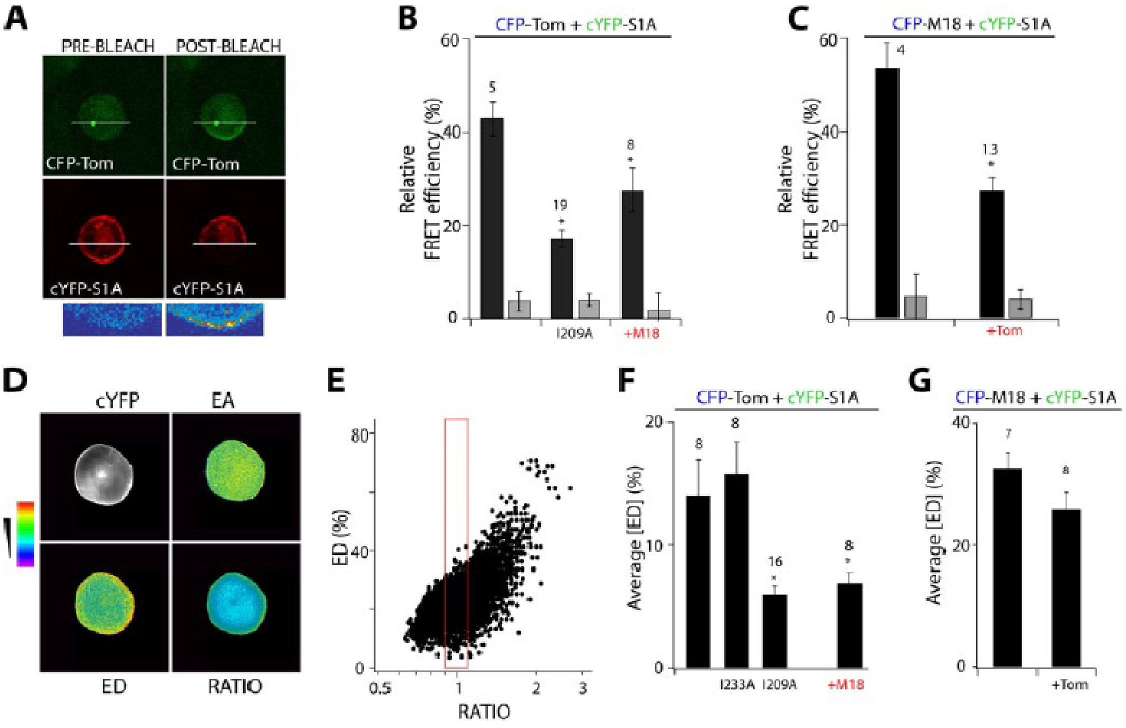

Figure 3.3. Interaction of CFP-tomosyn to cYFP-syntaxin1A in bovine chromaffin cells is sensitive to mutations in syntaxin1A SNARE motif and subject to competitive inhibition by Munc18-1. A, representative set of unmixed CFP-tomosyn and cYFP-syntaxin1A confocal images of fixed chromaffin cells taken before and following photobleach of cYFP-fluorescence below the plotted line. Increased post-bleach CFP intensity in photobleached region indicates FRET between CFP-tomosyn and cYFP-syntaxin1A. B, averaged FRET efficiency measured by acceptor (cYFP) photobleach in bleached (black bars) and unbleached (grey bars) regions of cells transfected with CFP-tomosyn together with cYFP-syntaxin1A, cYFP-syntaxin1A (I209A) or cYFP-syntaxin1A + Munc18-1. C, averaged FRET efficiency between CFP-Munc18-1 and cYFP-syntaxin1A in the absence or presence of coexpressed tomosyn. FRET efficiency was determined using acceptor photobleach method. D, representative image set comparing cYFP-syntaxin1A distribution (cYFP-S1A), apparent FRET efficiency (EA,ED), and molar ratio as detected by sensitized cYFP emission in living chromaffin cells. Transfection condition, CFP-tomosyn + cYFP-syntaxin1A. E, plot of apparent FRET efficiency (ED) determined by sensitized emission for all pixels of an imaged cell cotransfected with CFP-tomosyn and cYFP-syntaxin1A against its corresponding RATIO values. The box outlined (red) indicates the RATIO interval 0.9 to 1.1 over which ED values were averaged for each treatment condition. F, averaged ED for cells transfected with CFP-Tomosyn and with coexpression of cYFP-syntaxin1A (wt), cYFP-syntaxin1A (I233A), cYFP-syntaxin1A (I209A), cYFP-syntaxin1A + Munc18-1. G, Averaged ED determined by sensitized emission FRET approach for the cells cotransfected with cYFP-syntaxin1A and CFP-Munc18 in the absence or presence of coexpressed tomosyn.

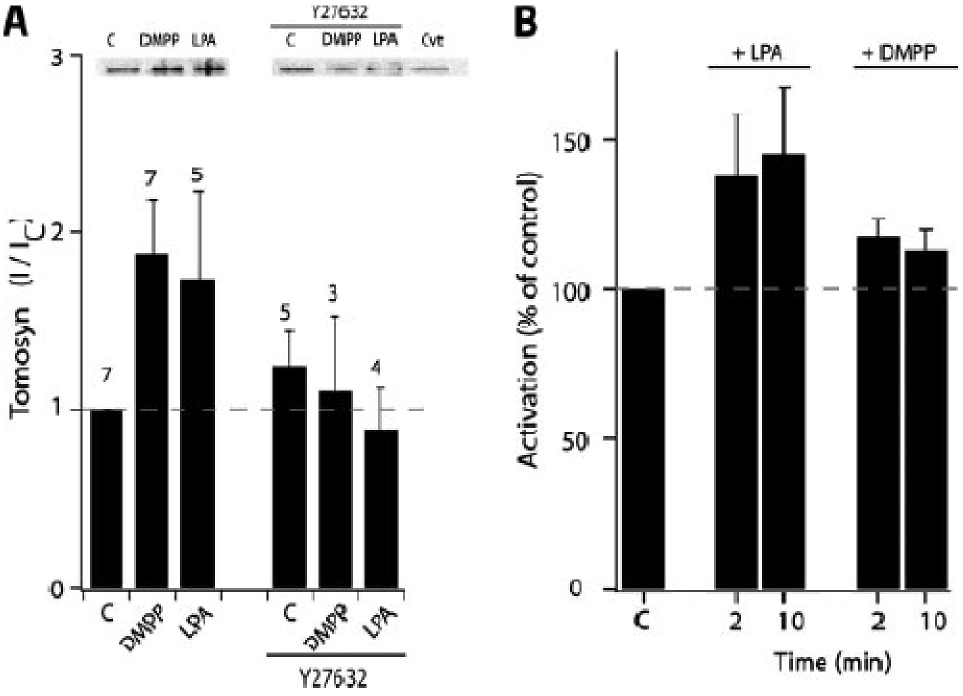

Figure 3.4. Agonist activation of nAChR and application of LPA induce translocation of endogenous tomosyn to a membrane fraction in chromaffin cells and activate endogenous RhoA. A, averaged level of endogenous tomosyn immunoreactivity in a membrane fraction of cultured chromaffin cells incubated with DMPP or LPA relative to that in control (C, non-stimulated) conditions. Translocation induced by receptor agonists was specifically blocked by co-incubation with the Rho kinase inhibitor. Serum starved chromaffin cells were treated with DMPP (30 min, 20 µm) or LPA (10 min, 10 µm) with subsequent NEM treatment (10 min, 100 µm). The Rho kinase inhibitor (Y27632, 20 µm) when included, was added to the serum starving medium 4 hours prior to stimulation and maintained throughout stimulation. Following treatment, cells were lysed, membrane fractions were extracted by ultra-centrifugation and tomosyn immunoprecipitated. Samples were then analyzed by SDS-PAGE and immunoblotting. Number of individual determinations comprising average shown above bars. Panel above plot shows representative immunoblot. B, level of activated RhoA (RhoA-GTP) in chromaffin cells treated with LPA (10 µM, 2 min or 10 min) or DMPP (20 µM, 2 min or 10 min) relative to control (C, non-stimulated, 10 min) conditions. Data shown is the average of 4 (DMPP) or 3 (LPA) separate experiments with each sample measured in duplicate.

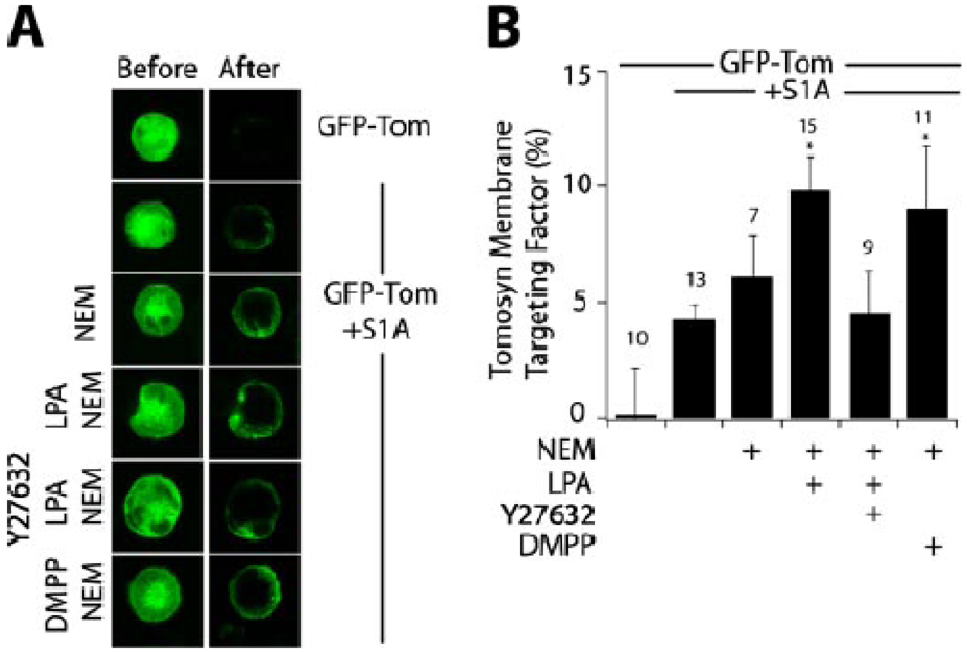

Figure 3.5. Monitoring targeting of EGFP-tomosyn to cell periphery in live chromaffin cells by photobleach of diffusible EGFP fluorescence. A, confocal images of EGFP fluorescence in serum starved chromaffin cells transfected with EGFP-tomosyn or cotransfected with EGFP-tomosyn and syntaxin1A. Images were taken before (left column) and after (right column) photobleach (using 488 nm line of Argon laser) of a square region in the cytosol with area of about a third of the total area of the cell's image. Treatments include stimulation with DMPP (30 min, 20 µm) or LPA (10 min, 10 µm), each followed by NEM treatment (10 min, 100 µm) as indicated. For Rho kinase inhibitor experiments, cells were preincubated for 4 hours with 20 µm Y27632, which was maintained throughout the stimulation period. The ring of EGFP fluorescence in the post-bleach images indicates the presence of the membrane-bound tomosyn. B, averaged membrane targeting factors of EGFP-tomosyn (see Methods section) for photobleached cells for the indicated experimental treatments.

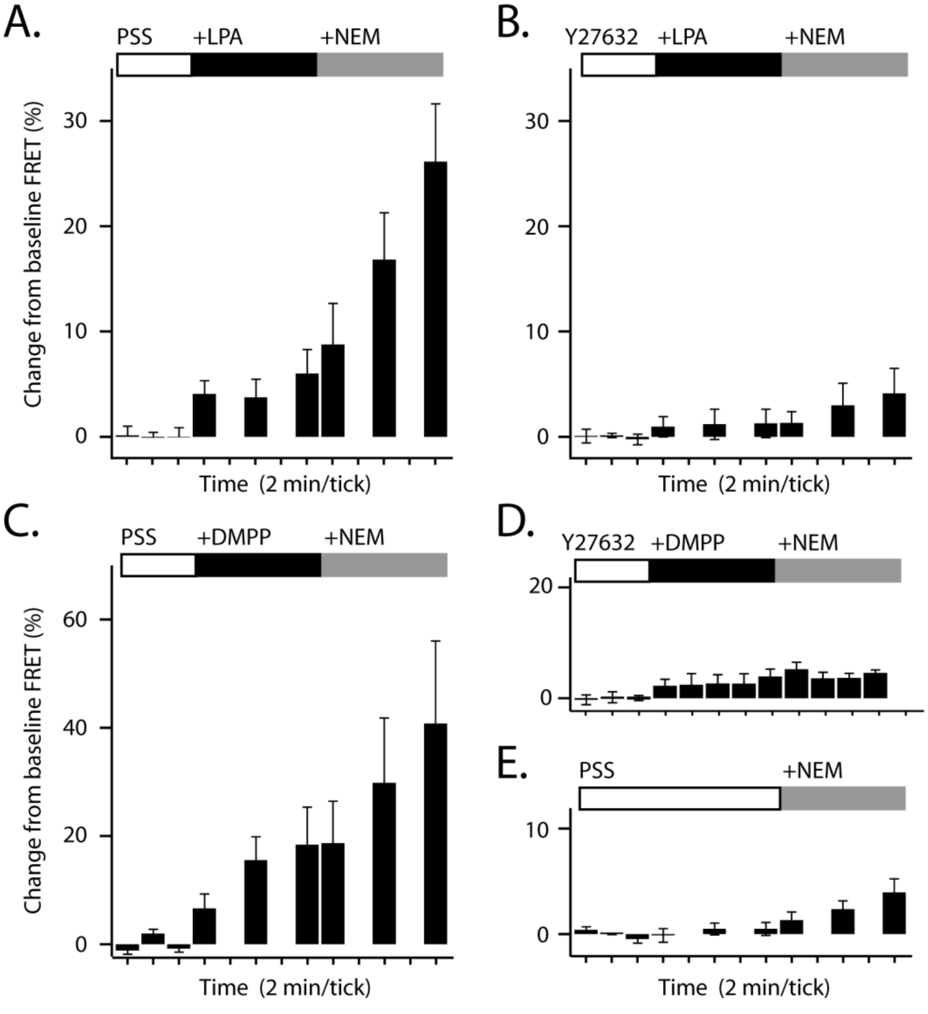

Figure 3.6. Time-lapse imaging of receptor-mediated changes in tomosyn-syntaxin1A interactions using dynamic FRET measurements in living chromaffin cells. Chromaffin cells were transfected with CFP-tomosyn and cYFP-syntaxin1A and imaged for FRET using the sensitized emission method. Images were analyzed offline using FRET stoichiometry calculations to determine EA (apparent efficiency of acceptor in complex) [48]. A, changes in the apparent FRET efficiency parameter EA in response to application of LPA, followed by LPA +NEM relative to the control period are plotted as a function of time. B, time-dependent changes in EA for cells preincubated with the Rho kinase inhibitor (Y27632, 10 µM) for 4 hours prior to exposure to LPA and then LPA + NEM for the intervals indicated above the plot. C, time-dependent effect of DMPP followed by DMPP + NEM on EA relative to the control period. D, preincubation with Y27632 (10 µM, 4 hrs) strongly inhibits DMPP-induced changes in FRET (EA). E, effect of NEM treatment alone on EA. For all treatments: Time-dependent changes in EA were determined relative to the averaged EA values for the initial 6 min period in PSS (or PSS+Y27632); LPA was 10 uM, DMPP 20 µM, NEM 100 µM and Y27632 20 µM. Data for each time point represent the average of measurements on A, 14; B, 4; C, 4; D, 3; E, 4 cells ± SEM.

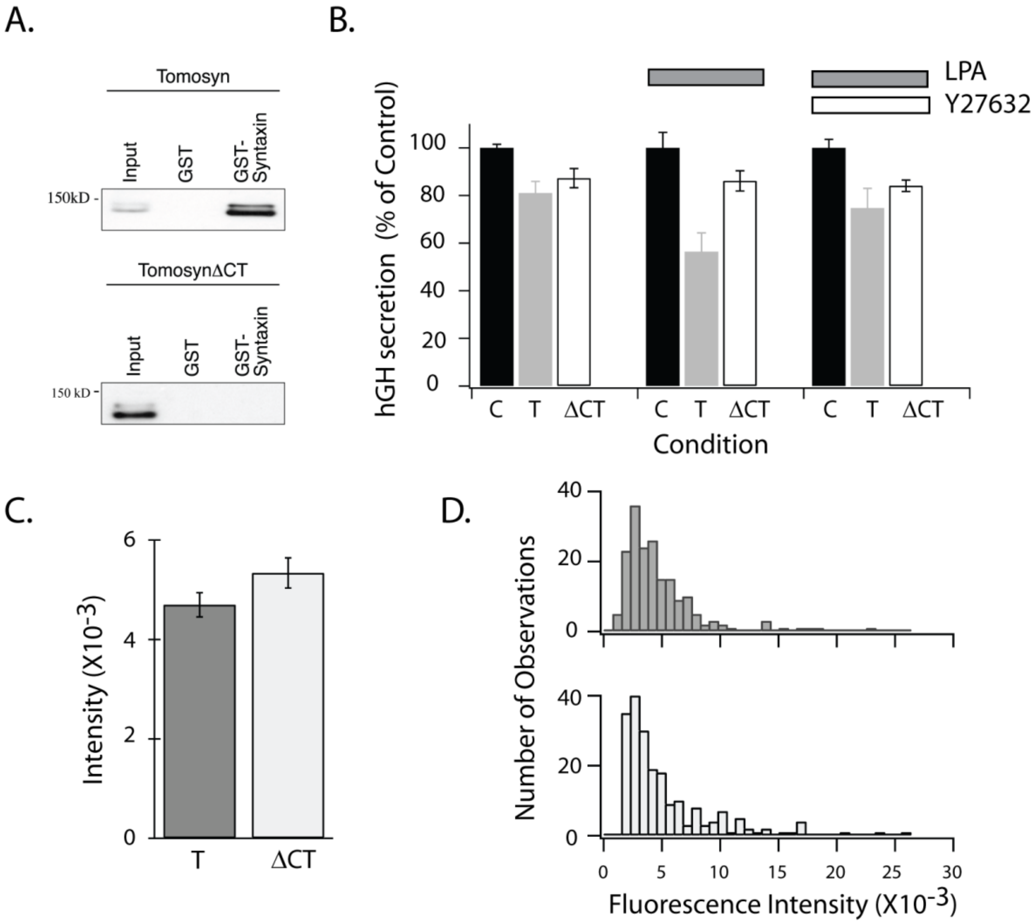

Figure 3.7. Effect of tomosyn translocation induced by LPA treatment on evoked hGH secretion from PC-12 cells. A, GST-syntaxin pull down assay of EGFP-fused tomosyn (upper panel) or EGFP-tomosyn ΔCT (lower panel). Lysates from PC-12 cells expressing EGFP-tomosyn or EGFP-tomosyn ΔCT were bound to GST or GST-syntaxin1A containing beads. Bound proteins were analyzed by SDS-PAGE and immunoblotted with anti-EGFP antibody. B, PC-12 cells were transfected with control empty plasmid (C, encodes only neomycin resistance), tomosyn (T), or a tomosyn construct (ΔCT) in which the SNARE motif at the C-terminus was deleted. Following two days expression, secretion was induced by application of elevated K^+ saline alone (left set of bars), with co-application of LPA (10 uM, middle set of bars) or in cells preincubated with Y27632 (4 hrs) prior to co-application of elevated K^+ saline and LPA. In each case the stimulus period lasted 10 min after which the media was collected for analysis of secreted hGH and cell lysates were prepared for determination of total cell hGH content. For each experiment hGH secretion was calculated as a percent of the total cell content using quadruplicate samples and then normalized to the control condition of each treatment. C, Averaged ECFP fluorescent intensity in tomosyn and tomosyn ΔCT transfected PC-12 cells (± SEM, N=184 and 207 cells for tomosyn and tomosyn ΔCT respectively). Cells were imaged 48 hours post-transfection and images of at least 50 random fields of cells were taken for each condition. D, Frequency distribution of spatially averaged ECFP intensity values for tomosyn (upper) and tomosyn ΔCT transfected cells.

References

1. Jahn, R., T. Lang, and T.C. Sudhof, *Membrane fusion.* Cell, 2003. **112**(4): p. 519-33.
2. Jahn, R. and T.C. Sudhof, *Membrane fusion and exocytosis.* Annual Review of Biochemistry, 1999. **68**: p. 863-911.
3. Sudhof, T.C., *The synaptic vesicle cycle.* Annu Rev Neurosci, 2004. **27**: p. 509-47.
4. Lin, R.C. and R.H. Scheller, *Mechanisms of synaptic vesicle exocytosis.* Annu Rev Cell Dev Biol, 2000. **16**: p. 19-49.
5. Sollner, T., et al., *A protein assembly-disassembly pathway in vitro that may correspond to sequential steps of synaptic vesicle docking, activation, and fusion.* Cell, 1993. **75**(3): p. 409-18.
6. Sollner, T.H. and J.E. Rothman, *Molecular machinery mediating vesicle budding, docking and fusion.* Cell Struct Funct, 1996. **21**(5): p. 407-12.
7. Weber, T., et al., *SNAREpins: minimal machinery for membrane fusion.* Cell, 1998. **92**(6): p. 759-72.
8. Tucker, W.C., T. Weber, and E.R. Chapman, *Reconstitution of Ca2+-regulated membrane fusion by synaptotagmin and SNAREs.* Science, 2004. **304**(5669): p. 435-8.
9. Geppert, M. and T.C. Sudhof, *RAB3 and synaptotagmin: the yin and yang of synaptic membrane fusion.* Annu Rev Neurosci, 1998. **21**: p. 75-95.
10. Takai, Y., et al., *Rab3A small GTP-binding protein in Ca(2+)-dependent exocytosis.* Genes Cells, 1996. **1**(7): p. 615-32.
11. Fischer von Mollard, G., et al., *Rab proteins in regulated exocytosis.* Trends Biochem Sci, 1994. **19**(4): p. 164-8.
12. Elferink, L.A. and R.H. Scheller, *Synaptic vesicle proteins and regulated exocytosis.* Prog Brain Res, 1995. **105**: p. 79-85.
13. Sollner, T.H., *Regulated exocytosis and SNARE function (Review).* Mol Membr Biol, 2003. **20**(3): p. 209-20.
14. Rizo, J. and T.C. Sudhof, *Snares and Munc18 in synaptic vesicle fusion.* Nat Rev Neurosci, 2002. **3**(8): p. 641-53.
15. Toonen, R.F., *Role of Munc18-1 in synaptic vesicle and large dense-core vesicle secretion.* Biochem Soc Trans, 2003. **31**(Pt 4): p. 848-50.
16. Weimer, R.M. and J.E. Richmond, *Synaptic vesicle docking: a putative role for the Munc18/Sec1 protein family.* Curr Top Dev Biol, 2005. **65**: p. 83-113.
17. Kee, Y., et al., *Subunit structure of the mammalian exocyst complex.* Proc Natl Acad Sci U S A, 1997. **94**(26): p. 14438-43.
18. Hsu, S.C., et al., *The exocyst complex in polarized exocytosis.* Int Rev Cytol, 2004. **233**: p. 243-65.
19. EauClaire, S. and W. Guo, *Conservation and specialization. The role of the exocyst in neuronal exocytosis.* Neuron, 2003. **37**(3): p. 369-70.
20. Lipschutz, J.H. and K.E. Mostov, *Exocytosis: the many masters of the exocyst.* Curr Biol, 2002. **12**(6): p. R212-4.
21. Silinsky, E.M. and T.J. Searl, *Phorbol esters and neurotransmitter release: more than just protein kinase C?* Br J Pharmacol, 2003. **138**(7): p. 1191-201.
22. Martin, T.F., *Prime movers of synaptic vesicle exocytosis.* Neuron, 2002. **34**(1): p. 9-12.
23. Betz, A., et al., *Functional interaction of the active zone proteins Munc13-1 and RIM1 in synaptic vesicle priming.* Neuron, 2001. **30**(1): p. 183-96.

24. Brose, N., C. Rosenmund, and J. Rettig, *Regulation of transmitter release by Unc-13 and its homologues.* Curr Opin Neurobiol, 2000. **10**(3): p. 303-11.
25. Scales, S.J., et al., *Amisyn, a novel syntaxin-binding protein that may regulate SNARE complex assembly.* J Biol Chem, 2002. **277**(31): p. 28271-9.
26. Constable, J.R., et al., *Amisyn regulates exocytosis and fusion pore stability by both syntaxin-dependent and syntaxin-independent mechanisms.* J Biol Chem, 2005. **280**(36): p. 31615-23.
27. Fujita, Y., et al., *Tomosyn: a syntaxin-1-binding protein that forms a novel complex in the neurotransmitter release process.* Neuron, 1998. **20**(5): p. 905-15.
28. Yizhar, O., et al., *Tomosyn inhibits priming of large dense-core vesicles in a calcium-dependent manner.* Proc Natl Acad Sci U S A, 2004.
29. Hatsuzawa, K., et al., *The R-SNARE motif of tomosyn forms SNARE core complexes with syntaxin 1 and SNAP-25 and down-regulates exocytosis.* J Biol Chem, 2003. **278**(33): p. 31159-66.
30. Lehman, K., et al., *Yeast homologues of tomosyn and lethal giant larvae function in exocytosis and are associated with the plasma membrane SNARE, Sec9.* J Cell Biol, 1999. **146**(1): p. 125-40.
31. Kagami, M., A. Toh-e, and Y. Matsui, *Sro7p, a Saccharomyces cerevisiae counterpart of the tumor suppressor l(2)gl protein, is related to myosins in function.* Genetics, 1998. **149**(4): p. 1717-27.
32. Mechler, B.M., W. McGinnis, and W.J. Gehring, *Molecular cloning of lethal(2)giant larvae, a recessive oncogene of Drosophila melanogaster.* Embo J, 1985. **4**(6): p. 1551-7.
33. Musch, A., et al., *Mammalian homolog of Drosophila tumor suppressor lethal (2) giant larvae interacts with basolateral exocytic machinery in Madin-Darby canine kidney cells.* Mol Biol Cell, 2002. **13**(1): p. 158-68.
34. Pobbati, A.V., et al., *Structural basis for the inhibitory role of tomosyn in exocytosis.* J Biol Chem, 2004. **279**(45): p. 47192-200.
35. Masuda, E.S., et al., *Tomosyn binds t-SNARE proteins via a VAMP-like coiled coil [letter].* Neuron, 1998. **21**(3): p. 479-80.
36. Kim, Y.S., H.M. Chung, and K.H. Baek, *WD-40 repeat containing rat lethal giant larvae recessive oncogene, but not m-tomosyn, restores the salt sensitivity in Saccharomyces cerevisiae.* Int J Oncol, 2003. **23**(1): p. 229-33.
37. Groffen, A.J., et al., *Two distinct genes drive expression of seven tomosyn isoforms in the mammalian brain, sharing a conserved structure with a unique variable domain.* J Neurochem, 2005. **92**(3): p. 554-68.
38. Zhang, X., et al., *Lethal giant larvae proteins interact with the exocyst complex and are involved in polarized exocytosis.* J Cell Biol, 2005. **170**(2): p. 273-83.
39. Katoh, M., *Identification and characterization of human LLGL4 gene and mouse Llgl4 gene in silico.* Int J Oncol, 2004. **24**(3): p. 737-42.
40. Zhang, W., et al., *Tomosyn is expressed in beta-cells and negatively regulates insulin exocytosis.* Diabetes, 2006. **55**(3): p. 574-81.
41. Widberg, C.H., et al., *Tomosyn interacts with the t-SNAREs syntaxin4 and SNAP23 and plays a role in insulin-stimulated GLUT4 translocation.* J Biol Chem, 2003. **278**(37): p. 35093-101.
42. Dybbs, M., J. Ngai, and J.M. Kaplan, *Using microarrays to facilitate positional cloning: identification of tomosyn as an inhibitor of neurosecretion.* PLoS Genet, 2005. **1**(1): p. 6-16.
43. Gracheva, E.O., et al., *Tomosyn Inhibits Synaptic Vesicle Priming in Caenorhabditis elegans.* PLoS Biol, 2006. **4**(8): p. e261.

44. Sakisaka, T., et al., *Regulation of SNAREs by tomosyn and ROCK: implication in extension and retraction of neurites.* J Cell Biol, 2004. **166**(1): p. 17-25.
45. Baba, T., et al., *PKA-catalyzed phosphorylation of tomosyn and its implication in Ca2+-dependent exocytosis of neurotransmitter.* J Cell Biol, 2005. **170**(7): p. 1113-25.
46. Li, Q., et al., *Facilitation of Ca(2+)-dependent exocytosis by Rac1-GTPase in bovine chromaffin cells.* J Physiol, 2003. **550**(Pt 2): p. 431-45.
47. Wick, P.F., et al., *Transient transfection studies of secretion in bovine chromaffin cells and PC12 cells. Generation of kainate-sensitive chromaffin cells.* J Biol Chem, 1993. **268**(15): p. 10983-9.
48. Hoppe, A., K. Christensen, and J.A. Swanson, *Fluorescence resonance energy transfer-based stoichiometry in living cells.* Biophys J, 2002. **83**(6): p. 3652-64.
49. Liu, J., et al., *Fluorescence resonance energy transfer reports properties of syntaxin1A interaction with Munc18-1 in vivo.* J Biol Chem, 2004.
50. Gladycheva, S.E., et al., *Regulation of syntaxin1A-munc18 complex for SNARE pairing in HEK293 cells.* J Physiol, 2004. **558**(Pt 3): p. 857-71.
51. Rowe, J., et al., *Syntaxin 1A is delivered to the apical and basolateral domains of epithelial cells: the role of munc-18 proteins.* J Cell Sci, 2001. **114**(Pt 18): p. 3323-32.
52. Rowe, J., et al., *Blockade of membrane transport and disassembly of the Golgi complex by expression of syntaxin 1A in neurosecretion-incompetent cells: prevention by rbSEC1.* J Cell Sci, 1999. **112 (Pt 12)**: p. 1865-77.
53. Wu, M.N., et al., *Syntaxin 1A interacts with multiple exocytic proteins to regulate neurotransmitter release in vivo [published erratum appears in Neuron 2000 Mar;25(3):735].* Neuron, 1999. **23**(3): p. 593-605.
54. Kee, Y., et al., *Distinct domains of syntaxin are required for synaptic vesicle fusion complex formation and dissociation.* Neuron, 1995. **14**(5): p. 991-8.
55. Weimer, R.M., et al., *Defects in synaptic vesicle docking in unc-18 mutants.* Nat Neurosci, 2003. **6**(10): p. 1023-30.
56. Toonen, R.F., et al., *Munc18-1 stabilizes syntaxin 1, but is not essential for syntaxin 1 targeting and SNARE complex formation.* J Neurochem, 2005. **93**(6): p. 1393-400.
57. Yang, X., et al., *Domain Requirement for the Membrane Trafficking and Targeting of Syntaxin 1A.* J Biol Chem, 2006. **281**(22): p. 15457-63.
58. Hall, A., *Rho GTPases and the actin cytoskeleton.* Science, 1998. **279**(5350): p. 509-14.
59. Nobes, C. and A. Hall, *Regulation and function of the Rho subfamily of small GTPases.* Curr Opin Genet Dev, 1994. **4**(1): p. 77-81.
60. Hakoshima, T., T. Shimizu, and R. Maesaki, *Structural basis of the Rho GTPase signaling.* J Biochem (Tokyo), 2003. **134**(3): p. 327-31.
61. Toutant, M., et al., *Presence of three pertussis toxin substrates and Go alpha immunoreactivity in both plasma and granule membranes of chromaffin cells.* FEBS Lett, 1987. **215**(2): p. 339-44.
62. Gasman, S., et al., *Regulation of exocytosis in adrenal chromaffin cells: focus on ARF and Rho GTPases.* Cell Signal, 2003. **15**(10): p. 893-9.
63. Vitale, N., et al., *Insight in the exocytotic process in chromaffin cells: regulation by trimeric and monomeric G proteins.* Biochimie, 2000. **82**(4): p. 365-73.
64. Vitale, N., et al., *Trimeric G proteins control regulated exocytosis in bovine chromaffin cells: sequential involvement of Go associated with secretory granules and Gi3 bound to the plasma membrane.* Eur J Neurosci, 1996. **8**(6): p. 1275-85.

65. Ahnert-Hilger, G., et al., *Detection of G-protein heterotrimers on large dense core and small synaptic vesicles of neuroendocrine and neuronal cells.* Eur J Cell Biol, 1994. **65**(1): p. 26-38.
66. Gasman, S., et al., *Identification of a potential effector pathway for the trimeric Go protein associated with secretory granules. Go stimulates a granule- bound phosphatidylinositol 4-kinase by activating RhoA in chromaffin cells.* J Biol Chem, 1998. **273**(27): p. 16913-20.
67. Gasman, S., et al., *Involvement of Rho GTPases in calcium-regulated exocytosis from adrenal chromaffin cells.* J. Cell Sci., 1999. **112**: p. 4763-4771.

Chapter 4

Theory and Application of Sensitized Emission TIRF-FRET in Living Cells

Abstract

Biological processes are inherently rife with spatially and temporally regulated sequences of molecular interactions that must occur in order for cells to function properly. Unraveling each of these sequences in a functionally meaningful manner will undoubtedly shed new light onto our understanding of how these processes occur. To achieve the high temporal and spatial resolution required to visualize such sequences of interactions in living cells, we have implemented sensitized emission FRET (fluorescence resonance energy transfer) measurements using TIRF (total internal reflection fluorescence) microscopy. Importantly, sensitized emission FRET measurements allow for highly-sensitive visualization of bi-molecular interactions as they occur in real-time, while TIRF microscopy allows for the high spatial resolution of individual organelles closely apposed to the plasma membrane. A combination of these approaches would allow for changes in bi-molecular interactions to be directly correlated with the functional state of an organelle. Here, we have taken both an experimental and a theoretical approach to gain a quantitative understanding of the effects of evanescent illumination on sensitized-emission FRET calibrations and measurements, under a variety of conditions (ie, for multiple sub-cellular localizations of the molecules of interest). Importantly, our results define several parameters that are critical to the quantitative application of this method in living cells.

Introduction

One of the major goals of biology is to be able to understand, in exact molecular detail, the dynamic and regulated processes that occur within cells to drive the many functions essential for life. Inherent in all of these processes are the dynamic and regulated associations and dissociations of a plethora of molecular binding partners, eg, proteins, lipids, nucleic acids, and small chemical metabolites. For many biological processes, biochemical and genetic techniques, coupled with assays to gauge biological function, have allowed for identification of key molecules and interactions that regulate each of these processes. However, in most cases, what remains lacking is an integral understanding of how all of these molecular interactions come together, both in subcellular space and time, to carry out these important cellular functions.

FRET (fluorescence resonance energy transfer) imaging has rapidly become a common tool to study protein-protein interactions in living cells (for recent reviews, see [1, 2]). One of the key advantages of FRET imaging lies in its flexibility in being able to monitor not only protein-protein interactions, but also a wide range of cellular parameters, including (and certainly not limited to) protein activation states [3, 4], enzymatic activity [5], and even concentrations of small metabolites [6, 7]. FRET occurs when an excited-state donor fluorophore comes within close enough proximity (<10nm) to an acceptor fluorophore to transfer resonant energy to the acceptor. When this occurs, the donor decays back to the ground state nonradiatively (ie, without emission of a photon), and the acceptor fluorophore is raised from the ground state to the excited state. FRET can therefore be observed as a simultaneous quenching of donor fluorescence, and enhancement of the acceptor fluorescence (termed sensitized emission). Several methods have been employed to detect FRET in living cells, the most common of which are donor dequenching and sensitized emission. In donor dequenching, the acceptor fluorophore is rapidly destroyed by photobleaching, thus precluding FRET from occurring. FRET that was present before photodestruction of the acceptor is detected as an increase (ie, dequenching) in donor fluorescence following photodestruction of the acceptor. While donor dequenching is the simplest method by which to detect FRET and can be performed on a confocal microscope to achieve high spatial resolution, photodestruction of the acceptor complicates, and often precludes, the use of donor dequenching for time-lapse FRET imaging. Another commonly used method to detect FRET is sensitized emission, which quantifies the enhancement in acceptor fluorescence that occurs as a result of FRET. Measurement of sensitized emission FRET is more complex in that it requires the user to perform specific calibrations for the optical system and probes being used, to be able to isolate the sensitized emission signal from other spectral contaminants, and to normalize this signal to correct for variations in donor and acceptor concentrations between cells. FRET by sensitized emission, however, is fast, can be performed on an epifluorescence microscope, and most importantly, can be used to track spatial changes in FRET that occur over time, for example, to monitor changes in a protein-protein interaction that occur in response to a stimulus. Despite the high temporal resolution afforded by sensitized emission FRET imaging performed under an epifluorescence microscope, the approach is limited by poor axial resolution due to fluorescence from out-of-focus planes.

More recently, TIRF (total internal reflection fluorescence) microscopy has been applied to study processes occurring at or near the cell membrane, with unprecedented axial resolution (for review, see [8-11]). TIR results when light traveling through a medium of high refractive index, n_1 (such as glass) reaches an interface with a medium of lower refractive index, n_2 (such as water), at an angle of incidence that exceeds a critical angle, $\theta_c = \sin^{-1}(n_2/n_1)$. When this occurs, the light undergoes total internal reflection, and an evanescent field is generated at the glass-water interface, whose intensity decays exponentially with distance from the interface: $I(z) = I_o\, e^{-z/D}$ (where z is the distance from the glass-water interface, and D is the characteristic TIRF depth, i.e., the distance at which the evanescent field decays to 37% of its initial value). To achieve high axial resolution, TIRF microscopy takes advantage of this exponentially decaying evanescent wave, to illuminate a thin (roughly 100-300nm thick) 'footprint' of a cell, that includes only those regions of the cell that are closely apposed to the glass coverslip. Importantly, combination of the axial resolution afforded by TIRF imaging, with the sensitivity and high temporal resolution afforded by sensitized emission FRET imaging, could provide a powerful tool to be able to sequence the dynamics of molecular interactions occurring near the plasma membrane, and to spatially and temporally correlate these interactions to functional consequences.

Thus far, TIRF-FRET has only recently begun to be implemented. Most of the TIRF-FRET studies in living cells utilize the donor dequenching FRET method to examine proteins that localize specifically to the plasma membrane [12-15]. While sensitized emission TIRF-FRET has also been used, this method has been applied mainly to the study of in vitro interactions of single molecules adherent to glass coverslips [16, 17], and to limited situations in living cells, where a plasma-membrane protein is labeled with both donor and acceptor molecules [18]. This paper represents a first step in being able to implement sensitized emission TIRF-FRET under a variety of conditions in living cells. Parameters critical to the approach are defined experimentally and matched with theoretical predictions tested by mathematical models. The results provide guidelines regarding quantitative application of this method for cell biology. Importantly, the methods described here can be applied to proteins localized not only to the plasma membrane, but also to intracellular compartments (e.g., secretory granules, mitochondria, cortical cytoskeleton, etc) as well as the cytosol.

Materials and Methods

Cell culture and transfection

MIN6 cells were cultured in 5% CO_2, in DMEM containing 4.5g/L glucose and glutamine (Gibco, Carlsbad, CA), supplemented with 15% fetal bovine serum, penicillin (50U/mL), streptomycin (50µg/mL), and 0. 0005% β-mercaptoethanol. MIN6 cells were transfected using Lipofectamine 2000 (Invitrogen), according to the manufacturer's protocol. For TIRF experiments, MIN6 cells were plated onto poly-L-lysine coated #1.5 thickness coverslips 36-48 hours prior to use, and transfected 16-18 hours before imaging. Immediately prior to imaging, cells were switched from culture media to a physiological saline solution (PSS: 137mM NaCl, 3.4mM KCl, 1.6mM KH_2PO_4, 1.2mM $MgSO_4$, 2mM $CaCl_2$, 4.8mM $NaHCO_3$, 10mM HEPES, 2.5mM glucose, pH 7.4).

Molecular biology and generation of recombinant DNA constructs

All fluorescent constructs utilized the monomeric versions of the fluoroproteins cerulean (a cyan fluorescent protein mutant that exhibits a higher extinction coefficient and higher quantum yield) [19] and citrine (a yellow fluorescent protein derivative that exhibits reduced pH sensitivity and longer Forster distance) [20, 21]. A linked citrine-cerulean construct was generated by ligating sequence coding for cerulean onto the C-terminal end of citrine, with a 15 amino acid linker (linker sequence: SGLRSRDPLALPVAT) in between the two fluoroproteins. To generate a plasma membrane targeted linked FRET construct, the PH domain of PLC delta was PCR subcloned from a YFP-PH construct (a gift from Kees Jalink, Netherlands Cancer Institute) and ligated onto the C-terminal end of the linked citrine-cerulean sequence (with a flexible 11 amino acid linker (linker sequence: SGFSGGSGGSG) between the cerulean and the PH domain). To target the linked FRET probe to secretory granule compartments, a citrine-cerulean-VAMP2 construct was made by PCR subcloning the VAMP2 domain from synaptopHluorin [22] and ligating it to the C-terminal end of the linked citrine-cerulean sequence with the same 11 amino acid linker. The single fluorophore-labeled citrine-PH, cerulean-PH, citrine-VAMP2, and cerulean-VAMP2 constructs were generated from the citrine-cerulean-PH domain or –VAMP2 constructs, via restriction digests and ligations that removed either the citrine or cerulean coding regions from each construct. The sequence fidelity of all constructs was confirmed by DNA sequencing (University of Michigan DNA Sequencing Core).

Optical Rig Setup

A through-the-objective TIRF system (TILL Photonics, Germany) was built around an Olympus IX71 microscope and utilizes an Olympus 60x 1.49NA oil objective mounted on a PIFOC nanofocus z-drive controller (Physik Instrumente, Germany). For illumination, two lasers, a 45mW 442nm solid state DPSS (Toptica Photonics, Germany) and a 225mW Argon-ion laser (National Laser Company, Salt Lake City, UT) were combined into an AOTF (accousto-optic tunable filter) to allow for rapid selection of laser lines and powers. The output of the AOTF was coupled via a unimodal fiber optic into a TILL Photonics Polytrope unit fixed onto the back port of the microscope. Within the Polytrope, the light first undergoes a beam expansion before being reflected into the microscope body by a mirror. The angle of this mirror is adjustable via a galvanometer and sets the position of the laser beam in the back focal plane of the objective, thereby allowing fine and rapid control over the incident TIRF angle, as well as the ability to rapidly switch between epifluorescence and TIRF illumination modes. Between the mirror and the microscope objective is an additional achromatic tube lens, which focuses the laser on the back focal plane of the objective. The microscope's filter cube assembly contains a dual band laser clean-up filter (z442/514dbx) and a dual band laser polychroic mirror (z442/514rdc). Fluorescence emission from CFP/cerulean and citrine are separated using a Dual-View beam splitter (MAG Biosystems, Pleasanton, CA) containing a 505dcxr dichroic, and emission filters appropriate for CFP/cerulean (et480/40) and citrine (et555/55). (All filters were from Chroma Technologies, Rockingham, VT). Images are acquired using a 16-bit, 512x512 pixel Photometrics QuantEM 512SC EMCCD camera (Roper Scientific, Tucson, AZ) with a 16x16 μm pixel size. To achieve Nyquist sampling (with a limiting resolution of 200nm, sampled over 3 pixels), additional magnification from the 1.6x slide magnifier on the IX71 and a 2.5x beam expander placed in front of the DualView are employed. The laser lines, laser powers, TIRF angle, z-focus drive, and camera were controlled using Metamorph software (Molecular Devices, Sunnyvale, CA).

TIRF FRET Imaging

The 442nm DPSS and the 514nm line from the Ag-Ion laser were used for TIRF-FRET imaging. Laser powers for each laser line were kept constant for all experiments. At the beginning of each experiment, the Polytrope was aligned such that when the galvanometer position was set for epifluorescence imaging, the laser beam was directed straight overhead, through the center of the objective. Variations in this epifluorescence position resulting from wobble of the Olympus filter wheel turret were initially corrected by torsional stabilization of the filter wheel assembly. However, throughout the course of each experiment, the calibrated epifluorescence position was often checked and small readjustments to re-calibrate this position were made when necessary. Prior to each imaging experiment, the accuracy and repeatability of the Polytrope unit in switching between various galvanometer positions was confirmed by projecting the laser beam onto a wall using a 45-45-90 right angle prism (n=1.515) (Edmund Scientific, Tonawanda, NY) and verifying that the laser beam accurately returned to the same position on the wall for each different galvanometer setting. Sensitized-emission TIRF-

FRET imaging was carried out similarly to methods described in our previous publications using FRET imaging under epifluorescence illumination ([23, 24]). Except when stated otherwise, the incident TIRF angles were adjusted independently for the 442nm and 514nm lines, such that the characteristic TIRF depths (determined using fluorescently labeled silica beads; see methods below) of both laser lines were matched. For each FRET image, three different excitation/emission images were taken: 1) DD: donor excitation (442nm) / donor emission (480nm); 2) DA: donor excitation (442nm) / acceptor emission (555nm); and 3) AA: acceptor excitation (514nm) / acceptor emission (555nm). The electron multiplication gain and digital gain of the camera were set the same for all 3 images (DD, DA, AA), although exposure times of the 3 images were individually set to achieve appropriate intensity levels. Fluorescence intensity was determined to be linear to exposure time, allowing for correction. Images to determine FRET stoichiometry calibration constants (taken either of beads conjugated with, or cells expressing CFP or cerulean only, citrine only, or a linked CFP-citrine or citrine-cerulean protein) were collected for each experiment, using the same incident TIRF angles and laser powers used for collection of experimental data. Shade correction images were also collected at the same incident TIRF angles, by imaging glass coverslips conjugated with both CFP and citrine proteins and overlaid with PSS (see methods below), in order to correct for non-uniformities within the illumination fields for the 442nm and 514nm lines. All imaging was performed at room temperature.

FRET Image Analysis

TIRF-FRET images were analyzed offline using in-house written MATLAB scripts. Following alignment of images using an affine transformation, images were background subtracted using the averaged value within a user-defined background region of interest. Images were then shade-corrected by dividing each image (on a pixel-by-pixel basis) by the appropriate normalized shade image (each shade image was normalized to its median value). Lastly, images were linearly scaled to account for differences in exposure times between images. These corrected images (CIDD for acquired DD, CIDA for DA, and CIAA for AA) were then used for FRET analysis.

Sensitized emission FRET analysis was carried out using the method of FRET stoichiometry [21, 25]. This method requires the determination of 4 calibration parameters: α, β, γ, and ξ. α and β are proportionality constants that allow for correction of the contaminated FRET signal (CIDA) from both crosstalk (ie, direct excitation of the acceptor by donor excitation wavelengths) and spectral bleedthrough (ie, spillover of donor emission into the acceptor emission channel), respectively. α was determined by taking images of citrine expressing cells or beads conjugated with citrine, and calculating the ratio of the CIDA /CIAA images. β was determined by taking images of either cells expressing cerulean, or beads conjugated with CFP, and calculating the ratio of the CIDA / CIDD images. Following determination of α and β, the uncontaminated sensitized emission FRET signal can be calculated as: $\text{CIDA} - \alpha^*\text{CIAA} - \beta^*\text{CIDD}$. The parameter γ represents the ratio of extinction coefficients of acceptor to donor, at donor excitation wavelengths, and is required for determination of the fraction of acceptor in complex (fA). The parameter ξ relates the fluorescence intensity of the sensitized emission signal to the fluorescence intensity that would have arisen from the quenched donor (ie, the donor fluorescence lost due to FRET). Using ξ, the donor fluorescence quenched by FRET can be calculated as: $\xi^* (\text{CIDA} - \alpha^*\text{CIAA} - \beta^*\text{CIDD})$. Determination of ξ is necessary for calculation of the fraction of donor in complex (fD), and subsequently, for determination of the total donor fluorescence and molar ratio. Both γ and ξ are determined by imaging either cells expressing a linked citrine-cerulean protein, or beads conjugated with linked CFP-citrine protein, and solving the FRET equations (see below) for either γ or ξ, using the fact that for a linked construct, fA = fD

= 1. Note that determination of γ and ξ requires that the characteristic efficiency (Ec) of the linked constructs used for the calibration be pre-determined. The Ec for the CFP-citrine construct was previously reported using fluorescence lifetime measurements to be 0.40 in solution (pH 7.2) [21]. The Ec for the citrine-cerulean construct was determined to be ~0.39 in cells, by calculating the FRET value of this construct using calibration parameters determined based on a cerulean-citrine construct whose Ec had been determined using lifetime measurements to be 0.31 (A. Hoppe, University of Michigan, written communication).

Determination of the 4 calibration constants α, β, γ, and ξ, and collection of the 3 required images (CIDD, CIDA, and CIAA) allows for pixel-by-pixel calculations that generate 3 new images: EA (the apparent FRET efficiency of the acceptor), ED (the apparent FRET efficiency of the donor), and Ratio (the molar ratio of total acceptor : total donor). EA, ED, and Ratio images were calculated using the following equations:

$$EA = E_c \times f_A = \frac{\gamma\,(\mathrm{CIDA} - \alpha\times\mathrm{CIAA} - \beta\times\mathrm{CIDD})}{\alpha\times\mathrm{CIAA}} \quad (1)$$

$$ED = E_c \times f_D = \frac{\xi\,(\mathrm{CIDA} - \alpha\times\mathrm{CIAA} - \beta\times\mathrm{CIDD})}{\mathrm{CIDD} + \xi\,(\mathrm{CIDA} - \alpha\times\mathrm{CIAA} - \beta\times\mathrm{CIDD})} \quad (2)$$

$$Ratio = \frac{\xi}{\gamma} \times \frac{\alpha\times\mathrm{CIAA}}{\mathrm{CIDD} + \xi\,(\mathrm{CIDA} - \alpha\times\mathrm{CIAA} - \beta\times\mathrm{CIDD})} \quad (3)$$

FRET analysis on granules

FRET analysis of secretory granules labeled by expression of the linked citrine-cerulean-VAMP2 probe was carried out following alignment of images using an affine transformation, and correction of these images for background, shade, and exposure time. Granule detection was performed on CIDA images. These images were converted to binary images using a threshold cut-off of ~6-8x the mean value of the image; this threshold was determined on an image-by-image basis, and was guided by visual inspection of how well granules were detected at a specific threshold. Centroid coordinates of each granule were then determined from the binary image, and were subsequently used as markers of granule position. Each individual granule detected was visually inspected at its centroid coordinates in all three CIDD, CIDA and CIAA images to ensure that: 1) a granule-like fluorescence distribution was present at those coordinates for all 3 images; and 2) the granule had not moved noticeably in the x-y direction between images. Only granules that met these criteria and that exceeded a set minimum intensity threshold in all three images were used for subsequent analysis. (For cells that co-expressed soluble fluorophore, these criteria did not fully apply, as granules were often quite difficult to detect in the CIDD or CIAA images, due to the high background of the soluble fluorophore. However, this did not appear to affect granule detection from the CIDA image). For FRET analyses, mean granule intensities in a 13-pixel diamond centered on the centroid coordinates of each granule were determined for CIDD, CIDA, and CIAA images. These three mean intensity values for each granule were then used in determination of FRET calibration constants or the FRET values for EA, ED, and Ratio, using the above equations.

Purification of Bacterially Expressed Proteins

E. coli (strain BL21 DE3) expressing His-citrine or His-CFP, and E. coli (strain JM109) expressing His-citrine-CFP were a kind gift from Joel Swanson (University of Michigan). Cells were grown to an OD of 0.4-0.6, induced with 0.1mM IPTG, grown for an additional 7 hours at 30C, and pelleted by centrifugation (15 minutes, 5000g, Beckman JA-14 rotor). Following centrifugation, cells were resuspended in an equilibration buffer (50mM Na_2HPO_4, 300mM NaCl, 0.5% Triton X-100, pH 7.0, supplemented with protease inhibitors (G-Biosciences, St. Louis, MO)), and were mechanically lysed using a French press at 15000psi. Cell lysates were solubilized by shaking on ice for 1 hour, followed by centrifugation to remove insoluble debris (20 minutes, 20,000g, Beckman JA-20 rotor). His-tagged proteins were purified from the cell lysates using TALON metal affinity resin beads (Clontech, Mountain View, CA) according to the manufacturer's protocol. Following binding of His-tagged proteins to the TALON beads, the beads were rinsed several times in wash buffer (50mM Na_2HPO_4, 300mM NaCl, pH 7.0, supplemented with 5mM imidazole), and His-tagged proteins were eluted from the beads using wash buffer supplemented with 150mM imidazole. The purity of each protein was determined by fractionation by SDS-PAGE and Coomassie staining and was estimated to be ~90%. Prior to use in conjugation reactions (see methods below), proteins were dialyzed into a coupling buffer.

Conjugation of fluoroproteins to silica beads / coverslips

Fluoroproteins were conjugated to either 10μm silica beads (Discovery Scientific, Vancouver, Canada) or to glass coverslips (1.5 thickness, Warner Instruments, Hamden, CT). For conjugation of fluoroprotein to the silica surfaces, beads or coverslips were first amino-silylated for 30 seconds in a 2% solution of 3-aminopropyltriethoxysilane (Pierce Biotechnology, Rockford, IL) in acetone, followed by a thorough rinsing with acetone. Fluoroproteins were then crosslinked to this surface using a Sulfo-LC-SPDP cross-linker (Pierce) as follows. Proteins were first passed through a 0.22μm syringe filter to remove insoluble debris, and then equilibrated into coupling buffer (50mM Na_2HPO_4, 150mM NaCl, 10mM EDTA, 0.02% NaN_3, pH 7.2) by overnight dialysis at 4C using 3.5K Slide-a-Lyzer cassettes (Pierce). Equilibrated protein was then diluted to a concentration of ~ 0.6mg/mL in coupling buffer for the crosslinking reaction. Sulfo-LC-SPDP crosslinker was added to each protein solution to a final concentration of 1mM, and the reaction was allowed to proceed in the dark at room temperature for 30-60 minutes. Following this reaction, free crosslinker was removed from the protein solution by dialysis into coupling buffer for 12 hours at 4C using 3.5K Slide-a-Lyzer cassettes. The glass surfaces were separately modified with the Sulfo-LC-SPDP crosslinker, by covering the surfaces in a solution of 1mM Sulfo-LC-SPDP in coupling buffer for 30-60 minutes at room temperature. The modified glass surfaces were then rinsed in coupling buffer, and the bound crosslinker was reduced by treatment with 50mM DTT in coupling buffer for 30 minutes at room temperature, followed by several rinses in coupling buffer. The Sulfo-LC-SPDP modified protein solutions were then added to the modified and reduced glass surfaces, and the crosslinking reaction was allowed to proceed in the dark for 18 hours at 4C, with shaking. The protein-modified glass surfaces were rinsed in coupling buffer and stored at 4C (in coupling buffer) prior to use. Visual inspection of the surfaces under fluorescence microscopy demonstrated that the fluoroprotein-modification of the surfaces was largely uniform across the surfaces.

Measurement of evanescent field profile using fluorescently-labeled silica beads

Measurement of the evanescent profile using large, fluorescently labeled silica beads was carried out using methods similar to those previously described [26]. In brief, 10μm silica beads coated with bacterially expressed fluoroprotein (either CFP, citrine, or a linked CFP-citrine), were imaged in a solution of PBS-EDTA (50mM Na_2HPO_4, 150mM NaCl, 10mM EDTA, 0.02% NaN_3, pH 7.2) containing 31% glycerol (w/w), to achieve an index of refraction (n ~ 1.372, confirmed by refractometer measurement) similar to that of the beads (n= 1.37, as reported by the manufacturer). The beads were allowed to settle on to the glass coverslip, and images of the TIRF footprints of the beads were taken using a range of incident TIRF angles. As bead size and shape varied quite substantially, only beads that were ~10μm in diameter (approximated using a reticle micrometer) and that appeared to be spherical were chosen for imaging. All beads were imaged at approximately the same location in the TIRF field. Multiple consecutive images of beads taken at a single incident TIRF angle demonstrated that there occurs a rapid and non-uniform photobleaching of the fluorescent signal on the beads, with the bottom of the bead (ie, center of the TIRF footprint) exhibiting the fastest photobleach rate. Therefore, to ensure that the evanescent profile measured from each bead was accurate, each bead was used for only two TIRF measurements. Moreover, focusing of each bead was performed under dim epifluorescence illumination, with the focus initially set to the equatorial plane of the bead. The z-focus drive was then used to automatically move the focal position to the surface of the glass (which was set to one bead radius (5μm), below the equatorial plane of the bead) for acquisition of the TIRF images. Bead footprint images that exhibited bright debris or that were distinctly non-circular were discarded from analysis.

Determination of the evanescent profile from the TIRF images of the beads was automated using MATLAB scripts and the equations described in [26]. Images were background subtracted and a binary image of each bead was then generated and used to determine the centroid position of the bead. To better approximate the true center of the bead, the centroid coordinates were used to seed a 2D-Gaussian fit of the bead, and the determined center of each bead was visually inspected for accuracy. Pixels were then binned according to their radial distance (rounded to the nearest pixel) from the center coordinates of the bead (up to a radial distance of 75 pixels, or approximately 5μm). The averaged intensities of all pixels within each radial distance bin were then determined. These averaged intensities were then corrected for differences in the amount of bead surface area projected onto a pixel at that particular radial distance, using the equation:

$$Corrected\ Intensity = Averaged\ Intensity \times \cos\left(\sin^{-1}\left(\frac{Distance\ from\ Bead\ Center}{Bead\ Radius}\right)\right) \qquad (4)$$

Conversion of radial distance to z-distance was performed on a bead-by-bead basis, using bead radius values that were determined from epifluorescence images taken of each bead. Using the geometry of a sphere, the conversion of radial distance to z-distance was performed by solving the following equation for z:

$$(Bead\ Radius)^2 = (Distance\ from\ Bead\ Center)^2 + (Bead\ Radius - z)^2 \qquad (5)$$

Finally, the corrected intensity vs z-distance relationship for each bead image was plotted and fit to a double exponential, which was shown by Mattheyses and Axelrod (2006) to fit these data far more accurately than a single exponential.

$$Corrected\ Intensity = Ae^{-z/D_{p1}} + Be^{-z/D_{p2}} \qquad (6)$$

Here, the decay rate of the fast exponential component corresponds to the characteristic TIRF depth at a particular incident angle, whereas the slow exponential component is assumed to result from light scatter originating within the objective.

Relationships of FRET calibration constants and FRET measurements vs. z-distance were calculated from the bead images, using the FRET stoichiometry equations (see FRET methods section) with the corrected intensity vs z-distance relationships for the CIDD, CIDA, and CIAA images of each bead. For experiments in which soluble citrine was added to the imaging media, the glass coverslip was pre-blocked with a 1mg/mL solution of BSA prior to use, to prevent non-specific binding of the soluble fluoroprotein to the coverslip.

Determination of evanescent field depth using a prism

An alternative method for estimating the characteristic TIRF depths involved measuring the angle of incidence of the laser as it exits the objective, for each galvanometer setting. This was done by placing a 45-45-90° glass prism (n=1.515) (Edmund

Scientific, Tonawanda, NY) on top of the objective (with immersion oil), to couple the laser light coming out of the objective and project it onto a nearby wall. Use of Snell's Law of refraction allowed determination of the angle of incidence of the laser, θi, as it exits the objective. This angle, in conjunction with the wavelength of the laser (λ) and the indices of refraction of glass (n_1) and the cell or imaging media normally used (n_2) could then used to estimate the characteristic depth, Dp:

$$Characteristic\ depth, D_p = \frac{\lambda}{4\pi(n_1^2 \sin^2\theta_i - n_2^2)^{1/2}} \qquad (7)$$

Mathematical Simulation of TIRF-FRET

To compare our TIRF-FRET results to theoretical expectations based on illumination from an exponentially decaying evanescent field, we developed a mathematical model to simulate TIRF-FRET. The model used was similar to that described in [21], with the primary exception being that the illumination intensity, rather than being modeled as constant (as would be the case for epifluorescence) was modeled as following a double exponential decay in the z-axis. (The two exponentials represent the evanescent field component and a scatter component; see methods on using beads to determine evanescent profile). The relative contributions of the evanescent field and the scatter component were fixed at 85% and 15%, respectively, and the scatter component was fixed as decaying with a depth constant of 1500nm. (These values were chosen to approximate those typically measured on our system, using fluorescent silica beads):

$$I(z) = 0.85e^{-z/D_p} + 0.15e^{-z/1500} \qquad (8)$$

Beads and granules were modeled as spheres with diameters of 10µm or 350nm, respectively. To simulate a linked FRET probe that localizes to the surface of the bead/granule, we arbitrarily set the surface concentration (# of molecules per unit area) for both the acceptor and donor equal to 1000. The fraction of donor in complex (fD) was set to 1, and the FRET efficiency (E) for the donor and acceptor was set to 0.4 (the characteristic efficiency of CFP-citrine in solution). In some cases, a population of free, soluble acceptor molecules was added to this model. Here, the concentration (# molecules per unit volume) was set such that the ratio of the calculated fluorescence intensity from the bottom of the bead, to the calculated fluorescence intensity of the soluble component outside of the bead, matched the ratio value determined experimentally (ie, the ratio of the fluorescence intensity at the center of the bead footprint, to the fluorescent intensity of the soluble fluorophore in a region clearly outside the bead region, in the CIAA image).

Fluorescence intensities arising from the bead/granule surfaces and from soluble components were determined independently. For fluorescence arising from the surface of a bead/granule, DD, AA, and the sensitized emission FRET signal were modeled as:

$$DD_{surface}(x,y,z_1,z_2) =$$

$$P_1 \times [I(z_1) + I(z_2)] \times ([donor\ on\ surface] - [bound\ donor\ on\ surface] \times E) \tag{9}$$

$$AA_{surface}(x,y,z_1,z_2) = P_2 \times [I(z_1) + I(z_2)] \times [acceptor\ on\ surface] \tag{10}$$

$$FRET_{surface}(x,y,z_1,z_2) = \frac{\alpha \times P_2}{\gamma} \times [I(z_1) + I(z_2)] \times [bound\ donor\ on\ surface] \times E \tag{11}$$

The coordinate system used here (x, y, z_1, z_2) depicts the distances of the bottom and top surfaces of the bead/granule from the glass interface (z_1 and z_2, respectively) for a given (x,y) position on the bead/granule. P_1 and P_2 represent the initial intensities (I_o) of the donor and acceptor illuminations, respectively, at the glass-water interface (eg, z = 0). For completeness, fluorescence from both the bottom and top surfaces of the bead at each (x,y) point are taken into account; however, for a 10µm bead, the fluorescent arising from the top surface of the bead was negligible due to the large size of the bead.

Fluorescence intensity arising from the soluble acceptor was determined for each (x, y, z_1, z_2) point, as separate components arising from below the bottom surface of the bead/granule, and above the top surface of the bead/granule:

$$AA_{soluble}(x, y, z_1, z_2)$$

$$= \left(P_2 \times \int_0^{z_1} I(z) \times [soluble\ acceptor]\right) + \left(P_2 \times \int_{z_2}^{\infty} I(z) \times [soluble\ acceptor]\right) \qquad (12)$$

In this model, the total DD and FRET fluorescence originated from the surface of the bead, whereas the total AA fluorescence signal at each (x,y) point was calculated as the sum of $AA_{surface}$ and $AA_{soluble}$ at each (x,y) position.

The fluorescence intensities determined above were then used in conjunction with the FRET stoichiometry equations to calculate the expected values of EA, ED, and Ratio. The FRET calibration constants used for these calculations were taken from the averaged values of the constants over the first 525nm in z, measured from experiments that best approximated the situation being modeled (eg, same characteristic TIRF depth). Note that in order to use the experimentally determined FRET calibration parameters in this model, P_2 was held constant at the arbitrary value of 100, and ratio of P_1 to P_2 was adjusted for each set of constants used, such that EA, ED, and Ratio reported the expected theoretical FRET values (EA = ED = 0.4; Ratio = 1) when only bead/granule surface fluorescence (ie, no soluble fluorophore) was taken into account.

Results

Determination of evanescent field profiles for 442nm and 514nm laser lines

Initial characterization of the TIRF-FRET system involved measurement of the evanescent field profiles that resulted from a range of incident TIRF angles (using different galvanometer settings) of the 442nm and 514nm laser lines. Characterization of these settings is critically important for TIRF-FRET measurements, as FRET is an intensity based measurement, and as TIRF imaging is unique in that the illumination intensity decays exponentially in the z-axis.

Measurements of the TIRF angles of incidence of the lasers for a range of galvanometer settings initially used a glass prism method that coupled the laser light as it exited the objective and projected it onto a nearby target. Simple trigonometry and Snell's law allowed us to determine the angle of incidence, by measuring the height of the laser projected onto the target, and the distance from the target to the microscope objective. Following determination of the angle of incidence corresponding to each galvanometer setting, the evanescent field profile at each galvanometer setting was then measured. This was done by imaging large (10μm) spherical silica beads that were coated with fluoroprotein and resting on the surface of the glass coverslip [26]. Figures 4.1C and 4.1D (left) show representative bead footprints imaged under TIRF, using the 442nm or 514nm laser lines, respectively, where each laser line was optimally focused at the back focal plane of the objective. Each point on the bead footprint represents fluorescence originating from the surface of the bead, at a specific z-distance from the glass coverslip. This z-distance can be determined for each point on the footprint, given the radius of the bead and the radial distance of the point from the center of the footprint (Figure 4.1B). Assuming that the surface of the bead is coated uniformly with fluoroprotein, the fluorescence intensity at each point on the bead footprint is directly proportional to the intensity of the evanescent field at that point's corresponding z-distance. As shown by representative plots in the middle portions of Figures 4.1C and 4.1D, an intensity vs. z-distance relationship can be plotted for all points in the bead footprint to determine the decay of the evanescent field. The right portions of Figures 4.1C and 4.1D show the characteristic TIRF depths measured for a range of incident angles for the 442nm and 514nm lines (purple markers or green markers, respectively). The solid lines in these plots are the theoretically determined relationships for the 442nm or 514nm lasers respectively, calculated using Equation 7, and assuming two different indices of refraction of the imaging media (n= 1.37 or 1.38). Given that the beads were imaged in a solution in which the index of refraction was measured to be ~1.372, the experimentally determined values fall largely within the theoretically expected range.

For the experiments that follow, the focus was optimized for the 442nm line to maximize the visualization of our dimmest FRET probe (ie, CFP/cerulean) under TIRF, leaving the 514nm line slightly less focused. The evanescent field profiles for the 514nm line were therefore deeper than the theoretical expectations (right portion of Figure 4.1D, black markers).

Effects of mismatched evanescent field depths on sensitized emission FRET calibrations and measurements

The rationale driving the development of a sensitized emission TIRF-FRET method for use within living cells is that sensitized emission FRET imaging, unlike donor dequenching, is non-destructive and rapid, and is thus highly amenable to time-lapse imaging. Sensitized emission FRET imaging, however, requires calibration of the imaging system to be able to isolate the sensitized emission signal from contaminants such as spectral bleed-through and crosstalk, as well as to be able to calculate apparent FRET efficiencies and molar ratios of acceptor to donor, which allow for comparison of apparent FRET efficiencies across treatments and cells.

The sensitized emission FRET approach that we employ here is termed FRET stoichiometry ([21, 25]). This method allows for calculation of the instrument-independent indices termed EA (apparent FRET efficiency of the acceptor in complex), ED (apparent FRET efficiency of the donor in complex) and Ratio (the molar ratio of total acceptor to total donor), by determination of four calibration constants, α, β, γ, and ξ (see Methods section for a more complete description). Other sensitized emission methods yielding similar instrument-independent indices of FRET, have also been developed and could be similarly applied to TIRF-FRET measurements [27-29].

With conventional epifluorescence illumination, the FRET stoichiometry constants are determined in cells expressing soluble donor, acceptor, or linked donor-acceptor proteins, under the assumption that the illumination intensity across the specimen in the axial (z-) direction is constant. TIRF imaging, however, differs in that the illumination intensity decays exponentially in the z-direction. This is further complicated for sensitized emission TIRF-FRET imaging, where two different wavelengths of light are employed, whose evanescent fields decay with different depth constants, depending on each laser's angle of incidence, and the relative difference between laser wavelengths (see Figure 4.1A). To assess how FRET stoichiometry calibration constants are affected by evanescent illumination, particularly in regard to matching of the characteristic depths of the two illumination wavelengths, we imaged 10μm silica beads coated with either citrine or linked CFP-citrine protein. For these experiments, 3 different illumination sets were used, in which the characteristic depths for the 442nm (D_{442}) and 514nm (D_{514}) laser lines were either 1) matched at approximately 270nm, 2) mismatched, with D_{442} deeper than D_{514} (D_{442} = 280nm, D_{514} = 140nm) or 3) mismatched, with D_{442} shallower than D_{514} (D_{442} = 160nm, D_{514} = 270nm). Of particular interest was the relationship of the FRET stoichiometry calibration constants α, γ, and ξ, to the z-distance from the glass coverslip, under each of the imaging conditions. The calibration constant β was excluded here, as determination of β requires only the 442nm laser line. Indeed, as shown in Figure 4.3B, β remains constant with z-distance. The relationships of the FRET stoichiometry calibration constants vs. z-distance were calculated using the respective CIDD, CIDA, or CIAA vs. z-distance relationships determined from individual beads, and are shown as normalized plots in Figures 4.2A-C.

The effects of different evanescent field depths on α are shown in Figure 4.2A. Greater than two-fold variations in α occur across z-distance when TIRF depths are mismatched, with relatively little variation occurring when the TIRF depths are closely matched. α is a proportionality constant that represents the extent to which the donor excitation wavelength directly excites the acceptor as compared to the acceptor excitation wavelength. Therefore, the α vs. z-distance relationship largely reflects the ratio of the evanescent field profiles of the donor to the acceptor at each z-distance. This is borne out by the observation that with D_{442} deeper than D_{514}, α becomes progressively larger with z-distance, whereas with D_{442} shallower than D_{514}, α becomes progressively smaller with z-distance. Moreover, these variations in α occur within z-distances < 500nm from the glass-water interface, the distance over which most of the evanescent field decays. The relationships of γ and ξ vs. z-distance also demonstrate larger variations for γ and ξ when D_{442} and D_{514} are mismatched, compared to when they are matched (with γ showing larger changes overall compared to ξ). Theoretically, γ and ξ should remain constant over z-distance, as γ represents the ratio of extinction coefficients of the acceptor to donor at donor excitation wavelengths, and ξ represents a proportionality constant relating the brightness of the donor to the brightness of the acceptor. The changes in z-distance seen for γ and ξ when D_{442} and D_{514} are mismatched likely result from the fact that both calculations take into account the CIDD, CIDA, and CIAA images taken with the mismatched D_{442} and D_{514}, in addition to the varying α vs. z-distance relationships that result from the mismatched TIRF depths.

The experiments above indicate that mismatch between the evanescent profiles of the two illumination wavelengths used in sensitized emission TIRF-FRET results in large variations of the calibration constants over z-distance. In practical terms, then, to accurately determine the apparent FRET efficiency at any particular z-distance requires a different set of calibration constants at each z-distance. This is highly relevant in situations where time-dependent changes in FRET on mobile sub-cellular compartments (eg, a secretory granule, mitochondrion, or cortical cytoskeleton) are being examined. For example, a change in FRET may be interpreted as being physiologically important, when in fact the change results simply from the compartment moving in the z-axis, with inappropriate FRET calibration constants applied. The experiments above used in vitro imaging of large beads to determine how FRET calibration constants vary across z-distance for a given set of evanescent field depths; however, for experiments involving live cells, this z-information is typically not available.

In live cells, calculation of sensitized emission FRET calibration constants under TIRF results in values that represent a weighted average of each constant over the z-distances imaged. To estimate the magnitude of error one might expect to see in FRET measurements where the evanescent field profiles between illumination wavelengths are either matched or mismatched, we took the average of each constant vs. z-distance relationship over the first 525nm from the glass interface, and applied the averaged values of these constants toward calculations of EA, ED, and Ratio vs. z-distance, using images of beads coated with the linked CFP-citrine protein. The results are shown in Figure 4.2D-F. Here, error-free measurements of EA and ED would be apparent as a horizontal line at 0.40 (the FRET efficiency of the CFP-citrine linked probe); similarly, error-free measurements of Ratio would be seen as a horizontal line at 1.0. In Figures 4.2D and 4.2F, large variations of EA and Ratio are clearly seen with mismatched TIRF depths. Figure 4.2D shows that while ED measurements demonstrate some variation for mismatched depths, this error is remarkably less pronounced than for EA and Ratio. The differences in the magnitude of these effects are likely due to the fact that EA and Ratio measurements are largely dependent on the calibration constants α and γ, which demonstrated large variations across z-distance for mismatched TIRF depths; ED, however, is mostly dependent on ξ, which exhibited relatively small variations across z-distance with mismatched TIRF depths. Again, note that the largest errors in FRET measurement occur at depths < 500nm, where the most relevant TIRF-FRET measurements would occur.

Most importantly, errors in calculation of EA, ED, and Ratio are minimized when the evanescent profiles of the illumination wavelengths are closely matched. Matched TIRF depths minimize the variation in FRET calibration constants over z-distance, which in turn minimizes the error in FRET calculations in the z-dimension, when averaged calibration constants are applied. This is particularly important for TIRF-FRET imaging, as variations of the constants and of FRET measurements occur over the exact z-distances where the TIRF measurements of highest import occur. Therefore, in live cells, FRET calibration constants are best determined using probes that localize to the specific sub-cellular compartments of interest. This would ensure that constants are averaged only over the z-distances that are relevant to the FRET measurements at hand.

Effects of different but matched TIRF depths on FRET calibration constants

We next determined the effects of different, but matched, TIRF depths (ie, D_{442} and D_{514} both shallow, or D_{442} and D_{514} both deep) on the values of the FRET calibration constants. The FRET calibration constants were again measured using fluoroprotein-coated beads, this time, with the following illumination sets: 1) D_{442} and D_{514} matched at ~270nm; 2) D_{442} and D_{514} matched at ~ 200nm; or 3) D_{442} and D_{514} matched at ~150nm. The results are shown in Figure 4.3. Note that the calibration constants vs. z-distance relationships stay relatively constant across z-distance, as a result of the closely matched TIRF illumination depths. Interestingly, the magnitude of α is shown to increase with increasing TIRF characteristic depths (Figure 4.3A), whereas the value for γ decreases with increasing TIRF characteristic depths (Figure 4.3C). α and γ are determined largely by either the ratio or inverse ratio, respectively, of images acquired from excitation with the 442nm line and the 514nm line (CIDA and CIAA). While the characteristic depths of these evanescent fields are matched, this can only be achieved by setting the incident angles of the 442nm and 514nm lines to different values. Importantly, the initial intensity of an evanescent field at the glass-water interface is known to be dependent upon the angle of incidence, with larger angles of incidence resulting in weaker initial evanescent field intensities [11]. This property could explain the inversely-related changes in the magnitudes of α and γ with changes in the characteristic depth, as it appears that the relative difference between the initial evanescent field intensities between the 442nm and 514nm lines increases with increasing characteristic TIRF depth. Figure 4.3B and Figure 4.3D demonstrate that the magnitude of both β and ξ remains constant, regardless of the TIRF depths used. This result is in line with the fact that determination of both β and ξ depends primarily on the ratio of two images acquired using only the 442nm line (CIDA and CIDD). Thus, unlike α and γ, the absolute magnitude of β or ξ should not be expected to change with characteristic depth.

Sensitized Emission TIRF-FRET on moving compartments: Effects of z-distance motions on FRET calculations

The exponential decay of the evanescent field in the z-dimension allows fluorescence intensity under TIRF to be used as a highly sensitive gauge of motions in the z-axis. Indeed, one of the major uses of time lapse TIRF imaging in live cells to date involves studying the motions of specific sub-cellular compartments (eg., secretory granules) in cells over time, and relating these motions to the functional state of each compartment [30-34] . For TIRF-FRET imaging, however, these z-motions result in intensity changes that could potentially confound the interpretation of time lapse TIRF-

FRET measurements in which the FRET signal localizes to such a moving compartment. Therefore, we next characterized the effects of z-motions of sub-cellular compartments on TIRF-FRET measurements, initially under conditions where the "true" FRET signal on the compartment remained unchanged.

Initially, we considered a case where the FRET signal is localized to a sub-cellular compartment, and where all of the acceptor and donor molecules also localize to this compartment. This situation is in essence modeled in Figures 4.2D-F (with D_{442} and D_{514} matched), where each point on the bead can be thought of as a sub-cellular compartment at a specific z-distance from the glass coverslip. Motions of the compartment in the z-axis can be visualized by moving up or down along the bead surface. Note that the actual FRET efficiency on the compartment at any z-distance should remain constant at 0.4 (the characteristic FRET efficiency of the CFP-citrine probe). Figures 4.2D-F illustrate that, in this scenario, z-motions have virtually no effect on the apparent FRET efficiencies measured. This occurs, as movement of the compartment away from the glass interface in the z-direction decreases the sensitized emission FRET signal in equal proportion to the decrease in total donor and total acceptor fluorescence signals (as all signals localize only to the compartment). Likewise, the molar ratio of acceptor to donor also remains constant, as both acceptor and donor signals always change proportionally with movements of the compartment in the z-direction.

We next examined a more physiological scenario, where the FRET signal localizes to a subcellular compartment, but where only a portion of the total acceptor or donor localizes to that compartment, with the rest of the acceptor or donor displaying a soluble cytosolic distribution. This scenario is common in cell biology; a specific example is a Rab protein that, depending on its activation state, cycles onto or off of a secretory granule, and that may only interact with its effector protein when it is cycled onto the granule. To understand how changes in the z-motion of a compartment might result in apparent changes in the measured FRET values, we tested an experimental model of this situation. Similar to above, we imaged 10μm beads coated with the linked CFP-citrine protein, but this time, with 3 different concentrations of soluble citrine added to the imaging solution, to represent different extents of cytosolic localization of the acceptor (the donor remains fully localized to the compartment). The results of the apparent FRET efficiency calculations on these beads are shown in Figures 4.4A,C,E.

Figure 4.4A shows the measured EA vs. z-distance relationships for the beads, and demonstrates that the measured EA values decrease with increasing z-distances of the compartment from the glass interface. This effect is graded, with higher levels of soluble citrine resulting in larger overall decreases in EA. An explanation of these results is that as the compartment moves away from the glass interface, the intensity of the FRET signal (which is localized to the compartment) decreases exponentially; similarly, the intensity of the acceptor signal localized to the compartment also decreases exponentially. However, the growing space between the glass interface and the compartment is filled with the soluble population of acceptor, and depending on the relative concentrations of the soluble acceptor and the acceptor localized to the compartment, the intensity of the total acceptor signal might either decrease (in a less-than-exponential fashion), or increase. As EA represents the ratio of the sensitized emission FRET signal to the total acceptor signal, the result is that EA will decrease with increasing z-distance of the compartment from the glass interface. In Figure 4.4C, the measured ED vs. z-distance relationships are shown, indicating that ED exhibits minimal changes over z-distance, compared to EA. As expected, this results arises from the fact that both the FRET signal and the total donor signal localize to the compartment, and therefore are subject to the same relative changes in intensity as the compartment moves in the z-direction. As ED is the ratio of the FRET signal to the total donor signal, ED should remain unchanged with movement of the compartment in the z-direction. Figure 4.4E demonstrates that the measured Ratio increases as the compartment is moved away from the glass interface, with larger increases in ratio occurring with higher concentrations of soluble citrine in the imaging media. An explanation for this result is that as the compartment moves away from the glass interface, the total acceptor signal will either be decreasing in a less-than-exponential fashion, or increasing (as described above), while the total donor signal will be decreasing exponentially. As the molar ratio is the ratio of total acceptor signal to total donor signal, the result is that the molar ratio increases as the compartment moves away from the glass.

The data shown in Figures 4.4A,C,E use a simplified model (i.e., the surface of 10μm beads) to describe the effects of a moving subcellular compartment on FRET measurements. However, to examine a more physiologically relevant situation, such as that which might arise with a secretory granule (a spherical compartment with 350nm diameter) moving in the z-dimension, we generated a mathematical model to simulate TIRF-FRET under various conditions. This model is based on that described in [21], with the central difference being that in the current model, the illumination intensity decays exponentially in the z-dimension. To validate this model, we first simulated the experiments from Figures 4.4A,C,E, by modeling a bead of 10μm diameter coated with a linked FRET probe, resting on the surface of a glass coverslip with a set concentration of soluble acceptor in the surrounding media. To model each experimental condition (ie, each different concentration of soluble acceptor in the imaging media), the concentration of soluble acceptor in the model was adjusted, such that ratio of the maximum on-bead fluorescence intensity (ie, at the very bottom of the bead) to the off-bead fluorescence intensity (ie, determined in a region clearly outside of the bead) calculated by the model matched that determined for each experimental condition. The results of this model are shown in Figures 4.4B,D,F. Notably, the model accurately matched the shapes and trends of the EA, ED, and Ratio relationships as measured experimentally, with EA values decreasing, Ratio values increasing, and ED values remaining unchanged with increasing z-distance of the bead surface from the glass coverslip. Moreover, for EA and Ratio, the effects were graded with respect to the concentration of soluble acceptor. While the model did not fit the experimental data perfectly, this likely results from the underlying assumption used to match the conditions in the model with the experimental conditions. Namely, we assumed that the off-bead fluorescence determined in the experiments resulted solely from soluble acceptor, whereas the on-bead maximal fluorescence resulted solely from the linked fluorophore conjugated to the bead. In actuality, these fluorescence intensities likely also include contribution from non-specific binding of the soluble acceptor to the coverglass, and perhaps to the bead; moreover, there may have been a thin film of soluble acceptor between the bead and the coverglass. Each of these situations would result in an error in our estimate of the soluble concentration of the acceptor. These different non-specific localizations of the acceptor signal (ie, to the bead or to the coverglass), when incorporated into the model, resulted in shifts in the relationships determined for EA and Ratio vs. z-distance (see Supplemental Data, Figure 4.S1).

We next used this TIRF-FRET model to simulate how motions of secretory granules might affect TIRF-FRET measurements where FRET was localized to the granule. Granules were modeled as spheres with 350nm diameter (as opposed to the 10µm beads) coated with a linked FRET probe, and surrounded by a solution containing soluble acceptor. The distance of the bottom of the granule from the glass coverslip was varied in the model, and the apparent FRET measurements were calculated through the center of the granule (ie, from the bottom-most to top-most points on the granule). Characteristic TIRF depths of the donor and excitation wavelengths were matched at either 170nm or 270nm. The results of the simulation for EA and Ratio are shown in

Figure 4.4G-H. As before, ED remained constant at 0.4 regardless of the granule's z-position, and the results are therefore not shown here. The effects of the moving granule on EA and Ratio are similar, and at z-distances close to the bead, are slightly more pronounced than the results obtained from modeling a 10 μm bead. This effect is likely due to the contribution of the soluble fluorescence above the 350nm granule, which while small, is present, unlike the case for the 10μm granule, where there is in essence no soluble contribution of fluorescence above the bead. The 170nm TIRF depth resulted in a slightly larger effect on EA and Ratio at short z-distances (<500nm), compared to the 270nm depth, although this situation was reversed at larger z-distances.

Sensitized Emission TIRF-FRET in Living Cells

The application of sensitized emission TIRF-FRET in living cells was first tested using the simplest situation in which the donor and acceptor were directly linked and targeted to the plasma membrane. Targeting to the plasma membrane was achieved by fusing the linked FRET probe to the N-terminus of the pleckstrin homology (PH) domain of phospholipase Cδ. TIRF-FRET images were taken of MIN6 cells expressing the linked-PH probe either alone, or in addition to soluble cerulean (donor) or soluble citrine (acceptor), using D_{442} and D_{514} matched at ~160nm. Figure 4.5A shows representative TIRF images of these cell footprints. Note that while the fluorescence signal and calculated FRET values are largely uniform across the footprint, some streakiness can be detected in the images, which results from interference fringes generated by the scatter and diffraction of the coherent laser light. Figures 4.5B-D show the averaged values for the fraction of acceptor in complex (fA), fraction of donor in complex (fD), and molar ratio, for the three different protein expression conditions. Note that cells expressing the linked-PH probe alone correctly show fA = fD = 1, and ratio = 1. As expected, cells expressing the linked-PH probe with soluble cerulean demonstrate a decrease in fD, no change in fA, and an increase in the molar ratio on average. Importantly, there is a linear relationship between fD and ratio, while the fA values remain scattered around 1, as shown in Figure 4.5E. Conversely, cells expressing the linked-PH probe with soluble citrine demonstrate no change in fD, a decrease in fA, and an increase in the molar ratio on average. Notably, there is a clear linear relationship between fA and the inverse molar ratio for these cells, while fD remains scattered around 1 (Figure 4.5F). Taken together, these data demonstrate the validity of using sensitized emission TIRF FRET in cells where the FRET is localized to the plasma membrane.

We next tested the use of sensitized emission TIRF-FRET in cells in which the FRET signal was localized to intracellular compartments. For these experiments, MIN6 cells were transfected with a linked citrine-cerulean FRET probe that was fused to the N-terminus of the protein VAMP2. In addition to localizing to secretory granules, this probe also localized somewhat nonspecifically to a variety of constitutive trafficking organelles and other compartments likely involved in vesicle biogenesis. MIN6 cells were transfected with the citrine-cerulean-VAMP2 construct alone, or in addition to soluble cerulean or soluble citrine, and TIRF-FRET images were taken with D_{442} and D_{514} matched at ~270nm. Individual granules were detected in each frame, and the averaged CIDD, CIDA, and CIAA intensity values within a 13-pixel diamond centered on the granule were used to determine the FRET on the granule. Representative images of these cell footprints and the resulting FRET measurements are shown in Figure 4.6A. Note the diffuse fluorescent signal apparent in the CIDD and CIAA images for the cells co-expressing soluble cerulean or citrine, respectively. Importantly, as shown in Figures 4.6B and 4.6C, the averaged fractions of donor and acceptor in complex, as well as the averaged molar ratios, change as expected for cells co-expressing the linked-VAMP2 construct in addition to soluble cerulean or citrine.

Discussion

The ability to sequence protein-protein interactions as they occur in living cells in real-time, with high spatial resolution, is paramount to furthering our understanding of the detailed molecular underpinnings of many important biological functions. Sensitized emission TIRF-FRET has the potential and unique capability of being able to resolve, both temporally and spatially, exactly these kinds of details. However, this method is not without its complications, as precise calibrations to the imaging system and the fluorescent probes being used are required, such that instrument-independent indices of apparent FRET efficiencies and molar ratios of acceptor to donor can be reported accurately. Application of this method is largely straight-forward for simple situations in which both donor and acceptor are on the same molecule, which localizes to the plasma membrane. However, our results demonstrate that for more complex situations, for instance, where donor and acceptor tagged molecules localize to multiple intracellular compartments (such as secretory granules and the cytosol), and moreover, where the intracellular compartment may be moving in the z-axis over the time course of the experiments, additional considerations must be taken into account.

Setting the characteristic TIRF depths for the two excitation lines.

An important consideration in TIRF-FRET is the effects on sensitized emission FRET calibration constants when characteristic TIRF depths for the 442nm and 514nm excitation lines are matched versus slightly mismatched. Large silica beads conjugated with the fluoroproteins required for the FRET calibrations (eg, CFP, citrine, and a linked CFP-citrine) allowed for a direct measure of how each calibration constant varied with z-distance from the glass interface. The results demonstrate that when the characteristic TIRF depths of the illumination lines were mismatched, the calibration constant α demonstrated large variations across z-distance (which were most pronounced at distances close to the coverslip), with γ and ξ also exhibiting small but pronounced variations with z-distance. More importantly, when these calibration constants were averaged over the first 525nm in z-distance from the coverslip (to estimate the constants that might be obtained in a live-cell situation), and these averaged constants were applied to the FRET calculations, substantial errors arose in the calculated EA and Ratio over z-distance, with small but noticeable errors in ED as well. Again, these errors were most prominent close to the glass coverslip (<500nm), at a range where most important TIRF measurements are made. Notably, these errors were largely eliminated when the characteristic TIRF depths of the illumination lines were matched. Therefore, for sensitized emission TIRF-FRET measurements that involve compartments moving in the z-dimension over the course of the experiment, it is critical that the characteristic TIRF depths between excitation lines be closely matched. Failure to do so could result in apparent changes in FRET that are due to movement of the compartment, rather than being due to an actual change in protein-protein interaction / probe re-orientation on the compartment.

Of note, we have determined the effects of characteristic TIRF depths on sensitized emission FRET calibration constants, specifically with regard to the method of FRET stoichiometry [21, 25]. FRET stoichiometry is a 3-cube FRET method that is particularly advantageous in that it allows for simultaneous tracking of both acceptor occupancy and donor occupancy for a given bimolecular interaction (most other 3-cube FRET methods are only capable of tracking either the acceptor or donor only), and moreover, for determination of the molar ratio of total acceptor to total donor (this capability is unique to FRET stoichiometry). However, almost all 3-cube FRET imaging methods use calibration constants similar to α and β to correct for cross-talk and bleed-through, in order to specifically isolate the sensitized emission signal from these spectral contaminants. Conversion of the isolated sensitized emission FRET signal to instrument-independent measures of apparent FRET efficiency additionally requires another calibration constant, usually termed the G-factor [27, 29, 35] or alpha [28], that relates the fluorescence intensity of the acceptor molecule to that of the donor molecule. Importantly, the G-factor (or alpha) is equivalent to the quotient of the FRET stoichoimetry calibration parameters, γ/ξ. The G-factor can be calculated in a number of different ways, for example, by donor dequenching of a linked FRET probe, or by measurements of several different linked FRET constructs with different FRET efficiencies. Regardless, all of these measurements ultimately require imaging of a linked FRET probe with the imaging system used for the FRET experiment. Therefore, the effects described here of mismatched characteristic TIRF depths on FRET stoichiometry calibration constants are generalizable to other 3-cube sensitized emission FRET modalities as well.

Can sensitized-emission TIRF-FRET be used on cells with multiple probe localizations?

While time-lapse imaging using sensitized-emission TIRF-FRET has been reported in live cells for the simple case of a plasma-membrane associated protein double-labeled with both donor and acceptor [18], our goal was to expand the range of possibilities for FRET calculations using this method. For instance, do changes in FRET that are measured over time accurately reflect changes in the extent of protein-protein interactions or in re-orientation of probes on an intracellular compartment (eg, a secretory granule) over time? Moreover, does the same hold true if one or both of the probes demonstrates multiple subcellular localizations (eg, secretory granule and cytosol)? Lastly, how are these FRET measurements affected by motions of intracellular compartments in the z-dimension?

The results of our TIRF-FRET modeling offer some general guidelines for timelapse TIRF-FRET imaging of subcellular compartments in the presence of a partially cytosolic probe. First, if both donor and acceptor localize completely to an intracellular compartment, then changes in apparent FRET efficiency (both EA and ED) and molar ratio on the compartment can be accurately tracked, regardless of whether the compartment is moving in the z-axis. Second, if only one of probes exhibits partially cytosolic localization (for example, the acceptor), then the apparent FRET efficiency of the other probe (in this case, the apparent FRET efficiency of the donor, or ED) can be used as a measure of FRET that is independent of z-axis motions of the compartment. However, if the apparent FRET efficiency of the probe exhibiting multiple localizations (EA, in this case), as well as the molar ratio, are important to track, these values can be followed under limited circumstances. In the case of a 350nm granule, if the background soluble fluorescence signal is less than 5% of the peak fluorescence intensity of the acceptor on the granule, then large (up to 500nm) motions of the granule can be tolerated before a 10% change in EA or ratio results. However, with larger fractions of cytosolically distributed acceptor, a 10% change in EA or ratio could easily occur with less than 100nm movement in the z-direction. Theoretically, it may be possible to correct the EA and Ratio values for the z-motions of granules, using a model similar to the one used in this paper, to determine the signal of the soluble fluorescence component above and below the granule, and to correct for changes in this signal as the granule moves in the z-axis. This would require that the z-motions of the granule be accurately followed over time, either using a 3rd granule-filling, spectrally separated fluoresecent probe, or by following the total acceptor signal. The acceptor signal will be a valid measure only if it localizes completely to the granule, and if the distribution of the acceptor signal on the granule does not change over time. It is important to note that these caveats apply mainly for studies on subcellular compartments that may be moving in the z-dimension; studies of processes that occur only on the plasma membrane, for instance, are relatively free from the caveats discussed above.

Other considerations for sensitized emission TIRF-FRET.

The major benefit of sensitized emission TIRF-FRET, as opposed to other FRET methods performed under TIRF, lies in its potential for being used in time lapse imaging. However, under TIRF, we demonstrate that observed changes in apparent FRET efficiency over time may result from a variety of different factors, aside from actual changes in the bimolecular FRET interaction or re-orientation of the FRET probes. Our investigations have addressed effects on TIRF-FRET of motion of an intracellular compartment in the z-axis. Although not specifically addressed here, the effects of photobleaching also need to be considered for proper measurement and calculation of FRET; this is especially important for applications requiring high temporal resolution over prolonged periods of time. Prior reports have described specific photobleaching correction schemes for sensitized emission FRET under a widefield microscope [29], and these corrections may be used to correct for photobleaching in sensitized emission TIRF-FRET, provided that variations of the z-profile of the fluorophores over time is minimal. Another factor that should be considered is the interference fringes that arise with evanescent illumination, as a result of scattering of the coherent light source. In a worst-case scenario, these fringes could cause local differences in illumination intensity that result in incorrectly reported FRET values. Importantly, several effective solutions to this problem have been previously described, including rapid circling of the illumination light in the back focal plane of the objective [36, 37]. Lastly, other considerations that should be taken into account are instrumentation noise and noise associated with motion of subcellular compartments in between images.

We have applied these guidelines to perform sensitized emission TIRF-FRET in living cells expressing a linked citrine-cerulean FRET probe that localizes either to the plasma membrane, or to intracellular compartments (including secretory granules). Importantly, the apparent FRET efficiencies, EA and ED, and the molar ratio, shifted accordingly when cerulean or soluble citrine were co-expressed with the linked probe. Moreover, in cells expressing the linked probe localized to the plasma membrane, the calculated fraction of acceptor (fA) or donor (fD) in complex displayed a linear relationship with the calculated molar ratios.

The development and use of sensitized emission TIRF-FRET in living cells will likely have a large impact on our understanding of the dynamics of biological processes that occur close to or at the plasma membrane. At the plasma membrane, dynamic TIRF-FRET measurements have the possibilities of elucidating changes in conformational structure, post-translational modification, and even protein-protein interactions of channels that occur upon ligand binding or depolarization of the membrane. The field of membrane trafficking is also rife with possibilities. What molecular interactions must occur to allow for the regulated insertion or removal of specific cell receptors or channels to the plasma membrane? Are there protein-protein interactions that dictate, spatially, where these receptors or channels are inserted? Similarly, the fields of regulated exocytosis and endocytosis also have much to benefit from this approach. As exocytosis and endocytosis occur as a cycle, one of the major challenges in this field has been to tease apart whether specific protein-protein interactions must occur prior to or following membrane fusion events. However, sensitized emission TIRF-FRET has the capability not only to track when protein-protein interactions occur, but also to resolve the functional state and behavior of the individual secretory granules that these interactions may be occurring on. Therefore, being able to directly correlate the when and where of a protein-protein interaction to the functional state of a granule becomes a real possibility, and one that will be crucial to our understanding of these highly dynamic processes.

Figure 4.1. Measurement of evanescent field profiles for 442nm and 514nm laser lines. (A) Theoretical plots of the relationship between characteristic TIRF depth and angle of incidence, for 442nm (purple curve) and 514nm (green curve) laser lines, using n_1 = 1.515 and n_2 = 1.37 (Eq 7). (B) Schematic depicting the measurement of characteristic TIRF depths using large silica beads, based on methods developed in [26]. A spherical bead coated with fluorophore is shown resting on the surface of a glass coverslip (left). The image of the bead footprint under TIRF (right) can be used to determine the profile of the evanescent field, as the fluorescence intensity of the bead at a given radial distance, d, from the center of the bead footprint corresponds to fluorescence arising from the bead surface at a specific z-distance, z1, from the glass interface. Conversion of radial distance to z-distance is accomplished using the geometry of a sphere with known radius, R. (C) *Left,* Representative images (pseudo-colored below) of 10 μm silica beads conjugated with citrine and imaged with the 442nm laser line, under epifluorescence (EPI) or TIRF modes. Numbers above the bead footprints represent the characteristic depths determined for the incident TIRF angle used to acquire each image. *Center,* Average normalized intensity vs z-distance relationships, acquired from beads imaged using the 442nm laser line at three different incident TIRF angles. Relationships were fitted to a double exponential (Eq 6) to determine the characteristic depth at each incident angle; characteristic depths depicted are: 278nm, 221nm, and 150nm. *Right,* Average characteristic TIRF depths were calculated from beads imaged using 5 incident angles, and plotted (purple markers) against the incident TIRF angle, which was measured using the prism method. Solid curves indicate theoretical relationships between characteristic TIRF depth and angle of incidence (Eq 7) for a 442nm laser, using n_1 = 1.515 and n_2 = 1.37 (lower curve) or 1.38 (upper curve). Beads were imaged in a solution where n ~ 1.372. Markers represent the mean ± SEM. Numbers in parenthesis above each bead represent the number of beads used for each measurement. (D) Similar to (C), except that beads were imaged using a focused 514nm laser line. *Center,* Characteristic depths depicted are: 249nm, 194nm, and 151nm. *Right, M*arkers in green represent the characteristic depths measured for the focused 514nm laser line. Solid curves indicate the theoretically determined relationships for a 514nm laser. Markers in black indicate the characteristic depths measured for the 514nm line when it was slightly defocused. As expected, the depths measured for the defocused laser are deeper than the theoretical predictions.

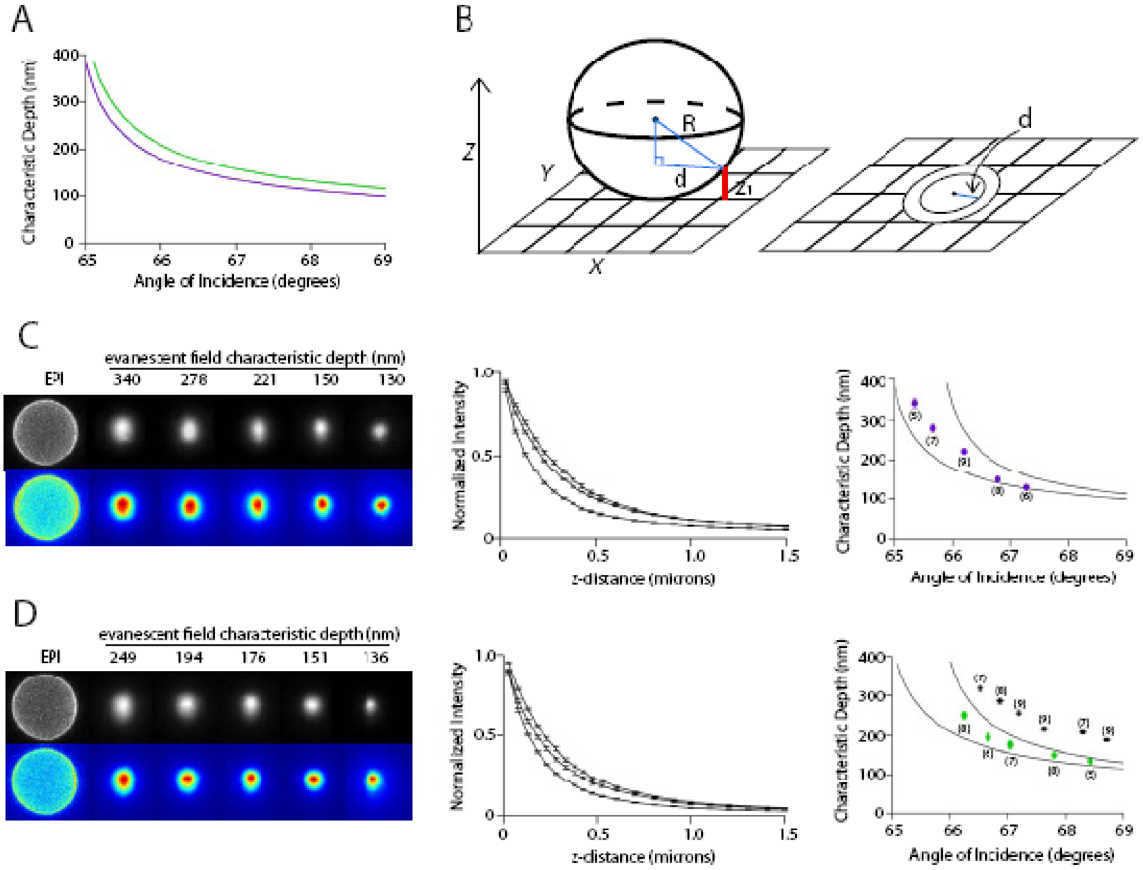
A
Characteristic Depth (nm)
400
300
200
100
0
65
66
67
68
69
Angle of Incidence (degrees)
B
Z
Y
X
R
d
Z1
d
C
EPI
evanescent field characteristic depth (nm)
340
278
221
150
130
Normalized Intensity
1.0
0.5
0
0
0.5
1.0
1.5
z-distance (microns)
Characteristic Depth (nm)
400
300
200
100
0
65
66
67
68
69
Angle of Incidence (degrees)
D
EPI
evanescent field characteristic depth (nm)
249
194
176
151
136
Normalized Intensity
1.0
0.5
0
0
0.5
1.0
1.5
z-distance (microns)
Characteristic Depth (nm)
400
300
200
100
0
65
66
67
68
69
Angle of Incidence (degrees)

Figure 4.2. Relationship of FRET values measured under TIRF, to differently matched characteristic TIRF depths of excitation wavelengths. For all plots, the open circles represent data obtained when the characteristic TIRF depth of the 442nm laser (D_{442}) was matched with the characteristic TIRF depth of the 514nm laser (D_{514}), at ~270nm. Open squares represent data obtained where $D_{442} > D_{514}$, with D_{442} ~ 280nm and D_{514} ~ 140nm. Open triangles represent data obtained where $D_{442} < D_{514}$, with D_{442} ~ 160nm and D_{514} ~ 270nm. Markers represent the mean ± SEM. (A-C) Relationships of FRET calibration constants vs. z-distance were determined by imaging 10µm beads conjugated with either citrine (for α) or a linked CFP-citrine protein (for γ and ξ). The intensity vs. z-distance relationships of each bead in the DD, DA, and AA images were then used to determine the relationships of (A) α vs z-distance, (B) γ vs z-distance, and (C) ξ vs z-distance. Determination of γ and ξ vs z-distance for each condition utilized the α- and β-vs z-distance relationships for that condition. All plots were normalized to the initial value of each constant at z = 0. β is not shown as β requires only the 442nm laser line (but, see Figure 4.3). The number of beads used for each average measurement in order of ($D_{442} > D_{514}$, $D_{442} < D_{514}$, and $D_{442} = D_{514}$) was: α: (7, 7, 12); β (6, 8, 6); ξ and γ: (7, 4, 10). (D-F) Estimation of the error associated with FRET measurements as a result of FRET calibration constants varying in the z-dimension. FRET calculations were carried out on images of beads conjugated with the linked CFP-citrine protein. A single “flat” set of FRET calibration constants was determined for each imaging condition, by calculating the average value of each constant for that condition over the first 0.525µm in the z-dimension. These “flat” estimates of the calibration constants were then used with the intensity vs. z-distance relationships for DD, DA, and AA images to determine the relationships of (D) EA vs z-distance, (E) ED vs z-distance, and (F) Ratio vs z-distance, for each imaging condition. Note that an error-free measurement of EA or ED would be evident as a flat horizontal line with EA, ED = 0.4. Error-free measurement of Ratio would be evident as a flat horizontal line with Ratio = 1. The number of beads used for each averaged measurement of EA, ED, Ratio was, in order of ($D_{442} > D_{514}$; $D_{442} < D_{514}$; and $D_{442} = D_{514}$): (7, 4, 10).

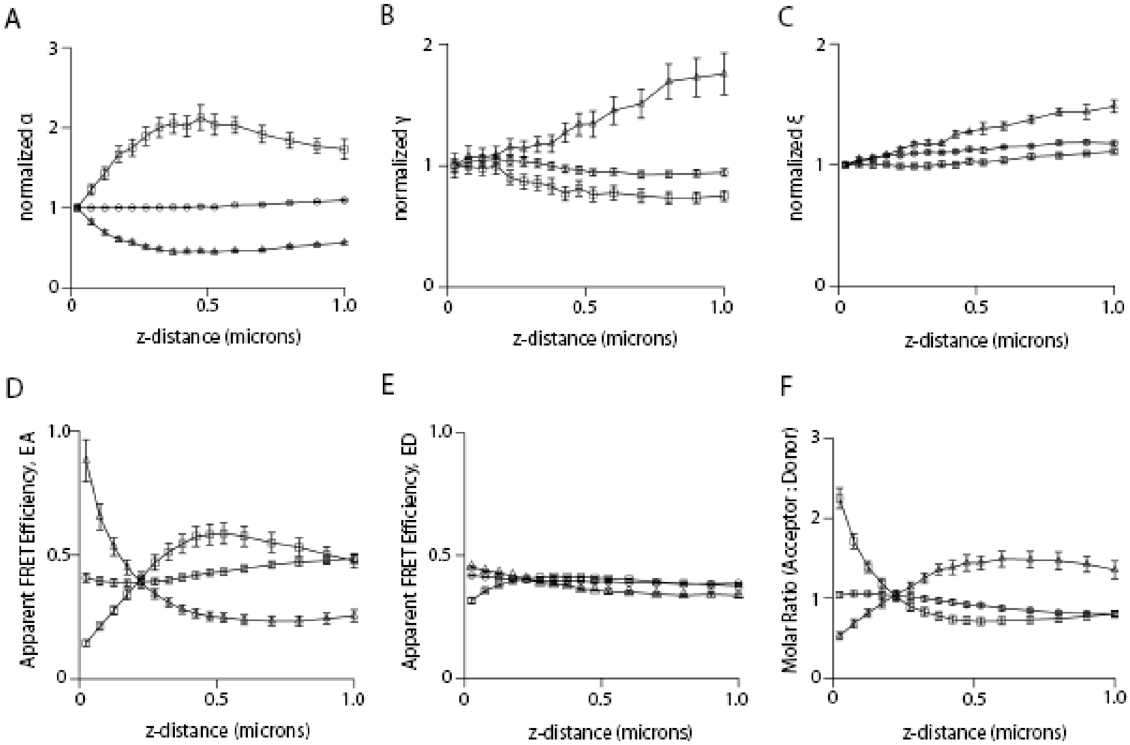
A
normalized α
3
2
1
0
0
0.5
1.0
z-distance (microns)
B
normalized γ
2
1
0
0
0.5
1.0
z-distance (microns)
C
normalized ξ
2
1
0
0
0.5
1.0
z-distance (microns)
D
Apparent FRET Efficiency, EA
1.0
0.5
0
0
0.5
1.0
z-distance (microns)
E
Apparent FRET Efficiency, ED
1.0
0.5
0
0
0.5
1.0
z-distance (microns)
F
Molar Ratio (Acceptor : Donor)
3
2
1
0
0
0.5
1.0
z-distance (microns)

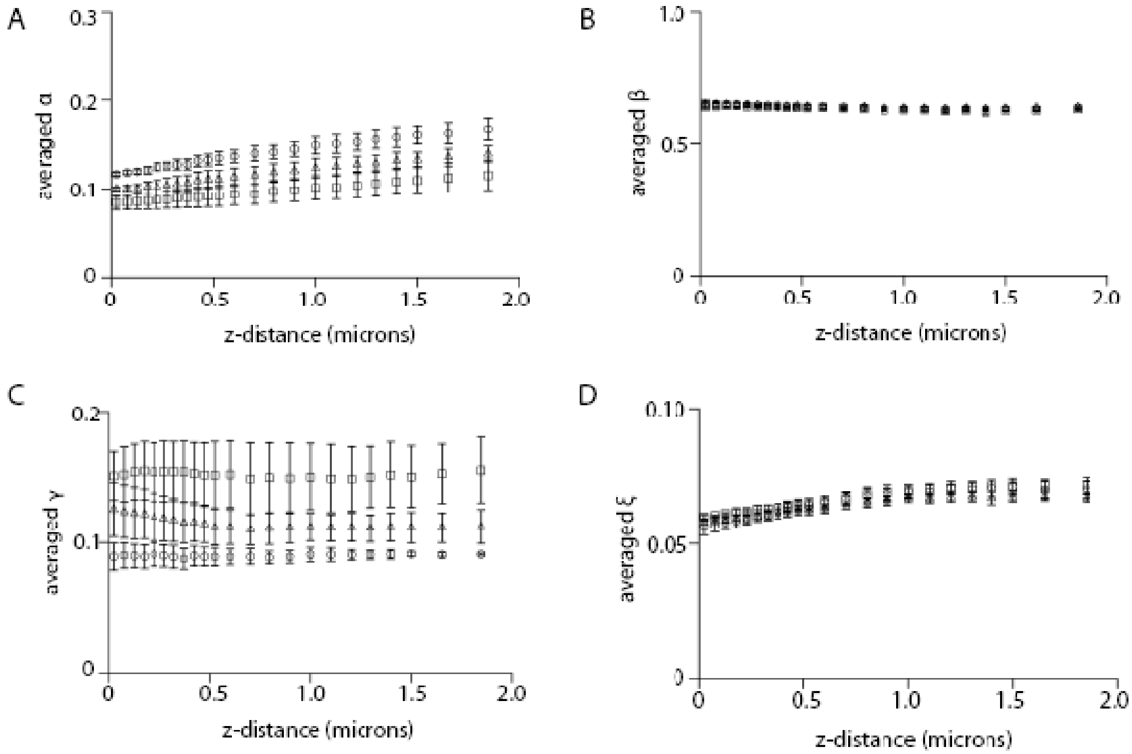

Figure 4.3. Effect of characteristic TIRF depth on FRET calibration constants. In these experiments, D_{442} and D_{514} were matched at either ~ 270nm (open squares), 200nm (open triangles), or 150nm (open circles). FRET calibration constants were determined by imaging 10µm beads conjugated with either CFP (for β), citrine (for α) or a linked CFP-citrine protein (for γ and ξ). The intensity vs. z-distance relationships of each bead in the DD, DA, and AA images were used to determine the relationships of (A) α vs z-distance, (B) β vs z-distance, (C) γ vs z-distance, and (D) ξ vs z-distance. Determination of γ and ξ vs z-distance for each condition utilized the α- and β-vs z-distance relationships for that condition. Averaged values of the FRET calibration constants vs z-distance were obtained from data pooled from 3 independent experiments, each of which used a minimum of 7 beads. Markers represent the mean ± SEM.

Figure 4.4. Effect of a soluble population of fluorophores on TIRF-FRET measurements. Relationships of (A) EA vs. z-distance, (C) ED vs. z-distance, and (E) Ratio vs. z-distance, were determined using 10μm silica beads conjugated with a linked CFP-citrine protein, with soluble citrine added to the imaging media. The 3 curves in each plot represent different concentrations of soluble citrine that were used, where the fluorescence intensity of a region outside the bead region (off-bead) was determined to be approximately 4% (red open squares), 12% (green open triangles), or 18% (blue open circles) of the peak fluorescence intensity in the center of the bead (on-bead), in AA images. TIRF-FRET imaging was carried out with D_{442} and D_{514} matched at ~ 270nm; calculations of EA, ED, and Ratio vs. z-distance used the FRET calibration constants vs. z-distance relationships obtained from beads imaged at this characteristic TIRF depth. Markers represent the mean ± SEM. The number of beads used for each set of averaged FRET measurements was (in order of 4%, 12%, 18% soluble acceptor): (8, 10, 11). (B, D, F) Mathematical TIRF-FRET simulation of a 10μm bead coated with a linked donor-acceptor FRET probe, modeled using the same experimental conditions as in (A,C,E). The theoretical relationships of (B) EA, (D) ED, and (F) Molar ratio vs. z-distance are shown for the 3 different concentrations of soluble acceptor (same color scheme as A,C,E). (G-H) Mathematical simulation of changes in measured (G) EA or (H) Ratio, when a linked FRET probe is localized to a 350nm granule moving in the z-dimension, with 3 different populations of free acceptor in the cytosol (as in A,C,E, the ratios of the soluble acceptor fluorescence to the peak acceptor fluorescence on the granule at z = 0 are 4% (red squares), 11% (green triangles), or 18% (blue circles). Two different characteristic TIRF depths (matched for D_{442} and D_{514}) were simulated: 270nm (open symbols) and 170nm (filled symbols).

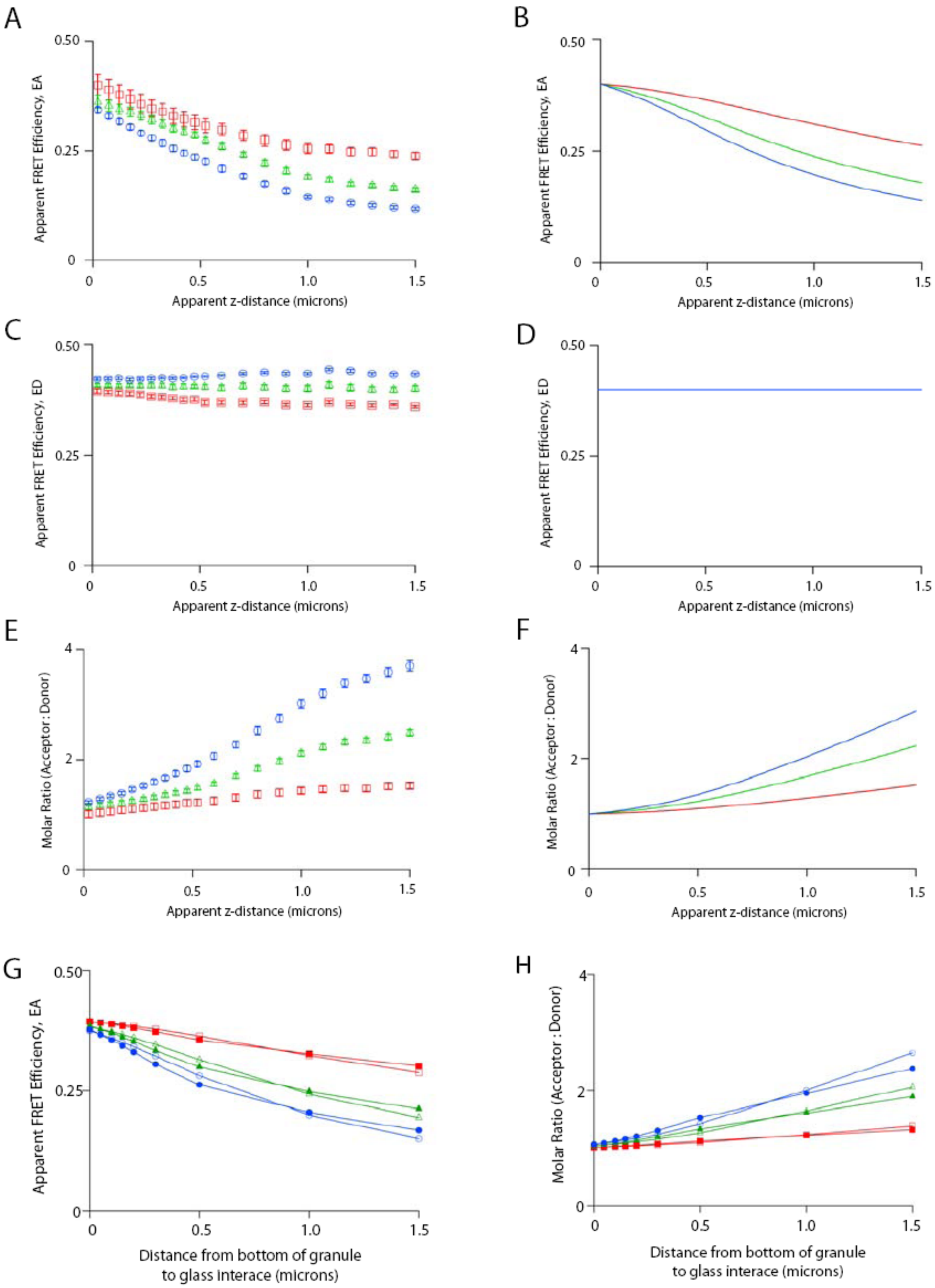
A
B
C
D
E
F
G
H
Apparent FRET Efficiency, EA
Apparent FRET Efficiency, ED
Molar Ratio (Acceptor : Donor)
Apparent z-distance (microns)
Distance from bottom of granule to glass interace (microns)
0
0.25
0.50
2
4
0.5
1.0
1.5

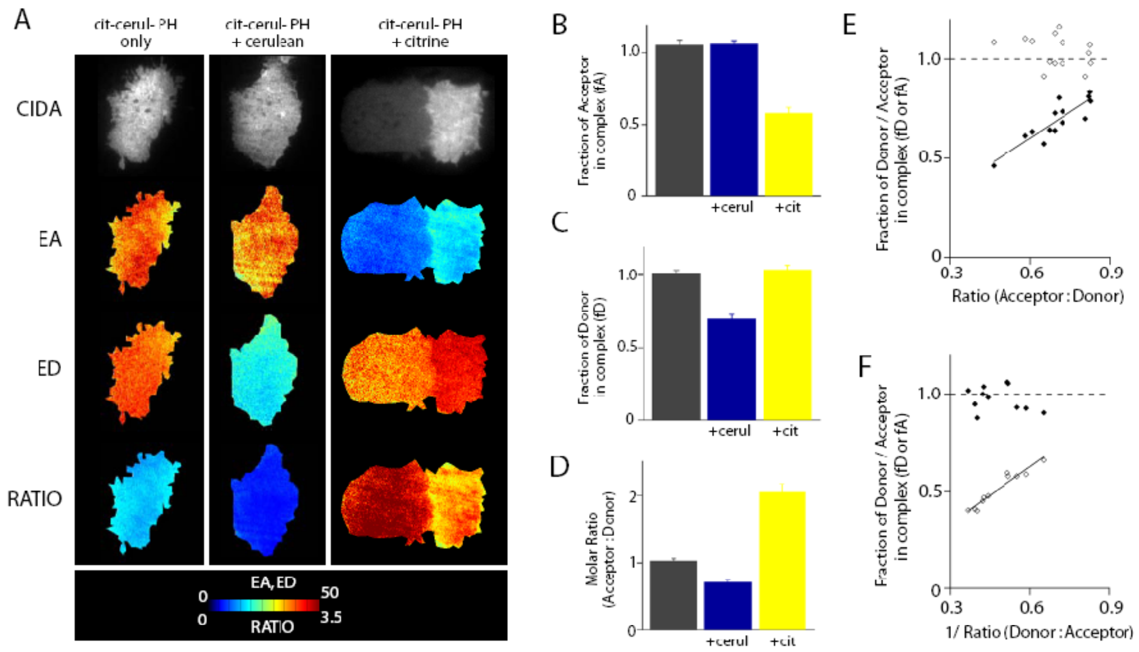

Figure 4.5. Sensitized-emission TIRF FRET measurements of a plasma-membrane targeted linked FRET probe in live MIN6 cells. Experiments utilized a linked citrine-cerulean FRET probe, fused to the pleckstrin homology (PH) domain of PLCδ, which results in this probe's targeting to the plasma membrane. (A) Representative images of MIN6 cells transfected with plasmids expressing citrine-cerulean-PH alone (left column), or in addition to soluble cerulean (middle column) or soluble citrine (right column). The image in the right column shows two adjacent cells that exhibit different fluoroprotein expression levels. (B) Averaged fraction of acceptor in complex, (C) Averaged fraction of donor in complex, and (D) Average molar ratio, determined from cells expressing citrine-cerulean-PH only (black), or in addition to soluble cerulean (blue) or soluble citrine (yellow). (E) Fraction of donor (fD, filled diamonds) or acceptor (fA, open diamonds) in complex vs molar ratio, plotted for individual MIN6 cells expressing citrine-cerulean-PH and soluble cerulean. The solid line indicates the linear fit for the fD vs. Ratio data. (F) Same as (E), but for MIN6 cells expressing citrine-cerulean-PH and soluble citrine. Here, the solid line represents the linear fit of the fA vs. ratio data. FRET stoichiometry calibration constants were obtained using cerulean-PH (for β), citrine-PH (for α), and citrine-cerulean-PH (for γ and ξ), and used the same TIRF angle of incidence as for the experiment. Bars represent the mean ± SEM. The number of cells used for each condition was: Linked-PH (12); Linked-PH + cerulean (14); Linked-PH + citrine (11).

Figure 4.6. Sensitized emission TIRF FRET measurements of a linked FRET probe, targeted to intracellular compartments in live MIN6 cells. These experiments utilized a linked citrine-cerulean FRET probe, fused to the N-terminus of VAMP2, which results in the probe primarily targeting to the surface of secretory granules. (A) Representative images of MIN6 cells transfected with plasmids expressing citrine-cerulean-VAMP2 alone (left column), or in addition to soluble cerulean (middle column) or soluble citrine (right column). Note the diffuse fluorescent signal in the CIDD image for the cell co-expressing soluble cerulean, and the diffuse signal in the CIAA image for the cell co-expressing soluble citrine. Apparent FRET efficiencies and molar ratios were determined on single granules, using averaged CIDD, CIDA, and CIAA intensities within a 13 pixel diamond centered on the granule. For images of EA, ED, and Ratio, the values calculated on each individual granule were pseudo-colored and overlaid on top of the CIDA image. (B) Averaged fraction of acceptor in complex, (C) Averaged fraction of donor in complex, and (D) Average molar ratio, determined from cells expressing citrine-cerulean-VAMP2 only (black), or in addition to soluble cerulean (blue) or soluble citrine (yellow). Averages were determined by pooling the EA, ED, or ratio values determined on individual granules. FRET stoichiometry calibration constants were obtained using cerulean-VAMP2 (for β), citrine-VAMP2 (for α) or citrine-cerulean-VAMP2 (for γ and ξ). Bars represent the mean ± SEM. The number of granules / cells used for each condition was: Linked-VAMP (417 granules/12 cells); Linked-VAMP + cerulean (358 / 13); Linked-VAMP + citrine (551 / 10).

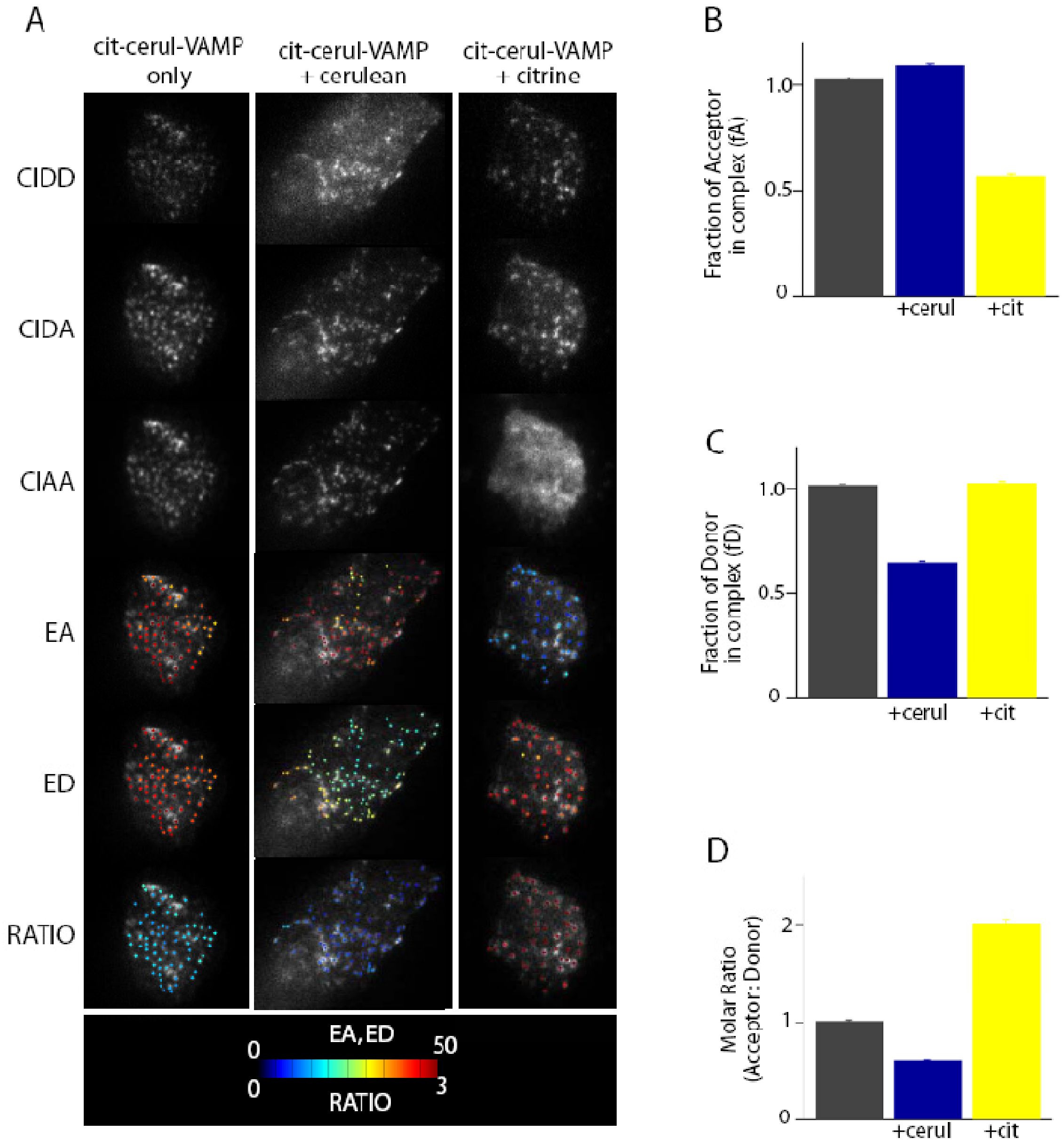
A
cit-cerul-VAMP only
cit-cerul-VAMP + cerulean
cit-cerul-VAMP + citrine
CIDD
CIDA
CIAA
EA
ED
RATIO
EA, ED
0
50
0
3
RATIO
B
Fraction of Acceptor in complex (fA)
1.0
0.5
0
+cerul
+cit
C
Fraction of Donor in complex (fD)
1.0
0.5
0
+cerul
+cit
D
Molar Ratio (Acceptor: Donor)
2
1
0
+cerul
+cit

Figure 4.S1. Modeling the effects of three alternative/nonspecific localizations of soluble acceptor on FRET calculations. (A) left, schematic of the first situation, where the bead floats on a thin layer of soluble acceptor. In this situation, the measured "on-bead" fluorescence consists of fluorescence arising from the linked probe conjugated to the bead, as well as from the soluble acceptor localized under the bead. Changing the thickness of this layer results in graded effects, mostly on the slope, of the calculated EA (middle) and Ratio (right) vs z-distance relationships. The thicknesses of the layers of soluble acceptor under the bead were modeled as: 50nm, 100nm, 200nm, and 300nm (shown as lines from red to blue). (B) left, schematic of the second situation, where a portion of the soluble acceptor is non-specifically bound to the glass coverslip. In this situation, the measured "on-bead' fluorescence arises both from the linked probe conjugated to the bead, as well as from the acceptor bound non-specifically to the coverglass underneath the bead. Similarly, the "off-bead" fluorescence arises from the soluble acceptor, as well as from the acceptor bound to the coverglass. Increasing the fraction of the soluble acceptor localizing to the coverglass result in graded decreases or increases in the magnitude of the measured EA (middle) or Ratio (right) vs. z-distance relationships, respectively, with no large changes in the overall shapes of the relationships. The percent of total "off-bead" fluorescence arising from acceptor bound non-specifically to the coverglass was modeled as: 10, 30, 50, 70, or 90% (from red to purple). (C) left, schematic of the third situation, where a portion of the acceptor is non-specifically bound to the surface of the bead. Here, the "on-bead" fluorescence arises from both the linked probe conjugated to the bead, as well as from the acceptor bound non-specifically to the bead. The "off-bead" fluorescence results solely from the soluble acceptor. Increasing the fraction of the "on-bead" fluorescence that arises from non-specific binding of the acceptor to the bead surface results in graded changes in the magnitude and to some extent, the slopes, of the EA (middle) and Ratio (right) vs. z-distance relationships. The percent of total "on-bead" fluorescence arising from acceptor bound non-specifically to the bead was modeled as: 2, 5, 10, 20, and 30% (from red to purple). In parts A-C, the black markers represent the experimentally measured values for the condition where the on-bead:off-bead fluorescence intensity ratio was determined to be 12%. The thick black line represents the original model (as shown in Figure 4.4) for this condition. The population of soluble acceptor in each of these modeled conditions was chosen such that the final "on-bead" fluorescence intensity : "off-bead" fluorescence intensity ratio was equal to 12%. In (A), increasing the layer of soluble acceptor between the coverglass and the bead required a decrease in the concentration of the soluble acceptor (pink to light pink background) to maintain an on-bead : off-bead ratio of 12%, whereas in (B) and (C), increasing the extent of soluble acceptor non-specifically localized to the coverslip or to the bead required increasing the concentration of soluble acceptor (pink to dark pink background) to maintain this ratio.

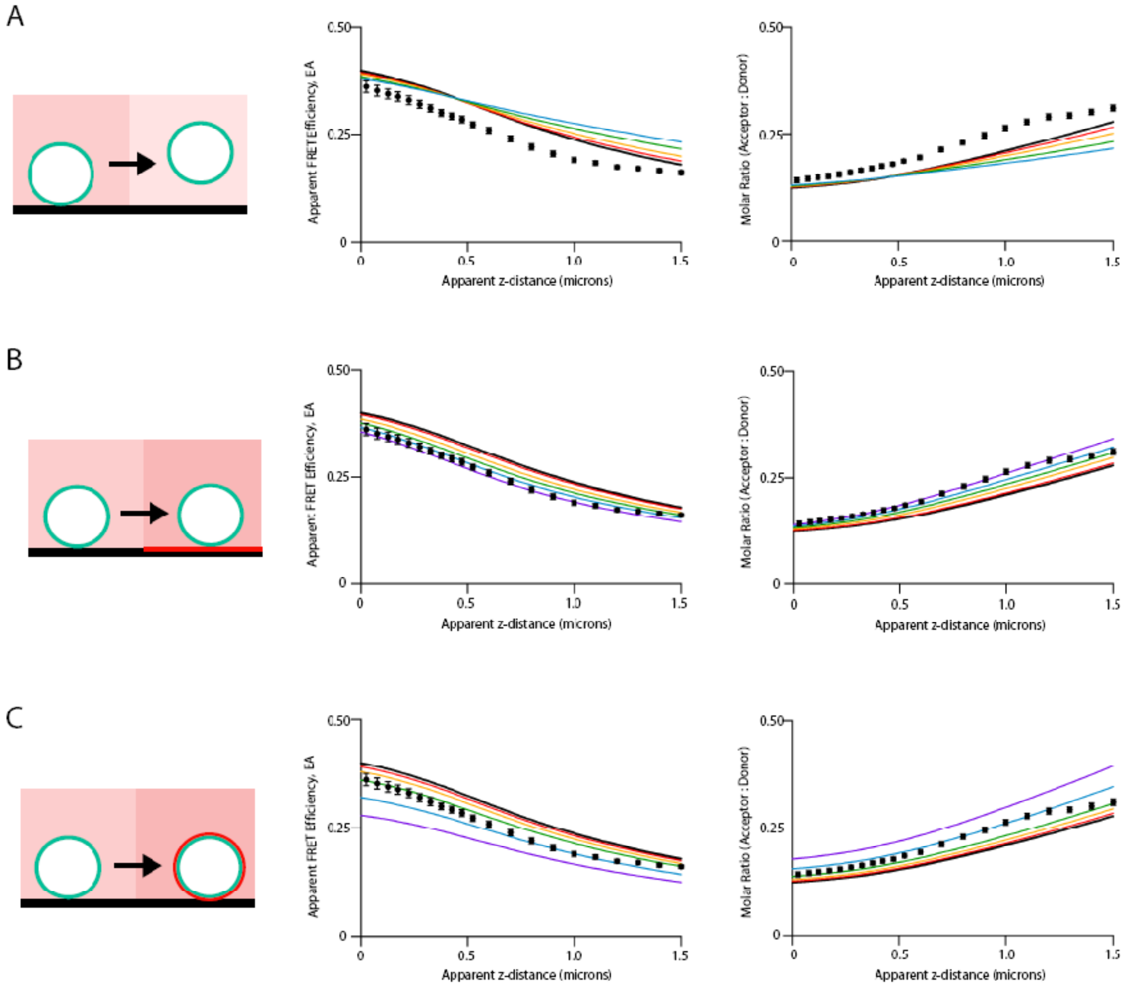
A
B
C
Apparent FRET Efficiency, EA
Molar Ratio (Acceptor : Donor)
Apparent z-distance (microns)
0.50
0.25
0
0
0.5
1.0
1.5

References

1. Lakowicz, J.R., *Principles of fluorescence spectroscopy*. 2nd ed. 1999, New York: Kluwer Academic/Plenum. xxiii, 698 p.
2. Periasamy, A. and R.N. Day, *Molecular imaging : FRET microscopy and spectroscopy*. 2005, New York: Oxford University Press. xv, 312 p.
3. Mochizuki, N., et al., *Spatio-temporal images of growth-factor-induced activation of Ras and Rap1.* Nature, 2001. **411**(6841): p. 1065-1068.
4. Murakoshi, H.H., et al., *Single-molecule imaging analysis of Ras activation in living cells.* Proceedings of the National Academy of Sciences of the United States of America, 2004. **101**(19): p. 7317-22.
5. Ni, Q., D.V. Titov, and J. Zhang, *Analyzing protein kinase dynamics in living cells with FRET reporters.* Methods, 2006. **40**(3): p. 279-286.
6. Miyawaki, A., et al., *Fluorescent indicators for Ca2+based on green fluorescent proteins and calmodulin.* Nature, 1997. **388**(6645): p. 882-887.
7. Zaccolo, M.M., et al., *A genetically encoded, fluorescent indicator for cyclic AMP in living cells.* Nature cell biology, 2000. **2**(1): p. 25-9.
8. Oheim, M., *Imaging Transmitter Release. II. A Practical Guide to Evanescent-wave Imaging.* Lasers in Medical Science, 2001. **16**(3): p. 159-170.
9. Jaiswal, J.K. and S.M. Simon, *Imaging single events at the cell membrane.* Nat Chem Biol, 2007. **3**(2): p. 92-98.
10. Greaves, J., et al., *Use of ANF-EGFP for the Visualization of Secretory Vesicles in Bovine Adrenal Chromaffin Cells.* Ann NY Acad Sci, 2002. **971**(1): p. 275-276.
11. Axelrod, D., T.P. Burghardt, and N.L. Thompson, *Total Internal Reflection Fluorescence.* Annual Review of Biophysics and Bioengineering, 1984. **13**(1): p. 247-268.
12. Bal, M.M., et al., *Calmodulin binding to M-type K+ channels assayed by TIRF/FRET in living cells.* The Journal of physiology, 2008. **586**(9): p. 2307-20.
13. Khakh, B.S., et al., *An Angstrom Scale Interaction between Plasma Membrane ATP-Gated P2X2 and {alpha}4{beta}2 Nicotinic Channels Measured with Fluorescence Resonance Energy Transfer and Total Internal Reflection Fluorescence Microscopy.* J. Neurosci., 2005. **25**(29): p. 6911-6920.
14. Riven, I., et al., *Conformational Rearrangements Associated with the Gating of the G Protein-Coupled Potassium Channel Revealed by FRET Microscopy.* Neuron, 2003. **38**(2): p. 225-235.
15. Fowler, C.E., et al., *Evidence for association of GABAB receptors with Kir3 channels and regulators of G protein signalling (RGS4) proteins.* J Physiol, 2007. **580**(1): p. 51-65.
16. Kozuka, J., et al., *Dynamic polymorphism of single actin molecules in the actin filament.* Nat Chem Biol, 2006. **2**(2): p. 83-86.
17. Margeat, E., et al., *Direct Observation of Abortive Initiation and Promoter Escape within Single Immobilized Transcription Complexes.* Biophys. J., 2006. **90**(4): p. 1419-1431.
18. Tateyama, M., et al., *Ligand-induced rearrangement of the dimeric metabotropic glutamate receptor 1[alpha].* Nat Struct Mol Biol, 2004. **11**(7): p. 637-642.
19. Rizzo, M.A., et al., *An improved cyan fluorescent protein variant useful for FRET.* Nat Biotech, 2004. **22**(4): p. 445-449.
20. Griesbeck, O., et al., *Reducing the Environmental Sensitivity of Yellow Fluorescent Protein. MECHANISM AND APPLICATIONS.* J. Biol. Chem., 2001. **276**(31): p. 29188-29194.
21. Hoppe, A., K. Christensen, and J.A. Swanson, *Fluorescence Resonance Energy Transfer-Based Stoichiometry in Living Cells.* Biophys. J., 2002. **83**(6): p. 3652-3664.

22. Miesenbock, G., D.A. De Angelis, and J.E. Rothman, *Visualizing secretion and synaptic transmission with pH-sensitive green fluorescent proteins.* Nature, 1998. **394**(6689): p. 192-195.
23. Liu, J., et al., *Fluorescence Resonance Energy Transfer Reports Properties of Syntaxin1A Interaction with Munc18-1 in Vivo.* J. Biol. Chem., 2004. **279**(53): p. 55924-55936.
24. Gladycheva, S.E., et al., *Receptor-mediated regulation of tomosyn-syntaxin 1A interactions in bovine adrenal chromaffin cells.* J Biol Chem, 2007. **282**(31): p. 22887-99.
25. Beemiller, P., A.D. Hoppe, and J.A. Swanson, *A Phosphatidylinositol-3-Kinase-Dependent Signal Transition Regulates ARF1 and ARF6 during Fcγ Receptor-Mediated Phagocytosis.* PLoS Biology, 2006. **4**(6): p. e162.
26. Mattheyses, A.L. and D. Axelrod, *Direct measurement of the evanescent field profile produced by objective-based total internal reflection fluorescence.* Journal of Biomedical Optics, 2006. **11**(1): p. 014006-7.
27. Chen, H., et al., *Measurement of FRET Efficiency and Ratio of Donor to Acceptor Concentration in Living Cells.* Biophys. J., 2006. **91**(5): p. L39-41.
28. Nagy, P., et al., *Novel calibration method for flow cytometric fluorescence resonance energy transfer measurements between visible fluorescent proteins.* Cytometry Part A, 2005. **67A**(2): p. 86-96.
29. Zal, T. and N.R.J. Gascoigne, *Photobleaching-Corrected FRET Efficiency Imaging of Live Cells.* Biophys. J., 2004. **86**(6): p. 3923-3939.
30. Allersma, M.W., et al., *Visualization of Regulated Exocytosis with a Granule-Membrane Probe Using Total Internal Reflection Microscopy.* Mol. Biol. Cell, 2004. **15**(10): p. 4658-4668.
31. Degtyar, V.E., et al., *Increased motion and travel, rather than stable docking, characterize the last moments before secretory granule fusion.* Proceedings of the National Academy of Sciences, 2007. **104**(40): p. 15929-15934.
32. Nofal, S., et al., *Primed Vesicles Can Be Distinguished from Docked Vesicles by Analyzing Their Mobility.* J. Neurosci., 2007. **27**(6): p. 1386-1395.
33. Oheim, M., et al., *The last few milliseconds in the life of a secretory granule.* European Biophysics Journal, 1998. **27**(2): p. 83-98.
34. Wiegand, U.K., et al., *Exocytosis Studies in a Chromaffin Cell-Free System: Imaging of Single-Vesicle Exocytosis in a Chromaffin Cell-Free System Using Total Internal Reflection Fluorescence Microscopy.* Ann NY Acad Sci, 2002. **971**(1): p. 257-261.
35. Gordon, G.W., et al., *Quantitative fluorescence resonance energy transfer measurements using fluorescence microscopy.* Biophys J, 1998. **74**(5): p. 2702-13.
36. Kuhn, J.R. and T.D. Pollard, *Real-Time Measurements of Actin Filament Polymerization by Total Internal Reflection Fluorescence Microscopy.* Biophys. J., 2005. **88**(2): p. 1387-1402.
37. Mattheyses, A.L., K. Shaw, and D. Axelrod, *Effective elimination of laser interference fringing in fluorescence microscopy by spinning azimuthal incidence angle.* Microscopy Research and Technique, 2006. **69**(8): p. 642-647.

Chapter 5

Conclusion

The present dissertation is largely focused on the regulation of SNARE protein function with respect to neurotransmitter release and neurosecretion. As SNARE proteins catalyze the final step of membrane fusion, these proteins represent the final molecular targets on which the signaling pathways and molecules regulating neurotransmitter release must converge. An understanding of these regulatory pathways and the mechanisms by which they modulate SNARE function is thus essential to an understanding of how the spatial and temporal properties of neurotransmitter release and neurosecretion are controlled. Accordingly, the first two studies of this dissertation focus on the mechanisms by which two different types of molecules, namely, bioactive lipids, and the protein tomosyn, exert control over SNARE protein function, and consequently, on regulated exocytosis. The third study of this dissertation focuses on the development of an imaging technique that could yield new insights into both the spatiotemporal dynamics and the functions of the molecular interactions that occur to elegantly orchestrate the process of regulated exocytosis.

Lipid Regulators of SNARE Function: PA and PI(4,5)P2

The merging of lipid bilayers and the formation of tight SNARE core complexes are two central and tightly coupled processes in membrane fusion. It is generally believed that the requirement of merging lipid bilayers sets a specific energy barrier that must be overcome for membrane fusion to occur, while the formation of SNARE core complexes generates the forces necessary to overcome this energy barrier and to catalyze membrane fusion. On the other hand, it has been shown that the presence of specific fusogenic lipids in the membrane can greatly reduce the energy barrier for fusion, and hence, the work that SNAREs would have to do to catalyze these events.

The first study of this dissertation addressed the questions of whether direct interactions between specific lipids and SNARE proteins exist, and moreover, whether these interactions might serve to regulate SNARE protein function. This study demonstrated that the soluble portion of the plasma membrane Q-SNARE Syntaxin1A (residues 1-267; lacks the transmembrane domain) formed direct interactions with acidic phospholipids, including the fusogenic lipid, phosphatidic acid, as well as PI(4,5)P2, a bioactive lipid that has been shown to exert considerable control over the process of regulated exocytosis. The ability of Syntaxin1A to interact with these lipids was mapped to Syntaxin1A's polybasic juxtamembrane domain, as progressive neutralizing mutations within this domain progressively reduced the binding affinity of Syntaxin1A for these lipids. To test the function of lipid binding-deficient Syntaxin1A mutant constructs, a BoNT-C knockdown and rescue assay was developed so that the secretory function of these exogenous Syntaxin1A constructs could be studied in isolation from endogenous Syntaxin1A. Importantly, these assays demonstrated that the progressive loss of Syntaxin1A's ability to bind acidic phospholipids could be correlated to a progressive loss in Syntaxin1A's secretory function. Amperometric analysis of individual fusion events catalyzed by mutant Syntaxin1A molecules subsequently revealed a lengthening in fusion pore duration, as well as a decrease in fusion pore diameter, compared to fusion events catalyzed by the wild-type Syntaxin1A, suggestive of an energetic defect in the mutant Syntaxin1A's ability to catalyze membrane fusion. Importantly, the inhibition of secretion observed with the lipid binding deficient Syntaxin1A constructs could be rescued by overexpression of phospholipase D1, an enzyme that generates phosphatidic acid, whereas knockdown of phospholipase D1 activity greatly inhibited control secretion, with little effect on secretion mediated by the lipid-binding deficient Syntaxin1A. Taken together, these experiments suggest that Syntaxin1A-lipid interactions are an important determinant of the energetics of membrane fusion. Moreover, they suggest that aside from playing a strictly mechanical role to overcome the energy barrier for fusion, SNARE proteins may also function to regulate the energy barrier itself at sites of fusion, through direct interactions with fusogenic lipids. Most importantly, these studies provide a link to bridge the gap between the protein-centered field of SNARE regulation, and the lipid-centered field of membrane fusion.

While these studies clearly demonstrated that direct interactions between a soluble portion of Syntaxin1A and specific acidic phospholipids occur in vitro, the critical questions remain as to whether these interactions would still occur for a full-length, membrane-reconstituted Syntaxin1A, and moreover, whether these interactions would occur in vivo. Notably, the full-length Syntaxin1A would be anchored to the plasma membrane via a transmembrane domain, and the polybasic juxtamembrane region would therefore be more structurally restricted in terms of its ability to interact with the headgroups of specific lipids.

One potential approach to detecting Syntaxin1A-lipid interactions in vivo might be to first determine whether Syntaxin1A and the lipid co-localize or co-cluster within the membrane compartment. While this approach would certainly not demonstrate a direct interaction, it would suggest that such an interaction might be functionally relevant in live cells. A previous study [1] examined the two-dimensional organization of PI(4,5)P2 and Syntaxin1A within the plasma membrane, using fixed PC-12 cell membrane sheets (in which the top portions of cells adherent to a glass coverslip are removed by a brief sonication pulse, leaving an intact layer of plasma membrane adherent to the glass).

Antibody labeling with Syntaxin1A resulted in distinct, bright puncta, suggesting that endogenous Syntaxin1A forms clusters within the plasma membrane. Antibody labeling of PI(4,5)P2 in these membrane sheets demonstrated that PI(4,5)P2 also distributed as bright, punctate clusters within a largely unlabeled plasma membrane. However, the PI(4,5)P2 distribution in fixed cells was quite different from that visualized in live cells by overexpression of an eGFP-labeled, PI(4,5)P2-specific PH domain, in which a few punctate structures could be discerned on top of a largely uniform bright background. These contrasting results leave it unclear as to what the "true" distribution of PI(4,5)P2 is in the plasma membrane. The diffuse labeling in the live, intact cells could have potentially arisen as an artifact of overexpression of the eGFP-PH domain and non-specific binding of this domain to the plasma membrane. Alternatively, the largely punctate structures of Syntaxin1A and PI(4,5)P2 in the plasma membrane sheets could have resulted as an artifact of the membrane sheet preparation, fixation, or even antibody labeling (as antibodies can, themselves, form clusters). Regardless, a small proportion (~13%) of large dense-core granules was found to colocalize with both Syntaxin1A and with PI(4,5)P2, and interestingly, this proportion of granules was greatly reduced in cells that had been stimulated to secrete (13% reduced to 3%), suggesting that exocytosis preferentially occurs from sites at which both Syntaxin1A and PI(4,5)P2 are present. On the other hand, the proportion of granules that colocalized with only PI(4,5)P2 clusters was similarly reduced (13% to 3%) following stimulation, suggesting several possibilities 1) syntaxin1A clusters do not actually facilitate secretion (fusion occurred equally on PI(4,5)P2 sites with or without syntaxin clusters); or 2) a more extreme case, fusion is more dependent on PI(4,5)P2 localization than it is on SNARE proteins! One other caveat to these studies is that the authors did not address whether the total granule number in cells was reduced following stimulation; in other words, while the decrease in the proportion of granules co-localized to PI(4,5)P2 that occurred following stimulation could imply that these granules preferentially fused, an alternative explanation would be that this shift in granule localization patterns could simply be due to recruitment or priming processes. Therefore, these studies require some additional clarification; however, they do illustrate the functional utility of the approach of colocalizing proteins and lipids in the membrane. Of interest, anti-phosphatidic acid antibodies have recently become commercially available (Cosmo Bio, Japan), and could be similarly used to determine whether Syntaxin1A and phosphatidic acid co-localize in cells, and whether these sites are functionally important to regulated exocytosis. It is important to note, however, that while these studies might support a functional role for the Syntaxin1A-lipid interaction, they would not be sufficient to demonstrate a direct interaction between Syntaxin1A and phosphatidic acid.

One potential method to visualize direct Syntaxin1A-lipid interactions in lipid bilayers might be to use synthetic fluorescently-labeled lipids (see Molecular Probes, Eugene, OR; or Avanti Polar Lipids, Alabaster, AL). Such lipids can be labeled on their acyl chains or on their headgroups (although depending on the specific lipid, the fluorescent tag could interfere with the function of the lipid or with its ability to interact with its normal molecular partners). These lipids could potentially be delivered to the plasma membranes of live cells, although one would need to be sure that the labeled lipid could “flip” or translocate from the outer leaflet of the plasma membrane (where it is delivered) to the inner leaflet (where its relevant interactions with Syntaxin1A would take place). One other complicating factor with this approach in live cells is that enzymatic activity within the cells could quickly metabolize the fluorescently labeled lipids into other by-products, making it unclear as to what the exact lipids / metabolites are that are being visualized with the fluorescent label.

Use of fluorescently labeled lipids in vitro, however, might be the most straightforward method for visualization of direct interactions between the full length

Syntaxin1A and a specific phospholipid. Here, the strategy would be to incorporate fluorescently tagged lipids into large unilamellar vesicles in which full-length Syntaxin1A would then be reconstituted. Conjugation of the full-length Syntaxin1A with a spectrally appropriate, small fluorescent tag near the juxtamembrane region would allow for direct interactions between Syntaxin1A and the lipid of interest to be detected using FRET. These studies would circumvent any confounding factors of lipid translocation or metabolism that might be problematic in live cells. While nonspecific FRET must always be considered as a confounding factor when dealing with high concentrations of donor and acceptor fluorophores restricted to a small compartment such as a liposome, this could be ruled out by decreasing the concentrations of the fluorescently labeled lipid and/or Syntaxin1A, as well as by testing similar concentrations of lipids to which Syntaxin1A should not bind. These experiments should clearly indicate whether the full-length Syntaxin forms direct interactions with specific lipids in the setting of a lipid bilayer. However, extrapolation of the relevance of these experiments to the live cell setting is ultimately limited by issues such as whether or not the concentrations of proteins/lipids used adequately reflect the concentrations seen in vivo; and moreover, whether there exist specific regulatory mechanisms in live cells that might preclude certain of the protein-lipid interactions detected in vitro from actually occurring in vivo.

Assuming that the Syntaxin1A-lipid interactions that occur in vitro do actually occur in vivo, the next questions to address would be to determine the specific function of these interactions with respect to regulated exocytosis; in other words, what are the specific stages of regulated exocytosis at which these SNARE-lipid interactions are important? The current study demonstrated that lipid binding-deficient Syntaxin1A molecules exhibited a reduction in secretory function. This defect, however, could encompass any of the stages of docking, priming, or fusion. Importantly, this study uncovered a defect in fusion pore widening in successful full-fusion events catalyzed by lipid-binding deficient Syntaxin1A molecules. This suggests that one role of Syntaxin-lipid interactions is to generate the lateral tension required to expand the fusion pore once it has formed. However, this result does not clearly address the mechanism by which the loss of Syntaxin1A-lipid interactions resulted in the decrease in secretion (as the effect on fusion pore widening was determined for fusion events that were, in the end, successful). Therefore, important questions remain: 1) Do Syntaxin1A-lipid interactions play a role in hemifusion or in the initial formation of the fusion pore? 2) Given that Syntaxin1A-lipid interactions regulate fusion pore dynamics, might these interactions also control the type of fusion event that occurs, eg, kiss-and-run fusion vs. full fusion?, or 3) Given the role of PI(4,5)P2 in priming, might Syntaxin1A-PI(4,5)P2 interactions play a role in priming?

The first question, whether Syntaxin1A-lipid interactions might be important for hemifusion or initial formation of the fusion pore, could be addressed using in vitro SNARE-reconstituted liposome fusion assays [2]. In these assays, two different sets of liposomes are created: one in which the plasma membrane SNAREs Syntaxin1A and SNAP25 are incorporated, and another in which the vesicle membrane SNARE Synaptobrevin/VAMP2 is incorporated. Importantly, different types of fluorescent lipids, as well as different vesicle content-filling fluorescent dyes, can be uniquely incorporated into each set of liposomes, such that as these liposomes undergo SNARE-catalyzed fusion, either lipid mixing or content mixing can be closely monitored. Defects in lipid mixing seen for SNARE complexes containing lipid binding-deficient Syntaxin1A molecules would illustrate the importance of Syntaxin1A-lipid interactions in mediating hemifusion, whereas defects in content mixing would illustrate the importance of Syntaxin1A-lipid interactions in mediating the initial formation of the fusion pore. Importantly, in vitro assays allow the exact composition of these liposomes to be controlled, such that specific roles for specific lipids in these processes could be discerned.

The second question, of whether Syntaxin1A-lipid interactions may control the type of fusion event that occurs, could be addressed using a combination of amperometry and TIRF experiments. Kiss-and-run events represent fusion events in which the fusion pore opens briefly and then closes, without full dilation. As such, these events can be detected in amperometric recordings as a pre-spike foot (ie, opening of the fusion pore) in the absence of a spike (ie, without full dilation of the fusion pore). These events are somewhat difficult to identify, however, as usually the key characteristic distinguishing a pre-spike foot from the background amplifier noise is that the pre-spike foot immediately precedes a large spike; regardless, this method has been previously used for this type of analysis [3]. If the relative proportion of prespike feet without a subsequent spike, compared to the total number of spikes, is altered for cells expressing lipid-binding deficient Syntaxin1A compared to wild-type Syntaxin1A, this would suggest that Syntaxin1A-lipid interactions are important in determining the mode of fusion events. Similar information could be gleaned using TIRF experiments on cells co-expressing the wildtype or mutant Syntaxin1A constructs along with the exocytotic marker, synaptopHluorin. SynaptopHluorin is a fluorescent probe comprised of the vesicle SNARE protein synaptobrevin/VAMP2, fused to a lumenal, pH-sensitive superecliptic GFP. Under resting conditions, the acidic environment in the vesicle lumen quenches the fluorescence of the pHluorin; however, upon fusion of these vesicles with the plasma membrane, the pHluorin becomes exposed to the neutral pH of the extracellular solution, and its fluorescence is unquenched. As such, exocytotic events can be detected as bright flashes of fluorescence as each vesicle fuses and its associated pHluorin molecules become unquenched. Importantly, as the pHluorin molecules are anchored to the membrane, their diffusion and fluorescence properties following fusion can be used to distinguish between full-fusion events and kiss-and-run events. Namely, full fusion would be characterized by a bright flash, followed by a slowly spreading and decreasing fluorescence originating from the initial site of fusion (as the vesicle membrane collapses into the plasma membrane and the synaptopHluorin diffuses freely throughout the plasma membrane), whereas kiss-and-run fusion would be characterized as a bright flash that is confined spatially and that rapidly disappears without spreading (as the fusion pore closes and the vesicle is reacidified) [4].

The third question, of whether Syntaxin1A-lipid interactions are involved in priming could be determined using capacitance measurements under patch clamp recordings. Effects of a lipid binding-deficient mutant Syntaxin1A on the initial size of the RRP or on refilling of this vesicle pool following depletion would implicate this region of Syntaxin1A as being important in priming. Moreover, if these effects on capacitance measurements were similar to those seen for the cells in which the PI(4,5)P2 generating enzyme PIPKI has been genetically deleted [5], this could potentially indicate that the priming defect seen with the mutant Syntaxin1A might be related to its inability to bind PI(4,5)P2. A potentially important experiment would then be to determine whether overexpression of PIPKI in cells expressing the mutant Syntaxin1A construct would be sufficient to rescue the defect in priming.

Protein Regulators of SNARE Function: Tomosyn

Assembly and disassembly of SNARE core complexes is tightly controlled by a large number of different proteins. What regulates these regulators? In other words, are there specific signals that dictate, in general, what the total number of functional SNARE core complexes should be at any given time in any given cell? One possibility is that specific signaling pathways that reflect the secretory demand placed on each cell might play a key role in regulating the formation/dissolution of SNARE core complexes in a manner that would be appropriate for each cell.

Tomosyn is a soluble R-SNARE protein that exerts an inhibitory effect on regulated exocytosis, supposedly through the formation of non-fusogenic SNARE core complexes with Syntaxin1A and SNAP25. The second study of this dissertation focused on whether the inhibitory activity of tomosyn on SNARE core complex formation is regulated by secretory demand. Interestingly, in response to secretagogue stimulation with DMPP, tomosyn was found to rapidly translocate from the cytosolic to plasma membrane regions of bovine adrenal chromaffin cells. This translocation was associated with an increase in the interaction between tomosyn and syntaxin1A, as measured by FRET; importantly, this increased interaction resulted in part from the increased cycling of tomosyn into tomosyn-SNARE complexes. Notably, the secretagogue-induced interaction of tomosyn and syntaxin1A occurred downstream of the Rho-GTPase/Rho-associated coiled-coil forming kinase (ROCK) signaling pathway, as demonstrated by the findings that: 1) secretagogue stimulation resulted in activation of RhoA; 2) inhibition of ROCK blocked the secretagogue-induced interaction between tomosyn and syntaxin1A; and 3) stimulation with LPA, a non-secretory stimulus that activates RhoA, resulted in an increased tomosyn-syntaxin interaction, similar to that seen with DMPP treatment. In PC-12 cells overexpressing tomosyn, secretagogue stimulation in the presence of LPA increased the inhibitory effect of tomosyn on secretion. This effect was blocked by inhibition of ROCK and required the ability of tomosyn to interact with syntaxin1A. Taken together, the experiments of this study demonstrate that the activity of tomosyn is regulated by secretagogue activation. These studies thus uncovered a mechanism by which the formation of SNARE core complexes can be dynamically regulated by secretory demand. Moreover, these studies highlight the value of using fluorescence imaging approaches to follow the spatiotemporal dynamics of protein-protein interactions in response to a specific stimulus.

While the present study supports the currently accepted model in the field for tomosyn's mode of action, whereby formation of nonfusogenic tomosyn-SNARE core complexes results in the inhibition of secretion, it is important to note the shortcomings of such a model. Namely, many tomosyn homologues have been demonstrated to play regulatory roles in vesicle trafficking and membrane fusion, yet the R-SNARE motif, which is critical for tomosyn's formation into SNARE core complexes, is not highly conserved among tomosyn homologs. Moreover, the N-terminal region of tomosyn comprises the majority of tomosyn's structure and is the most highly conserved region among tomosyn homologs, yet its function remains largely unaccounted for in the current model. Since the publication of the present study, this model has been challenged by a collaborative study with the Ashery laboratory, which demonstrated that a tomosyn truncation mutant that lacks the R-SNARE domain and that cannot interact with Syntaxin1A, is still sufficient to inhibit vesicle priming. Moreover, tomosyn's inhibitory effect was found to require its intact N-terminal domain, as an N-terminal deletion mutant of tomosyn could still bind to Syntaxin1A, yet lacked the ability to inhibit secretion [6]. Interestingly, our earlier findings also hinted at the fact that tomosyn does not require the R-SNARE motif for inhibition of secretion, as Figure 3.7 demonstrates that a C-terminal truncation mutant of tomosyn was capable of inhibiting exocytosis similarly to the wild-type tomosyn in response to secretagogue stimulation. Figure 3.7 does, however, demonstrate that an intact C-terminal domain of tomosyn is necessary for the regulation of tomosyn's inhibitory activity by the Rho/ROCK pathway. These results suggest that the N-terminal domain of tomosyn may comprise the "business" portion of the molecule that functions to inhibit exocytosis, whereas the C-terminal domain may be important in regulating the activity of the N-terminal domain or in localizing the protein to sites where it may preferentially act to inhibit secretion. Notably, one of the first reports on tomosyn demonstrated that both the N- and C-terminal regions of tomosyn were required for its inhibitory effect on secretion; however, the C-terminal truncation mutant of tomosyn used in this study (residues 1-738) deleted not only the R-SNARE motif, but also a large portion of the hypervariable linker between the R-SNARE motif and the N-terminal β-propellers [7]. These results would therefore suggest that the hypervariable linker plays a critical role in tomosyn's inhibitory effect on secretion.

In general, it appears that a new model for how tomosyn functions to regulate secretion may be in order. This model would need to account for how the N-terminal and hypervariable regions of tomosyn could inhibit secretion, which underscores the need to identify other proteins with which tomosyn (in particular, regions of tomosyn outside of the R-SNARE domain) might interact. One approach to solving this problem would be to purify tomosyn protein that lacks the R-SNARE domain, and to use this protein to pull down interacting proteins from a brain lysate; such interacting molecules could be subsequently identified using mass spectrometry. One shortcoming of this technique is that functionally significant but low affinity protein-protein interactions may not be identified in such an assay; the same would hold true for interacting proteins that might require binding to both the N- and C-terminal domains of tomosyn. Alternatively, the full-length tomosyn could also be used to pull down binding partners from a brain lysate. A complicating factor in this case is that the high affinity of tomosyn for syntaxin (~15nM), and the high level of syntaxin expression in the brain (~1% of total brain protein), would likely out-compete any potential binding partners from being detected. To circumvent this problem, the brain lysate could first be immunodepleted of syntaxin prior to binding to tomosyn, in order to maximize the chances of detecting novel binding partners. Again, mass spectrometry could then be used to identify these novel interaction partners.

Aside from uncovering new protein-protein interactions for tomosyn, another approach to understanding its mechanism of action might be through understanding the functions of its different isoforms. In mice, there are two paralogous genes for tomosyn (tomosyn-1 and tomosyn-2) that result in the expression of 7 different isoforms. Notably, the structural differences between these isoforms all occur within the hypervariable region of tomosyn that links the N-terminal β-propellers to the C-terminal R-SNARE motif. Interestingly, the expression of tomosyn isoforms has been shown to be regulated developmentally, with levels of tomosyn-1 exceeding levels of tomosyn-2 during embryonic stages (E10-E18), and with tomosyn-2 expression levels exceeding tomosyn-1 expression levels in postnatal stages of development (P12 to adult) [8]. Furthermore, expression levels of tomosyn-2 increase substantially over development (31-fold increase from E10 to P12), whereas the expression levels of tomosyn-1 remain relatively constant over development (only 2.7-fold increase from E10-P12). Moreover, the splice variants of tomosyn-2 are also modulated during development, with b-tomosyn-2 selectively expressed early on (E10-E12), and with all four tomosyn-2 splice variants being equally expressed by P12. This differential regulation of expression of tomosyn's genes and splice variants suggests that tomosyn may play other important roles in development, and that the regulation of neurotransmitter release by tomosyn may be more intricate than is currently understood. Importantly, there has been no study of the differences in tomosyn genes or isoforms with regard to synaptic function or regulated exocytosis (almost all studies have been performed on the m-tomosyn-1 isoform). However, the developmental regulation of the expression patterns suggests that tomosyn-2 might be more important for regulation of neurotransmitter release in a fully developed nervous system compared to tomosyn-1. Thus, it will be critical to elucidate how the different tomosyn isoforms differ functionally. Moreover, as the isoforms differ largely in the hypervariable linker region of tomosyn, these studies will also likely be informative as to the specific function of this region. Notably, this region has been demonstrated to contain a PKA phosphorylation site [9], suggesting that post-translational modification of this region may provide a key mechanism by which tomosyn's function in neurotransmitter release can be additionally regulated.

Development of an Optical Method to Visualize the Spatiotemporal Dynamics of Molecular Interactions that Regulate SNARE Complex Activity

The first two studies of this dissertation utilized the FRET imaging technique to some extent, as a gauge of specific protein-protein interactions that occur in intact, live cells. In the first study, FRET experiments demonstrated that, under resting conditions, the lipid binding-deficient Syntaxin1A construct bound to Munc18-1 similarly to the wild-type Syntaxin1A. The second study expanded upon this technique to visualize time-lapse changes in the tomosyn-syntaxin1A interaction that occurred in response to a stimulus. In the final study of this dissertation, the FRET methodology was extended even further, through the development of a new optical technique, termed sensitized emission TIRF FRET imaging. This technique could potentially allow for the visualization of the spatiotemporal dynamics of molecular interactions occurring at or near the plasma membrane, with concomitant tracking of the functional state of the individual secretory vesicles at which these interactions may be occurring. Notably, this technique is likely to yield many novel findings in the area of regulated exocytosis, as one of the critical remaining problems in the field lies in determining the sequencing of a number of different molecular interactions that must take place during the process of exocytosis of a secretory vesicle.

The third study of this dissertation focused on development of the theoretical and experimental considerations required for quantitative application of the sensitized emission TIRF FRET imaging in live cells. The motivating factors driving the utility of this technique are that: 1) unlike other methods of FRET imaging, sensitized emission FRET imaging is highly amenable to time-lapse imaging of bi-molecular interactions with high sensitivity and high temporal resolution; and 2) TIRF imaging provides extremely high axial resolution of the plasma membrane region (exactly where exocytosis occurs) to allow individual vesicles to be identified and tracked over time. While the combination of these methodologies would afford the sensitivity and high spatiotemporal resolution to sequence the dynamics of molecular interactions occurring near the plasma membrane, and to correlate changes in these interactions with changes in the functional state of granules, this technique is not without complications. Namely, sensitized emission FRET imaging requires calibration of the imaging system and fluorescent probes used to allow for determination of apparent FRET efficiencies and molar ratios. Moreover, TIRF imaging utilizes, for its illumination source, an evanescent field whose intensity decays exponentially in the z-direction. This complicates the interpretation of FRET results, which are inherently intensity-based and thus may differ depending on the z-position of the molecular interaction that is being tracked.

Prior to this study, there had been no indications as to how the sensitized emission calibration parameters or FRET measurements would be affected by evanescent illumination. Importantly, the current study adapted a technique of imaging large (10μm) fluorescent beads, to determine the exact relationships of the sensitized emission FRET calibration parameters and apparent FRET measurements with respect to z-distance from the glass/water interface. Of note, matching of the characteristic depths of the 442nm and 514nm laser lines was found to be critically important in minimizing z-distance dependent changes in FRET calibration parameters (ie, in creating flat FRET calibration parameter vs. z-distance relationships). Moreover, matching of the 442nm and 514nm TIRF depths was found to be critical for minimizing errors in the calculation of the apparent FRET efficiency at different z-distances from the glass-water interface.

This study also addressed the potential use of sensitized-emission TIRF FRET imaging in experiments in which the donor and acceptor probes exhibit subcellular localizations to compartments other than just the plasma membrane (eg, secretory granules, mitochondria, cytoskeleton, cytosol). These considerations are especially important in that many of these compartments may exhibit z-axis movements over the course of the experiment that could confound “true” changes in apparent FRET, with changes in apparent FRET that occur as a result of a change in z-position. Importantly, a combination of in vitro experiments and mathematical modeling led to several useful guidelines. First if both the donor and acceptor molecules localize exclusively to the same compartment and these localizations do not change over the course of the experiment, then the apparent FRET efficiencies and molar ratios measured will be independent of any changes in the compartment’s z-position. Second, if one of the probes (eg, the donor) localizes exclusively to a compartment, whereas the other probe (eg, the acceptor) localizes partially to that compartment and partially to the cytosol, then measurement of the apparent FRET efficiency of the probe localized exclusively to the compartment (eg, ED) will be independent of changes in the compartment’s z-position. Moreover, in this case, the extent to which the apparent FRET efficiency EA is dependent on changes in z-position of the compartment, will be dictated by a combination of the extent of cytosolic localization of the donor, and the extent to which the compartment moves in the z-direction. In these situations, mathematical modeling to simulate the specific imaging conditions (eg, subcellular localizations, proportion of probes on or off compartments, etc) can provide guidelines as to the amount of error that can be expected in EA measurements as a result of change in the compartment’s z-position. Lastly, this study implemented sensitized emission TIRF FRET in a controlled situation in live cells, and demonstrated that apparent FRET efficiencies and molar ratios changed linearly, as expected for linked citrine-cerulean FRET probes localized to either the plasma membrane or to secretory granules, in the presence of cytosolic citrine or cytosolic cerulean. Importantly, this study expands the possibilities for the application of sensitized emission TIRF FRET in living cells, and highlights some of the major issues which must be considered when applying this methodology to complex situations.

Full implementation of this technique for simultaneously tracking changes in FRET with changes in the functional status of individual granules will require incorporation of a spectrally distinct, vesicle-content filling probe, in addition to the FRET probes. Such a probe will allow for tracking of the X, Y, and Z motions of granules adjacent to the glass-water interface, as well as determination of when each granule undergoes fusion. Moreover, judicious selection of the FRET probes used in these experiments will likely make analysis of the data far more straightforward (ie, consider a situation in which both donor and acceptor fully localize to a granule, as opposed to a situation in which both FRET probes exhibit multiple subcellular localizations and change their localization patterns over time, on a subcellular compartment that moves substantially in the z-axis).

Importantly, full implementation of sensitized emission TIRF FRET concomitant with granule tracking capability should provide several key parameters that will be immediately helpful in sequencing the function of molecular interactions with respect to granule fusion. For instance, do the molecules interact before or after membrane fusion occurs? If they interact before membrane fusion, what is the latency time distribution of when the molecules interact compared to when the granule fuses? Do molecular interactions occur preferentially on granules that fuse vs. those that don’t fuse? Do the molecular interactions occur on granules that are highly mobile vs. those that are immobile? Do the molecular interactions change the mobility status of a granule? Do the molecular interactions appear to be spatially restricted to hotspot clusters of granules, or do they occur globally? While these are seemingly simple questions, the answers to such questions remain largely unknown for most proteins involved in regulated exocytosis, including even the SNARE proteins! This undermines the clear need to be able to resolve changes in these molecular interactions on a single vesicle level.

High temporal resolution visualization of the protein-protein interactions and the functional states of granules is ultimately limited by the brightnesses of the fluorescent probes used, as well as the sensitivity of the camera, both of which ultimately determine the exposure time required to achieve a sufficiently high signal-to-noise ratio. For instance, low fluorescence intensity signals would necessitate higher exposure times, which would ultimately dictate the maximum rate of image acquisition. Moreover, the total length of time for which these interactions can be followed at such a high temporal resolution will largely be dependent on the rate at which these probes undergo photobleaching. Photobleaching is likely to be the largest problem for sensitized-emission TIRF-FRET imaging, as this is a process that will likely be difficult to correct for, given that the rate of photobleaching will depend on not only the fluorophores used, but also the extent to which FRET occurs, as well as the z-positions of the fluorophores being imaged. Technological advances, including development of new genetically encoded fluorescent probes with higher extinction coefficients, high quantum yields, and higher resistance to photobleaching, as well as development of highly sensitive cameras that can largely reduce the required exposure times, are likely to play important roles in circumventing the problem of photobleaching.

Ultimately, the implementation of sensitized emission TIRF FRET is likely to transform the current understanding of the molecular processes that underlie regulated exocytosis. This type of transformation has many analogies to how the recordings of stochastic single channel currents from ion channels undoubtedly transformed the macroscopic view of how ion channels functioned. Importantly, the ability to visualize specific changes in protein-protein interactions in the context of individual secretory granules will be paramount to developing an understanding of the sequencing of molecular interactions that must be integrated for regulated exocytosis to occur.

Final Remarks

In summary, this dissertation comprises three somewhat distinct research projects that contribute to the fields of SNARE protein function and neurotransmitter release. Combined, the first two studies of this dissertation employ a wide variety of experimental approaches including molecular biology, biochemistry, electrophysiology, and fluorescence imaging, to analyze specific protein-protein and protein-lipid interactions that are critical to the process of membrane fusion. The final study of this dissertation lays the groundwork for a novel optical approach by which the spatiotemporal dynamics of bi-molecular interactions can be directly correlated to the activity of secretory granules or synaptic vesicles during regulated exocytosis. Altogether, the studies of this dissertation further our understanding of the molecular mechanisms that govern the final stages of neurotransmitter release, and take the additional step to develop a new technology that is likely to drive our understanding of the dynamic processes that occur in the field of membrane trafficking.

References

1. Aoyagi, K., et al., *The Activation of Exocytotic Sites by the Formation of Phosphatidylinositol 4,5-Bisphosphate Microdomains at Syntaxin Clusters.* J. Biol. Chem., 2005. **280**(17): p. 17346-17352.
2. Yoon, T.-Y., et al., *Multiple intermediates in SNARE-induced membrane fusion.* Proceedings of the National Academy of Sciences, 2006. **103**(52): p. 19731-19736.
3. Wang, C.T.C.-T., et al., *Synaptotagmin-Ca2+ triggers two sequential steps in regulated exocytosis in rat PC12 cells: fusion pore opening and fusion pore dilation.* The Journal of physiology, 2006. **570**(Pt 2): p. 295-307.
4. Gandhi, S.P. and C.F. Stevens, *Three modes of synaptic vesicular recycling revealed by single-vesicle imaging.* Nature, 2003. **423**(6940): p. 607-613.
5. Gong, L.-W., et al., *Phosphatidylinositol phosphate kinase type I{gamma} regulates dynamics of large dense-core vesicle fusion.* Proceedings of the National Academy of Sciences, 2005. **102**(14): p. 5204-5209.
6. Yizhar, O., et al., *Multiple functional domains are involved in tomosyn regulation of exocytosis.* Journal of Neurochemistry, 2007. **103**(2): p. 604-616.
7. Fujita, Y., et al., *Tomosyn: a Syntaxin-1-Binding Protein that Forms a Novel Complex in the Neurotransmitter Release Process.* Neuron, 1998. **20**(5): p. 905-915.
8. Groffen, A.J.A., et al., *Two distinct genes drive expression of seven tomosyn isoforms in the mammalian brain, sharing a conserved structure with a unique variable domain.* Journal of Neurochemistry, 2005. **92**(3): p. 554-568.
9. Baba, T., et al., *PKA-catalyzed phosphorylation of tomosyn and its implication in Ca2+-dependent exocytosis of neurotransmitter.* J. Cell Biol., 2005. **170**(7): p. 1113-1125.